



upna

Universidad Pública de Navarra  
Nafarroako Unibertsitate Publikoa

UNIVERSIDAD PÚBLICA DE NAVARRA

DOCTORAL THESIS

---

# Multidisciplinary design of wind turbine blades

---

*Author:*  
Fernando ECHEVERRÍA DURÁ

*Supervisor:*  
Dr. Fermín MALLOR

September 2, 2019

*“Donde todos los hombres piensan igual, nadie piensa mucho.”*

Walter Lippmann (1889-1974)



UNIVERSIDAD PÚBLICA DE NAVARRA

## *Abstract*

Doctorado en Tecnologías de las Comunicaciones, Bioingeniería y Energías  
Renovables (TECOMBER)

### **Multidisciplinary design of wind turbine blades**

by Fernando ECHEVERRÍA DURÁ

The impressive growth of the wind energy in the recent years makes necessary to improve the traditional design tools in order to respond to the high competitiveness. One of the most challenging component to be designed is the blade that plays an important role in the wind turbine performance and loads. The design of blades involves several technical tasks such as the geometry design, structural layout design, controls setting, loads calculations and structural verifications. In the traditional design process these tasks are performed by different experts in a sequential manner. At the end of each design loop, changes are applied to the design due to failures to fulfill any of the requirements of the design: excessive loads and/or deflections, low energy yield, non acceptable cost, transportation or logistic problems, undesirable surface fairness, etc. The implementation of the changes in the following design loop is decided with the basis of the intuition and experience of the different experts involved. In contrast to this procedure, a new process is proposed in this thesis with an important core stage based on optimization techniques that takes into account the complex interactions between the different technical tasks with a holistic view. The optimization engine is a code developed in this thesis that calculates, with the support of different subordinate codes, the wind turbine responses in terms of loads and performance under the design variables from the assorted technical tasks. Different research studies have been carried out in order to provide methods based on data analysis to obtain knowledge about the relationships between design variables and outputs. In spite of the complexity of the different types of calculations involved in the optimization, the computational cost is affordable in a real case design. The results of this thesis have been successfully applied to serial production blades.



## *Acknowledgements*

Quiero agradecer a mi tutor Fermín por todo el tiempo y esfuerzo destinado a la consecución de la tesis. A Elena, Javi, Unai y Álvaro por su gran ayuda técnica y moral. A la compañía Nordex Energy Spain por proporcionarme tiempo y recursos para la realización de la tesis. Y sobre todo a Cristina, Iñigo y Paula por estar siempre a mi lado.



# Contents

<b>Abstract</b>	<b>iii</b>
<b>Acknowledgements</b>	<b>v</b>
<b>1 Introduction</b>	<b>1</b>
1.1 Introduction to wind turbines	1
1.1.1 History of wind turbines	1
1.1.2 Wind turbine general description	2
1.1.3 Blade general description	4
1.2 Blade geometry	4
1.2.1 Coordinates system	5
1.2.2 Basic Definitions	5
1.2.3 B-spline fundamentals	7
1.2.4 B-spline for airfoil representation	9
1.2.5 B-splines for representing longitudinal laws	11
1.2.6 B-spline for blade surface representation	13
1.3 Blade structure	16
1.3.1 Introduction to composite materials	17
1.3.2 Basic terminology of fiber-reinforced composite materials	17
1.3.3 Blade general composite configuration	19
1.4 Traditional blade design process	20
1.5 Literature review of multidisciplinary blade optimization	22
1.6 Objectives of the thesis	25
1.7 Critical discussion and main contributions of the thesis	26
1.8 Organization of the thesis	29
1.9 Note about confidentiality	30
<b>2 Methods</b>	<b>31</b>
2.1 Aeroelasticity	31
2.1.1 Blade element momentum theory (BEM)	32
2.1.2 Panel methods	35
2.1.3 Structural analysis	35
2.1.4 Acoustic emission	37
2.1.5 Wind turbine control	37
2.1.6 Calculation codes	39
2.1.7 Calculation codes in this thesis	40
2.1.8 Wind modeling	41
2.1.9 Annual Energy Production (AEP) calculation	42
2.1.10 Loads assessment	43
2.2 Statistical methods	43
2.2.1 Surrogate models	45
2.2.2 Graphical Techniques	46
2.3 Sensitivity analysis	47

2.3.1	Linear regression . . . . .	48
2.3.2	Variance based methods . . . . .	48
2.4	Blade surface quality . . . . .	49
2.4.1	Airfoil curvature . . . . .	49
2.4.2	Surface interrogation methods . . . . .	50
2.5	Optimization . . . . .	52
2.5.1	Optimization statement . . . . .	53
2.5.2	Classification of optimization problems . . . . .	53
2.5.3	The curse of dimensionality . . . . .	54
2.5.4	Classical optimization algorithms . . . . .	55
2.5.5	Metaheuristic optimization algorithms . . . . .	56
<b>3</b>	<b>Blade design process</b> . . . . .	<b>59</b>
3.1	Overview of blade design process . . . . .	59
3.1.1	Explanatory design case . . . . .	59
3.2	Communication of the goals and requirements . . . . .	60
3.3	Input parameters . . . . .	61
3.3.1	Technical classification of inputs . . . . .	61
3.3.2	Classification of inputs according to the role in the optimization . . . . .	63
3.4	Optimization . . . . .	64
3.4.1	Optimization statement . . . . .	64
3.4.2	Design space exploration and sensitivity analysis prior to optimization . . . . .	65
3.4.3	Optimization strategy . . . . .	65
3.4.4	Potential solution . . . . .	66
3.5	AGORA . . . . .	66
3.5.1	Blade surface generation . . . . .	67
3.5.2	Calculation of aerodynamic coefficients . . . . .	67
3.5.3	Sizing of the pieces . . . . .	68
3.5.4	Positioning of caps and shear webs . . . . .	68
3.5.5	Positioning of trailing edge reinforcement (TER) and leading edge reinforcement (LER) . . . . .	70
3.5.6	Cross-sectional structural properties calculation . . . . .	71
3.5.7	Creation of aeroelastic model . . . . .	73
3.5.8	Types of aeroelastic simulations . . . . .	74
3.5.9	Aero-acoustic calculation . . . . .	76
3.5.10	Spar cap longitudinal strain estimation . . . . .	77
3.6	Verifications post-optimization . . . . .	77
3.6.1	Control setting adjustment . . . . .	77
3.6.2	Complete aeroelastic calculation set . . . . .	77
3.6.3	Structural verification of components . . . . .	77
3.6.4	Surface interrogation . . . . .	77
3.6.5	Aerodynamic assessment . . . . .	78
3.6.6	Manufacturing and logistic viability . . . . .	78
<b>4</b>	<b>Representation of airfoils with B-splines</b> . . . . .	<b>79</b>
4.1	Introduction of chapter . . . . .	79
4.2	Type of approximating error . . . . .	79
4.2.1	Geometrical error . . . . .	80
4.2.2	Aerodynamic error . . . . .	80
4.2.3	Wind turbine performance error . . . . .	81

4.3	Methodology of approximation . . . . .	82
4.4	Statistical treatment . . . . .	82
4.4.1	B-splines candidate configurations . . . . .	83
4.4.2	First analysis. Independent parametrization . . . . .	83
4.4.3	Second analysis. Control point selection. . . . .	84
4.4.4	Third analysis. Control point selection based on performance error . . . . .	86
4.5	Conclusions of the chapter . . . . .	86
<b>5</b>	<b>Fatigue estimation in the frequency domain</b>	<b>89</b>
5.1	Fatigue estimation in the frequency domain . . . . .	90
5.1.1	Wind turbine linearized model . . . . .	90
5.1.2	Effective wind speed . . . . .	91
5.1.3	Calculation of the DEL of the signal PSD . . . . .	92
5.2	Validation of the frequency domain method . . . . .	93
5.2.1	DEL calculation in the time domain. . . . .	94
5.2.2	DEL calculation in the frequency domain. . . . .	95
5.2.3	Results . . . . .	95
5.3	The frequency domain fatigue calculation in a blade design optimization . . . . .	96
5.4	Conclusions of the chapter . . . . .	98
<b>6</b>	<b>Analysis prior to the optimization</b>	<b>103</b>
6.1	Global sensitivity analysis . . . . .	103
6.1.1	Input variables . . . . .	103
6.1.2	Sensitivity analysis based on regression techniques . . . . .	104
6.1.3	Sensitivity Analysis based on Sobol-Saltelli indexes . . . . .	107
6.1.4	Conclusions of the sensitivity analysis . . . . .	108
6.2	Prediction of dynamic amplification of loads . . . . .	109
6.2.1	Graphical inspection . . . . .	111
6.2.2	Analysis of outliers . . . . .	112
6.2.3	Multiple logistic regression . . . . .	114
6.2.4	Analysis with fast and frugal trees . . . . .	115
<b>7</b>	<b>Application of the blade optimization methodology</b>	<b>119</b>
7.1	DTU reference model . . . . .	119
7.1.1	Validation of DTU 10MW RWT model in AGORA . . . . .	120
7.2	Introduction to optimizations . . . . .	122
7.2.1	Design space exploration . . . . .	122
7.2.2	Optimization techniques . . . . .	123
7.2.3	Setting parameters of genetic algorithm (GA) . . . . .	125
7.2.4	Setting parameters of particle swarm optimization (PSO) . . . . .	125
7.2.5	Setting parameters of simulated annealing (SA) . . . . .	127
7.2.6	Setting parameters of pattern search (PS) . . . . .	128
7.2.7	Setting parameters of gradient based algorithm (GB) . . . . .	128
7.3	Optimization scenarios . . . . .	129
7.3.1	Scenario A . . . . .	130
7.3.2	Scenario B . . . . .	132
7.3.3	Scenario C . . . . .	134
7.3.4	Scenario D . . . . .	136

<b>8</b>	<b>Conclusions</b>	<b>141</b>
<b>A</b>	<b>Open inputs of AGORA</b>	<b>145</b>
A.1	Geometrical inputs . . . . .	145
A.1.1	Spanwise laws . . . . .	145
A.1.2	Master airfoils . . . . .	146
A.2	Structural inputs . . . . .	146
A.2.1	Skin 1 . . . . .	146
A.2.2	Skin2 . . . . .	146
A.2.3	Skin3 . . . . .	147
A.2.4	Skin4 . . . . .	147
A.2.5	Root 1 . . . . .	147
A.2.6	Root 2 . . . . .	147
A.2.7	Cap 1 . . . . .	148
A.2.8	Cap 2 . . . . .	149
A.2.9	Shear webs . . . . .	150
A.2.10	Trailing edge reinforcement (TER) . . . . .	151
A.2.11	Leading edge reinforcement (LER) . . . . .	152
A.2.12	Core near LE . . . . .	153
A.2.13	Core near TE . . . . .	153
A.2.14	Core between caps . . . . .	153
A.2.15	Core of shear webs . . . . .	154
A.2.16	Extra mass . . . . .	154
A.2.17	Positioning of structural layout . . . . .	155
A.3	Environmental inputs . . . . .	155
A.4	Control inputs . . . . .	155
A.5	Other inputs . . . . .	155
<b>B</b>	<b>Sampling variation in Design Exploration</b>	<b>157</b>
<b>C</b>	<b>List of outputs from aeroelastic simulation</b>	<b>171</b>
	<b>Bibliography</b>	<b>173</b>



# List of Figures

1.1	ACCIONA Windpower AW3000 wind turbine . . . . .	2
1.2	Nordex wind turbine of Gamma generation . . . . .	3
1.3	Blade coordinates system. . . . .	5
1.4	Basic features of the airfoil . . . . .	6
1.5	3D view of a (a) straight blade and a (b) prebent blade . . . . .	7
1.6	Example of B-spline. . . . .	8
1.7	B-spline curve representing aerodynamic airfoil . . . . .	9
1.8	Geometrical transformations applied to a unit length length airfoil. . . . .	11
1.9	B-splines of longitudinal laws: a) chord, b) twist, c) thickness and d) stacking law along Y-axis. . . . .	12
1.10	B-spline of prebending law. . . . .	13
1.11	Unit length surface. Section curves are represented by red lines. . . . .	14
1.12	Final surface $SF$ , unprebent airfoil $M$ , prebent airfoil $M_p$ and prebending curve $p$ . . . . .	15
1.13	Blade final surface . . . . .	16
1.14	Main components of structural layout. . . . .	18
1.15	Section sample of a real wind turbine blade. . . . .	19
1.16	View of a manufactured blade prior to painting process . . . . .	19
1.17	Traditional blade design flowchart . . . . .	22
2.1	Collar's aeroelasticity triangle. . . . .	32
2.2	Airfoil 2D local loads and velocities . . . . .	34
2.3	(a) Electrical power, rotor speed, pitch angle and generator torque in function of wind speed. (b) Generator torque versus rotational speed. . . . .	39
2.4	Porcupine plot of an airfoil . . . . .	50
2.5	Isophotes map in a blade surface. . . . .	52
2.6	Schwefel function . . . . .	54
2.7	Optimization efficiency in Schwefel resolution . . . . .	54
3.1	Blade design flowchart. . . . .	60
3.2	Flowchart of explanatory design case. Design loop 1. . . . .	61
3.3	Flowchart explanatory design case. Design loop 2. . . . .	62
3.4	Nomenclature of the structural layout components. . . . .	63
3.5	Classification of inputs according to their role in the optimization. . . . .	63
3.6	Flowchart of calculation in AGORA. . . . .	66
3.7	Prebending curve before and after rotation with $p_{rotationd}$ . . . . .	67
3.8	Number of laminae along span in CAP1. . . . .	68
3.9	Reference plane and points in the blade surface with $\alpha_1 = 0^\circ$ , $\alpha_2^o = 1$ and $\alpha_3 = 0^\circ$ . . . . .	69
3.10	CAP1 positioning: A: surface generation. B: creation of reference plane. C: calculation of intersection. . . . .	70
3.11	3D view of B-spline surface and boundaries of CAP1, CAP2, LER and TER. . . . .	71

3.12	End position of TER and LER by cumulative length calculation along contour. . . . .	72
3.13	Relevant distances in the structural layout. . . . .	72
3.14	Extradados part of the airfoil where separation points and associated sectors are distinguished. . . . .	73
3.15	Outputs of steady calculation. . . . .	73
3.16	Time series of dynamic calculation with 10 m/s mean wind speed. . .	74
3.17	Hub and tower coordinate systems. . . . .	75
4.1	Geometrical error of an approximating curve $C(t)$ . . . . .	80
4.2	(a) Baseline airfoil and approximating B-spline. (b) Comparison of lift coefficient in function of angle of attack. (c) Comparison of drag coefficient in function of angle of attack (d) Comparison of moment coefficient in function of angle of attack. . . . .	81
4.3	Box and whisker diagram for the geometrical errors of the approximating B-spline configurations. . . . .	82
4.4	Box-and-whisker diagram for the geometrical error of the approximating B-spline configurations with centripetal parameterization. . . .	83
4.5	QQ plots of the errors associated to the approximating B-spline configurations with centripetal parametrization. . . . .	84
4.6	Wind turbine performance errors of airfoil approximations performed with B-splines of 15 control points ( $cp15$ ). . . . .	85
4.7	Histogram of (a) $\mu_{cp13} - \mu_{cp15}$ . Differences of means of groups $cp13$ and $cp15$ from all permutations. (b) $\mu_{cp13} - \mu_{cp17}$ . . . . .	87
4.8	Approximations with thirteen control points and centripetal parametrization to fifteen airfoils of UUIIC database. . . . .	88
5.1	Flow chart describing the DEL calculation in the frequency domain . . .	89
5.2	Cumulative variance of the PSD of the pitch rate signals under three blades id1, id2 and id3 and three wind fields seed1, seed2 and seed3. . . .	90
5.3	Cumulative variance of the PSD of the generator torque signals under three blades id1, id2 and id3 and three wind fields seed1, seed2 and seed3. . . . .	91
5.4	Power spectral density (PSD) of effective wind speed $V_{eff}$ ). Excitation frequencies 1P, 3P, 6P, 9P and 12P are presented in vertical lines. . . . .	92
5.5	Spanwise distributions: (a) chord, (b) twist and (c) relative thickness of the ten test blades. . . . .	93
5.6	DEL calculated in the frequency domain versus calculated in the time domain. Each point represents the result for one blade (mean wind speed of 14 m/s). (a) Blade root Mx, (b) Blade root My, (c) Blade 75% span My, (d) Hub Mx, (e) Hub My in stationary axes and (f) Tower base My. . . . .	94
5.7	Time series (a) and PSD (b) of moment Mx in root for two test blade models (id7 and id9). . . . .	96
5.8	First-order mass function versus DEL in the time domain. Each point represents the results for one blade. (a) Blade root Mx, (b) Blade root My, (c) Blade Mx (75% span) and (d) Tower base Mx. . . . .	97
5.9	DEL of stationary hub My with respect to blade. Values for the thirty wind seeds and the mean are presented. . . . .	98
5.10	Spanwise distributions: (a) Chord (b) Twist and (c) Relative thickness of solution and baseline. . . . .	99

5.11	Time history of the moment $M_y$ in hub for baseline and solution (simulation with 14 m/s mean wind speed).	100
6.1	Airfoil design variables in the sensitivity analysis.	104
6.2	Chord design variables in the sensitivity analysis.	104
6.3	Twist design variables in the sensitivity analysis.	105
6.4	AEP as function of the input variables: (a) <i>air6</i> , (b) <i>c3</i> and (c) <i>tw4</i> .	105
6.5	Standardized regression coefficients of multi-variable linear regression of <b>AEP</b> . Vertical lines represent the 95% confidences intervals.	106
6.6	Standardized regression coefficients of linear regression of <i>dxs_tip_max</i> . 95% confidence intervals are included.	106
6.7	Standardized regression coefficients of linear regression of blade <b>mass</b> . 95% confidence intervals are included.	107
6.8	Standardized regression coefficients of linear regression of <b>OAPWL</b> . 95% confidence intervals are included.	107
6.9	Sobol-Saltelli sensitivity indexes.	108
6.10	Histogram of design variable $X_1$ (Chord inboard knot) and $X_{26}$ (Gearbox ratio).	110
6.11	(a) DEL of moment $M_x$ in drive train in function of gearbox Ratio.(b) Maximum tip deflection along X-axis in function of outboard thickness knot.	111
6.12	Left: violin plot of DEL of $M_x$ moment in blade root based on gravitational cyclical loads. Right: violin plot of DEL calculated from dynamic aeroelastic calculations	111
6.13	DEL of $M_x$ moment in blade root based on gravitational cyclical loads with respect to DEL calculated from dynamic aeroelastic calculations: (a) 8 m/s, (b) 10 m/s, (c) 14 m/s and (d) 18 m/s	112
6.14	AEP from dynamic simulation. with respect to AEP from steady simulations.	113
6.15	$M_x$ moment in root at 8 m/s mean wind speed in (a) Time domain and (b) Frequency domain.	114
6.16	Decision tree calculated with FFTree technique to predict binary response <i>UNSTABLE</i>	117
7.1	Comparison of performance of DTU 10MW RWT: report I-0092 (table 3.5) versus model created in <i>AGORA</i> : (a) Mechanical power, (b) Thrust Force, (c) Rotor speed and (d) Pitch angle.	121
7.2	Design variables $x_1$ to $x_{22}$	122
7.3	Matrix of Pearson's coefficients between responses (rows) and design variables (columns).	123
7.4	MBO versus population size, number of elite individuals, crossover function and mutation rate.	124
7.5	METC versus population size, number of elite individuals, crossover function and mutation rate.	125
7.6	METC versus swarm size and relative weight. MBO versus swarm size and relative weight	126
7.7	METC versus temperature function and annealing function. MBO versus temperature function and annealing function	126
7.8	METC versus polling method, cache option, complete poll option and initial mesh	127

7.9	MBO versus polling method, cache option, complete poll option and initial mesh . . . . .	128
7.10	METC versus method (a) and step size (b). MBO versus method (c) and step size (d) . . . . .	129
7.11	Spanwise distributions of A7 optimization (PSO) and DTU 10MW RWT	130
7.12	Ratio of AEP in function of the mean annual wind speed of case A7 solution. . . . .	131
7.13	Electrical power, generator speed, maximum thrust force and maximum tip deflection of A7 optimization and DTU 10MW RWT . . . . .	131
7.14	Pareto points: Blade mass versus AEP, maximum blade tip deflection versus AEP, maximum thrust versus AEP and Mz at rated wind speed versus AEP . . . . .	132
7.15	Spanwise laws and main performance of B3 pareto points with AEP 99%, 100% and 101%. . . . .	133
7.16	Spanwise distributions of DTU 10MW RWT, solution of C7 and solution of C11. . . . .	136
7.17	Performance of DTU 10MW RWT, solution of C7 and solution of C11: electrical power, generator speed, thrust force and maximum blade tip deflection. . . . .	137
7.18	Surface of DTU 10MW RWT (upper part) and C11 solution (lower part). Color map represent longitudinal curvatures $k_v$ . . . . .	138
7.19	Surface between $z= 10\text{m}$ and $z= 25\text{m}$ of C11 solution (upper surface) and D solution (lower surface). Color map represent longitudinal curvatures $k_v$ . . . . .	139
A.1	Main structural components. . . . .	146
A.2	Laminae along span in Root1 . . . . .	148
A.3	Laminae along span in Root2 . . . . .	149
A.4	Laminae along span in cap2 . . . . .	150
A.5	Laminae along span in web . . . . .	151
A.6	Laminae along span in TER . . . . .	152
A.7	Laminae along span in LER . . . . .	153
B.1	Design variable 1. Chord knot inner . . . . .	157
B.2	Design variable 2. Chord knot outter . . . . .	158
B.3	Design variable 3. Chord coefficient inner . . . . .	158
B.4	Design variable 4. Chord coefficient inner-intermediate . . . . .	159
B.5	Design variable 5. Chord coefficient intermediate . . . . .	159
B.6	Design variable 6. Chord coefficient outer intermediate . . . . .	160
B.7	Design variable 7. Chord coefficient outter . . . . .	160
B.8	Design variable 8. Twist knot . . . . .	161
B.9	Design variable 9. Twist coefficient inner . . . . .	161
B.10	Design variable 10. Twist coefficient intermediate . . . . .	162
B.11	Design variable 11. Twist coefficient outter . . . . .	162
B.12	Design variable 12. Thickness knot inner . . . . .	163
B.13	Design variable 13. Thickness knot outter . . . . .	163
B.14	Design variable 14. Thickness coefficient inner . . . . .	164
B.15	Design variable 15. Thickness coefficient intermediate . . . . .	164
B.16	Design variable 16. Thickness coefficient outter . . . . .	165
B.17	Design variable 17. Prebending knot . . . . .	165
B.18	Design variable 18. Prebending coefficient . . . . .	166

B.19 Design variable 19. Stacking law along y inner coefficient . . . . .	166
B.20 Design variable 20. Stacking law along y intermediate coefficient . . .	167
B.21 Design variable 21. Stacking law along y outter coefficient . . . . .	167
B.22 Design variable 22. Main cap outter Thickness . . . . .	168
B.23 Design variable 23. Main cap intermediate Thickness . . . . .	168
B.24 Design variable 24. Main cap outter Thickness . . . . .	169
B.25 Design variable 25. Optimal gain . . . . .	169
B.26 Design variable 26. Gearbox Ratio . . . . .	170



# List of Tables

1.1	Recent wind turbine models of top ten wind energy companies. . . . .	4
1.2	Bibliography of blade design optimization . . . . .	28
2.1	List of calculation codes connected with aeroelasticity. . . . .	40
2.2	Confusion table. . . . .	47
4.1	$\phi$ -values of Wilcoxon paired hypothesis test . . . . .	85
5.1	Ratio between DEL of solution with respect to baseline: (a) Nominal expected, (b) Maximum expected, (c) Minimum expected and (d) Real. . . . .	98
5.2	Linear regression fitness for 6 m/s: Goodness of fit $R^2$ and regression coefficients. . . . .	99
5.3	Linear regression fitness for 10 m/s: Goodness of fit $R^2$ and regression coefficients. . . . .	100
5.4	Linear regression fitness for 14 m/s: Goodness of fit $R^2$ and regression coefficients. . . . .	100
5.5	Linear regression fitness for 18 m/s: Goodness of fit $R^2$ and regression coefficients. . . . .	100
5.6	Linear regression fitness for 22 m/s: Goodness of fit $R^2$ and regression coefficients. . . . .	101
5.7	Linear regression fitness for 10 m/s: Goodness of fit $R^2$ and regression coefficients. The time domain DLE values are the mean values of the simulations with thirty wind seeds. . . . .	101
6.1	Description of aeroelastic simulations of one task. . . . .	110
6.2	Wind turbulence intensities (%) of <i>DYNAMIC 1</i> group of simulations . . . . .	110
6.3	Coefficients and p-values of logistic regression performed to the binary response <i>UNSTABLE</i> . . . . .	115
6.4	Confusion table of multiple logistic regression (fitting observations). $P_{th} = 0.5$ . . . . .	115
6.5	Confusion table of multiple logistic regression (validation observations). $P_{th} = 0.5$ . . . . .	116
6.6	Confusion table of multiple logistic regression (fitting observations). $P_{th} = 0.85$ . . . . .	116
6.7	Confusion table of multiple logistic regression (validation observations). $P_{th} = 0.85$ . . . . .	117
6.8	Confusion table of FFTree (fitting observations) . . . . .	117
6.9	Confusion table of FFTree (validation observations) . . . . .	117
6.10	Summary of prediction performance of logistic regression and FFTrees . . . . .	117
7.1	Main features of the DTU 10MW reference wind turbine . . . . .	120
7.2	Comparison of main parameters of DTU 10MW RWT . . . . .	121
7.3	Goodness of fit ( $R^2$ ) of surrogate models. . . . .	123
7.4	Summary of recommended algorithm options . . . . .	129

7.5	Summary of optimizations of scenario A . . . . .	129
7.6	Summary of optimizations of scenario C . . . . .	135
C.1	. . . . .	172



# List of Abbreviations

ABCA	Ant Bee Colony Algorithm
AEP	Annual Energy Production
ALGA	Augmented Lagrangian Genetic Algorithm
ALPS	Augmented Lagrangian Pattern Search
BEM	Blade Element Momentum theory
BO	Best objective
BPM	Brooks, Pope and Marcolini model
BTM	Blade Total Mass
CAD	Computational-Aided Design
CFD	Computational Fluid Dynamics
CLPT	Classical Laminate Plate Theory
CLT	Classical Lamination Theory
COE	Cost Of Energy
DEL	Damage Equivalent Load
DTU	Technical University of Denmark
DTU 10MW RWT	DTU 10-MW Reference Rotor
ETC	Evaluations to convergence
FFTrees	Fast and frugal trees
FRF	Frequency Response Function
GA	Genetic Algorithms
GB	Gradient Based
GEBT	Geometrical Exact Beam Theory
KKT	Karush-Kuhn-Tucker
LE	Leading Edge
LSH	Latin Hypercube Sampling
MBO	Mean best objective
MBTD	Maximum Blade Tip Deflection
MDO	Multidisciplinary Optimization
METC	Mean evaluations to convergence
MSE	Mean Squared Error
NM	Nelder Mead
NTM	Normal Turbulence Model
NURBS	Non-Uniform Rational B-splines
OAPWL	Overall sound PoWer Level
PMC	Polymer-Matrix Composites
PS	Pattern Search
PSD	Power Spectral Density
PSO	Particle Swarm Optimization
QQ-plot	Quantile-Quantile plot
RC	Regression Coefficients
SA	Simulated Annealing
SLP	Sequential Linear Programming
SQP	Sequential Quadratic Programming

TE	Trailing Edge
TI	Turbulence Intensity
UIUC	University of Illinois Urbana-Champaign
VAM	Variational-Asymptotic Method
1D	One Dimensional
2D	Two Dimensional
3D	Three Dimensional

# List of Symbols

$p$	B-spline degree
$k$	B-spline order
$l$	number of pieces of the B-spline
$C^m$	m continuity of representations
$G^n$	n geometric continuity
$R_x$	stacking law along X-axis
$R_y$	stacking law along Y-axis
$c$	chord
$tw$	twist
$p$	prebending
$e$	thickness
$Cl$	lift coefficient
$Cd$	drag coefficient
$Cm$	moment coefficient
$\alpha$	angle of attack
$gain_{tsr}$	optimal gain
$kv$	longitudinal isoparametric curvature
$V_{eff}$	rotor effective wind speed
$c_i$	inequality constraint
$ceq_i$	equality constraint
$obj$	objective function
$X$	vector of design variables
$X_l$	lower boundary of design variables
$X_u$	upper boundary of design variables
$SF$	B-spline surface
$Fm$	first moment of mass
$C_p$	power coefficient
$\rho$	air density
$\omega$	rotational speed
$fxs\_yaw\_max$	maximum thrust force calculated from steady simulations
$dxs\_tip\_max$	maximum blade tip deflection along X-axis calculated from steady simulations
$dys\_tip\_max$	maximum blade tip deflection along Y-axis calculated from steady simulations
$mxs\_r\_del$	damage equivalent load estimated from steady simulations and $Fm$
$mys\_r\_max$	maximum out of plane moment in root calculated from steady simulations
$mzs\_r\_rated$	torsional moment in root at rated wind speed calculated from steady simulations
$rotzs\_tip\_amax$	torsional deformation of blade tip calculated from steady simulations



*Dedicado a Fernando, Fina, Cristina, Iñigo y Paula*



# Chapter 1

## Introduction

This thesis deals with the design of blades for horizontal axis wind turbines. The problem is addressed following a multidisciplinary point of view by considering the different technical sub-tasks as an unique problem which is solved by applying optimization techniques.

In this chapter, different introductory aspects are presented:

- The section 1.1 introduces the history and main components of modern wind turbines.
- In section 1.2 the construction of the blade geometry is described with special focus on B-splines that are the mathematical basis for the blade surface generation.
- The section 1.3 introduces the main fundamentals of composite materials and the blade internal structural layout.
- The traditional blade design as was conceived prior to the realization of the thesis is presented in section 1.4.
- The section 1.5 describes a review of the relevant literature regarding wind turbine blade multidisciplinary optimization.
- The main objectives of the thesis are presented in section 1.6.
- A critical discussion of the literature review and the summary of the contributions of this thesis are presented in section 1.7.
- Finally, the main organization of the thesis is presented in section 1.8.

### 1.1 Introduction to wind turbines

#### 1.1.1 History of wind turbines

The wind energy, as all the renewable energies has primary source on sun. 1-2% of the energy from sun is transformed into wind (air circulation). The wind is created due to difference of temperatures of different regions, the effect of the Coriolis force and the roughness of the earth's surface ([Danish wind industry association website](#)).

The wind has been used for more than 3000 years for several purposes: pumping water, ship sailing, grain grinding etc. The use of wind turbines to generate electricity can be traced back to the late nineteenth century with the 12kW DC windmill generator constructed by Brush in the USA and the research undertaken by LaCour in Denmark. The increase in the price of oil in the 1970s stimulated a number of



FIGURE 1.1: First propotype of ACCIONA Windpower AW3000 wind turbine

substantial Government-funded programs of research, development and demonstration. The so-called Danish wind turbine concept emerged of a three-bladed, stall-regulated rotor and a fixed-speed, induction machine drive train. This deceptively simple architecture has proved to be remarkably successful and has now been implemented on novel wind turbines (Burton, 2001).

In 1997 the Commission of the European Union published its White Paper calling for 12 percent of the gross energy demand of the European Union to be contributed from renewable by 2010. Wind energy was identified as having a key role to play in the supply of renewable energy with an increase in installed wind turbine capacity from 2.5 GW in 1995 to 40 GW by 2010 (Burton, 2001).

The European Union's renewable energy directive sets a binding target of 20% final energy consumption from renewable sources by 2020. To achieve this, EU countries have committed to reaching their own national renewable targets ranging from 10% in Malta to 49% in Sweden. Every two years, the EU publishes a renewable energy progress report. The 2017 report states that the EU as a whole achieved a 16% share of renewable energy in 2014. In 2016, the estimated share of renewable energy in the EU's gross final energy consumption was 17%. The vast majority of EU countries are well on track to reach their 2020 binding targets for renewable energy.

Renewable energy will continue to play a key role in helping the EU meet its energy needs beyond 2020. EU countries agreed in 2014 on a new renewable energy target of at least 27% of EU's final energy consumption by 2030, as part of the EU's energy and climate goals for 2030. On 14 June 2018 the Commission, the Parliament and the Council reached a political agreement which includes a binding renewable energy target for the EU for 2030 of 32%, with a clause for an upwards revision by 2023 (*European Commission website*).

### 1.1.2 Wind turbine general description

Among the possible wind turbine configurations, the present research is applied for a specific type: 3-blades, horizontal-axis, upwind, variable speed and active pitch





FIGURE 1.2: Nordex wind turbine of Gamma generation

regulated wind turbine, which is a widely adopted configuration for large multi-megawatt wind turbines ([ACCIONA Windpower products](#)).

The horizontal axis wind turbines contain the following components:

- The rotor is made up of blades (three is the general consensus in the wind energy industry) which transform the wind energy into torque. Blades are connected to hub which is connected to a gearbox by a low speed shaft.
- The pitch actuator rotates the blade about its axis to regulate the operation governed by the control of the wind turbine.
- The nacelle harbors the drive train components and sits atop the tower.
- Mechanical brake is a hydraulic caliper that ensures the stopping of the wind turbine under a failure of the pitch drive. It serves also as parking brake when maintenance is being performed.
- The gearbox increases the rotational speed (and decreases torque) to the range required by electrical generators. The high speed shaft connects gearbox to electrical generator.
- The electrical generator converts the torque into electricity. The heat exchanger maintains the generator at adequate temperature.

- The controller governs the wind turbine operation under fluctuation of wind environmental conditions. The anemometer measures wind speed and provides it to the controller. The wind vane measures wind direction and transmits it to the controller for nacelle orientation.
- The yaw drive rotates the nacelle in order to be aligned with the wind.
- The tower holds the nacelle providing necessary height to take advantage of the energy of wind.

Embedded in these main components many other sub components perform necessary functions. Additional extensive information can be found in (Burton, 2001) or (Hau, 2006).

Table 1.1 presents a list of relevant wind turbines developed by the main wind turbine manufacturers in recent years. Figures 1.1 and 1.2 show respectively AW3000 and Gamma generation wind turbines.

TABLE 1.1: Recent wind turbine models of top ten wind energy companies.

Company	Country	Name	Rated power (MW)	Blade length (m)	On/offshore	Diameter (m)
VESTAS	Denmark	V164-8.0 MW	8	80	Off and On	164
VESTAS	Denmark	V150-4.2MW	4.2	73.7	On	136
SIEMENS-GAMESA	Germany-Spain	SG 4.5-145	4.5	71	On	145
SIEMENS-GAMESA	Germany-Spain	SG 8.0-167	8	81.5	Off	167
GE	USA	Haliade-X 12MW	12	107	Off	220
GE	USA	Cypress	5.3	-	On	158
SENVION	Germany	6.XM	6.3	74.4	Off	152
GOLDWIN	China	GW 6.X	6.7	-	Off and On	154
ENVISION	China	148-4.5	4.5	72	On	148
ENERCON	Germany	E-141 EP4	4.2	-	On	141
ENERCON	Germany	E-126 7.580	7.58	-	On	127
SUZLON	India	S128	2.8	63	On	129
NORDEX	Germany	N149	4.5	72.4	On	148
UNITED POWER	China	UP6000-136	6	-	Off and On	136

### 1.1.3 Blade general description

The huge expansion of wind energy industry and the aggressive competence make necessary the development of bigger and more efficient wind turbines where the blades play an important role in the performance. The blade is a key wind turbine component that transforms the kinetic energy from the air to torque in the drive train. The blade can be divided in two important interconnected parts: the blade surface and the internal layout. The external geometry is designed to interact with the inflow wind to obtain the mechanical torque in the drive train that at the end is transformed to energy. Besides, the blade transmits forces and moments to the wind turbine components. Ideally, the ratio energy/loads should be maximum. The internal layout is conceived to withstand the ultimate and fatigue loads maintaining the structural integrity.

As important foundation for comprehension of following chapters, blade geometry is explained in section 1.2 and blade structural layout in section 1.3.

## 1.2 Blade geometry

In this section the blade geometry is introduced. The B-splines are the mathematical tools that support the generation of the geometry.

### 1.2.1 Coordinates system

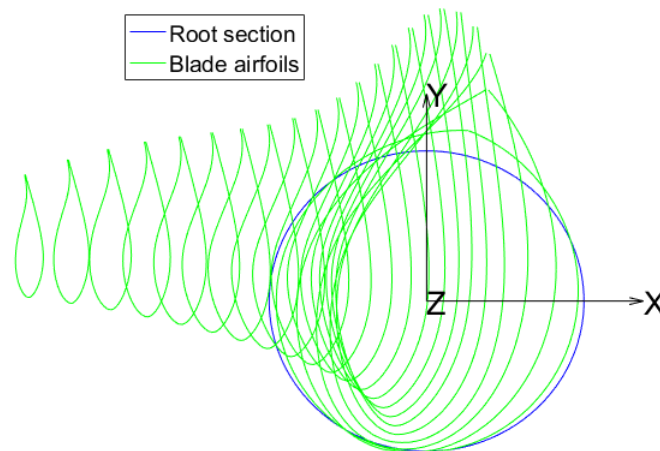


FIGURE 1.3: Blade coordinates system.

The blade reference system that will be applied along this thesis is a Cartesian right-hand system with the following convention:

1. Origin in blade root center.
2. Z-axis: normal to the blade root plane, positive towards the blade tip.
3. Y-axis: towards the trailing edge of the section with zero twist of the straight blade.

Figure 1.3 shows the coordinates system. Root section (at  $z = 0$ ) and several blade airfoils are also included.

The **out of plane moment** refers to moment about Y-axis, **in plane moment** refers to moment about X-axis and **torsional moment** refers to moment about Z-axis. The **flapwise** bending moment is the moment about chord line and **edgewise** bending moment about the perpendicular line to chord.

These terms are used extensively along the document.

### 1.2.2 Basic Definitions

The external blade geometry is a surface constructed by lofting or skinning the unit length airfoils after applying geometrical transformation (Piegl and Tiller, 1997). Some basic definitions are necessary for describing properly the blade. Figure 1.4 shows the main features of the airfoil.

- An **airfoil** is the intersection curve between the blade surface and a reference plane. This plane is parallel to XY plane in straight blades and prebent blades with sheared shape. In prebent blades with rotated shape (Bak, 2013), which is the approach applied in this thesis, the reference plane is normal to the prebending curve. The blade surface construction is based on **master** airfoils whose geometry and aerodynamic performance are known. The geometry and

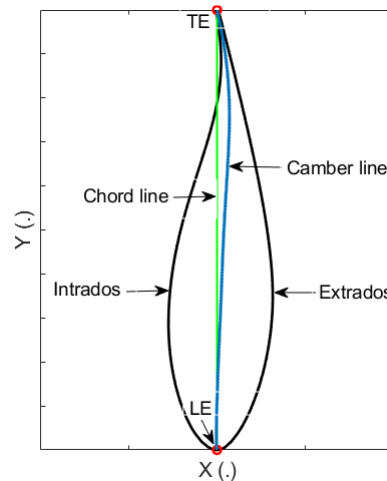


FIGURE 1.4: Basic features of the airfoil

aerodynamics of the intermediate airfoils between master airfoils are obtained by interpolation techniques.

- The **extrados** and **intrados** or **suction** and **pressure** sides are respectively the low and high pressure sides of the airfoil.
- The **trailing edge point (TE)** of an airfoil is the middle point of trailing edge segment that connects extrados and intrados.
- The **leading edge point (LE)** of an airfoil is the furthest point from TE point.
- The **chord** length is the segment that connects LE and TE.
- The **mean camber line** is formed by the points that lie halfway between extrados and intrados. The maximum distance between chord and camber lines is called the **camber**. The camber and chord lines are the same in non-cambered airfoils.
- The **thickness** is the maximum distance between the extrados and intrados in the direction normal to the chord line. The **relative thickness** is the ratio in percentage between thickness and chord. The relative thickness and camber are used to denominate master airfoils (*NASA guide to Aeronautics 2019*).
- The **unit length airfoil or airfoil in nondimensional form** is an airfoil without geometrical transformations: chord length is one, LE is in origin of coordinates and TE in  $\begin{bmatrix} x \\ y \end{bmatrix} = \begin{bmatrix} 0 \\ 1 \end{bmatrix}$ .
- The blade **span** is the position along Z-axis. Accordingly, **spanwise** means along Z-axis.
- The **longitudinal laws** are spanwise functions or curves that determine the geometric transformations performed to the unit length airfoils along span in order to obtain the blade surface.
- The **stacking law** defines the translation of the airfoils.

- The **chord law** defines the scaling of the airfoils along span.
- The **twist law** determines the rotation about Z-axis of airfoils along span.
- The **split lines** are two curves along span that correspond to connection between half molds in the manufacturing process. One split line coincides with TE and the other is close to LE.

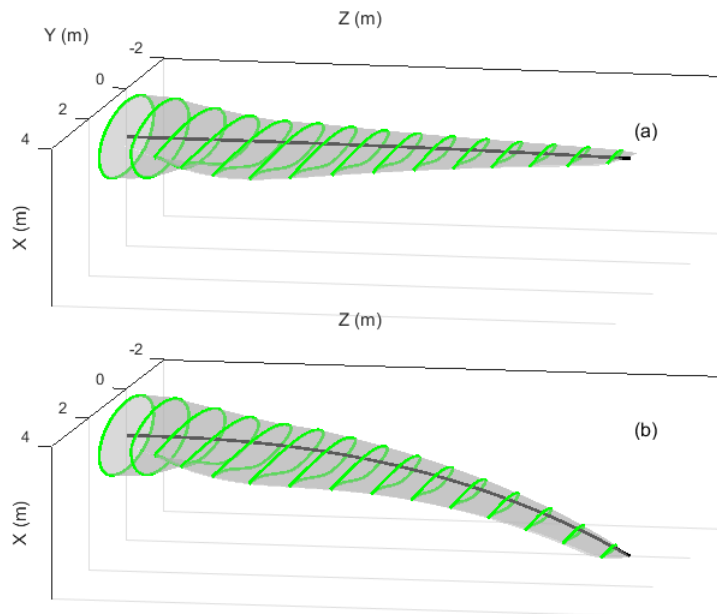


FIGURE 1.5: 3D view of a (a) straight blade and a (b) prebent blade

- **Prebending law** is a curve that defines translation and rotation of airfoil from the original position to a point in the prebending curve. In upwind horizontal axis wind turbine, the result of this transformation is a curved blade that gets away from tower to avoid collision. Figure 1.5 shows a straight blade (no prebending law is applied) and a prebent blade.
- **Root** is the circular section in  $z = 0$ .
- **Blade length**  $L$  is the  $Z$  coordinate of furthest airfoil from root.

### 1.2.3 B-spline fundamentals

For the representation of airfoils, longitudinal laws and resultant surface, the piecewise polynomial B-splines (Piegl and Tiller, 1997) are extensively adopted mathematical tools (Han, 2011)(Fuglsang and Dahl, 1999)(Obayashi, Tsukahara, and Nakamura, 2000). Non-uniform rational B-splines (NURBS) and particularly B-splines provide a unified mathematical basis for representing shapes. Designing with B-splines provides many advantages. They are intuitive, related tools and algorithms have a geometric interpretation and they are fast and numerically stable (Piegl and Tiller, 1997).

B-spline curve is a linear combination of control points and B-spline basis functions. Let  $Q = \{q_0, q_1, \dots, q_n\}$  be  $n + 1$  control points and  $U = \{u_0, u_1, \dots, u_m\}$

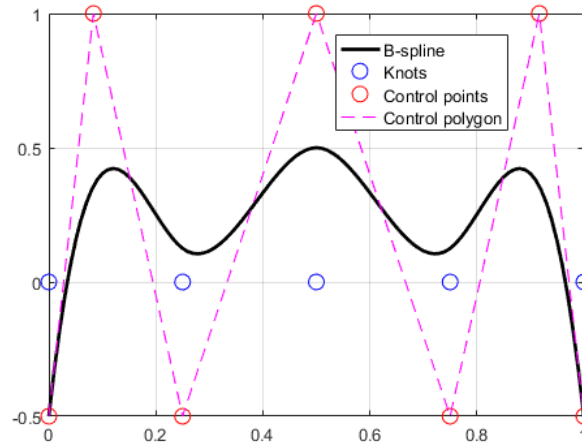


FIGURE 1.6: Example of B-spline.

a non-decreasing sequence called knot vector, the B-spline curve  $\mathbf{C}$  of degree  $p$  is defined by the equation 1.1 (Shene, 2011).

$$\mathbf{C}(u) = \sum_{i=0}^n N_{i,p}(u)q_i \quad (1.1)$$

$N_{i,p}(u)$  is a B-spline basis function of degree  $p$  defined by the Cox-de Boor recursion formula (Boor, 2001),(Shene, 2011):

$$\begin{aligned} N_{i,0}(u) &= \begin{cases} 1 & \text{if } u_i \leq u < u_{i+1} \\ 0 & \text{otherwise} \end{cases} \\ N_{i,p}(u) &= \frac{u-u_i}{u_{i+p}-u_i}N_{i,p-1}(u) + \frac{u_{i+p+1}-u}{u_{i+p+1}-u_{i+1}}N_{i+1,p-1}(u) \end{aligned} \quad (1.2)$$

The domain of B-spline basis functions is subdivided by knots:  $N_{i,p}(u)$  is a composite curve of degree  $p$  polynomial functions connected at knots  $(u_i, u_{i+p+1})$ .

B-form has become the standard way to represent a spline during its construction and manipulation (Shene, 2011). Figure 1.6 shows an example of cubic B-spline function created with (MATLAB curve fitting toolbox 2019).

Splines can be expressed in polynomial or pp-form. Let  $\xi_1, \dots, \xi_{l+1}$  be the breaks that divide the spline in  $l$  parts and  $c_{ji}$  the local polynomial coefficients, the spline  $p_j$  of order  $k$  is defined as:

$$p_j(x) = \sum_{i=1}^k (x - \xi_j)^{k-i} c_{ji}, j = 1 : l \quad (1.3)$$

The B-spline of figure 1.6 can be represented as pp-form in (MATLAB curve fitting toolbox 2019). The polynomial spline presents four pieces ( $l = 4$ ) and  $l * k = 16$  coefficients.

Prior to describe the properties of B-splines, the concept of continuity on curves is introduced. A curve can be described by several parametric representations. Essentials of the representation are its derivatives which allow to determine geometrical attributes of the curve like tangents and curvatures. Such geometrical attributes are independent of the representation. So it is necessary to distinguish between the continuity of representations  $C^m$ -continuity and the continuity of geometrical attributes



$G^n$ -continuity (Hartmann, 2003). Two connected parametric curves are  $C(u)^w$  continuous in the contact point  $u$  if the first  $w$  derivatives of the curves are continuous. However, the geometric continuity is inherent of the curve itself and independent of the parametrization. For example, the curves are curvature continuous or  $G(u)^2$  if the curvature vector is continuous. Analogous concepts can be defined for surfaces.

Some relevant properties of B-splines are the following (Shene, 2011):

1. The following equality is satisfied:  $m = n + p + 1$ , where  $m$  is the length of array of knots minus one,  $n$  is the number of control points minus one and  $p$  the polynomial degree.
2. Convex hull property: B-spline curve is always contained in the convex hull of the control points.
3. Local modification property: by changing the control point  $q_i$ , the curve  $C(u)$  is modified only on interval  $[u_i, u_{i+p+1}]$ . This local modification scheme is very important because a curve can be modified locally without changing the shape in a global way.
4. Affine invariance: an affine transformation applied to a B-spline curve can be constructed from the affine images of the control points.
5. Knot multiplicity: at a knot of multiplicity  $k$ , the B-spline is  $C^{p-k}$  continuous.
6. Bézier curves are special cases of B-spline curves. If  $n = p$  and there are  $2(p + 1) = 2(n + 1)$  knots with  $p + 1$  of them clamped at each end, this B-spline curve is a Bézier curve.
7. Interpolation of points. Given a set of points  $D = D_0, D_1 \dots D_w$  and a knot vector  $U$ , a set of control points  $Q$  can be calculated to construct a B-spline that passes through the points  $D$ . (*MATLAB curve fitting toolbox 2019*) provides the appropriate tools to perform this interpolation.

#### 1.2.4 B-spline for airfoil representation

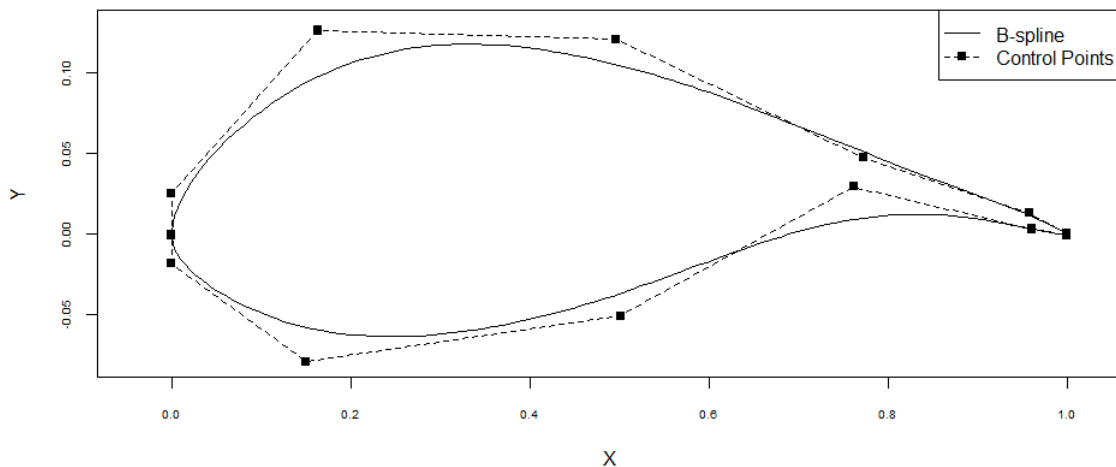


FIGURE 1.7: B-spline curve representing aerodynamic airfoil

With respect to airfoil geometry representation, different approaches are employed in the literature. The choice of the method is relevant for the design of airfoils as determines the type and number of design variables. (Samareh, 2001) presented a detailed summary of techniques. The discrete approach uses a set of coordinates of the airfoil, currently 100-200 points. This option is of a great simplicity and widely used but implies a great disadvantage for the design phase as the number of variables is very high. (Hicks and Henne, 1978) proposed a formulation where some functions are added to an initial geometry. The contribution factors of these functions, called shape or bump functions are set as the design variables whose modifications results in the desired geometry. PARSEC methodology (Vecchia, Daniele, and DAmato, 2014) expresses the geometry as a linear combination of base functions. The control variables are geometric characteristics of the airfoil such as the leading edge radius or trailing edge thickness. Piecewise polynomial B-splines are suitable functions of airfoil geometry generation (Piegl and Tiller, 1997) and are applied in this thesis.

The following introduces several practical aspects of the airfoil representation with B-splines. Currently, the master airfoil geometry is available as a set of points. A B-spline curve can be generated to interpolate or approximate the points. Furthermore, B-spline curves are appropriate to generate new airfoils in an optimization problem.

A knot vector for a given polynomial degree directly determines the distribution of the polynomial basis functions and hence the composition of curve segments. Many possibilities may be chosen to generate the knots sequence, for example uniformly spaced. (Han, 2011) proposes a formula which ensures that B-spline passes through the two edges of the trailing end and the leading edge (middle of vector sequence). In a cubic B-spline, the resulting knot sequence method produces a triple knot in the leading edge area and thus the inconvenience of producing a discontinuity in B-spline first derivative. However, the continuity can be restored by locating aligned three control points (Piegl and Tiller, 1997). An example is shown in figure 1.7. This methodology is applied in this thesis for airfoil representation.

To represent the airfoil curve in parametric form, the coordinates are represented as an explicit function of the independent parameter  $t$ .

$$\begin{aligned} \mathbf{C} : \mathbb{R} \supset [0, 1] &\rightarrow \mathbb{R}^2 \\ t &\mapsto \mathbf{C}(t) = [x(t); y(t)] \end{aligned}$$

For each value of the independent parameter  $t_i$ , there corresponds a point in the 2D space  $[x(t_i), y(t_i)]$ . The type of relation between the cartesian coordinates and the independent parameter is called independent parametrization.

The independent parametrization is relevant for the efficiency of the interpolation or approximation and different method are available in the literature (Lee, 1989).

Let  $D_0, D_1 \dots D_w$  be a set of airfoil points, the independent parameter  $t$  is specified according to equation 1.4.

$$t_{i+1} = t_i + |D_{i+1} - D_i|^a \quad (1.4)$$

The following methods are contemplated in function of the blending parameter  $a$  (Floater and Surazhsky, 2006):

- If  $a = 0$  the parametrization follows the uniform method.



- The chord length parametrization ( $a_1$ ) when  $a = 1$  corresponds to the distance between two adjacent points (Kleinmichel, 1970).
- Centripetal parametrization ( $a_{0.5}$ ) where  $a = \frac{1}{2}$  (Lee, 1989).

### 1.2.5 B-splines for representing longitudinal laws

Spanwise laws (stacking, chord, twist and prebending) determine the geometric transformations performed to the unit length airfoils in order to get the blade surface. These distributions are defined by B-splines. The geometrical transformations, applied to an airfoil in nondimensional form, are represented in figure 1.8. Besides, blade relative thickness determines the position of master airfoils along span.

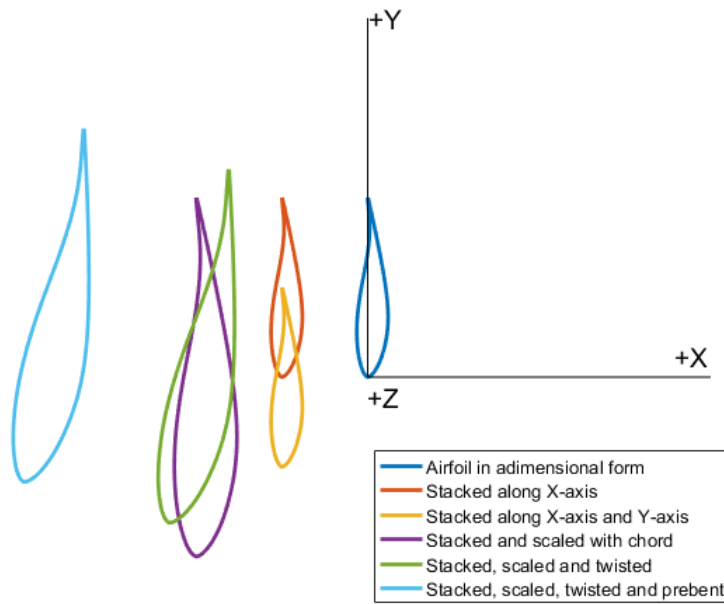


FIGURE 1.8: Geometrical transformations applied to a unit length airfoil.

The stacking law functions  $R_x$  and  $R_y$  define translations along X-axis and Y-axis performed to unit length airfoils depending on the Z coordinate:

$$R_x : \mathbb{R} \supset [0, L] \rightarrow \mathbb{R}$$

$$z \mapsto R_x(z)$$

$$R_y : \mathbb{R} \supset [0, L] \rightarrow \mathbb{R}$$

$$z \mapsto R_y(z)$$

Stacking law along Y-axis is also called sweep or presweep by some authors (Pavese et al., 2017). An example of stacking law along Y-axis is presented in figure 1.9 (d).

The chord function  $c$  defines scaling of stacked unit length airfoil depending on the Z coordinate:

$$c : \mathbb{R} \supset [0, L] \rightarrow \mathbb{R}$$

$$z \mapsto c(z)$$

An example of chord is presented in figure 1.9 (a).

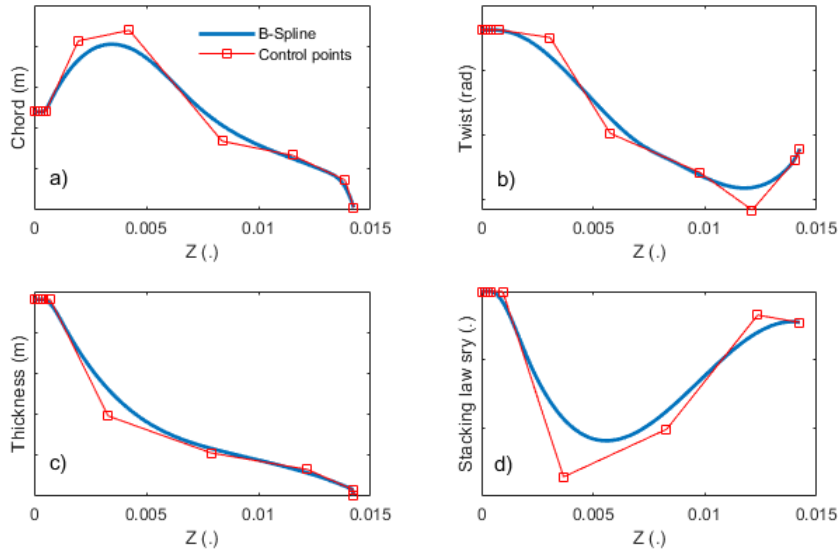


FIGURE 1.9: B-splines of longitudinal laws: a) chord, b) twist, c) thickness and d) stacking law along Y-axis.

The twist function  $tw$  defines twist angle of scaled and stacked unit length airfoil depending on the  $Z$  coordinate:

$$tw : \mathbb{R} \supset [0, L] \rightarrow \mathbb{R}$$

$$z \mapsto tw(z)$$

An example of twist is presented in figure 1.9 (b).

The prebending law  $p$  is the last operation performed to the unit length blade that consists of a translation with the aim of increasing the clearance between the tower and blade in an upwind wind turbine (Bazilevs et al., 2012). The prebending is represented as a B-spline curve with the following form:

$$\mathbf{p} : \mathbb{R} \supset [0, L] \rightarrow \mathbb{R}^3$$

$$z \mapsto \mathbf{p}(z) = [p_x(z); p_y(z); z]$$

An example of prebending is presented in figure 1.10.

Blade relative thickness  $tc$  is a B-spline function that determines the position of the master airfoils along span. An equivalent alternative is to employ the thickness  $e$  by multiplying the relative thickness by the chord.

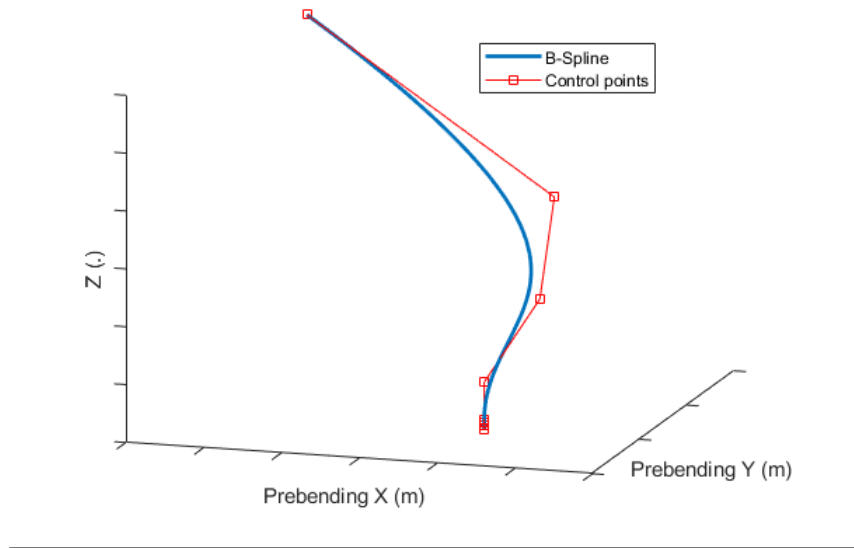


FIGURE 1.10: B-spline of prebending law.

$$e : \mathbb{R} \supset [0, L] \rightarrow \mathbb{R}$$

$$z \mapsto e(z)$$

An example of thickness is presented in figure 1.9 (c).

### 1.2.6 B-spline for blade surface representation

Prior to describe blade surface a brief explanation of parametric surfaces is introduced. Implicit or algebraic surfaces present the following general form:

$$\mathbf{SF} = \{(x, y, z) \in \mathbb{R}^3 \mid f(x, y, z) = 0\}$$

Parametric surfaces are defined in function of two independent parameters  $(u, v)$  according to next form:

$$\mathbf{SF} : \mathbb{R}^2 \supset [0, 1] \times [0, L] \rightarrow \mathbb{R}^3$$

$$(u, v) \mapsto \mathbf{SF}(u, v) = [x(u, v); y(u, v); z(u, v)]$$

In contrast with implicit surface representation, a parametric representation allows to directly generate points by evaluating values of the independent parameters  $(u, v)$  in the surface. Methods to fit and manipulate free-form shapes in implicit form are more complex than those for the parametric form both with respect to computation and geometric intuition (Patrikalakis M., 2009).

A B-spline surface is constructed as a tensor product surface that results from multiplying two basis functions of B-spline curves (Shene, 2011). The surface is characterized by a control net in two directions  $u$  and  $v$ , equivalent to a control polygon for a B-spline curve. One main advantage of this construction is that many operations to be performed to the surfaces are generalizations of curve operations. Most

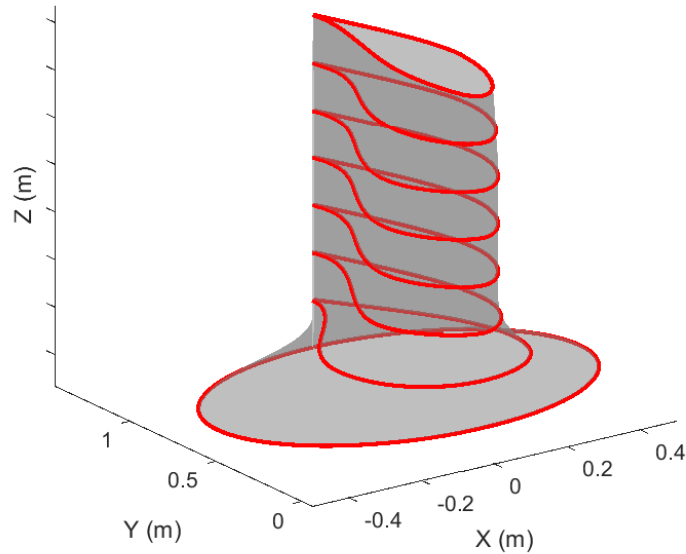


FIGURE 1.11: Unit length surface. Section curves are represented by red lines.

of B-spline properties can be extended from curve to surface e.g. convex hull, affine invariance, local transformation properties or knot multiplicity.

Given the following information (Shene, 2011):

- A matrix control of points  $q_{i,j}$ , where  $0 \leq i \leq m$  and  $0 \leq j \leq n$ .
- A knot vector of  $h + 1$  knots in the  $u$ -direction,  $U = \{u_0, u_1, \dots, u_h\}$ .
- A knot vector of  $k + 1$  knots in the  $v$ -direction,  $V = \{v_0, v_1, \dots, v_k\}$ .
- The degree  $p$  in the  $u$ -direction.
- The degree  $q$  in the  $v$ -direction.

The B-spline surface  $\mathbf{SF}$  is defined as:

$$\mathbf{SF}(u, v) = \sum_{i=0}^m \sum_{j=0}^n N_{i,p}(u) N_{j,q}(v) q_{i,j} \quad (1.5)$$

Where  $N_{i,p}(u)$  and  $N_{j,q}(v)$  are B-spline basis functions of degree  $p$  and  $q$  respectively.

With this mathematical basis, the blade surface is constructed as a lofted or skinned surface which is a widely used method for shipbuilding, automotive and aircraft design (Piegl and Tiller, 1997). Given a set of master airfoils and the longitudinal laws, all in B-spline form, these stages are distinguished in the blade surface construction:

- The unit length surface  $G$  is calculated by linear interpolation of B-spline curves in function of a mixing law, currently relative thickness. The unit length surface is expressed as a tensor product surface. The resulting surface is not a ruled surface (Piegl and Tiller, 1997) as the interpolation is performed as function of the mixing law and not as function of  $Z$  coordinate. The master airfoils should be compatible and thus should have a common knot vector and same degree. If the knot vector and/or degree of the B-splines are different, the B-splines should be modified in advance to insert knots and increase the degree without causing any modification of the curves. By taking advantage of affine invariance property, the interpolation performed to the control points is sufficient. Figure 1.11 shows a unit length surface.
- The unit length surface  $G$  is evaluated in several  $Z$  coordinates to get several section curve B-splines. The Greville and Chebyshev-Demko sites (Boor, 2002) are adequate ones for this purpose. These section curves form the skeleton of the blade.
- The section curves are transformed according to longitudinal laws. For a specific airfoil in nondimensional form  $M_0$  in  $z = z_0$  the following transformations are performed resulting the transformed airfoil  $M_p$ :
  1. Translate according to stacking law :  $R(z_0) = [R_x(z_0); R_y(z_0); 0]$ .
  2. Scale with the chord  $c(z_0)$ .
  3. Rotate about the  $Z$ -axis an angle of  $-tw(z_0)$ .
  4. Prebend: translate to a point in the prebending curve  $p(z_0)$  and rotate the section curve to be in a plane normal to the prebending curve. Figure 1.12 presents airfoil before and after prebending transformation. Final blade surface and prebending curve are also included in the figure.

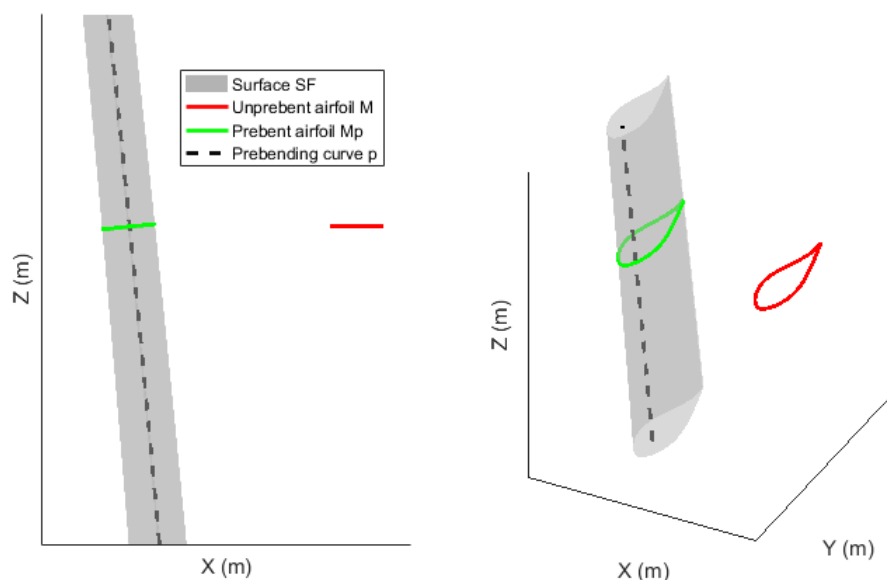


FIGURE 1.12: Final surface  $SF$ , unprebent airfoil  $M$ , prebent airfoil  $M_p$  and prebending curve  $p$ .

The equation 1.6 expresses the transformations 1 to 3.

$$M = \theta_{-tw(z_0)} c(z_0) (M_0 - R(z_0)) \quad (1.6)$$

Where matrix  $\theta_{-tw(z_0)} = \begin{bmatrix} \cos(tw(z_0)) & \sin(tw(z_0)) & 0 \\ -\sin(tw(z_0)) & \cos(tw(z_0)) & 0 \\ 0 & 0 & 1 \end{bmatrix}$ .

Besides, in transformation 4, airfoil  $M$  is translated and rotated according to equation 1.7 resulting airfoil  $M_p$ . This airfoil corresponds to a blade with prebending.

$$M_p = \theta_p \left( M - \begin{bmatrix} 0 \\ 0 \\ z \end{bmatrix} \right) + \begin{bmatrix} p_x(z_0) \\ p_y(z_0) \\ z \end{bmatrix} \quad (1.7)$$

By applying transformation expressed in equation 1.7, the resultant blade is a rotated blade shape in contrast to a sheared blade shape (Bak, 2013) where sections are only translated to the point of the prebending curve with same  $Z$  coordinate and remain parallel to  $XY$  plane.

- The definitive surface  $\mathbf{SF}(u, v)$  is calculated by lofting the section curves in the Greville sites (Boor, 2002) with the relative thickness as mixing law. Figure 1.13 shows a final blade surface B-spline. LE and TE curves are also represented in the figure.

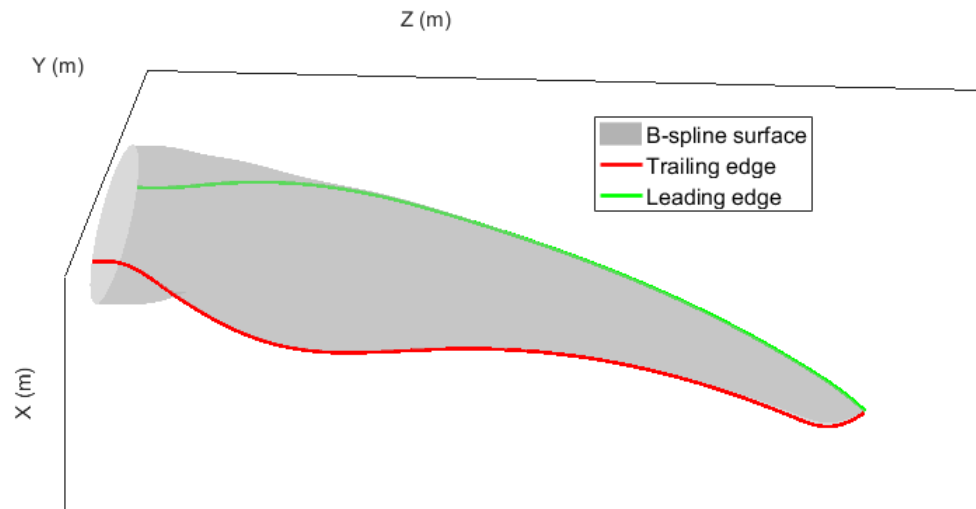


FIGURE 1.13: Blade final surface

### 1.3 Blade structure

Once the blade geometry is described, the second fundamental part of the blade is the internal layout that provides stiffness to ensure the integrity of the blade under different sources of loading. The structure is based on composite materials which are generally introduced in next subsection.

### 1.3.1 Introduction to composite materials

Composite materials are multiphase materials obtained through the artificial combination of different materials in order to attain properties that the individual components by themselves can not. The different phases are not formed by reactions, phase transformations, or other phenomena (Chung, 2010). Therefore, metal alloys do not belong to composites.

Composites are usually classified conforming to the matrix-binder material. Accordingly, the composite are polymer-matrix, cement-matrix, ceramic-matrix etc.

Within polymer-matrix composites (PMC), the fiber-reinforced composites consist in combining synthetic resins and embedded fibers to provide better strength properties than the basic resin material. At the end of 50's in aeronautic industry and later in aerospace, high performance composites were developed owing to demand for light-weight high resistance materials. Composites have become successfully employed in the construction of boats and for manufacturing all possible types of containers. Fiber-reinforced composite materials are adopted as preferred type of material for blade manufacturing.

The internal blade structure is a fiber-reinforced composite based system obtained by embedding continuous fibers in one or more orientations in a polymer matrix. This configuration provides attractive properties (Chung, 2010):

- Low density.
- High resistance.
- High stiffness.
- Good fatigue resistance.
- Low friction coefficient and wear resistance.
- Chemical and corrosion resistance.
- Dimensional stability. Low coefficient of thermal expansion.
- Vibration damping ability.
- Low electrical resistivity.

The use of fiber-reinforced composite materials in the blades is based on several factors. The reduced density with respect to metal alloys is an advantage as the gravity loads have an important impact in the wind turbine resistance (Burton, 2001). The versatility of the composite structural layout makes possible to adapt to the complex geometry of blades. The behavior under corrosion environments permits to install the blades in wind turbines located in aggressive locations, even in off-shore wind farms. Moreover, the structural properties of this type of materials are adequate to resist the high requirements of fatigue and extreme loads with a very competitive cost.

### 1.3.2 Basic terminology of fiber-reinforced composite materials

The basic components of laminated fiber-reinforced composite materials are presented in this subsection (Jones, 1998):

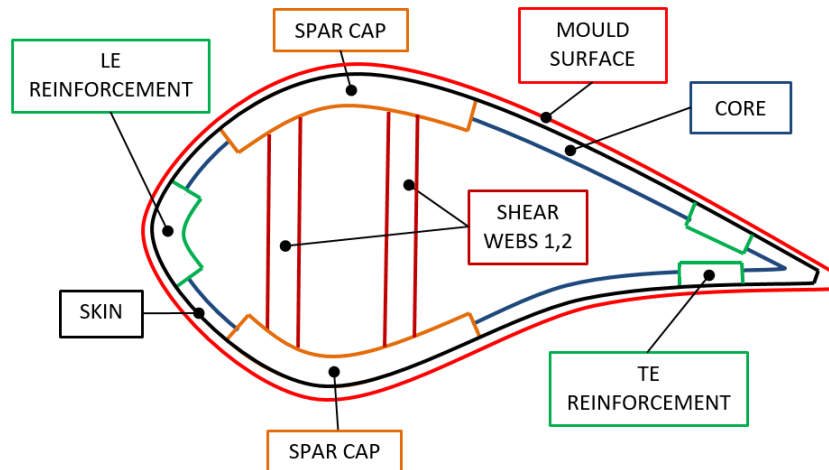


FIGURE 1.14: Main components of structural layout.

- Fibers are long and continuous threads or filaments. The fibers are conceived to resist the external loads aligned with their longitudinal axis. The material of the fibers can be glass (silica based), carbon, aramid or ceramic. In the wind energy industry, it is common practice to use long fibers of glass or carbon (Burton, 2001). Glass fibers present lower structural properties, higher density but a more competitive cost than carbon fiber. There are two main types of glass fiber: *E* (electrical) and *S* (strength). The first one presents lower mechanical properties but lower cost.
- A lamina (or ply) is a flat arrangement of fibers in a matrix.
- A laminate is a bonded stack of laminae with various orientations. The architecture can be unidirectional, bi-directional or tridimensional. The interlaminar interface is the space between adjacent laminae.
- A matrix is a continuous material that fills the space between fibers. The aim of this material is to transmit the loads between fibers, provide the desired geometry to the composite, protect fibers from degradation and provide specific surface roughness characteristics. The matrices can be organic (thermoplastic or thermoset), ceramic and metallic. Thermoplastic organic matrices are the preferred ones in the blades manufacturing as present several advantages. The manufacturing cost is lower and the performance is generally better (Chung, 2010). Vinilester, vinylheter, epoxy and fenolic are typical thermoplastic organic resin matrix materials, although polyester and epoxy are the most common in wind energy.
- The core is a component with low strength, high thickness and low density material that, in conjunction with laminates that cover the core, forms a sandwich panel. Common core materials are polyvinyl chloride (PVC), polyethylene terephthalate (PET), styrene-acrylonitrile resin (SAN) or balsa wood.



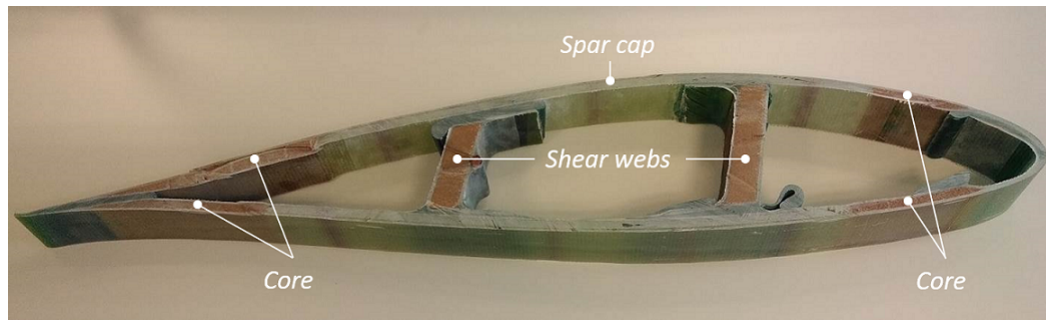


FIGURE 1.15: Section sample of a real wind turbine blade.

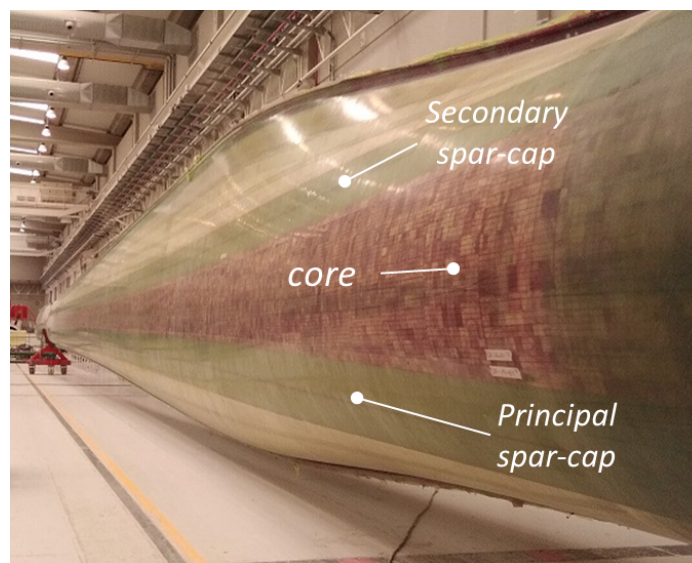


FIGURE 1.16: View of a manufactured blade prior to painting process

### 1.3.3 Blade general composite configuration

The simplest blade configuration is a full hollow blade that resists efficiently the flexural and torsional loads for small scale wind turbines. A sandwich panel compounded by layers and core material surrounds all the internal blade surface (Pourrajabian et al., 2016).

This configuration has evolved to two main concepts: box beam (Buckney et al., 2012) and shear web configuration (Thomsen, 2009). The shear web concept is considered in this thesis. The main components of this concept are:

- Spar caps are formed by laminates concentrated in the highest thickness part of the traverse section in both blade sides to withstand flapwise bending moment.
- Shear webs are stabilizing sandwich structures that connect spar caps to avoid buckling failure (Gaudern and Symons, 2010) and provide shear and torsional stiffness.
- LE and TE reinforcements are laminates in the blade contour near LE and TE to provide resistance in these weak areas of the blade.
- Skins are laminates that cover the complete contour of the blade.

- Core material fills space between main components without providing significant stiffness to blade. However, the core should withstand the compression loads without experimenting buckling phenomenon.
- Bonding joints connect layout components to ensure blade integrity and correct transmission of loads. Besides, the whole blade is connected with the hub by a bolted system.

According to this description, the architecture is depicted in figure 1.14.

Moreover, figure 1.15 shows a section cut where spar cap, shear webs and core material are distinguished. Figure 1.16 shows a manufactured blade prior to painting process where main structural components are shown.

## 1.4 Traditional blade design process

This section introduces the traditional blade design process which is described in the flowchart of figure 1.17. The following stages are distinguished:

1. The blade design requires detailed inputs from several fields and the environmental conditions:
  - Baseline structural inputs: mechanical properties, size and location of the structural internal components of the blade: spar caps, shear webs, cores, reinforcements, skins and other components.
  - Environmental inputs: mean hourly annual wind speed, turbulence intensity, mean air density, wind shear and extreme wind conditions.
  - Baseline geometrical inputs: master airfoil family information, and baseline spanwise laws. The geometrical inputs are generally provided as a set of points along span.
  - Control inputs: rotational speeds, rated power, torque-speed gain and gearbox ratio.
  - Other properties of the components of the wind turbine: tower, drive train, hub, generator and other minor components.
2. The baseline chord and twist are re-designed by means of an unconstrained optimization problem that maximizes power coefficient ( $C_p$ ) for the wind environmental conditions. The resulting distributions are represented as sets of points in different Z coordinates. Other spanwise laws are defined according to the experience of the designer.
3. Blade geometry is calculated by performing geometrical transformations to the master airfoils according to the spanwise laws from previous stage. The geometry is represented as a hull of points.
4. The baseline blade structural layout is modified. The structural components are sized and positioned along span. The resultant structural layout information and blade geometry are fed to a structural code that calculates the structural properties: mass, stiffness and positions of the relevant structural points.
5. Blade geometry, blade structural properties, main control parameters and other inputs are used to create an aeroelastic model and simulate the operation of the wind turbine under different wind conditions.

6. A detailed adjustment of the control regulation is performed with the aim of maximizing the ratio between annual energy production (AEP) and loads (Bossanyi, 2003) and ensuring the safe operation of the wind turbine. Besides, a supervisory control is defined to protect the wind turbine under specific abnormal environmental conditions.
7. The aeroelastic wind turbine model and the adjusted control are used to perform a complete load calculation set that provides a set of ultimate and fatigue loads in the wind turbine. The aeroelastic stability of the wind turbine is investigated in the simulations. Besides, the avoidance of collision between blade and tower is assessed. Furthermore, a power curve and a subsequent AEP are obtained.
8. Structural verification of components. Ultimate and fatigue loads from aeroelastic calculations serve to assess the viability of the wind turbine components. The blade internal layout components are also subjected to structural verification with different specific computational codes.
9. Surface generation with computational-aided design (CAD). The points of the blade geometry are introduced in a CAD software and an approximating surface to the points is generated.
10. The blade surface is subjected to interrogation methods in the CAD software environment to assess the fairness of the surface. If the fairness of the surface is not sufficient the geometry should be modified.
11. Decision making. At the end of the process and based on the results obtained, the blade design process is repeated (new loop) if some component experiments excessive ultimate or fatigue loading and/or wind turbine energy production is not successful. This is a crucial stage where the experience and intuition of engineers play an important role to change the blade geometry and/or structural layout and/or other parameters with the aim of correcting the design and getting a successful result in terms of loads and performance. The blade surface is transmitted to the mold manufacturing process if the design loop is successful.

The following weaknesses are identified in the traditional design process:

- The process requires computational expensive calculations and consequently, the time to complete one design loop is very long.
- The changes in the decision making phase are based on the intuition and the experience of the involved engineers. Nevertheless, the problem involves high complexity and implicates many engineering fields.
- The chord and twist are designed to maximize  $C_p$ . Other geometrical design variables, objective functions and/or constraints cannot be contemplated in the optimization.
- Interactions between geometry and blade dynamics are not taken into account in the geometry design. The geometry affects directly the aerodynamics but besides, presents important influence on the structural properties and on the blade dynamics which affect the aerodynamic response. These complex interactions and others that involve loads and controls are not taken into account in this traditional design process.

- Blade geometry is expressed in form of points. The process of approximating points by a blade surface with a CAD software involves errors and is time consuming. The approximation errors induce uncertainty about the validity of the calculations performed to the geometry represented by the original points.
- The process involves different experts. Aerodynamic, structural, loads, control and CAD engineers take part in some of the stages of the design. This segmented approach complicates a holistic view to the problem. A lack of global insight is identified.

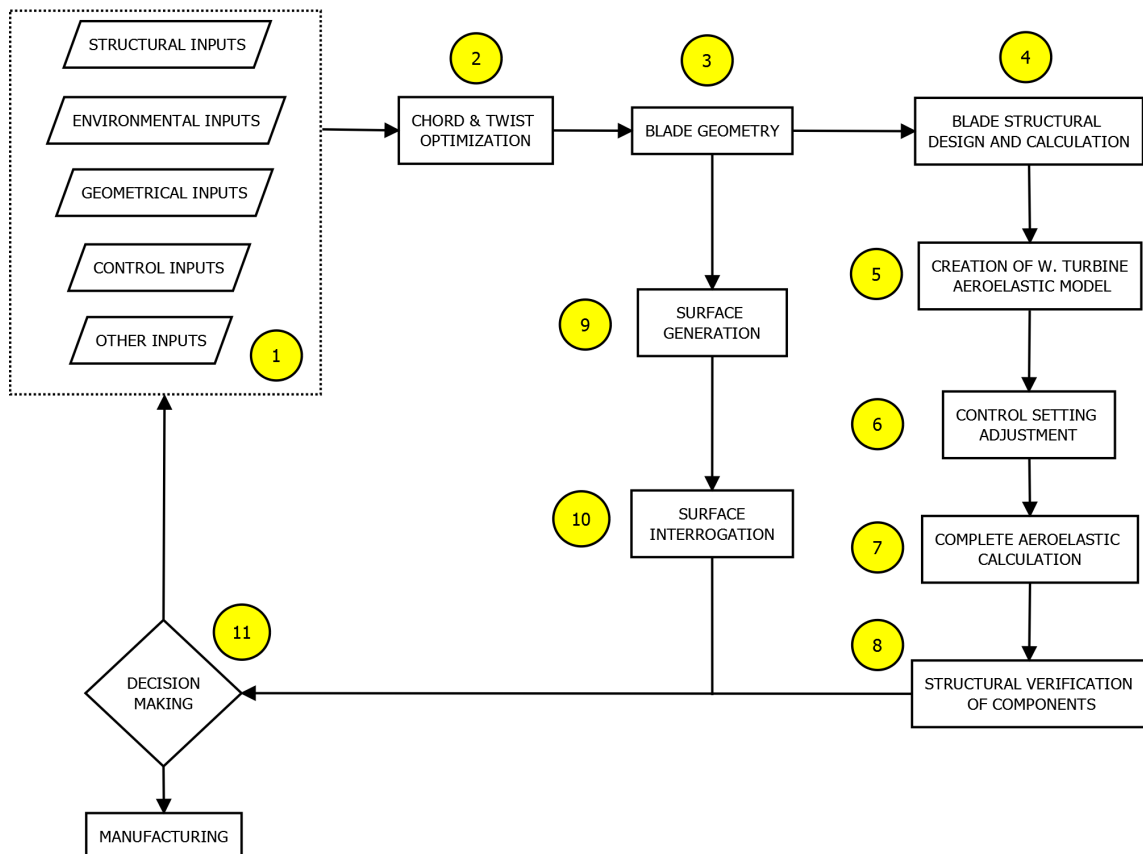


FIGURE 1.17: Traditional blade design flowchart

## 1.5 Literature review of multidisciplinary blade optimization

In this section, a literature review of research articles dealing with blade multidisciplinary optimization is presented. Table 1.2 summarizes in chronological order research papers in terms of type of the optimization characteristics: algorithm, objective functions and design variables.

Although the literature review is focused on wind turbine blade design, some articles that investigated aircraft wing design (Hicks and Henne, 1978), (Buckley, Zhou, and Zingg, 2010), (Han, 2011), (Kozziel and Leifsson, 2011), (Gagnon and Zingg, 2012), (Grasso, 2008) are included as problem presents many equivalences with the wind turbine blade design.

Many research papers address the design of single airfoil geometry. The adopted mathematical representation of the airfoil geometry is of great interest. B-splines are the most common mathematical tools although other methods are also applied (Samareh, 2001). Regarding the computational techniques for aerodynamic calculation, computational fluid dynamics (CFD) codes based on Navier–Stokes equations (Koziel and Leifsson, 2011), (Han, 2011), (Ebrahimi and Jahangirian, 2014) and panel method codes (Bizzarrini, Grasso, and Coiro, 2011), (Méndez, Munduate, and SanMiguel, 2014), (Grasso, 2008) are generally employed. These papers set some kind of aerodynamic efficiency as objective function. (Ebrahimi and Jahangirian, 2014) sets ratio of aerodynamic coefficients lift and drag. (Méndez, Munduate, and SanMiguel, 2014) develops a more complex airfoil objective function that combines specific performance characteristics of the airfoil such as sensitivity under rough condition or aerodynamic performance under specific angle of attack.

More recent articles incorporate additional engineering disciplines and design variables into the optimization problem. Blade geometry (length, chord, twist, relative thickness, prebending), structural internal layout (mainly spar cap), wind turbine control (pitch, rated power and rotational speed) and tower design are currently part of the design. Each particular research selects a different set of design variables depending on the particular purpose. In contrast, airfoil geometry design variables are removed from more modern papers and fixed master airfoils are employed (Ning, Damiani, and Moriarty, 2014), (Ashuri et al., 2014), (Zahle et al., 2015). Blade element momentum (BEM) theory (Hansen, 2008) based codes are generally used for calculations of wind turbine power, loads and deflections (Zahle et al., 2015), (Bottasso, Campagnolo, and Croce, 2012), (Fuglsang and Madsen, 1999). The objective function is related to the performance of the wind turbine in terms of energy production and loads (Zahle et al., 2015), (Fischer, Kipouros, and Savill, 2012). Cost of energy (COE) based on a theoretical cost model (Tegen, 2011) is set as objective function in recent papers (Bortolotti, Bottasso, and Croce, 2016), (Sartori et al., 2016).

Regarding the algorithms, Genetic Algorithms (GA) are widely used for single objective problems (Lee et al., 2013) or multi-objective problems (Obayashi, Tsukahara, and Nakamura, 2000). Gradient based (GB) algorithms are also a preferred option for many authors (Lee et al., 2013). Specifically, sequential quadratic programming (SQP)(Zahle et al., 2015) and sequential linear programming (SLP) (Fuglsang and Madsen, 1999) are common algorithms. The particle swarm optimization (PSO) (Chen et al., 2013), simulated annealing (SA) (Grasso, 2008), ant bee colony algorithm (ABCA)(Derakhshan, Tavaziani, and Kasaeian, 2015) and tabu search (TS) (Fischer, Kipouros, and Savill, 2012) are less employed alternatives.

The following is a more detailed description of the most relevant recent papers in multidisciplinary optimization (MDO).

- (Bortolotti, Bottasso, and Croce, 2016). This article describes *Cp-Max* MDO tool. The methodology consists of two level of optimization. Upper level calculates global design variables such as rotor radius, hub height, cone angle and tilt angle with the aim of minimizing COE. The low level optimizations deal with aerodynamic, blade structure and tower optimization with different objective functions and constrains. Control laws are also updated during optimization.



- (Croce et al., 2016). This work is also based on computational MDO tool *Cp-Max* (Bortolotti, Bottasso, and Croce, 2016) for computation of loads, AEP, deflections and cost. As novelty, it incorporates two set of structural design variables: offset of spar cap between intrados and extrados and fiber orientation along spar cap. The change of these design variables can produce a bend-twist coupling effect that alleviates loads (McWilliam et al., 2018). The flapwise bending moment induces a reduction of the angle of attack as result of coupled torsional deformation.
- (Sartori et al., 2016). Prebending related design variables are included in the optimization *Cp-Max* framework and the implications are investigated. The optimum curvature of prebending curve is searched.
- (Pavese et al., 2017). This paper assesses the benefits of adding sweep (stacking along Y axis) as design variable into the MDO problem. Ultimate and damage equivalent loads are estimated using steady-state and frequency-domain-based models (Tibaldi et al., 2016).
- (Macquart et al., 2017). Within the MDO problem, this article proposes a structural model to provide reliable structural properties with affordable computational cost. The framework relies on the use of B-spline surfaces and lamination parameters to provide a compact and continuous way of describing blade structures.
- (Dykes, Damiani, and Ning, 2017). This research goes one step further by optimizing the system-level performance. The WISDEM platform integrates turbine design (blade and support structure design included) and the wind plant design.
- (Bortolotti et al., 2018). This study integrates aeroacoustic frequency-based models within a wind turbine design procedure to include overall sound pressure levels as design constraints. The computational tool *Cp-Max* is the computation engine (Bortolotti, Bottasso, and Croce, 2016). Multi-objective and single objective problems are performed with GA and GB algorithms respectively.
- (McWilliam et al., 2018). This paper presents a holistic assessment to evaluate the impact of bend-twist coupling. Computational MDO tool *HAWTOpt2* is used. Besides material bend-twist coupling (Croce et al., 2016), geometry bend-twist coupling effect (Verelst and Larsen, 2010) is assessed. The objective function is a maximization of AEP with constraint of loads. This is a common industrial design problem where a manufacturer wants to develop a new set of blades for a platform already in existence. (*HAWC2*) is the commercial BEM theory based aeroelastic code.
- (Zahle et al., 2018). This research incorporates CFD simulations into the MDO problem for aerodynamic calculation. The associated high computational cost of CFD is dealt by generating a surrogate model with a reduced number of samples generated with latin hypercube sampling (LHS). The aim of the work is evaluating the impact of changes in the blade tip.

## 1.6 Objectives of the thesis

The main objective of the thesis is to improve the design of wind turbine blades in order to increase the efficiency of the wind turbine. This thesis is framed in the research field of blade multidisciplinary optimization.

The following sub-objectives are considered:

1. Develop a holistic methodology for the design of wind turbine blades that incorporates the different phases of the blade design and takes into account the complex interactions between engineering fields. The methodology is based on optimization techniques and will supersede the traditional methodology described in section 1.4. The blade geometry and the size and position of the main structural layout components that affect the dynamics of the blade should be determined in the design process. However, the detailed design of the structural layout is not dealt.
2. In order to achieve the first objective, create a computational code that calculates the relevant outputs of the wind turbines to assess the compliance of the blade design. The code should be affordable in terms of computational cost and should be ready to be launched automatically with the aim of being governed by optimization algorithms.
3. The blade source distributions (spanwise laws and airfoils) and subsequent surface will be expressed as reasonably smooth functions, not in form of points, to avoid manual CAD manipulation and the associated uncertainties.
4. Provide important knowledge about the important design variables in the blade design by applying data analysis methods.
5. Provide fast accurate estimation of loads and performance of wind turbines with a reduced computational cost.
6. Provide recommendations about the optimization techniques in the context of the blade multidisciplinary optimization.

The main challenge of the research consists in acquiring knowledge of several complex disciplines with different levels of insight:

- Wind turbines aerodynamics.
- Wind turbine control.
- Wind turbine noise.
- Mechanics of composite materials.
- Aeroelasticity.
- Elementary differential geometry of curves and surfaces.
- Data analysis.
- Optimization techniques.

Consequently, the handling of different complex computation codes is required.

## 1.7 Critical discussion and main contributions of the thesis

### Holistic approach

In wind turbine handbooks and guides (Burton, 2001)(Hau, 2006), it is assumed that optimizing a blade design corresponds to the maximization of the power output. In the variable speed area of the control, the maximum  $C_p$  at a specific tip speed ratio should be developed regardless the wind speed. With this assumption, in (Burton, 2001), analytic expressions are provided for the chord and twist distributions. Moreover, the blade geometry and structural designs are identified as clearly separated processes although it is explained that blade thickness needs to be large enough to accommodate a spar cap. In (Hau, 2006), it is explained that the aerodynamically optimum distributions of chord and twist of the rotor blades depend on the selection of a particular lift coefficient. As a rule, this lift coefficient will be selected such that at the design tip-speed ratio of the rotor, the blade is operated at the best possible lift to drag ratio.

These theoretical assumptions/rules are rejected in this thesis and the geometry is varied with the aim of optimizing a specific objective function and fulfilling constraints regarding the performance of the wind turbine. The potential objective function and constraints are assorted and depend on the particular requirements and conditions of each project and the vicissitudes of the progress of the project.

Recent research publications proposed a multidisciplinary approach but the geometry is optimized in a low level sub-optimization. Articles based on  $C_p$ -Max computational tool (Bortolotti et al., 2018), (Sartori et al., 2016), present a segmented problem in two levels of optimization. The designs of chord, twist and relative thickness are performed in a sub-optimization problem where maximization of AEP is the objective function. In the upper level optimization, the objective function is the cost of energy.

This thesis presents the design as a holistic problem where the design variables representing the blade geometry are considered at the same level as other types of design variables belonging to other technical fields as the structural layout design or control setting. All the design variables are governed by the optimization of the same objective function and the fulfillment of the constraints.

As a result of the approach presented in this thesis, the available design space is larger and there are more potential solutions. The main challenge that appears is the associated increase of computational effort to explore the design space with respect to more segmented approaches.

### Assessment of the sensitivity

In the consulted bibliography of blade multidisciplinary optimization, the design variables are listed and described with no prior justification of their importance in the objective function and constraints. This aspect is not a minor issue because the increment of design variables in the problem implies a great rise of computational cost in the optimization problem. Thus, knowing the importance of the design variables in order to reject the ones that are not necessary is a valuable information. Chapter 4 presents a method to identify the minimum necessary variables to represent airfoils with B-splines. Chapter 6 describes a global sensitivity analysis that ranks the design variables in function of the importance and permits to discard some of them from the optimization.

### Design exploration prior to the optimization

The exploration of the design space before performing the optimization provides



useful insight into the problem besides the assessment of the sensitivity. The exploration serves to detect abnormal performance and combinations of design variables to be avoided. Chapter 6 explains a design space exploration that reveals abnormal performance under specific combinations of design variables. With the aid of novel data analysis techniques, the undesired phenomenon is predicted.

### **Fast estimation of loads**

The aeroelastic simulations involve a very significant proportion of the total optimization loop time. Some authors deal with this aspect by performing stationary calculations (Pavese et al., 2017). Despite the computational cost, other authors use dynamic aeroelastic calculations (Ashuri et al., 2014), (Fischer, Kipouros, and Savill, 2014), (Bottasso, Campagnolo, and Croce, 2012). In addition to these alternatives also employed in the thesis, chapter 5 presents a novel frequency domain method to estimate fatigue loads. This method is an alternative to time consuming dynamic calculations for fatigue assessment. The accuracy and applicability of the method in the blade design are evaluated.

### **Deep analysis of the optimization techniques**

The consulted articles related to multidisciplinary optimization usually select one optimization algorithm for the problem as table 1.2 shows without further explanation or justification. However, a detailed evaluation of the most appropriate optimization techniques in the performance is not found. Chapter 7 presents an extensive set of optimizations performed to a public available wind turbine model. Conclusions about the suitability of the type of algorithm are provided. Besides, different optimization problems which are likely to appear in the design process are calculated. The influence of the optimization statement in the obtained solution obtained is very significant.

Three articles have been published in relevant scientific journals with the contents of this thesis:

- Global sensitivity analysis of the blade geometry variables on the wind turbine performance (Echeverria, Mallor, and San Miguel, 2017).
- Fast estimation of the damage equivalent load in the blade geometry multidisciplinary optimization (Echeverria, Mallor, and Sanz, 2017).
- Design exploration prior to blade multidisciplinary optimization (Echeverria, Mallor, and San-Miguel, 2018).

TABLE 1.2: Bibliography of blade design optimization

Year	Citation	Algorithm	Objective function	Design variables
1978	Hicks and Henne, 1978	GB	Aerodynamic performance	Wing geometry
1998	Dahl and Fuglsang, 1998	SLP	Aero. and structural performance	Airfoil geometry
1999	Fuglsang and Madsen, 1999	SLP	COE	Blade geometry, rotor $\emptyset$ , airfoil polars, pitch and rot. speed
2000	Giguere and Selig, 2000	GA/GB	Aero., struc. performance, noise and COE	Chord, twist, pitch, rotor $\emptyset$ , airfoil family and no. of blades
2000	Obayashi, Tsukahara, and Nakamura, 2000	GA	Aerodynamic performance	Airfoil geometry
2002	Bak and Fuglsang, 2002	GB	Aerodynamic performance	Airfoil geometry
2002	Benini and Toffolo, 2002	GA	AEP and COE	Tip speed, Hub/tip ratio, chord and twist
2005	Overgaard and Lund, 2005	GB	Structural performance	Structural layout
2006	J. Méndez, 2006	GA	Structural performance	Chord and twist
2008	Grasso, 2008	GB, SA and GA	Aerodynamic performance	Airfoil geometry
2009	Xudong et al., 2009	GB	COE	Chord, twist, relative thickness and pitch
2009	Richard W. Vesel, 2009	GA	AEP and noise	Airfoil geometry, chord, twist, pitch, and rot. speed
2010	Buckley, Zhou, and Zingg, 2010	SQP	Aerodynamic performance	Airfoil geometry
2011	Han, 2011	SQP	Aerodynamic performance	Airfoil geometry
2011	Koziel and Leifsson, 2011	PS	Aerodynamic performance	Airfoil geometry
2011	Petrone et al., 2011	GA	Aero., structural performance and noise	Airfoil geometry, chord and twist
2011	Bizzarrini, Grasso, and Coiro, 2011	GA	Aerodynamic performance	Airfoil geometry
2012	Bottasso, Campagnolo, and Croce, 2012	SQP	COE	Rotor $\emptyset$ , cone, tilt, hub height, blade geometry, struct.layout and tower
2012	Døssing et al., 2012	SLP	DEL of out of plane loads	Chord, twist and relative thickness
2012	Gagnon and Zingg, 2012	GB	Aerodynamic performance	Blade geometry
2012	Kwon, You, and Kwon, 2012	GB	Aerodynamic performance	Airfoil geometry
2012	Mukesh, Lingadurai, and Karthick, 2012	PSO	Aerodynamic performance	Airfoil geometry
2012	Ribeiro, Awruch, and Gomes, 2012	GA	Aerodynamic performance	Airfoil geometry
2012	Fischer, Kipouros, and Savill, 2012	TS	AEP and flap root moment	Blade length, twist and chord
2013	Lee et al., 2013	GA	Noise	Airfoil geometry, chord and twist
2013	Chen et al., 2013	PSO	Blade mass	Structural layout
2014	Ning, Damiani, and Moriarty, 2014	GA	AEP, Turbine mass/ AEP and COE	Chord, twist, tip speed ratio, spar cap, rotor $\emptyset$ , rated power
2014	Ashuri et al., 2014	GB	COE and AEP	Chord, twist, rotor $\emptyset$ , struct. layout, rot. speed and tower length
2014	Ebrahimi and Jahangirian, 2014	GA	Aerodynamic performance	Airfoil geometry
2014	Vecchia, Daniele, and DAmato, 2014	GA	Aerodynamic performance	Airfoil geometry
2015	Derakhshan, Tavaziani, and Kasaean, 2015	ABCA	Power production	Chord, twist and regulation
2015	Zahle et al., 2015	SQP	Blade mass and AEP	Chord, twist, relative thickness, pitch axis and structural layout
2016	Bortolotti, Bottasso, and Croce, 2016	SQP	COE	Rotor $\emptyset$ , cone, tilt, hub height, blade geometry, struct. layout, tower
2016	Sartori et al., 2016	SQP	COE	Rotor $\emptyset$ , cone, tilt, hub height, blade geometry, struct. layout, tower
2016	Jelena et al., 2016	PSO	AEP	Chord, twist and structural layout
2016	Croce et al., 2016	SQP	COE	Structural layout (spar cap offset and fiber orientation)
2017	Macquart et al., 2017	GB	COE	Blade length, hub height, airfoil family, blade geometry and struct. layout
2017	Pavese et al., 2017	SQP	Blade mass and DEL of root moments.	Blade geometry and structural layout
2017	Dykes, Damiani, and Ning, 2017	GB	COE	Chord, twist, prebending, spar cap, tip speed ratio and support structure
2018	Sartori et al., 2018	GB	COE	Rotor $\emptyset$ , cone, tilt, hub height, blade geometry, structural layout, tower
2018	Bortolotti et al., 2018	GA and GB	AEP, noise emission and COE	Chord, twist, relative thickness and tip speed ratio
2018	Caboni, Minisci, and Riccardi, 2018	MPAIDEA	Aerodynamic performance	Airfoil geometry
2018	Zahle et al., 2018	SQP	AEP	Chord, twist and tip shape
2018	McWilliam et al., 2018	GB	AEP	Blade length, blade geometry, tip speed ratio, and structural layout

## 1.8 Organization of the thesis

The thesis is divided in the following chapters besides the introduction:

- Chapter 2 describes the methods applied in the thesis. They are grouped in aeroelasticity, statistical techniques, sensitivity analysis, blade surface quality methods and optimization methods.
- Chapter 3 presents the novel blade design process with special focus on the computational code created in the context of this thesis (*AGORA*).
- Chapter 4 presents statistical treatment to identify the suitable variables in the airfoil representation.
- Chapter 5 presents a novel approach of the damage equivalent load calculation in the frequency domain that provides a significant reduction of simulation time.
- Chapter 6 shows two practical analyses prior to the blade optimization. A global sensitivity analysis of the blade geometry variables (airfoil and longitudinal laws) in the main performance of the wind turbine is developed. Besides, a design space exploration that identifies an undesired design space leading to aeroelastic instability is presented. The phenomenon is predicted with the aid of statistical treatment.
- Chapter 7 deals with optimization techniques by performing several scenarios to a public available wind turbine model.
- Chapter 8 provides conclusions and future research.

## 1.9 Note about confidentiality

Along the document some figures are provided without scaling to preserve confidential information of *NORDEX* group.

## Chapter 2

# Methods

This chapter introduces the fundamentals of the methods used for the completion of this thesis with the following organization:

- The section 2.1 describes the main theory behind aeroelasticity of wind turbines that is the basis of *AGORA*. An overview of other technical fields involved in the aeroelasticity are included in the section.
- The section 2.2 introduces the statistical techniques employed in the different analyses of the thesis applied to the results of *AGORA* calculations.
- The section 2.3 explains the basic theory of sensitivity analyses applied to identify the significant design variables in the blade design.
- The section 2.4 describes the blade surface quality methods that assess the fairness of the blade surface.
- Finally, section 2.5 introduces the optimization techniques that serve to calculate the optimal blade design.

The theory behind these methods is massive and assorted and thus, only an introduction of the several topics is provided in conjunction with appropriate bibliography.

### 2.1 Aeroelasticity

Aeroelasticity is the study of the interaction of inertial, elastic and aerodynamic forces. Aerodynamics provide the forces and moments acting on a body of a given shape produced by the air flow. Elasticity provides the transformation of the shape of an elastic body under an external load. Dynamics investigates how the deformations develop in time. A flexible body reacts to periodic forces by vibrating according to geometric patterns or modal shapes at a specific modal frequency. The modal shapes of elastic bodies are determined mainly by the mass and stiffness distributions. The rotation of blades modifies the mode shapes due to the Coriolis and centrifugal effects. Arthur Roderick Collar (Bishop, 1987) was a pioneer on aeroelasticity who defined a triangle that represents connections between inertial, elastic and aerodynamic forces as shown in figure 2.1. Additionally, for wind turbines, controls are important players that interact significantly with the forces of Collar's triangle. Aerothermoelasticity effects (Garrick, 1963) extend aeroelasticity by accounting stresses, deformations, and modifications in material properties due to thermal effects. This phenomenon is very relevant in high speed aero-planes but gets out of the scope of wind turbines. For the design of blades and wind turbine components, an aeroelastic detailed wind turbine model should predict the loads and dynamic response under the turbulent wind that inflows the wind turbine. The model

should take into account the complex interactions between aerodynamics, structural dynamics and control. The design standards (IEC61400-1, 2005) determine the conditions for load calculations. The wind turbine operation shall be governed by a control and supervisory system representative of real ones.

Aerodynamics of blades are predicted with several theories. BEM theory is the most popular. Vortex models are less common alternatives where the rotor blades, trailing and shed vorticity in the wake are represented by lifting lines and surfaces (Hansen et al., 2006), (Garrel, 2001).

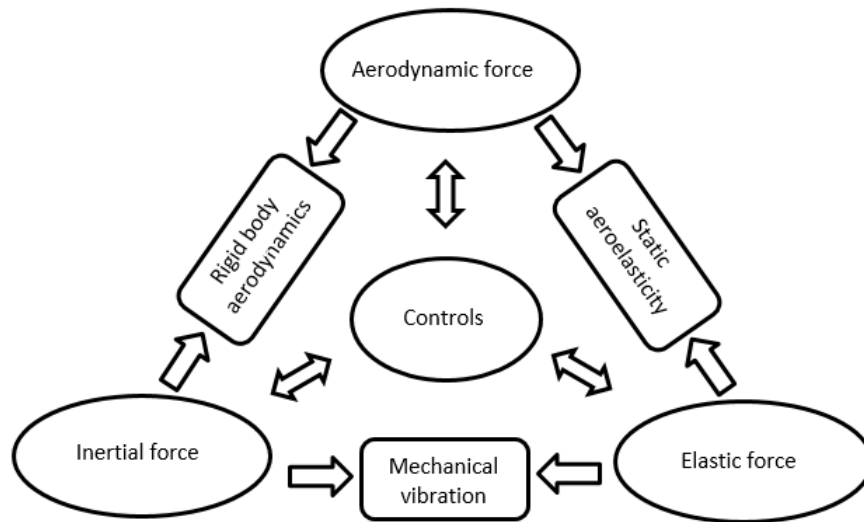


FIGURE 2.1: Collar's aeroelasticity triangle.

### 2.1.1 Blade element momentum theory (BEM)

BEM theory is the most common theory for calculating the aerodynamic loads on wind turbine rotors. BEM theory based codes are computationally fast (Hansen et al., 2006). Seven out of eight aeroelastic codes use the BEM model (Hansen, 2003). With this model it is possible to calculate the loads for different wind speeds, rotational speeds and pitch angles. The method was introduced by (Glauert, 1935) as a combination of one dimensional (1D) momentum theory with the blade element theory. Detailed description of the BEM theory is found in (Hansen, 2008), (Burton, 2001) or (theory manual *BLADED*).

The blade element theory allows to use the two dimensional (2D) model of a blade element and integrating it over the blade. The wind turbine rotor is considered as a simple permeable ideal disc that extracts kinetic energy from the flow. The rotor disc slows the wind speed by a pressure drop. Downstream, the pressure recovers gradually the atmospheric pressure. Bernoulli equation is applied as the flow is assumed stationary, incompressible and frictionless. The change of flow speed from the upstream  $U_0$  to the velocity at the rotor  $U_D$  depends on the axial flow induction factor  $a$ :

$$U_D = (1 - a)U_0 \quad (2.1)$$

From the Bernouilli's equation, the extracted power  $P$  and thrust  $T$  are calculated according to equation 2.2.

$$\begin{aligned} P &= 2\rho AU_0^3 a(1-a)^2 \\ T &= 2\rho AU_0^2 a(1-a) \end{aligned} \quad (2.2)$$

Where  $\rho$  is the air density and  $A$  of the rotor disc.

The non-dimensional coefficients  $C_P$  and  $C_T$  are obtained with equation 2.3. The maximum value of  $C_P$  is 16/27 when  $a = 1/3$ . This threshold value is called Betz limit.

$$\begin{aligned} C_P &= \frac{P}{0.5\rho AU_0^3} = 4a(1-a)^2 \\ C_T &= \frac{T}{0.5\rho AU_0^2} = 4a(1-a) \end{aligned} \quad (2.3)$$

It is assumed that the extracted power  $P$  is equal to the product of torque  $Q$  and rotor angular velocity  $\Omega$ . The tangential velocity that produces the rotation is zero upstream and  $\Omega r a'$  on the rotor at a radius  $r$ , where  $a'$  is the tangential induction factor. The rotor torque which is produced by the change of angular momentum can be expressed according to equation 2.4.

$$Q = \pi\rho R^4(1-a)a'\Omega \quad (2.4)$$

The results of the 1D momentum theory is applied in annular elements of the blade. Each element acts as an independent actuator disc.

The BEM model has different limitations requiring the introduction of sub-models to ensure accurate predictions (Hansen, 2003)(Hansen et al., 2006):

1. When dynamic aerodynamics are considered, the aerodynamic loads exhibit a delay and a large hysteresis with respect to the instantaneous angle of attack. This effect is more pronounced when angles of attack are high and are in the stall part of the polar curves. Thus, the steady state assumption should be corrected by an appropriate dynamic stall model.
2. The BEM theory assumes that the induced velocities react instantaneously to changes in the blade loading. However, the dynamic effects should be accounted by a complementary dynamic inflow model.
3. The axial flow assumption requires to be corrected by a skewed flow model when the rotor is not aligned with the incoming flow.
4. At high axial induction factors ( $a > 0.4$ ), the BEM theory estimates reversed flow around the rotor. To avoid this incorrect effect a correction of induction is needed.
5. The wake of rotor is formed of vortices trailed from the blades tip. Consequently, the induced velocities in a fixed point vary with the blade rotation. Then, a tip loss model to reproduce this phenomenon is required.

The wind inflow of a wind turbine blade has a dominant streamwise component while the spanwise is much lower. It is generally assumed that flow at a fixed radial position is two dimensional and thus, 2D airfoil data can be applied (Hansen, 2008).

In a 2D level, the shape of the airfoil induces the flow streamlines to curve around the geometry producing a pressure gradient that generates aerodynamic forces. The theory calculates the local velocities and forces in the airfoil which are presented in figure 2.2. In this figure, the blade is located in the upper position of the rotor. The YZ plane, perpendicular to axis of rotation, is usually called rotor plane. The relative

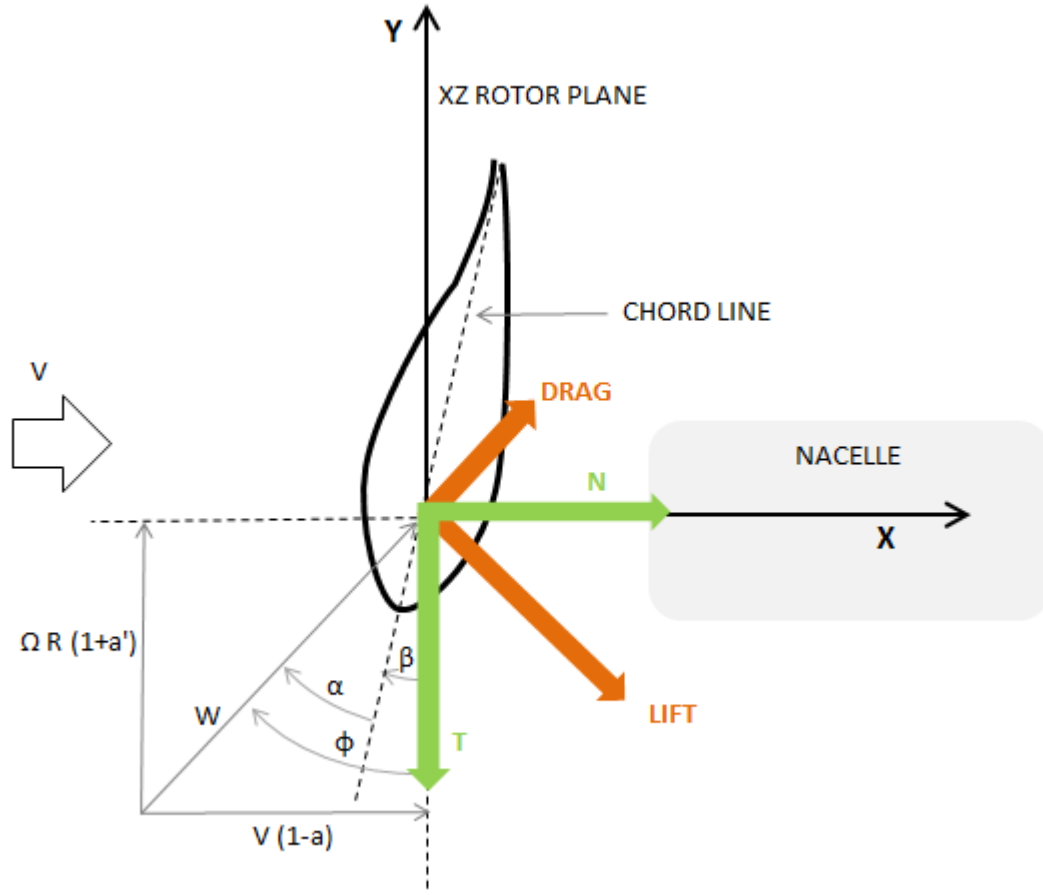


FIGURE 2.2: Airfoil 2D local loads and velocities

wind speed  $W$  that inflows to the airfoil has two components in  $X$  and  $Y$  direction that are function of the axial and tangential induction factors  $a$  and  $a'$  respectively. The angle of attack  $\alpha$  is the angle between the relative wind speed  $W$  and the chord line. The angle  $\beta$  comprises pitch angle, torsional deformation and blade set angle. The sum of  $\alpha$  and  $\beta$  is named inflow angle  $\phi$ . The forces  $L$  lift and drag  $D$  are perpendicular and in the direction of the relative wind speed  $W$  respectively. These forces are calculated according to equation 2.5.

$$\begin{aligned} L &= 0.5\rho W^2 c C_L \\ D &= 0.5\rho W^2 c C_D \end{aligned} \quad (2.5)$$

Where  $\rho$  is the air density,  $W$  relative wind speed,  $c$  is the chord length,  $C_L$  the lift coefficient and  $C_D$  the drag coefficient. The projection of the aerodynamic forces in the direction of  $Y$ -axis produces the torque  $T$  that is transformed into electrical power by the generator. In contrast, the projection in the normal direction ( $X$ -axis) provides the thrust  $N$  according to equation 2.6:

$$\begin{aligned} T &= L \sin \phi - D \cos \phi \\ N &= L \cos \phi + D \sin \phi \end{aligned} \quad (2.6)$$

In the aeroelastic codes, tables with coefficients  $C_L$ ,  $C_D$  and moment coefficient  $C_M$  for a range of angles of attack should be provided for BEM calculation. These



coefficients are obtained from wind tunnel calculations (Llorente et al., 2014) or computation. CFD codes solve Navier-Stokes equations (Hansen et al., 2006). In origin CFD codes have been widely employed in the design of helicopter rotors. For wind turbines the low Mach regime near root is a limitation that has been overcome in the recent years (Ageze, Hu, and Wu, 2017). The complexity of the blade surface makes the generation of an appropriate mesh for the CFD be a challenging issue. Panel methods are alternative tools to accomplish the aerodynamic calculations with a much lower computational cost.

### 2.1.2 Panel methods

Panel or potential flow methods solve the Prandtl-Glauert equation which is a simplification of Navier-Stokes equation for linear, inviscid, non-rotational flow at subsonic or supersonic free-stream Mach numbers (Erickson, 1990). These methods were first developed in the 60's (Woodward, 1968) and are based on the superposition of singularity panels, such as source panels, doublet panels and vortex panels. The absence of any explicit viscous effects causes subsonic flow solutions to be non-unique unless a Kutta condition at sharp trailing edges is somehow imposed (Erickson, 1990). With panel methods the pressure distribution along the airfoil is calculated and subsequently aerodynamic coefficients  $C_L$ ,  $C_D$  and  $C_M$  are obtained.

### 2.1.3 Structural analysis

The dynamic response of the wind turbine under time varying loads is calculated by taking into consideration an appropriate structural model. The slenderness of blades permits the separation of the three dimensional (3D) problem in two sub-problems: 1D beam and 2D cross-sectional analysis.

The development of 1D beam models is very extensive and complex. In this section only a brief introduction is provided. A rigorous review of the state of art is found in (Hodges, 2006). 1D beam models replace governing equations of the original three-dimensional structure kinematics, kinetics and energetics into a set of equations in terms of one fundamental variable, the beam axis. Kinematics relate displacement field and strain field. Kinetics deal with stress field in the equilibrium equations and energetics relate stress and strain fields (equivalent to Hooke's law for isotropic materials.). The beam models introduce a set of reasonable assumptions that simplify the 3D strain, stress and displacement fields into 1D. Depending on the type of assumptions different models are developed.

The Euler-Bernoulli beam model (Przemieniecki, 1968), (Hui, Wenbin, and Mark, 2010) assumes these simplifications to the beam element:

1. The cross-section is infinitely rigid in its own plane. Any material point in the plane of the cross-section solely consists of two rigid body translations.
2. The cross-section of a beam remains plane after deformation.
3. The cross-section remains normal to the deformed axis of the beam.

Euler-Bernoulli assumptions provide lower displacements than a theory without these assumptions. However, experimental observations show that these assumptions are reasonable for slender structures made of isotropic materials with solid cross sections subjected to extension or bending deformations.

Timoshenko model removes the third Euler-Bernoulli assumption and thus, the cross section remains plane but not necessarily normal to the deformation axis. Timoshenko model takes into account shear deformation effects and consequently provides higher displacements than Euler-Bernoulli.

In order to deal with torsion, Saint Venant model relaxes the second Euler-Bernoulli assumption. Thus, the cross section does not remain plane in general. Saint Venant model introduces the following assumptions (Blair, 2012):

- The shape and size of the cross section in its own plane are preserved, which imply that each cross section rotates like a rigid body.
- The cross section does not remain plane after deformation but warp proportionally according to the rate of twist.
- The rate of twist is uniform along the beam, which implies that the twist angle is a linear function of the beam axis.

Geometrical exact beam theory (GEBT) is an evolution of the classical linear models for nonlinear analysis of composite beams to meet the challenges associated with highly-flexible composite beams. GEBT captures all geometric non-linear effects due to large deflections and rotations, subject to the strains being small (Blair, 2012). This theory uses variational-asymptotic method (VAM) as mathematical tool to reduce the original 3D problem into a 1D analysis.

The 1D beam structural model requires to be fed by the cross-sectional (2D) properties of the blade. Besides mass and stiffness properties along span, other properties such as elastic center, shear center or mass center should be provided (manual *Pre-Comp*).

In recent years, many approaches are proposed to calculate these properties. (Hui, Wenbin, and Mark, 2010) provides a rigorous assessment of methods for cross-sectional analysis. A 2D finite element discretization of the complex internal layout topology in form of 2D mesh and the material properties serve to calculate the cross sectional properties. Other methods based on classical lamination theory (CLT) are developed during recent years.

CLT is an extension of the classical laminate plate theory (CPLT) for isotropic and homogeneous material that determines the total effective structural properties from the basic building block or lamina properties and orientation. Complete description of the theory is found in (Jones, 1998). The theory is based on underlying assumptions that permit the reduction of the 3D elasticity problem to 2D:

- The laminae are perfectly bonded so displacement is continuous through thickness.
- The laminae are homogeneous.
- There is a state of plane stress in the lamina.
- The lamina is isotropic, orthotropic or transversely isotropic.
- The deformation of the lamina follows Kirchhoff-Love assumptions (Love, 1888).

### 2.1.4 Acoustic emission

Operation of wind turbines produces noise that can disturb people living near to wind farms. This issue has been subject of research during many years. The noise from wind turbines comes from two general sources: aerodynamics and mechanics. Mechanical noise is mainly caused by gearbox, generators and other auxiliary devices such as the cooling system. Aerodynamic noise is produced by the interaction of the flow and the blade surface. An extensive overview of aeroacoustics is available in (Wagner, Bareiss, and Guidati, 1996). The main sources of aerodynamic noise are due to three types of effects:

- Noise caused by the blade rotation and passage through tower which is in the low-frequency part of the spectrum.
- Noise produced by the turbulence that contributes in a broadband spectra.
- Airfoil self-noise which is mainly associated with the laminar or turbulent boundary layer.

For the estimation of the wind turbine acoustic emission different analytical methods are available in the literature. (Sucameli et al., 2018) provides an extensive review of methodologies which are classified in two main families: frequency and time domain methods.

In time domain methods Ffowcs and Hawkings equation (Williams and Hawkings, 1969) is employed. This equation is derived by manipulating the continuity equation and the Navier-Stokes equations.

In frequency domain methods, total noise is computed as superposition of the turbulent inflow noise and airfoil self-noise. Contribution of (Brooks and Marcolini, 1989) was relevant to predict self produced noise. The Brooks, Pope and Marcolini (BPM) model accounts for summation of different sources: turbulent boundary layer/trailing edge, laminar boundary layer/vortex shedding, separation/stall noise, trailing edge bluntness/vortex shedding noise and tip vortex formation noise. Boundary layer parameters need to be calculated for BPM model. Panel method codes or CFD provide these parameters. Turbulent inflow noise was characterized by (Amiet, 1975) and (Paterson and Amiet, 1976). (Lowson, 1993) developed corrections to the former equations.

Frequency domain methods are usually coupled with BEM codes due to the affordable computational cost and accuracy in a range of frequencies between 20 Hz to 20 kHz (Sucameli et al., 2018).

### 2.1.5 Wind turbine control

The wind turbine control governs the actuation of the wind turbine ensuring that the operation is maintained within the normal limits. The safety system assures that the wind turbine is always in a safe situation. The main critical operating parameters that trigger the safety system are the drive train rotational speed, electrical power and vibration level (Burton, 2001).

Regarding the control system, different concepts have been developed in the wind energy industry. An extensive review is provided by (Hoffmann, 2002) and (Hansen, 2004). They are classified according to the drive train rotational speed: single speed, two-speeds or variable speed concepts. The variable speed type is able to adapt the speed to maximize the aerodynamic performance.

Another classification depends on the way of limiting the power available from the wind when a threshold (rated power) is reached. If the blades are installed fixed in the hub, the limitation of power is produced by the stall regime of the blade when wind speed and angles of attack in the blade are high. This concept is called passive stall control. In contrast, the blades mounting system in the hub can allow the rotation of the blades about the Z-axis by means of the actuation of an hydraulic or electrical device. By turning the blades, the angles of attack and consequently the aerodynamic forces are modified. There are two possibilities: active stall control that rotates the blade to fine pitch to increase angles of attack in order to induce stall regime and reduction of power. Pitch controlled or pitch to feather system performs the opposite actuation. The pitch actuation reduces angles of attack to decrease aerodynamic torque.

In the present thesis the pitch controlled and variable speed concept is selected as a preferred option in the wind industry (Hansen, 2004).

The following introduces the main functioning of the control. The cut-in wind speed is the lowest that permits the wind turbine to produce energy. The cut-out is the highest allowable wind speed to produce energy due to safety reasons. The fluctuations of the energy caused by changes of the wind speed and direction are controlled by generator torque or pitch actuation.

- Torque control. For low to moderate wind speeds where power output is below rated power, the objective of the control is to maximize the electrical power. The generator speed is controlled with the actuation of the torque of resistance of the electric generator. The generator speed remains constant for low wind speed just above cut-in wind speed and with increasing wind speed starts to be variable. In this variable speed area of the control the generator speed and torque follow a quadratic relation (Bossanyi, 2003):

$$Q_d = gain\_tsr W_{gen}^2 \quad (2.7)$$

Where  $Q_d$  is the demanded generator torque and  $W_{gen}$  is the measured generator speed.  $gain\_tsr$  is named optimal gain and is calculated according to equation 2.8 if the objective is the maximization of the power coefficient  $C_p$ .

$$gain\_tsr = \frac{\pi \rho R^5 C_{p-max}}{2 \lambda^3 G_{bx}^3} \quad (2.8)$$

Where  $\rho$  is the air density,  $R$  the rotor radius,  $C_{p-max}$  the maximum power coefficient,  $G$  the gearbox ratio and  $\lambda$  the tip speed ratio.

- Pitch control. In this regime there is a surplus of wind energy and due to safety reasons the aerodynamic torque is limited. The pitch actuator rotates the blade to feather in order to decrease the angle of attack. This implies a reduction of lift coefficient and consequently a decrease of aerodynamic torque.

Figure 2.3(a) shows the progress of control variables with wind speed. At low and medium wind speeds, the torque is varied and pitch is kept constant. Between rotational speeds  $w_{min}$  and  $w_{max}$  the rotational speed is variable. At higher wind speeds the rated power is achieved. From rated power to cut-out wind speed the torque remains constant and pitch angle starts to increase. In figure 2.3(b), the generator torque in function of rotor speed is presented. In the variable speed area, there is a quadratic relationship according to equation 2.7.

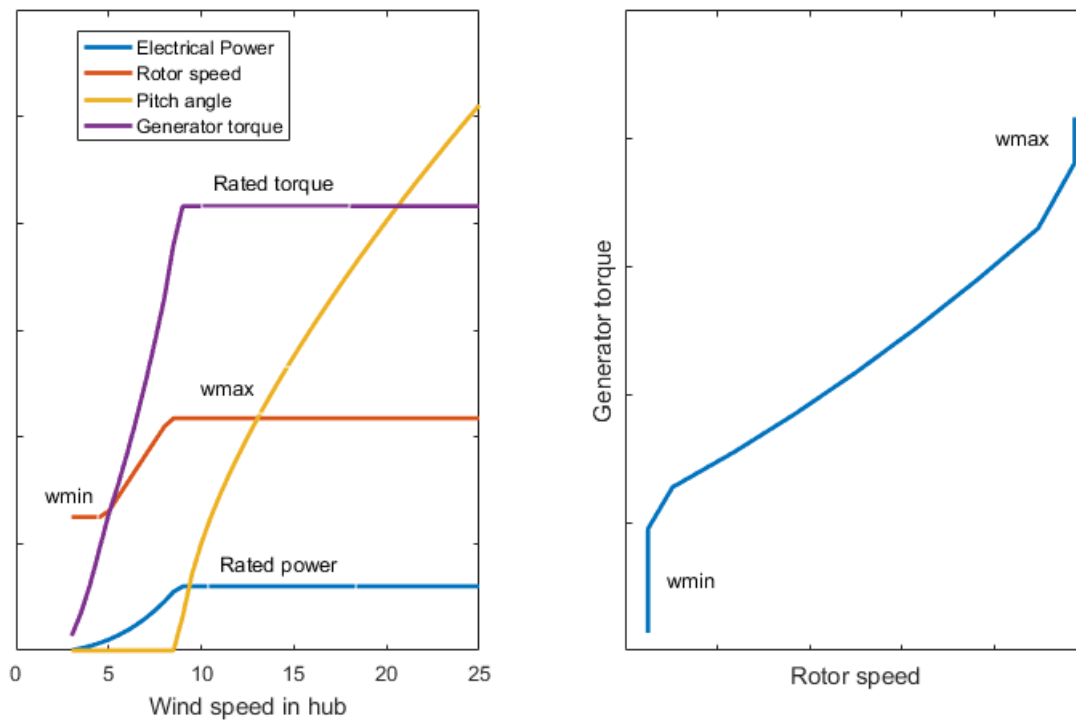


FIGURE 2.3: (a) Electrical power, rotor speed, pitch angle and generator torque in function of wind speed. (b) Generator torque versus rotational speed.

The wind turbines should incorporate a braking system to ensure the safe stop of the rotational speed. The aerodynamic brake is applied by pitching the blade to feather position. Due to safety reasons an independent mechanical brake in the high speed shaft is incorporated.

Horizontal axis wind turbines use electrical or hydraulic orientation yaw system to align the wind turbine with wind. Yaw drive reacts under misalignment detected by signals from wind vane on nacelle top. Besides, the system incorporates a set of hydraulic brakes that lock the nacelle yawing.

### 2.1.6 Calculation codes

With the impressive growth of wind energy industry many commercial codes simulate the aeroelasticity of wind turbines. In parallel, field campaigns are undertaken on experimental wind turbines to validate and improve these codes (Snel, Schepers, and Montgomerie, 2007). The aeroelastic codes include an aerodynamic model, currently BEM based, and a 1D beam model. In order to accomplish aeroelastic calculations, cross-sectional properties have to be supplied from a cross-sectional code and 2D aerodynamic coefficients from an aerodynamic code or wind tunnel tests. The aeroelastic codes are able to simulate the operation of real control and safety systems under different environmental conditions. Besides, if an assessment of the acoustic emission is needed a post-processing of the aeroelastic results has to be performed with an adequate acoustic code. Table 2.1 presents a list of relevant codes involved in this process. They are labeled according to the main theoretical basis with the aim of having a rough classification. More extensive information about

TABLE 2.1: List of calculation codes connected with aeroelasticity.

Software	Field	Organization	Theoretical basis
ALASKA	Aeroelasticity	Chemnitz University of Technology (Germany)	BEM
BLADED	Aeroelasticity	DNV-GL Garrad Hassan (UK)	BEM
FAST	Aeroelasticity	National Renewable Energy Laboratory (USA)	BEM
FLEX5	Aeroelasticity	Risø National Laboratory (Denmark)	BEM
HAWC2	Aeroelasticity	Technical university of Denmark	BEM
PHATAS	Aeroelasticity	Energy Research Centre of Netherlands	BEM
GAST-GenUVP	Aeroelasticity	National Technical University of Athens (Greece)	Vortex
AWSM	Aeroelasticity	Energy Research Centre of Netherlands	Vortex
FLUENT	Aerodynamics	ANSYS (USA)	CFD
RFOIL	Aerodynamics	Energy Research Centre of the Netherlands	Panel method
XFOIL	Aerodynamics	Energy Research Centre of the Netherlands	Panel method
VABS	Cross sectional analysis	AnalySwift (USA)	FEA
FOCUS	Cross sectional analysis	Knowledge Centre WMC (Denmark)	CLT
PRECOMP	Cross sectional analysis	National Renewable Energy Laboratory (USA)	CLT
CROSTAB	Cross sectional analysis	Energy Research Centre of the Netherlands	CLT
BPE	Cross sectional analysis	Sandia National Laboratories (USA)	FEA
BECAS	Cross sectional analysis	Technical university of Denmark	FEA
NAFNOISE	Acoustic emission	National Renewable Energy Laboratory (USA)	Freq. Domain method
SILANT	Acoustic emission	Energy research Centre of the Netherlands	Freq. Domain method

available codes can be found in (Wang, Liu, and Kolios, 2016) and (Hui, Wenbin, and Mark, 2010).

### 2.1.7 Calculation codes in this thesis

From the wide portfolio of available codes, the calculations in this thesis are performed with the following selection of them.

*BLADED* for Windows is an integrated simulation package for wind turbine design and analysis. The Garrad Hassan approach to the calculation of wind turbine performance and loading has been developed over the last fifteen years and has been validated against monitored data for a wide range of turbines of many different sizes and configurations. *BLADED* incorporates two major extensions of the BEM to deal with the unsteady nature of the aerodynamics. The first of these extensions allows a treatment of the dynamics of the wake and the second provides a representation of dynamic stall through the use of a stall hysteresis model (manual *BLADED*). Besides, *BLADED* applies a structural model based on linear finite element technique assuming that deformations are small. The finite elements are modeled following Timoshenko beam theory (Przemieniecki, 1968). For the computation of the equation of motion, the calculation of mode shape functions follows Craig-Bampton method (Bampton and Craig, 1968) that reduces a complex finite element model into generalized mass and stiffness matrices of linear flexible components (or bodies) which are interconnected by fixed boundary points. The deformations are obtained by linear combination of precalculated mode shape functions. The scalars of linear combinations are the modal amplitudes. This approach provides reduced problem size and low computational cost (manual *BLADED*).

*PreComp* is used to predict the cross-sectional properties needed for the 1D beam model of *BLADED*. The bending stiffnesses are calculated using the area-segments-based numerical integration. The torsional stiffness is computed by neglecting the effects of the warping functions altogether. It is based on a novel approach that integrates a modified CLT with a shear flow approach. It applies some simplifications such as thin-walled assumption and free warping. Because of its adoption of oversimplified assumptions, there are some concerns about its accuracy in addition to



its admitted approximation in shear center calculations. The main advantage of the code is the very low computational cost (Hui, Wenbin, and Mark, 2010).

*XFOIL 2013* is an interactive program for the design and analysis of subsonic isolated airfoils that combines the speed and accuracy of high-order panel methods with fully-coupled viscous in-viscid interaction code.

*Silant* is a noise prediction code based on BPM, Amiet and Lawson equations. Analytical predictions have been validated with experimental measurements of the project *Silent Rotors by Acoustic Optimization* (SIROCCO) between 2003 and 2007 (Schepers, 2007).

### 2.1.8 Wind modeling

For the completion of the aeroelastic simulations, the time history of the wind speed field affecting the rotor should be modeled. The time fluctuations are categorized according to the frequency spectra. Long term fluctuations of wind speed in a time scale higher than one year are difficult to be predicted. However, the Weibull probability distribution presented in equation 2.9 provides accurate representation of annual variation of hourly mean wind speed in most of standard sites (Burton, 2001).

$$F(U) = \exp\left(-\left(\frac{U}{c}\right)^k\right) \quad (2.9)$$

where  $F(U)$  is the fraction of time for which the hourly mean wind speed exceeds  $U$ ,  $c$  is the scale parameter and  $k$  the shape parameter. The Rayleigh distribution which is a specific case of the Weibull distribution when  $k = 2$  is commonly used to represent the annual hourly mean wind speed variation. Some specific sites show a clear distinction between summer and winter wind regime. Thus, a combined distribution formed by two distinct Weibull distributions fits better with the annual variation (Burton, 2001). In a shorter scale, day-night variations can be fairly predicted. This effect is significant in places with an important heating during the daytime following by an intense cooling at night. Short term random fluctuations in a time scale of less than ten minutes are represented by turbulence and gusts. These variations have a very significant impact on the design of wind turbines (Burton, 2001). Turbulence is produced by thermal effects that make warm wind rise and friction with ground surface. Accordingly, the turbulence decreases when height increases. The turbulence intensity (TI) measures the level of short term wind fluctuation according to equation 2.10 (Burton, 2001).

$$TI = \frac{\sigma}{\bar{U}} \quad (2.10)$$

Where  $\sigma$  is the standard deviation in ten minutes wind speed data and  $\bar{U}$  the mean value. The speed variations are considered normally distributed in a short time period.

The spectrum of turbulence describes the frequency content of wind speed. There are several spectra applied in the wind aeroelastic calculations. The specification (IEC61400-1, 2005) recommends the Mann uniform shear model and Kaimal spectral and exponential coherence model as alternatives. Besides, Von Karman spectra is widely used (Burton, 2001).

For the design of wind turbines, it is necessary to determine the maximum extreme wind speeds (gusts) that the wind turbine can experiment. The extreme wind speed  $V_t$  is defined as the wind speed with a return period of  $t$  years (currently 1 or

50 years) (IEC61400-1, 2005). For ultimate loads assessment, the international specifications (IEC61400-1, 2005) defines a number of transient events under which the turbine must be designed (Burton, 2001).

The mean annual wind speed, TI and extreme wind speeds are used to classify the severity of sites. Accordingly, wind speed class can be 1, 2 or 3 (from higher to lower mean annual wind speed) and *A*, *B* or *C* (from higher to lower TI). In addition, a class *S* is reserved for considering specific values distinct from the standard types.

### 2.1.9 Annual Energy Production (AEP) calculation

The international standard (IEC61400-12-2, 2013) specifies a procedure for verifying the power performance characteristics of a single electricity producing horizontal axis wind turbine utilizing nacelle-anemometer methods. Although the procedure is intended to the measurement in field some aspects such as the method of bins and the calculation of AEP are used for the results of aeroelastic simulations and assess the performance of the blade during the design. In field measurements, the data should be collected at a sampling of 1Hz or faster. The statistics are collected for periods of 10 minutes. The data are sorted using the method of bins and must cover from cut-in to 1.5 times the wind speed at 85% of the rated power. The range is divided in 0.5 m/s bins. The power values are corrected depending on the air density.

For the calculation of power curve and AEP based on dynamic aeroelasticity, several simulations of ten minutes virtual duration are performed incorporating a synthetic wind field that fulfills the required turbulence intensity class and the frequency spectra according to (IEC61400-1, 2005). The simulations cover the wind range from cut-in to cut-out in bins of 0.5 m/s of separation. No misalignment of the rotor with respect to the wind inflow is considered. The air density is defined in all simulations at the standard sea level air density  $1.225 \text{ kg/m}^3$ , therefore no further correction is required. After completion of simulations, the time histories of power and wind speed are collected.

Let  $V_i$  be the mean wind speed and  $P_i$  the mean power output of simulations of bin  $i$ ,  $N$  the number of bins and  $N_h$  the total number of hours in one year. The AEP is calculated (IEC61400-12-2, 2013) according to equation 2.11:

$$AEP = N_h \sum_{i=1}^N [F(V_i) - F(V_{i-1})] \left( \frac{P_{i-1} + P_i}{2} \right) \quad (2.11)$$

Where  $F(V)$  is the Rayleigh cumulative probability distribution function for wind speed.

Alternatively to the AEP calculation from 10-minute dynamic simulations, the power curve can be calculated from steady simulations performed for the operational range from cut-in to cut-out wind speeds.

The weighed average method (Stablein and Hansen, 2016) estimates the mean power  $P_i$  for a bin  $i$  of mean wind speed  $v_i$  and  $TI$  according to equation 2.12.

$$P_i(v_i) = \int_{v=cut_{in}}^{v=cut_{out}} P_{ss}(v) f(v|v_i, \sigma_i) dv \quad (2.12)$$

Where  $f(v|v_i, \sigma_i)$  is the density function of the normal distribution with mean  $v_i$  and standard deviation  $\sigma_i = TI v_i$  and  $P_{ss}(v)$  is the steady state power curve over the operational range of the turbine.



This equation is applied for each bin wind speed and subsequently the AEP is calculated according to equation 2.11.

### 2.1.10 Loads assessment

The wind turbine should be designed to withstand the loads that come from different sources: aerodynamics, gravity, inertia (including centrifugal and gyroscopic effects) and loads from control system actuation: pitch, torque, yaw and brakes. The loads are analysed in two different categories:

- **Ultimate loads.** Specific normal wind conditions are combined with normal control operation in aeroelastic simulations. Besides, extreme wind events are simulated in conjunction with normal control operations. Furthermore, normal wind conditions are combined with specific control failures. Extreme wind events and control failure are not intended to occur simultaneously. International specifications (IEC61400-1, 2005) provide guidance to perform the simulations. The extremes of the external forces and moments in different wind turbine locations (blades, drive train, tower,...) are calculated for assessing the integrity of the wind turbine components.
- **Fatigue loads.** The wind turbine suffers very demanding fatigue loads. Rotation provokes a periodic 1P (one cycle per revolution) in plane loading caused by gravity. Wind turbulence causes fluctuations of wind speed in short time term and differences in the parts of the rotor causing mainly out of plane loading. Besides, wind flow generates cyclically varying loads due to asymmetry of the inflow caused by increase of wind speed with height (wind shear) and changes in wind direction that can not be corrected by yaw control. Furthermore, the tower causes a wind speed deficit, even in up-wind configurations, with a consequent reduction of aerodynamic loading in the blades. Potential flow theory is applied to account for this effect that is called tower shadow (Hau, 2006). The fatigue loading is assessed by means of aeroelastic simulation. To account for the different effects, ten minutes aeroelastic simulations are performed. The wind turbine model is fed with a turbulent synthetic wind file. The number of simulations should be sufficient to cover the wind speed range divided in bins and possible wind misalignment. After simulation, the load signals in different wind turbine locations are collected and processed in terms of constant amplitude fatigue cycles by a counting method. The Rainflow Counting method represents a family of methodologies to transform the spectrum into loading cycles (Passipoularidis and Brøndsted, 2010). Besides, a damage equivalent load (DEL) on the basis of the Palmgren-Miner method is calculated as the range of a sinusoidal load of constant frequency which would produce the same fatigue damage as the original signal. The evaluation of the fatigue in the time domain requires a time expensive process. As alternative, chapter 5 explains a calculation of the damage equivalent load in the frequency domain that implies a lower computational cost (Echeverria, Mallor, and Sanz, 2017).

## 2.2 Statistical methods

### Statistical hypothesis testing

The statistical hypothesis testing serves to decide between a null hypothesis  $H_0$

which is considered as true a priori.  $H_0$  is contrasted with an alternative or research hypothesis  $H_1$ .

Given two samples, an hypothesis test can determine whether the sample means are significantly different and how likely is that both sample means were drawn from same population. When samples are independent, variances constant and errors normally distributed, the Student's t-test is applied (Crawley, 2011).

The Shapiro-Wilk test (Shapiro and Wilk, 1965) is appropriate for testing normality. The test statistic measures how close the empirical quantiles of the sample follow the corresponding theoretical quantiles of a normal distribution. Accordingly, low values of the test statistic lead to the rejection of the null hypothesis that states that the distribution of samples is normal.

The Wilcoxon Rank sum test is a non-parametric alternative to Student's test with no necessity of prior assumption of normality (Wilcoxon, 1945). In the null hypothesis it is stated that the underlying distributions of two samples are assumed to be identical. This test is commonly applied to means and medians.

### Permutation test

The fundamental idea behind the permutation test (Edgington, 1986) in a two-sample problem is the assumption that if no difference exists between two groups of samples, all data sets obtained by randomly assigning the data to the two groups have an equal probability of being observed. This method is particularly useful when data are sampled from unknown distributions, when sampling sizes are small or when there are outliers. The test is based on computing the highest amount of values of a test statistic when reordering randomly the labels of the data. The randomly generated statistics are compared with the observed one to determine if the observation presents significance.

### Bootstrapping method

The bootstrapping method is a widely applicable and extremely powerful statistical tool that can be used to quantify the uncertainty associated with a given estimator or statistical learning technique. The method is based on the construction of many random sampling sets with replacement of the observed data. As a simple example, the bootstrapping method can be used to estimate the standard errors of the coefficients from a linear regression fit (James and Witten, 2013, Efron, 1982).

### Latin Hypercube Sampling (LHS)

The LHS method (McKay, 1992) is a way of generating random samples of parameters. It is widely used because reduces drastically the number of samples necessary to achieve a reasonably efficient exploration. LHS is an appropriate tool to generate input data for global sensitivity analysis (Saltelli, 2004). One-dimensional LHS involves dividing your cumulative density function into equal partitions and then choosing a random data point in each partition. In two-dimensional LHS you perform the one dimensional sampling separately and then you combine them randomly into two-dimensional pairs.

### Correlation matrix

The correlation is an analysis that measures the strength of linear association between variables and the direction of the relationship. The correlation coefficient lies between minus one and one. The extremes mean perfect linear association and the sign reveals if the relationship is direct or inverse. Values close to zero mean that no correlation exists between variables. Pearson-product moment, Spearman's rank

and Kendall rank correlation are common correlation coefficients (Crawley, 2011).

### 2.2.1 Surrogate models

A surrogate model  $\hat{f}$  approximates a function  $f$  that depends on the variables  $X$ . There are two main objectives to estimate the function  $f$ : prediction and inference (James and Witten, 2013).

For prediction purposes, the approximate function  $\hat{f}$  form is not important, provided it approximates the function  $f$  with enough accuracy to be used as predictor. The error in the prediction depends on two types of error: reducible error by increasing the goodness of the approximation and irreducible error that contains unmeasured variation and is not possible to be reduced by improving the approximate function (James and Witten, 2013).

For inference, it is necessary to understand the way that the response changes as function of each input. With this information, the important input variables can be revealed. The positive relation meaning that increasing the input variable is associated with increasing response or the opposite relation are determined (James and Witten, 2013).

Prior to detail some methods, an introduction to one of the main problems of these techniques is approached. Overfitting is the phenomenon in complex surrogate models that fit the known data very accurately but predict poorly new observations. If the number of observations to fit the model is much larger than number of variables this phenomenon is not likely to occur (James and Witten, 2013). In order to detect overfitting, the observations are usually divided in two groups: one larger group that serves for training the predicting model and second group for validation and assessment of accuracy under unknown data.

The linear model is a parametric method that assumes that the response can be modeled according to equation 2.13:

$$\hat{f} = \beta_0 + \sum_{i=1}^p \beta_i X_i \quad (2.13)$$

The approximation problem is reduced to calculate the  $p+1$  parameters  $\beta_0, \beta_1, \dots, \beta_p$  to minimize the mean squared error (MSE).

The  $R^2$  statistic measures the quality of the fitness. It takes a value between zero (no linear correlation) and one (functional linear relationship). It is independent of the scale of the response and is calculated according to:

$$R^2 = \frac{TSS - RSS}{TSS} \quad (2.14)$$

where  $TSS$  or total sum of squares measures the total variance in the response and  $RSS$  or residual sum of squares measures the amount of variability after performing the regression (James and Witten, 2013). Thus,  $TSS - RSS$  provides the variability explained by the regression.

With the intent to account for non-linear effects a second order model function is an evolution of linear regression calculated according to equation 2.15:

$$\hat{f} = \beta_0 + \sum_{i=1}^p \beta_i X_i + \sum_{j=1}^p \sum_{k=1}^p \beta_{j,k} X_j X_k \quad (2.15)$$

When assessing the relationship between the design variables and a quantitative response defined according to a binary coding: 0/1, logistic regression is a valid

tool. The linear model is not an appropriate method for this type of problems. The linear regression can provide values outside the interval  $[0, 1]$  in the prediction of new points.

In multiple logistic regression, the relationship between probability  $p(X) = Pr(Y = 1|X)$  and  $X$  is determined by a logistic function according to equation 2.16:

$$p(X) = \frac{e^{\beta_0 + \sum_{i=1}^p \beta_i X_i}}{1 + e^{\beta_0 + \sum_{i=1}^p \beta_i X_i}} \quad (2.16)$$

After mathematical manipulation, equation results:

$$\log\left(\frac{p(X)}{1 - p(X)}\right) = \beta_0 + \sum_{i=1}^p \beta_i X_i \quad (2.17)$$

Instead of minimum least square method, the maximum likelihood method is used to estimate regression coefficients  $\beta_i$  (James and Witten, 2013). The values of coefficients  $\beta_i$  serves to assess if there is direct or inverse proportionality. The significance of each design variable is determined with a contrast hypothesis to the corresponding regression coefficient  $\beta_i$ :

$$\begin{aligned} H_0 : \beta_i &= 0 \\ H_1 : \beta_i &\neq 0 \end{aligned} \quad (2.18)$$

A  $\varphi$ -value lower than significance level means a rejection of null hypothesis  $H_0$ . This rejection implies that  $\beta_i \neq 0$  and the associated design variable is considered significant.

The decision trees are methods that stratify the design space in regions and predict the response. The rules to split the design space are organized in a tree scheme. The main advantage is the simplicity of interpretation, however the level of accuracy is generally lower than more complex methods (James and Witten, 2013). The cue-based questions are called nodes, the answers to these questions are branches and leaves are decisions. Different techniques related with decision trees are bagging, random forests, boosting (James and Witten, 2013) and fast and frugal trees (FFTrees). The fundamentals of FFTrees can be consulted in (Gigerenzer and Todd, 1999), (Gigerenzer and Czerlinski, 1999) or (Phillips et al., 2017). The advantages of FFTrees with respect to other techniques are that they are fast, frugal (use little information), simple and transparent algorithms. Moreover, they are robust against overfitting (Phillips et al., 2017). The FFTrees and non-compensatory algorithms, they deliberately ignore information. These trees have two branches from each node and either one or both branches is an exit branch leading to a leaf.

### 2.2.2 Graphical Techniques

The quantile-quantile plot (QQ-plot) is a graphical tool to evaluate if a set of observation is likely to belong to a theoretical distribution such as a normal. The QQ-plot is a scatterplot of two sets of quantiles, the theoretical ones assuming a type of distribution and the observed data. If the points are close to follow the theoretical distribution they should fall approximately along the reference line. The greater the departure from this reference line, the greater the evidence that the data set has come from different distribution. Besides, this type of plots is used to determine if two data sets come from same population comparing quantiles of both data sets.

Box and whisker plot is a popular method for comparing groups of numerical data through their median and quartiles. The box plots present vertical lines from

the boxes (whiskers) indicating variability outside the upper and lower quartiles. Outliers are plotted as individual points. The box plots show four main features about a variable: centering, spreading, asymmetry and presence of outliers.

A violin plot (Adler, 2005) is a combination of box and whisker plot and a rotated kernel density plot. The bottom and top of the box represent the first and third quartiles and the horizontal line inside the box represents the median. The ends of the whiskers represent the minimum and maximum of all data. The kernel density non-parametric function estimates the probability density function of the variable.

The confusion table presents the results of a binary prediction model (e.g. logistic regression or decision tree). The rows refer to decision according to model and columns to true values. Accordingly, the diagonal provides correct decisions and off-diagonal erroneous values (Phillips et al., 2017). The results are classified according to this nomenclature:

- Hits ( $hi$ ) are predictions of response as 1 that are correct.
- Correct rejections ( $cr$ ) are predictions of response as 0 that are correct.
- Misses ( $mi$ ) are predictions of response as 0 that are incorrect.
- False alarms ( $fa$ ) are predictions of response as 1 that are incorrect.

Table 2.2 presents a general confusion table with the related terminology.

TABLE 2.2: Confusion table.

		Truth	
		1	0
Prediction	1	hi	fa
	0	mi	cr

Based on the confusion table, the following metrics assess the performance of the predictor:

- Sensitivity ( $sens$ ). Probability of correctly identifying a true positive case:

$$sens = \frac{hi}{hi + mi} \quad (2.19)$$

- Specificity ( $spec$ ). Probability of correctly identifying a true negative case:

$$spec = \frac{cr}{cr + fa} \quad (2.20)$$

- Accuracy ( $acc$ ). Probability of correctly identifying any case.

$$acc = \frac{hi + cr}{hi + cr + mi + fa} \quad (2.21)$$

## 2.3 Sensitivity analysis

In the context of this thesis, sensitivity analysis can be defined as the measure of the sensitivity/influence of the design variables on the outputs. Sensitive design

variables are those which have a significant influence on wind turbine responses so that small changes in the input value result in significant changes in the output. The local sensitivity methods evaluate sensitivity at one point in the design space. The simplest method to perform sensitivity analysis is to repeatedly vary one parameter at a time while holding the others fixed (Hamby, 1994). In contrast, global sampling methods scan in a random or systematic way the entire range of possible parameter values and possible parameter sets. Essential to this method is the sampling strategy. The LHS method is massively used in this thesis and specifically in sensitivity analysis.

Independently of the method, the following steps are recommended to be followed in a sensitivity analysis (Saltelli, 2004):

1. Define the goal of the analysis and accordingly, the outputs that respond more efficiently to goals.
2. Establish the design variables that are candidates to be sensitive and the distribution functions that are likely to follow.
3. Choose a sensitivity method according to the nature of the problem.
4. Generate a sample of design variables.
5. Calculate the outputs for the sampling observations.
6. Analyse the response with respect to inputs according to the sensitivity method.

### 2.3.1 Linear regression

The model responses obtained from LHS input samples are typically analysed with multi-variable linear regression. The standardized regression coefficient for a given factor plays the role of a sensitivity measure for the associated design variable. The effectiveness of the regression coefficients is conditional on the  $R^2$  of the fit. With this approach, each effect for a design variable is in fact an average over the possible values of the other factors.

A disadvantage of linear regression based methods is their poor performance for non-linear relationships (Saltelli, 2004).

### 2.3.2 Variance based methods

These methods conceive the sensitivity analysis as the study of how the variance in the output of a model can be apportioned to different sources of variance in the model inputs. Variance based methods are valid alternatives to deal with nonlinear responses (Saltelli, 2004),(Wainwright et al., 2014).

The conditional expectation  $E(Y|X_i)$ , conditional on  $X_i$  being fixed, can be calculated empirically by cutting the  $X_i$  domain into slices and averaging the values of  $E(Y)$  within the same slice (Saltelli, 2004).

An integrable function  $Y = f(X_1, X_2, \dots, X_p)$  can be decomposed into terms of increasing dimensionality and the variance of the output  $V(Y)$  can be decomposed in function of the following terms:

$$\begin{aligned}
 V_i &= V(E(Y|X_i)) \\
 V_{ij} &= V(E(Y|X_i, X_j)) - V_i - V_j \\
 V_{ijk} &= V(E(Y|X_i, X_j, X_k)) - V_i - V_j - V_k - V_{ij} - V_{ik} - V_{jk} \\
 &\vdots
 \end{aligned} \tag{2.22}$$



The relative contribution of the variance of each input to the variance of the output  $V(Y)$  is the first order sensitivity index  $S_i$  calculated according to equation 2.23.

$$S_i = \frac{V_i}{V(Y)} \quad (2.23)$$

The second-order sensitivity index  $S_{ij}$  expresses the contribution of the interaction of inputs  $X_i$  and  $X_j$  in the variance of the output:

$$S_{ij} = \frac{V_{ij}}{V(Y)} \quad (2.24)$$

And the third-order sensitivity index expresses the contribution of the interaction of three inputs  $X_i$ ,  $X_j$  and  $X_k$  in the variance of the output:

$$S_{ijk} = \frac{V_{ijk}}{V(Y)} \quad (2.25)$$

Accordingly, it is possible to define higher order sensitivity indexes until order  $p$ . The total effect index  $S_{Ti}$  accounts for the total contribution to the output variation due to a single input  $X_i$  by computing the sum of all the sensitivity indexes where the input  $X_i$  is involved.

The main disadvantage of this method is the high size of the sampling necessary to perform an efficient analysis (Saltelli, 2004).

## 2.4 Blade surface quality

The interrogation methods inspect and assess the quality and fairness of surfaces. Prior to deal with surfaces some concepts about curves are introduced.

### 2.4.1 Airfoil curvature

The fairness of a curve is evaluated by inspecting the curvature which is introduced in this subsection. The tangent line of the curve  $C$  in a point  $p$  is the line passing through two consecutive points of the curve. The osculating plane passes through at least three consecutive or infinitesimally close points of the curve. It also passes through the tangent line. The line in the osculating plane at a point  $p$  perpendicular to the tangent line is called the principal normal (Struik, 1961). The unit vector along the principal normal is  $n$ . If the arc length  $s$  is defined as parameter, the first derivative is  $t = dC/ds$ . The vector  $k$  is called curvature and is defined according to equation 2.26. The curvature vector expresses the rate of change of the tangent when proceeded along the curve (Struik, 1961).

$$k = \frac{dt}{ds} = kn \quad (2.26)$$

The curvature or porcupine plot consists of segments normal to the curve emanating from a number of points on the curve and whose lengths are proportional to the magnitude of the curvature. The point where the curvature changes sign is an inflection point. The inflection points and the variation of curvature can be easily identified with porcupine plot (Patrikalakis M., 2009). Figure 2.4 shows a porcupine plot of a typical master airfoil. The highest curvature is found near the LE point. The extrados side presents no inflection point and lower curvature than intrados side which experiments one inflection point.

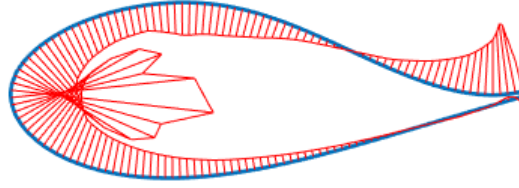


FIGURE 2.4: Porcupine plot of an airfoil

## 2.4.2 Surface interrogation methods

To assess the quality of the surface, the interrogation methods are appropriate tools included in CAD codes. There are two main categories of methods, the first one is based on theory of classical differential geometry and the second family includes methods that examine the surface with illumination models (Guid, Oblonsek, and Zalik, 1995).

The geometry of surfaces involved in the interrogation methods here described depends on two quadratic differential forms that are now introduced.

Let  $\mathbf{SF}(u, v) = [x(u, v), y(u, v), z(u, v)]$  be a parametric surface and  $(u, v)$  the curvilinear coordinates. The unit surface normal  $\mathbf{N}$ , calculated from parametric derivatives according to equation 2.27, defines a tangent plane to the surface.

$$\mathbf{N} = \frac{\mathbf{SF}_u \times \mathbf{SF}_v}{\|\mathbf{SF}_u \times \mathbf{SF}_v\|} \quad (2.27)$$

The first fundamental form  $I$  is expressed according to equation 2.28:

$$\begin{aligned} I = ds^2 &= (\mathbf{SF}_u du + \mathbf{SF}_v dv) \cdot (\mathbf{SF}_u du + \mathbf{SF}_v dv) = Edu^2 + 2Fdudv + Gdv^2 \\ E &= \mathbf{SF}_u \cdot \mathbf{SF}_u \\ F &= \mathbf{SF}_u \cdot \mathbf{SF}_v \\ G &= \mathbf{SF}_v \cdot \mathbf{SF}_v \end{aligned} \quad (2.28)$$

Where  $E$ ,  $F$  and  $G$  are the coefficients of the first fundamental form of the surface that are functions of the curvilinear coordinates. The square root  $ds$  is called the element of arc and  $s$  is the arc length between two points along a curve of the surface (Struik, 1961). The coefficients of the first fundamental form are used to calculate the area  $A$  according to equation 2.29.

$$A = \int \int \sqrt{EG - F^2} dudv \quad (2.29)$$

The second fundamental form  $II$  is obtained by taking a curve  $\mathbf{C}$  on the surface at the point  $\mathbf{p}$ . The curvature  $\mathbf{k}$  of  $\mathbf{C}$  at  $\mathbf{p}$  is decomposed into a component normal and a component tangent vector to the surface or geodesic curvature vector:  $\mathbf{k} = d\mathbf{t}/ds = \mathbf{k}_n + \mathbf{k}_g$ . The normal curvature vector  $\mathbf{k}_n$  can be expressed as  $\mathbf{k}_n = k_n \mathbf{N}$  where  $k_n$  is the normal curvature and  $\mathbf{N}$  the unit surface normal vector.

The second fundamental form measures how the first fundamental form of the surface changes as the normal vector changes (Chase, 2012) and provides information about the surface curvature. The second fundamental form  $II$  is calculated according to equation 2.30.



$$\begin{aligned}
II &= edu^2 + 2fdudv + gdv^2 = \\
e &= \mathbf{SF}_{uu} \cdot \mathbf{N} \\
f &= \mathbf{SF}_{uv} \cdot \mathbf{N} \\
g &= \mathbf{SF}_{vv} \cdot \mathbf{N}
\end{aligned} \tag{2.30}$$

Where  $e$ ,  $f$  and  $g$  are the second fundamental form coefficients.

The Meusnier theorem states that all curve lying on a surface  $\mathbf{SF}$  and having at a given point  $\mathbf{p} \in \mathbf{SF}$  the same tangent line have at this point the same normal curvature.

The principal curvatures  $k_1$  and  $k_2$  of a point are the extremal values of the normal curvatures of all curves through the point obtained by intersecting the surface by all planes containing the normal vector. These curvatures are not intrinsic properties of the surface and depend on the surface parametrization (Chase, 2012). The normal curvature in an arbitrary direction can be expressed in terms of  $k_1$  and  $k_2$  as Euler's theorem states (Struik, 1961).

The Gaussian or total curvature is an intrinsic property that depends only on the first fundamental form as Gauss' Egregious theorem states (Chase, 2012). Gaussian curvature is defined according to equation 2.31 and can also be expressed as the product of the two principal curvatures.

$$K = k_1 k_2 = \frac{eg - f^2}{EG - F^2} \tag{2.31}$$

The mean curvature is the average of the principal curvatures as stated in equation 2.32.

$$H = \frac{1}{2}(k_1 + k_2) = \frac{Eg - 2fF + eG}{2(EG - F^2)} \tag{2.32}$$

The absolute curvature is defined in equation 2.33.

$$k_{abs} = |k_1| + |k_2| \tag{2.33}$$

$k_u$  and  $k_v$  are the curvatures of the isoparametric curves in the surface:  $v = constant$  and  $u = constant$  respectively.

For the surface smoothness assessment an intensity-coded map of any of the introduced curvature parameters is an useful tool (Guid, Oblonsek, and Zalik, 1995). The iso-lines or contour lines of curvature are the curves that connect points with the same curvature. The inspection of these lines serves to check fairness of the surface.

The minimum strain energy (mse) calculated according to equation 2.34 is widely used in engineering applications as fairing criterion (Hosseini, 2017), (Sapidis, 1994).

$$mse = \int [(k_1)^2 + (k_2)^2] dA \tag{2.34}$$

The interrogation methods based on illumination models depend on normal vectors and derivatives of the surface. The main background of the models is the creation of lines or light rays from a fixed vision point and compare them with surface features.

The isophotes or equi-brighness curves are formed by the points in the surface that present the same angle between the light rays  $\mathbf{l}_r$  originated from a source point and the normal vector  $\mathbf{n}(u, v)$  of the surface. Thus, isophotes fulfill equation 2.35. If the surface is  $C^m$  continuous in one point, the isophote line will be  $C^{m-1}$  continuous (Hagen, Schreiber, and Gschwind, 1990). By expecting fairness of isophotes the

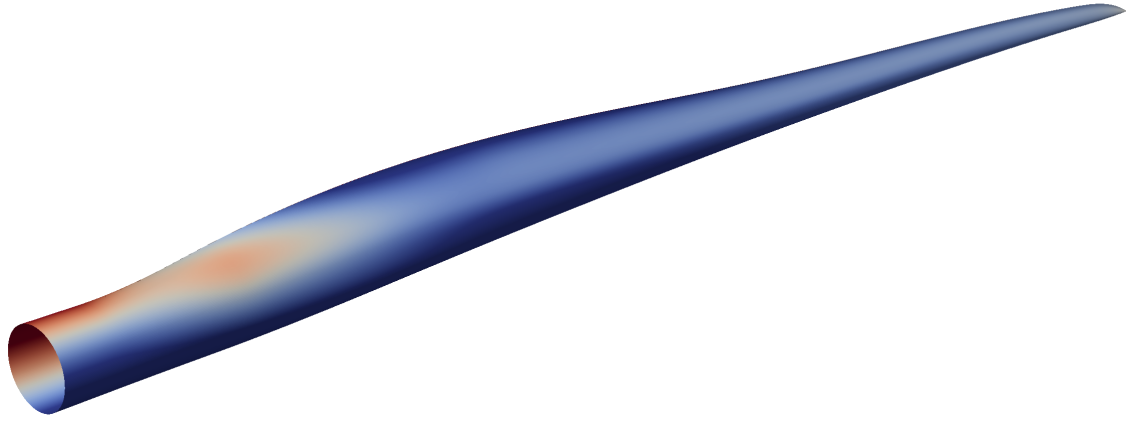


FIGURE 2.5: Isophotes map in a blade surface.

surface quality is assessed. Figure 2.5 presents isophotes of blade surface from an arbitrary vision point.

$$\mathbf{n}(u, v) \cdot \mathbf{l}r = \text{constant} \quad (2.35)$$

The reflection lines are used in the automotive industry to assess the fairness of a surface. They simulate the reflection of parallel straight lights on the surface. Irregularities in the reflection lines indicate that the surface is not fair (Patrikalakis M., 2009).

Let be  $\mathbf{q}_i(t)$ ,  $i = 1 \dots n$  be a family of intersection curves between the surface and a family of planes parallel to vector  $\mathbf{v}$ . For a given angle  $\phi$ , the point in the intersection curve  $\mathbf{q}_i(t_i)$  that satisfies equation 2.36 is searched.

$$\frac{\mathbf{q}_i'(t_i)}{|\mathbf{q}_i'(t_i)|} \cdot \mathbf{v} = \cos \phi \quad (2.36)$$

The points that satisfy the equation 2.36 for different intersection curves are connected to form the reflection lines. The process is repeated for different values of  $\phi$  (Patrikalakis M., 2009).

An extensive literature regarding interrogation methods can be found in (Patrikalakis M., 2009), (Guid, Oblonsek, and Zalik, 1995), (Hagen, Schreiber, and Gschwind, 1990) and (Sapidis, 1994).

## 2.5 Optimization

In this section, an introduction of the general fundamentals of optimization is presented. More detailed information is available in specialized bibliography, e.g. in (Rao, 2009), (Jorge Nocedal, 1999), (Alba et al., 2009), (Antoniu and Lu, 2007) or (Lagaros and Papadrakakis, 2016).

### 2.5.1 Optimization statement

A general optimization problem is stated as follows:

$$\text{Find } X = \left\{ \begin{array}{c} x_1 \\ x_2 \\ x_3 \\ \cdot \\ \cdot \\ x_n \end{array} \right\} \text{ which minimizes } obj(X) \quad (2.37)$$

In addition, if the problem is constrained and presents boundaries for the design variables, the following should be fulfilled:

$$\begin{aligned} ceq_i(X) &= 0 & i = 1, \dots, m_1 \\ c_j(X) &\leq 0 & j = 1, \dots, m_2 \\ X_l &< X < X_u \end{aligned} \quad (2.38)$$

Where  $X$  is the vector of design variables,  $X_l$  are the lower boundaries,  $X_u$  are the upper boundaries,  $ceq(X)$  are  $m_1$  equality constraints,  $c(X)$  are  $m_2$  inequality constraints and  $obj(X)$  is the objective function to be minimized. The initial array of design variables is called initial guess or starting point of the optimization.

### 2.5.2 Classification of optimization problems

The optimization algorithms can be classified in base of several considerations.

- The problem is defined as constrained if at least one constraint should be fulfilled. The points in the search that satisfy the constraints are called feasible points.
- The constraints and objective function can be linear or nonlinear. When objective function and constraints are linear functions of design variables, the problem is a linear programming problem. The problem is labeled as nonlinear programming problem when at least one of the constraints and/or objective function is nonlinear.
- The problem is convex if the objective and constraints are convex functions. This property increases the probability of finding the optimum feasible point.
- The type of problem depends on the nature of design variables. The value of design variables can be continuous or integer. Mixed integer problems present both types.
- Depending on the number of objective functions, the problem can be single or multiobjective. There is a special case, the feasibility problem, where even there is no objective function and the aim of the problem is to find feasible points.
- Local optimization if the algorithm seeks only a local solution in nearby points. The global optimization searches the global optimum or point with best objective function value among all feasible points.

### 2.5.3 The curse of dimensionality

The curse of dimensionality (Bellman and Corporation, 1957) applied for optimization problems, is referred to the complexity that arises when the number of design variables is increased. This complexity is reflected as the great increment of necessary iterations to achieve the optimum and the decrease of probability of finding the optimum.

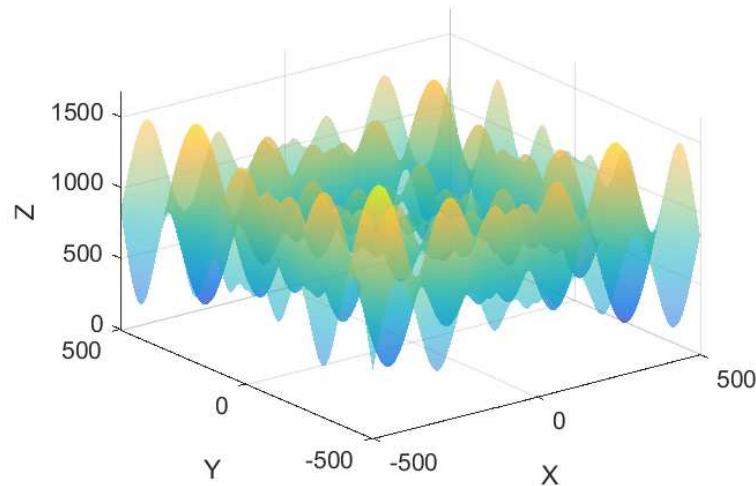


FIGURE 2.6: Schwefel function

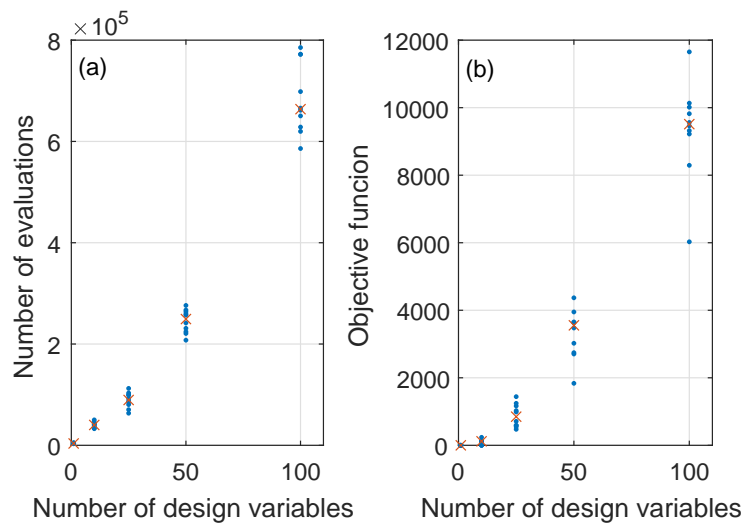


FIGURE 2.7: (a) Number of evaluations of the objective in function of number of variables and (b) Value of the objective of the solution in function of number of variables.

The curse of dimensionality phenomenon is explained by a practical exercise in this subsection. The well known Schwefel function shown in figure 2.6 is a non-smooth function employed to test the efficiency of optimization algorithms (Molga and Smutnicki, 2005). The minimum of Schwefel function is known in advance. The Genetic Algorithm (Rao, 2009) is chosen as a powerful algorithm to search the

minimum of this function. The problem is repeated with several number of design variables:  $n = 1, 10, 25, 50$  and  $100$ . Ten optimizations are run for each case maintaining the same stopping criteria. Figure 2.7 shows that the higher number of variables, the higher the number of evaluations of the objective function is required. Moreover, with ten or more design variables, the algorithm fails to find the optimum in any of the realizations. With twenty-five or more variables the algorithm does not find the optimum in any attempt. This exercise depicts the dramatic consequences of increasing the number of design variables in an optimization problem: the algorithm needs many more evaluations of the objective function and it is much more probable that the optimum is not found.

To respond to the wide variety of optimization problems, many different optimization methods have been developed. None of the algorithms are efficient for all types of problems. In each particular case the most suitable algorithm needs to be chosen. The literature about optimization algorithms is massive. The following introduces some popular optimization algorithms classified in two main categories (Rao, 2009): classical modern optimization methods and nontraditional optimization methods that have emerged as powerful and popular methods for solving complex engineering optimization problems in recent years.

## 2.5.4 Classical optimization algorithms

### Gradient based (GB)

The gradient of a function is an useful property to search a local optimum. If the search direction is followed along the direction of the gradient, the function value changes at the fastest rate. However, the gradient direction is not useful to perform a global search. Furthermore, the calculation of the gradient requires that the function is differentiable which is not fulfilled in all the optimization problems.

The GB methods denominate the optimization techniques that perform calculation of gradients of the objective function and/or constraints. Among them, the interior-point algorithm is introduced. The interior-point algorithm or barrier method re-formulates the original problem stated in subsection 2.5.1 as a minimization of the approximating function  $f_\mu$  where the inequality constraints are transformed into equality constraints according to equation 2.39.

$$\min f_\mu = obj(X) - \mu \sum_i \ln(s_i) \text{ subject to } c_i(X) + s_i = 0 \quad (2.39)$$

The approximating function depends on two parameters:  $\mu$  is the barrier parameter and  $s_i$  are the slack variables, as many as the number of inequality constraints. When  $\mu$  approaches to zero, the minimum of the original function and the approximating function converge. The approximate problem is solved by means of two types of step methods (manual *MATLAB Optimization Toolbox 2019*):

- A newton step to solve the Karush-Kuhn-Tucker (KKT) conditions that are the first-order necessary conditions for the solution. The algorithm employes the Hessian of the Lagrangian of the approximate function. If the Hessian is not positive definite the algorithm uses the following step method.
- A conjugate gradient step. The approach is to minimize a quadratic approximation to the function  $f_\mu$  in a trust region.

Further information of the algorithm is available in (Byrd, Hribar, and Nocedal, 1999) and (manual *MATLAB Optimization Toolbox 2019*)

### Nelder Mead algorithm (NM)

The NM (Nelder and Mead, 1965) or downhill simplex method is a direct local search method. The technique is based on the concept of simplex, which for  $n$  dimension, is a polytope of  $n + 1$  vertices (line for  $n = 1$ , triangle for  $n = 2$ , tetrahedron for  $n = 3$  etc...). The basic concept in the simplex method is to compare the values of the objective function at the  $n + 1$  vertices of the simplex and perform transformations to the simplex gradually to search the optimum. The vertex that resulted the maximum is reflected assuming that the opposite direction provides the minimum. Depending on the result of the reflection, two transformations are performed. The simplex is expanded if the reflected simplex provides a new minimum in order to follow the direction of improvement. In contrast, the simplex is contracted if a higher value is found (Rao, 2009).

### Pattern search (PS)

PS methods are extremely effective for some engineering design problems with expensive function evaluations (Audet and Dennis, 2002). It is a direct search method that does not require the calculations of gradients. The algorithm starts with an initial point and performs a search named poll. Depending on the poll method and the number of design variables, a pattern is created. For example, for a two design variable optimization problem the Positive basis 2N poll method (Lagaros and Papadrakakis, 2016) provides the following pattern that consists on four vectors: [1 0], [0,1], [-1,0] and [0,-1]. The algorithm generates points by adding these vectors to current iterate. Previously a mesh size multiplies the pattern vectors. Then, the mesh points are evaluated and if an improvement is found the successful new point replaces the current point and an expansion factor is applied to the mesh for the next poll. In contrast, if the poll is not successful, a contraction factor is applied. The algorithm can complete the poll even if an improvement is found to speed up the convergence. The pattern search algorithm uses the augmented lagrangian pattern search (ALPS) (Conn, Gould, and Toint, 1991) algorithm to solve nonlinear constraint problems. A subproblem is formulated by combining the objective function and nonlinear constraint function using the Lagrangian and the penalty parameters.

## 2.5.5 Metaheuristic optimization algorithms

The metaheuristic optimization algorithms present these general characteristics (Dreo et al., 2006):

- In origin the algorithms are intended to deal with discrete variables.
- The gradients of the objective function or constraints are not employed
- They are inspired by analogies with biology, physics or ethology.
- Most of methods involve some kind of stochastic process.

### Genetic Algorithms (GA)

The origin of the algorithm concept comes from (Rechenberg, 1965) and work the presented by (Holland, 1992). Conceptually, the algorithm is based on mechanism of natural selection of Darwinian evolutionary theory, specifically on principles of genetics: reproduction, crossover and mutation. The algorithm requires that design variables are coded as string of binary digits. Therefore, in essence, the nature of the variables should be discrete. However, continuous variables are suitable after

transformation into discrete sequence. A single individual or possible solution is called chromosome or genotype. The chromosome has several binary digits (alleles). A group of chromosomes is named population (or generation). The diversity of the population is the distance between chromosomes. The algorithm starts from a population of initial chromosomes. Next, the algorithm performs operations to the string of binary elements: reproduction, crossover and mutation.

- **Reproduction.** The reproduction is the first operation applied to the population (parents) to choose chromosomes with better objective function. The probability of being selected for next population (elite children) depends on the value obtained in the objective function: the lower the objective function, the most probable to survive.
- **Crossover.** Following operation after reproduction consists on creating new chromosomes by mixing the survivors from reproduction. Two chromosome (parents) are randomly picked and a portion of the string are interchanged obtaining modified chromosomes (crossover children). The consequences of the crossover is not always beneficial as the children can improve or not the performance of parents. Moreover, it is desirable to maintain some of the good original parents. To account to this effect, the probability of crossing is adjusted by user with a factor that determines the percentage of strings that are crossed.
- **Mutation.** The resulting chromosomes are subjected to mutation. The alleles can be mutated (change from 1 to 0 or vice versa) with a probability. Thus, this operation alters the genetic information and permits an increase of diversity of the population allowing to explore more extensive design space.

([MATLAB Global Optimization Toolbox 2019](#)) provides a lagrangian genetic algorithm (ALGA) (Conn, Gould, and Toint, 1991) or a penalty algorithm (Deb, 1998) to deal with non-linear constrained problems.

### Particle swarm optimization (PSO)

PSO is an optimization technique inspired in the behavior of cooperative groups of animals such as flock of birds or swarm of insects. The motion of each particle depends on the own and group memory. The velocity of the particles is adjusted according communication interchanged between particles. In an intermediate iteration  $t + 1$  the velocity of each particle is calculated according to equation 2.40:

$$v_i(t + 1) = v_i + c_1 r_1 (p_i^{best} - p_i(t)) + c_2 r_2 (p^{gbest} - p_i(t)) \quad (2.40)$$

$p_i^{best}$  are the coordinates that provided the best value of the objective function in the past iterations of the particle  $i$ .  $p^{gbest}$  are the coordinates that provided the best value of the objective function in the past iterations of all the particles.  $c_1$  and  $c_2$  are weighting coefficients to give importance to individual or group memory.  $r_1$  and  $r_2$  are random values from an uniform distribution between  $[0, 1]$ .

The convergence of the optimization is achieved when the positions of all particles coincide to the same point.

### Simulated annealing (SA)

SA is inspired in thermal annealing process that consists on applying heating and slow cooling to a metal. The movement of atoms is restricted as material is cooled providing a solidification with ordered crystals with the lowest internal energy state.



The slow cooling in the real application is interpreted in the optimization algorithm as the slow decrease of the probability of accepting worse solutions.

During a minimization, a candidate solution  $x_i$  is accepted if the objective function is improved:  $f(x_i) < f(x_{i-1})$ . Besides, even if the objective function is worse ( $f(x_i) > f(x_{i-1})$ ),  $x_i$  can be accepted with a probability that depends on the temperature and the difference  $\delta = f(x_i) - f(x_{i-1})$ . The Boltzmann probability distribution determines the probability of acceptance according to equation 2.41

$$P_b = e^{-\delta/kT} \quad (2.41)$$

Where  $T$  is the temperature lowering function and  $k$  is the Boltzmann constant. At high temperatures the probability of accepting worse candidates is high but as the temperature falls, the probability decreases. The process of heating and cooling is repeated till the convergence of the optimization is achieved.



## Chapter 3

# Blade design process

In this chapter, the new blade design process proposed in this thesis is presented. Section 3.1 provides an overview of the process. Sections 3.2 to 3.6 explain the different stages from the communication of goals to the verification process. Detailed information is provided in section 3.5 about the code *AGORA*, created in the context of this thesis, that is launched recursively in the optimizations performed during the design process.

### 3.1 Overview of blade design process

The main stages of the process are described in flow chart of figure 3.1. The process starts with the communication of goals and requirements of the design to the engineering team. Prior phases to the communication that involve company strategic considerations get out of the scope of the design process. In next phase, goals and requirements are transformed into a mathematical optimization statement by the engineering team. Besides, among the technical inputs of the wind turbine, some of them are identified as design variables and other are considered as fixed parameters. Next step consists of performing the optimization. The computational tool for blade multidisciplinary calculations used in the optimization is designated with the name of *AGORA*. This code is automatically and recursively driven by optimization algorithms for the search of the optimum blade design. The result of the optimization is a potential solution.

Afterward, potential solution is subjected to several technical verifications that include several fields: a detailed control adjustment, complete calculation of aeroelastic set of load cases, structural verification of components, aerodynamic checking, stability assessment, surface fairness evaluation and manufacturing / logistic viability. If the verification is successful, the design process is ended and solution is considered as definitive. Subsequently, blade surface is supplied to the blade mold manufacturer as first step of the blade manufacturing process. Normally, some verification gives not successful results and thus a new design loop should be performed. In this case the optimization is re-stated again.

#### 3.1.1 Explanatory design case

A simplified explanatory design case is presented in this section with the intention of describing the process. Figure 3.2 shows first loop of the design process. Taking into account the goals and requirements transmitted to the engineering team, an optimization statement is defined. The objective function is the maximization of AEP with general main restriction of maintaining the loading level inside the current envelope to avoid re-design of wind turbine components. Due to the impossibility of performing recursively a complete set of load calculations in the optimization, an

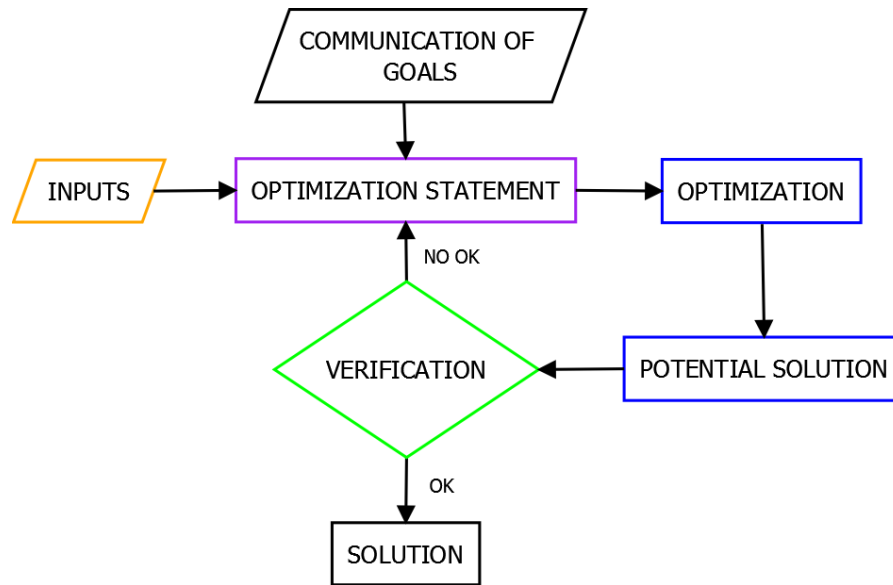


FIGURE 3.1: Blade design flowchart

estimation of the loading level and AEP is used by means of steady aeroelastic calculations or a reduced set of dynamic simulations. These calculations are performed by the code *AGORA*. Thereupon, the optimization is launched and a potential solution is obtained and subjected to several multidisciplinary verifications. Prior to them, a detailed control setting adjustment is performed by specific control engineer. Subsequently, a complete set of aeroelastic load cases is performed resulting a set of ultimate and fatigue values. Suppose that the analysis of the results shows that the fatigue loading of the fore-aft moment  $M_y$  in the base of the tower exceeds the design envelope and thus is not acceptable. In contrast, the remaining loads are acceptable with a significant margin. Therefore, the potential solution is rejected and no more verifications are performed. Afterward, another design loop with a modified optimization statement is executed. In the optimization statement, fatigue loading of the moment  $M_y$  is set as objective function to be minimized. Accordingly, the objective function is evaluated by performing a set of dynamic aeroelastic simulations. *AEP* is now included as a constraint of the problem. After performing optimization of second loop, the control adjustment and subsequent verifications are accomplished with successful result meaning that a solution of the design process is found. This second design loop is presented in figure 3.3.

In following sections, the different stages of the design process are explained in detail.

## 3.2 Communication of the goals and requirements

The project of designing a new blade starts with the communication of goals and requirements of the design by the managers to the engineering team. The following data are provided and made official in an appropriate document:

- Goal of AEP.
- Goal of blade mass and/or cost.
- Wind environmental target conditions.

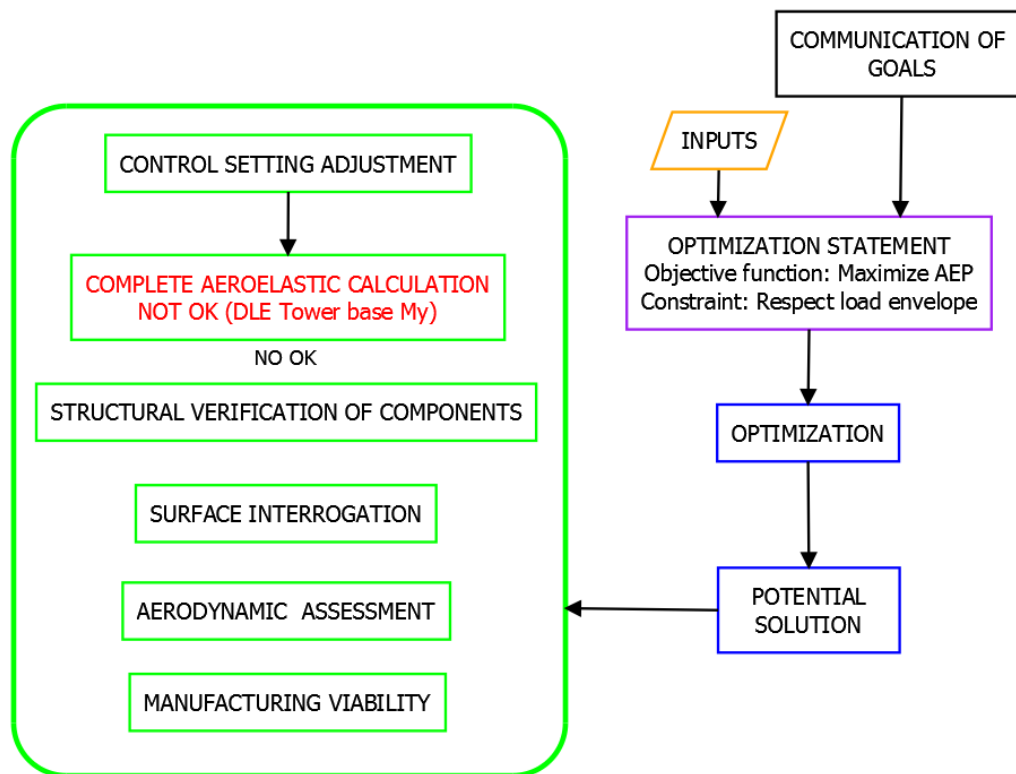


FIGURE 3.2: Flowchart of explanatory design case. Design loop 1.

- Type of wind turbine.
- List of wind turbine components that cannot be re-designed. Consequently, ultimate and fatigue load levels should not exceed the maximum envelope of the component.
- Logistic and manufacturing constraints.
- List of recommendable or forbidden materials.
- Time deadline for the project with intermediate milestones for delivering blade surface, structural layout, control setting and loads.

The goals and requirements vary from one project to another and even can be changed in the course of the project. Thus, it is not possible to generalize and state an unique statement for the blade design. Instead of that, the design procedure is conceived to account for a wide range of potential statements.

### 3.3 Input parameters

This section describes the inputs required to accomplish the design process.

#### 3.3.1 Technical classification of inputs

Depending on the technical field the inputs are classified in the following groups:

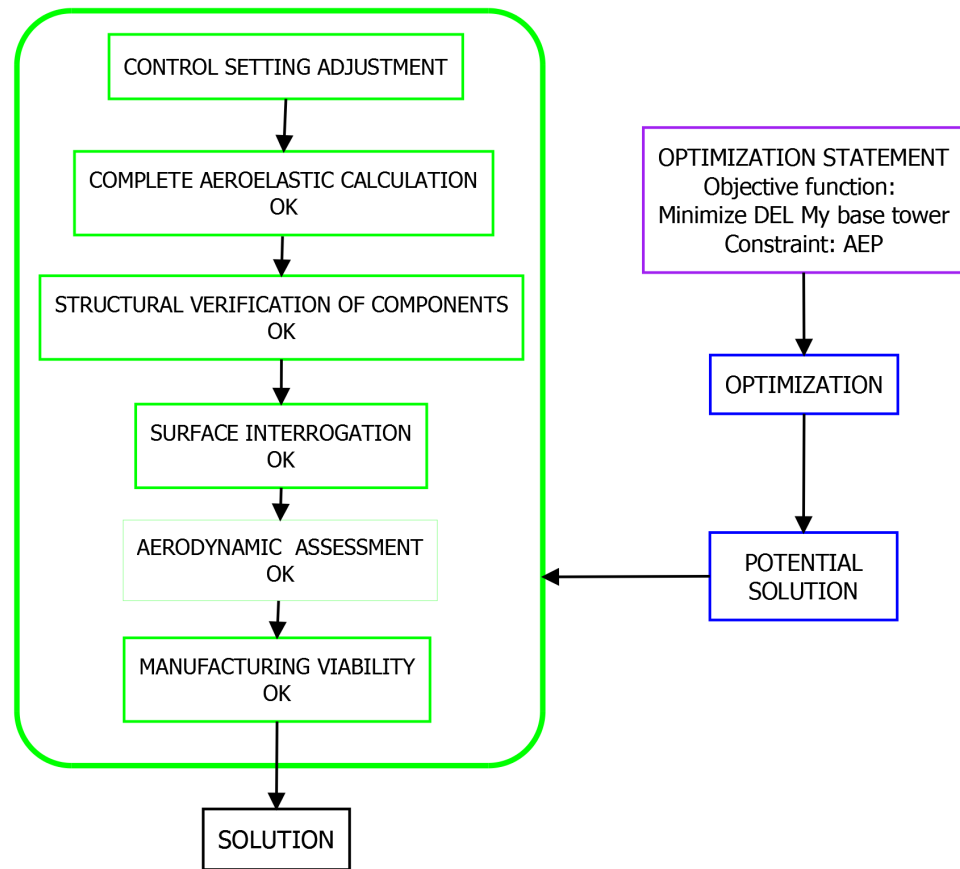


FIGURE 3.3: Flowchart explanatory design case. Design loop 2.

1. Blade geometrical inputs. The knots and control points listed in section A.1 of appendix A are provided to define spanwise laws and master airfoils. These values in conjunction with B-spline order are sufficient to construct B-splines that serve to generate the blade surface as presented in section 1.2. The B-splines are defined in nondimensional form (from  $z=0$  to  $z=1$ ).
2. Structural inputs. The structural layout inputs (see section A.2 in appendix A) define sizing, positioning and mechanical properties of the structural pieces. The structural pieces are presented in figure 3.4. They are identified in the code with this nomenclature:
  - Main spar cap near LE point is named *CAP1* and secondary spar cap near TE point is named *CAP2*.
  - Two side shear webs in *CAP1* are named *WEB1* and *WEB2*. Alternatively, one shear web in the middle of *CAP1* is named *WEB4*.
  - Middle shear web in *CAP2* is named *WEB3*.
  - Leading edge reinforcement is designated as *LER*.
  - Trailing edge reinforcement is designated as *TER*.
  - Laminae that cover the complete contour of the blade between two Z coordinates are designated as *SKIN*.

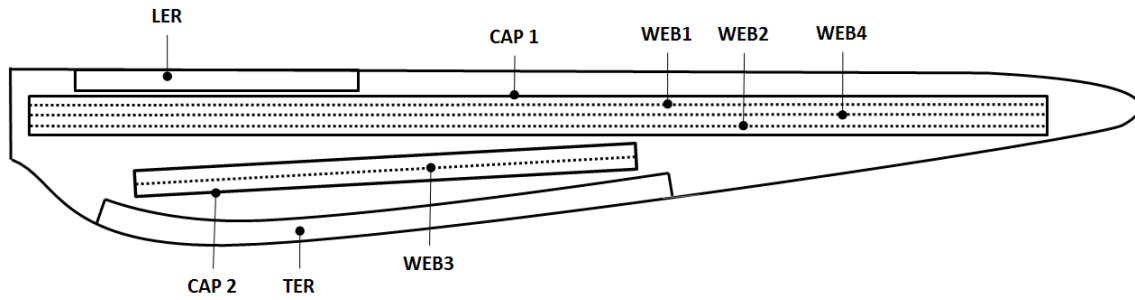


FIGURE 3.4: Nomenclature of the structural layout components.

- Laminae that cover the complete contour of the blade between root and a specific  $Z$  coordinate are designated as *ROOT*.

The aeroelastic and structural codes employed in the process require the necessary input data in several  $Z$  positions along the span. Besides, the codes generate outputs in the same positions. The array that contains these  $Z$ -positions is called  $Z_{eval}$ .

3. Environmental inputs. Wind conditions according to specification (IEC61400-1, 2005) are provided: wind class, turbulence intensity, mean air density, wind shear and wind upflow angle.
4. Control inputs. The basic control features that govern the wind turbine operation have to be introduced: rated power, rotational speeds, gearbox ratio and torque-speed gain. Further detailed features of control and protection system gets out of the scope of the code and are set in the verification stage.
5. Other inputs. Geometrical and structural properties of the wind turbine components: tower, hub, nacelle, drive train,...

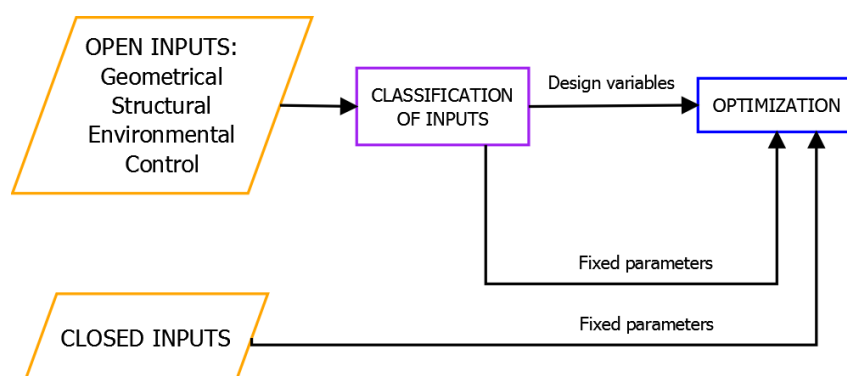


FIGURE 3.5: Classification of inputs according to their role in the optimization.

### 3.3.2 Classification of inputs according to the role in the optimization

Depending on the role in the optimization, the technical inputs are classified as described in figure 3.5:

- Open inputs are potential design variables of the optimization problem. In the definition of the optimization statement, depending on the goals and requirements, engineering team classifies open inputs as fixed parameters or design variables that will be varied in the optimization. In the blade design process open inputs related to blade geometry and structural layout are currently defined as design variables. Besides some control inputs, e.g. rotational speeds or torque-speed gain, are likely to be chosen as design variables. More rarely wind environmental inputs, e.g. air density or mean annual wind speed, can be design variables if they have not been fixed in the goals and requirements communication phase.
- Closed inputs are always considered fixed parameters in the optimization. For instance, drive train losses model determines the difference between energy entering in the rotor and the energy output of the wind turbine due to mechanical and electrical inefficiencies. The parameters of the losses model are not contemplated to be design variables of the problem.

### 3.4 Optimization

The optimization is the core of the blade design process and involves different tasks. At first, the optimization statement is established as subsection 3.4.1 explains. A preliminary design space exploration is introduced in subsection 3.4.2. The optimization strategy and an associated algorithm is defined according to subsection 3.4.3. The optimization involves recursive calculations of code *AGORA* as explained in section 3.5. The resultant potential solution (see subsection 3.4.4) is subjected to several verifications out of the optimization frame to confirm its suitability as presented in subsection 3.6. If the potential solution satisfies the verification, the solution is achieved.

#### 3.4.1 Optimization statement

The inputs, design goals and requirements are transformed into a mathematical optimization statement. Goals and requirements are converted into objective function  $obj(x)$  to be maximized (or minimized) and constraints  $c_i(x)$ ,  $ceqi(x)$  to be fulfilled. Besides, a subgroup of inputs parameters are identified as design variables  $X$ . The others are set as fixed parameters. Boundaries  $X_l$  and  $X_u$  for design variables are also defined.

Common outputs that are potential objective functions or constraints of the optimization problem are the following:

- Performance of the wind turbine (AEP).
- Structural integrity outputs. Extreme blade deflections, ultimate loads, and fatigue loads in the different locations in the wind turbine.
- Transportation viability outputs. The geometry should be adequate to be transported and should not exceed determinate boundaries.
- Acoustic emission. The wind turbine should not exceed a determinate level of noise.
- Acceptable blade surface fairness.

### 3.4.2 Design space exploration and sensitivity analysis prior to optimization

Prior to the optimization a design space exploration investigates the design space with the intent of obtaining knowledge to understand the relationships between design variables and outputs, determine the most important design variables and identify anomalous performance under determinate combinations of design variables. This undesired performance can be avoided in the optimization by setting appropriate constraints based on surrogate modeling. Chapter 6 is dedicated to design space exploration.

### 3.4.3 Optimization strategy

An optimization strategy is accomplished to provide a potential solution of the problem. Practical optimization cases are explained in chapter 7. The optimization algorithm governs the variation and evaluation of design variables  $X$  within the boundaries  $X_l$  and  $X_u$ . The evaluation consists of calculations with code *AGORA* that involve subordinate multidisciplinary calculations as explained in section 3.5 to obtain the different wind turbine outputs. The result of *AGORA* provides values for objective function  $obj(x)$  and constraints  $c_i(x)$ .

For the completion of the optimization, different algorithms are ready for use. The algorithms are classified as local or global. A search is considered local if the algorithm scans in the proximity of the supplied initial point (basin of attraction). In contrast, the global search explores the whole design space.

Depending on the level of maturity of the design a local or global search is performed. In the initial design loops a global search is launched to approach to the basin of attraction of the global optimum. GA, SA, PSO and PS are appropriate algorithms for this global search. SA and PS require an initial point to start the search. The global search involves a more expensive computational cost and presents difficulties to find feasible solutions under high constrained problems. In advanced design loops, the solution obtained from global search is improved by applying local algorithms such as GB or NM algorithms.

Other criteria are taken into account to decide between algorithms. GB algorithm are not suitable for non-smooth objective function and constraints as the algorithm requires the calculation of gradients. Regarding the type of design variables, GA can address mixed-integer values.

Due to the nature of the problem, the algorithms should be able to solve constrained optimization problems where design variables and constraints present non-linear relationships.

The algorithm stops the search when any of these stopping criteria are fulfilled:

- The variation of the design variables is lower than a given threshold provided by the user.
- The variation of the objective function is lower than a given threshold provided by the user.
- The number of iterations exceeds a maximum number specified by the user.
- The time exceeds a maximum number specified by the user.

For facilitating the convergence of the algorithm and due to the difference of magnitudes, the design variables are normalized (centered and scaled) before being introduced into the algorithm. Moreover, the objective function and constraints

are also normalized with the same purpose. The feasibility of starting values helps the algorithm to find a feasible optimum. Accordingly, a prior optimization to find feasible starting values is a valuable practice. The use of boundaries in the design variables, when some non coherent values are known, are useful to reduce the design space.

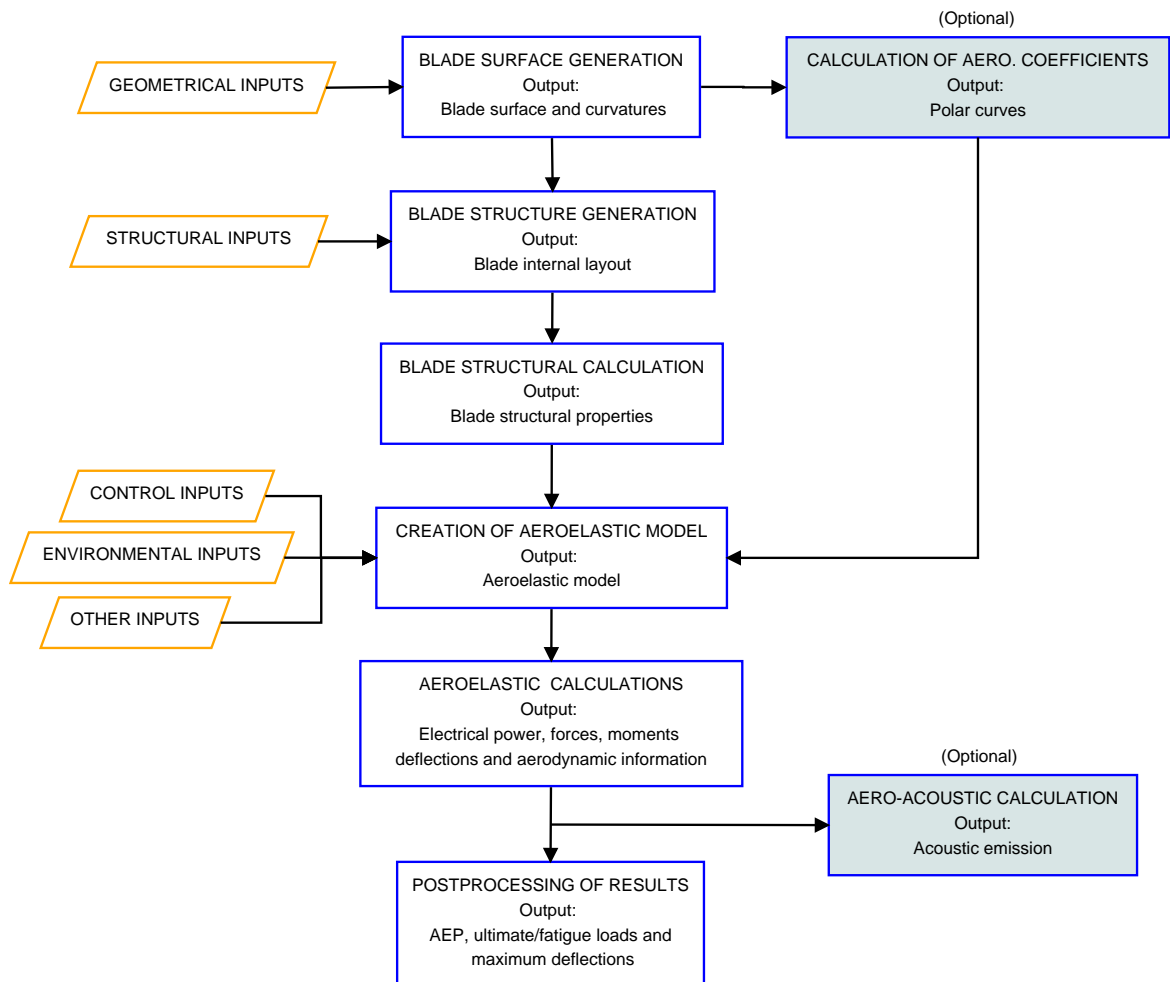


FIGURE 3.6: Flowchart of calculation in AGORA.

### 3.4.4 Potential solution

The optimization algorithm performs recursively stages from section 3.5.1 to section 3.5.10 and identifies a set of design variables as solution of the optimization. The solution is checked and subjected to several technical verifications. If the verifications are not satisfactory, the optimization is repeated with some modifications in the optimization (change of design variables, boundaries, constraints, type of algorithm,...). However, if the solution is successful, it is considered as definitive.

## 3.5 AGORA

The different phases of *AGORA* are explained in this section and described in flowchart of figure 3.6. The code is programmed in (*MATLAB 2019*).



### 3.5.1 Blade surface generation

The cubic B-splines representing spanwise laws and master airfoils are constructed with geometrical inputs (knots and control points). The code scales the laws according to blade length  $L$  and evaluates them in the spanwise coordinates  $Z_{eval}$ .

The direction of the prebending curve is determined by a reference plane. In origin, the prebending curve is contained in a baseline plane parallel to XZ plane. According to open input angle  $p\_rotationd$ , the prebending curve is rotated about Z-axis as figure 3.7 shows.

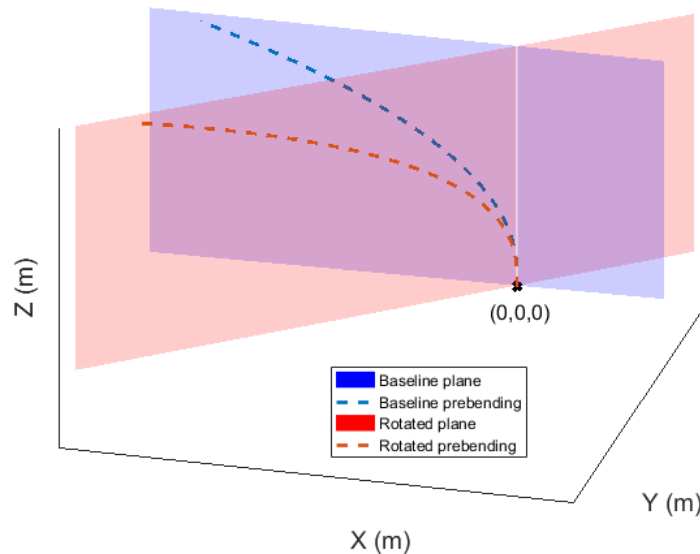


FIGURE 3.7: Prebending curve before and after rotation with  $p\_rotationd$ .

Blade external geometry is constructed as a B-spline lofted surface created by transforming the master airfoils in form of B-spline according to transformations defined by the spanwise laws, also in B-spline form.

Interrogation parameters are calculated in a grid of points of the surface. Isoparametric curvatures  $k_u$ ,  $k_v$  and isophotes are computed and compiled.

### 3.5.2 Calculation of aerodynamic coefficients

This stage is optional because it is accomplished only if master airfoil geometry is being designed and thus airfoil control points are design variables of the optimization problem. In that case, B-spline curve representing airfoil is evaluated in a grid of points and subjected to calculation in panel method code ([XFOIL 2013](#)) for specific conditions such as the Reynolds number or Mach number. The code provides aerodynamic coefficients for a range of angles of attack, currently from  $-15^\circ$  to  $15^\circ$ . The coefficients are extrapolated to the whole range  $-180^\circ$  to  $180^\circ$  according to Viterna method (Viterna and Janetzke, 1982).

After the blade surface construction, the pieces of the structural layout are sized and positioned along the blade surface.

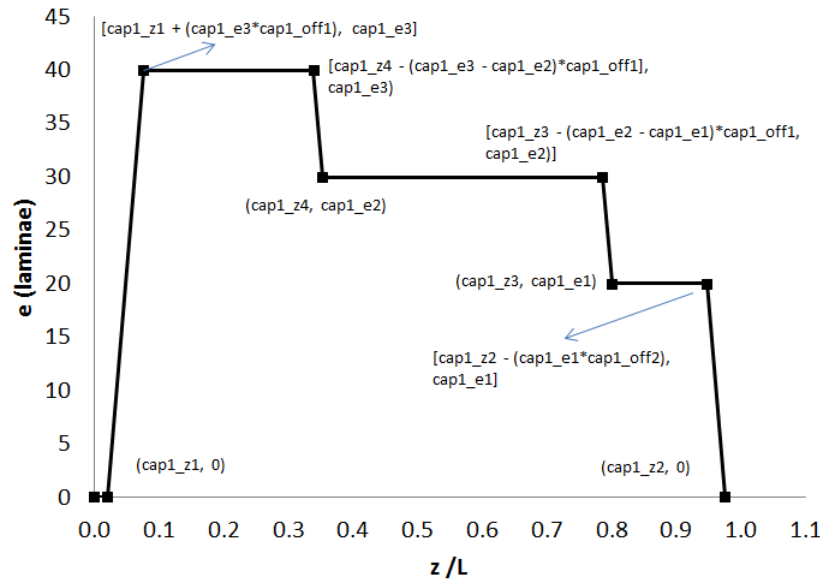


FIGURE 3.8: Number of laminae along span in CAP1.

### 3.5.3 Sizing of the pieces

For each structural piece, the number of laminae and single lamina thickness are defined. These properties vary along span according to the corresponding structural inputs. Besides, the type of material is defined. Figure 3.8 shows the sizing of *CAP1* along span which is determined by several structural inputs.

### 3.5.4 Positioning of caps and shear webs

The spar caps and shear webs are positioned according to a system of reference planes:

- *CAP1* reference plane defines middle line of *CAP1* and *WEB4*. Besides, *CAP1* boundary planes are parallel planes to *CAP1* reference plane that define the extremes of *CAP1*. *WEB1* reference plane and *WEB2* reference plane, parallel to *CAP1* reference plane, define *WEB1* and *WEB2* respectively. As example, figure 3.10 shows the steps for the *WEB4* positioning process: A.- the bladed lofted surface is generated, B.- the *CAP1* reference plane is created by transforming XZ plane and C.- the intersection points between plane and surface are calculated.
- *CAP2* reference plane defines middle line of *CAP2* and *WEB3*. The *CAP2* boundary planes are parallel to *CAP2* reference plane.

The following describes how reference planes are positioned in the space. The parameters that govern the position are open inputs and consequently are potential design variables of the optimization problem. *CAP1* and *CAP2* reference planes are in origin XZ plane. The planes are translated and rotated according to three open inputs. The following explains the transformations and the associated open inputs for the positioning of *CAP1* reference plane:

1. The plane XZ is the baseline reference plane.

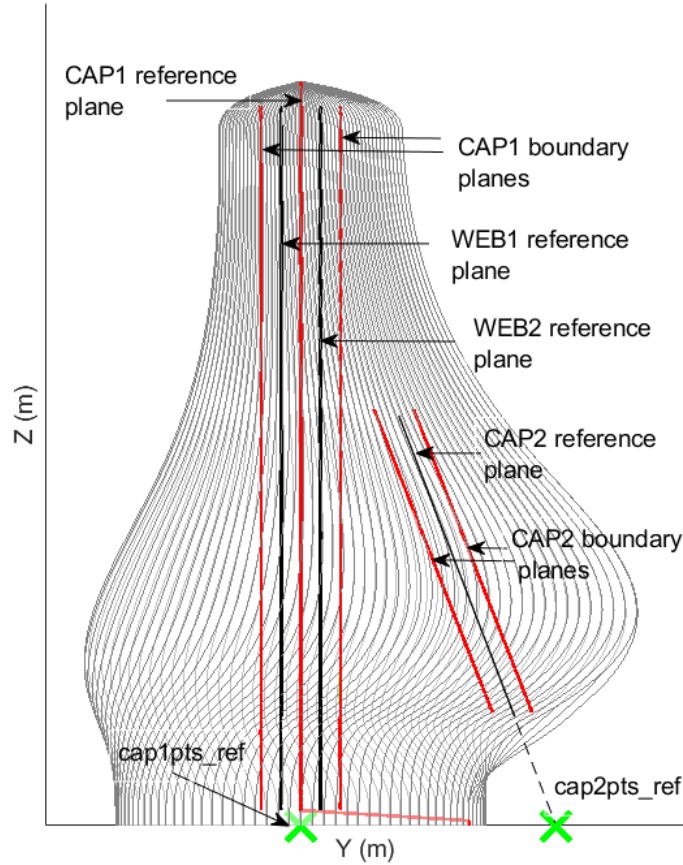


FIGURE 3.9: Reference plane and points in the blade surface with  $\alpha_1 = 0^\circ$ ,  $\alpha_2 = 1^\circ$  and  $\alpha_3 = 0^\circ$ .

2. Rotation about Z-axis an angle  $\alpha_1$  is performed.
3. Rotation about X-axis an angle  $\alpha_3$  is performed.
4. Finally the plane is translated to point  $cap1\_ptsref$ .

Accordingly, the sequence of rotations 2 to 3 applied to normal vector of XZ plane that results in the normal vector  $\mathbf{n}_1$  of CAP1 reference plane are the following of equation 3.1.

$$\mathbf{n}_1 = \begin{pmatrix} 1 & 0 & 0 \\ 0 & \cos(\alpha_3) & -\sin(\alpha_3) \\ 0 & \sin(\alpha_3) & \cos(\alpha_3) \end{pmatrix} * \begin{pmatrix} \cos(\alpha_1) & -\sin(\alpha_1) & 0 \\ \sin(\alpha_1) & \cos(\alpha_1) & 0 \\ 0 & 0 & 1 \end{pmatrix} * \begin{pmatrix} 0 \\ 1 \\ 0 \end{pmatrix} \quad (3.1)$$

Moreover, the similar operations are performed for CAP2 reference plane:

1. The plane XZ is the baseline reference plane.
2. Rotation about Z-axis an angle  $\alpha_1$  is performed.
3. Rotation about X-axis an angle  $\alpha_2$  is performed.
4. Finally, the plane is translated to point  $cap2\_ptsref$ .

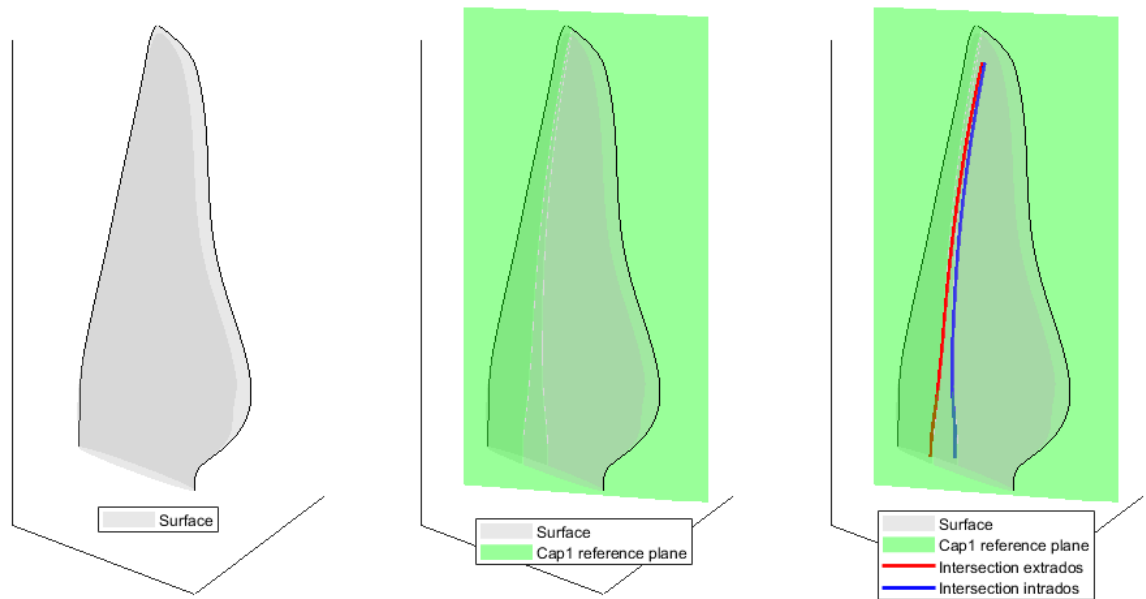


FIGURE 3.10: *CAP1* positioning. A: surface generation. B: creation of reference plane. C: calculation of intersection.

In figure 3.9 reference planes are shown for a case with  $\alpha_1 = 0^\circ$  and  $\alpha_3 = 0^\circ$ . Thus, *CAP1* reference plane is parallel to  $XZ$ . *CAP2* reference plane presents a rotation of  $\alpha_2 = 1^\circ$  about  $X$ -axis.

The code calculates the intersections between planes and blade surface to provide the positions of main structural components in the surface which are necessary data to be provided to the structural code for cross sectional properties calculation. The distance  $D(u, v)$  in form of B-spline between surface  $\mathbf{SF}(u, v)$  and a reference plane defined by a point  $\mathbf{X}_0$  and a normal vector  $\mathbf{n}$  is calculated according to equation 3.2.

$$D(u, v) = (\mathbf{SF}(u, v) - \mathbf{X}_0) \cdot \mathbf{n} \quad (3.2)$$

The intersection points of the plane with the surface are the points that belonging to surface  $\mathbf{SF}(u, v)$  present null distance with the plane ( $D(u, v) = 0$ ).

### 3.5.5 Positioning of trailing edge reinforcement (TER) and leading edge reinforcement (LER)

*LER* and *TER* are structural pieces with constant transverse width along span. Instead of a system of reference planes, the end position of these pieces along the airfoil contour are determined as figure 3.12 shows. For a given section, starting from *TE* point, the cumulative length along extrados contour is calculated. The end of *TER*, named *ter\_end\_extra* is the point with cumulative length equal to width *ter\_w*. Analogous calculation is performed for intrados side to calculate *ter\_end\_intra*. *LER* end positions in extrados and intrados sides (*ler\_end\_extra* and *ler\_end\_intra*) are obtained by calculating the cumulative length along contour from *LE* point and finding the point along contour with cumulative distance equal to *ler\_w*.

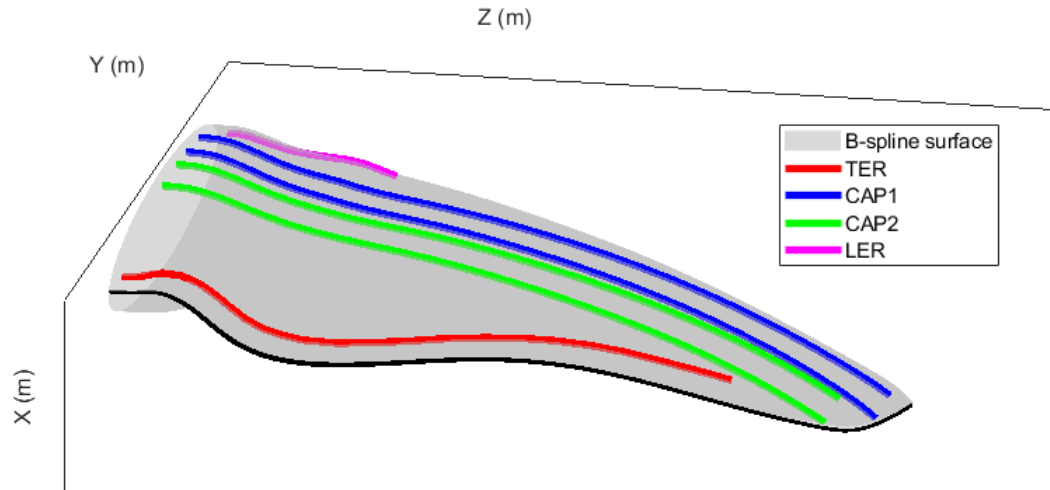


FIGURE 3.11: 3D view of B-spline surface and boundaries of  $CAP1$ ,  $CAP2$ ,  $LER$  and  $TER$ .

In figure 3.11 the boundaries of  $CAP1$  and  $CAP2$ , calculated as intersections between blade surface and boundary planes are presented. Besides,  $TER$  and  $LER$  boundaries, obtained from cumulative lengths along contour, are shown.

The gaps between structural pieces and between structural pieces and the surface are relevant data for manufacturing viability. Figure 3.13 shows distances along span between split line and  $CAP1$ ,  $CAP2$  and  $TE$ ,  $CAP1$  and  $CAP2$  and finally between  $CAP2$  and  $TER$ .

### 3.5.6 Cross-sectional structural properties calculation

The structural code requires geometrical blade data and layout information (sizing and position of the structural pieces). Accordingly, the following information is provided in the span coordinates of array  $Z_{eval}$ :

- Chord, twist, stacking and prebending.
- Geometry of sections in positions of  $Z_{eval}$ . The sections are provided as sets of points in dimensional form. These points are calculated by evaluating the blade surface in the positions of  $Z_{eval}$ .
- Layout information in the sections. Each section is divided in sectors which are defined by the relevant separation points that define boundaries of layout pieces. In figure 3.14 the extrados side of a section is shown. Besides  $LE$  and  $TE$  points, five intermediate separation points ( $P1$ ,  $P2$ ,  $P3$ ,  $P4$  and  $P5$ ) are identified to describe the boundaries of pieces.
  - $LER$  is located in sector  $LE - P1$ .
  - Cores are located in sectors  $P1 - P2$  and  $P4 - P5$ .
  - $CAP1$  is located in sector  $P2 - P4$ .
  - $TER$  is in sector  $P5 - TE$ .

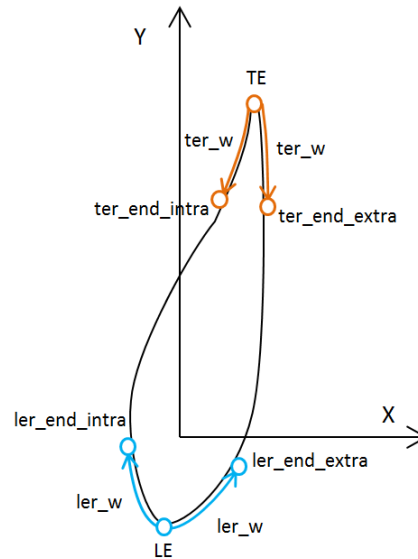


FIGURE 3.12: End position of TER and LER by cumulative length calculation along contour.

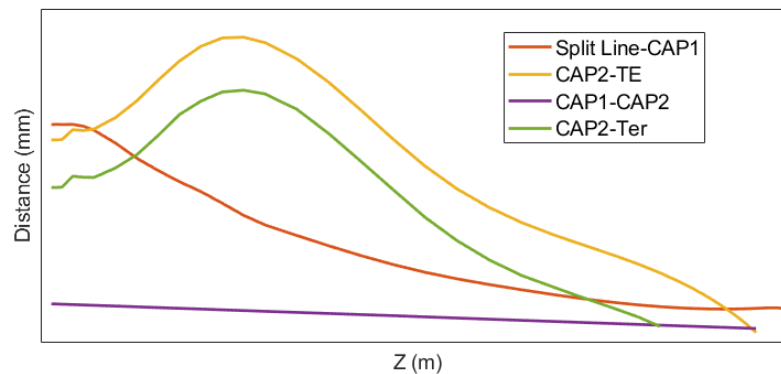


FIGURE 3.13: Relevant distances in the structural layout.

- Finally, point  $P3$  defines the shear web middle point in extrados.

The same separation in sectors is provided in intrados side of the section. For each sector the number of laminae, thickness of single lamina and type of material should be provided in the correct stacking order.

- The properties of the materials (Bir, 2001):
  - $E_1$ : Young's modulus in  $X$ -axis. Same for tension and compression.
  - $E_2$ : Young's modulus in  $Y$ -axis. Same for tension and compression.
  - $G_{12}$ : shear modulus.
  - $\mu_{12}$ : is the Poisson's ratio defined as the contraction strain in lateral caused by unit extensional strain in principal direction.
  - Material density.

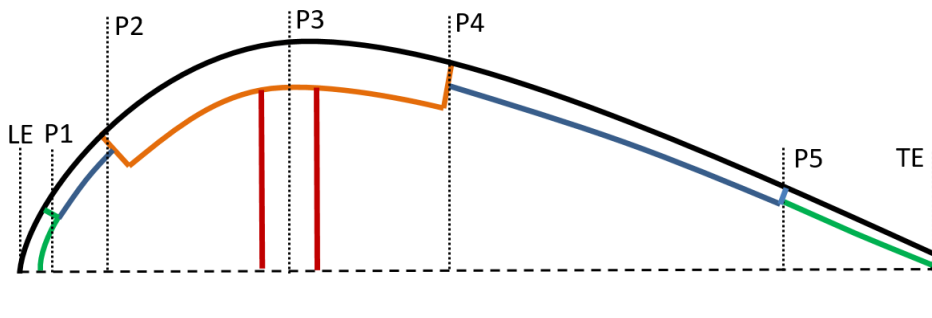


FIGURE 3.14: Extrados part of the airfoil where separation points and associated sectors are distinguished.

The structural code provides as outputs of the calculation the cross sectional properties (Bir, 2001): mass, stiffness and relevant structural points in the spanwise positions of the array  $Z_{eval}$ .

### 3.5.7 Creation of aeroelastic model

AGORA requires a baseline aeroelastic wind turbine model that contains all the wind turbine relevant data to perform aeroelastic simulations. During the progress of the optimization, the fixed parameters are maintained unaltered in the model. However, the new values of the design values provided by the algorithm are updated automatically by AGORA.

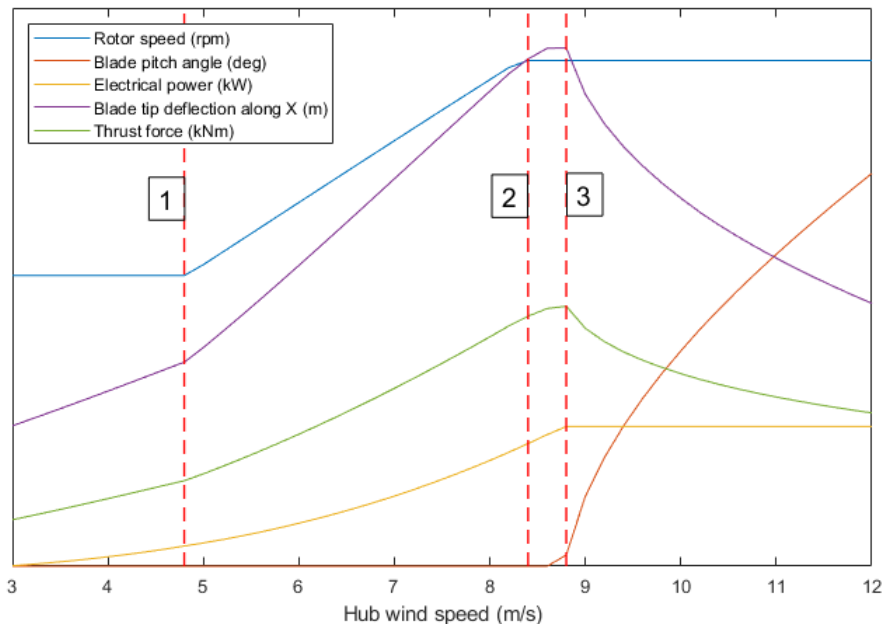


FIGURE 3.15: Outputs of steady calculation.

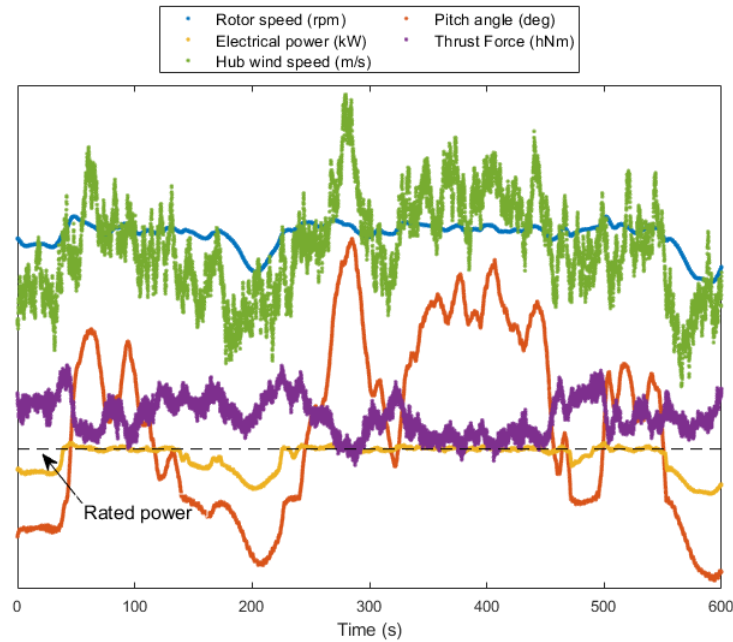


FIGURE 3.16: Time series of dynamic calculation with 10 m/s mean wind speed.

### 3.5.8 Types of aeroelastic simulations

Different types of aeroelastic simulations can be performed in the optimizations: eigen-frequencies calculation, steady calculations or dynamic calculations.

- Eigen-frequencies calculation. The aeroelastic code performs a modal analysis to obtain the uncoupled eigen-frequencies and mode shapes of the flexible bodies. In the steady and dynamic simulations these modes are coupled to calculate the dynamic response of the wind turbine.
- Steady simulations provide wind turbine loads and deflections in the flexible bodies in function of steady wind speeds. One steady calculation includes computation for a range of wind speeds. The basic control features such as pitch angle, generator torque, optimal gain and rotational speeds should be defined. Figure 3.15 shows typical outputs of a steady calculation. Between vertical lines 1 and 2 the wind turbine is operating in the variable speed area. Vertical line 3 marks the rated wind speed. From point 3 to cut-out wind speed, the wind turbine is in pitch regulating operation.
- Dynamic simulations. In dynamic simulations, the wind turbine is affected by a turbulent varying wind field. The control logic is acting to regulate the operation replicating the real wind turbine behavior under same environmental conditions. Figure 3.16 shows progress of different outputs in a simulation of six-hundred seconds of duration with wind field of 10 m/s mean speed.

In addition to blade coordinates system introduced in section 1.2, coordinate systems in hub and tower are used to express forces and moments in these components. The hub coordinate system is defined as follows:

1. Origin: hub center.



2.  $X_{hub}$ : along drive train axis, and pointing towards the tower.
3.  $Z_{hub}$ : vertical direction.
4.  $Y_{hub}$ : to give a right-handed coordinate system.

The tower coordinates axes are parallel to axes of hub coordinate system but with origin in center of tower base.

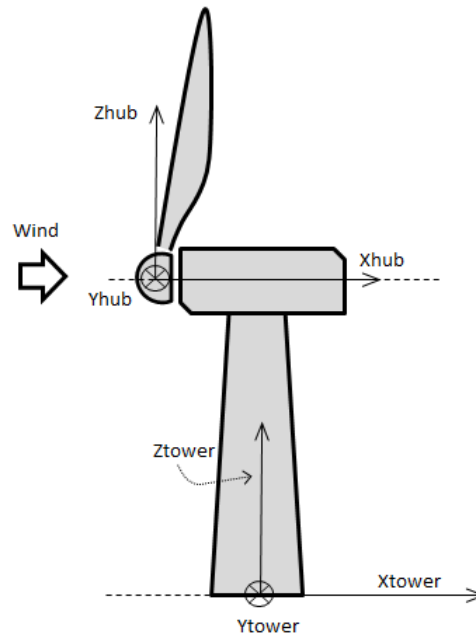


FIGURE 3.17: Hub and tower coordinate systems.

The dynamic simulations provide time series of loads, deflections, aerodynamic coefficients and control outputs such as electrical power, pitch angle, generator speed or rotor speed. Similarly, steady calculations provide stationary results of the same outputs.

Within all the information, a set of more significant loads and deflections are selected for post-processing the results due to their importance in the structural integrity assessment and the wind turbine performance:

- Blade root moments to assess the blade root-hub connection.
- Thrust force in yaw bearing to evaluate the integrity of tower and the general loading level.
- Torsion moment in drive train to assess the gearbox integrity.
- Torsion moment in the blade root to evaluate the pitch actuator capacity.
- Deflections in the blade to check the clearance with the tower.
- Electrical power to assess the performance of the wind turbine.

The raw data are post-processed for different purposes. The ultimate loading level is assessed by calculating the extreme values of loads and deflections. Besides,

fatigue damage equivalent loads are calculated. Finally, the power curve is constructed from electrical power mean values and AEP is calculated.

With respect to results of steady simulations, extreme loads and deflections are employed to estimate ultimate loading without taking into account dynamic effects. The power curve and AEP are also estimated from results of steady simulations.

Additionally, the results of steady simulations in conjunction with the static mass moment  $Fm$  are used to estimate the  $Mx$  moment in root (edgewise). The cyclical variation of moment  $Mx$  is caused by the periodic gravity loading that presents a maximum when blade is horizontal and a minimum when blade is vertical. Accordingly, an estimator of the DEL is employed (Echeverria, Mallor, and Sanz, 2017) accounting for the number of cycles and the first moment of mass. This estimator named  $mxs\_r\_del$  is calculated according to equation 3.3.

$$\begin{aligned} mxs\_r\_del &= \sqrt[n]{Rev_{total}(Fm^m)} \\ Fm &= Z_{cdg} \cdot Mass \end{aligned} \quad (3.3)$$

Where  $Fm$  is the first moment of mass,  $Z_{cdg}$  the Z-coordinate of center of gravity,  $m$  the material fatigue slope and  $Rev_{total}$  is the total number of revolutions in twenty years obtained from steady calculation and the mean hourly annual wind speed distribution.

The outputs of the aeroelastic simulations are post-processed and get ready to be used in the optimizations as objective function or constraint. The post-processed outputs are identified according to the following nomenclature that consists of five labels:

1. Label1. Type of load or blade deflection.
  - Force:  $Fx$ ,  $Fy$  or  $Fz$  in kN.
  - Moment:  $Mx$ ,  $My$  or  $Mz$  in kNm.
  - Blade deflection:  $dx$  along X in meters,  $dy$  along Y in meters and rotation  $rotzd$  about Z-axis in degrees.
2. Label2. Type of aeroelastic simulation: steady ( $s$ ) or dynamic ( $d$ ).
3. Label3. Location in the wind turbine: hub center ( $hub$ ), blade root ( $r$ ), blade tip ( $tip$ ), yaw center ( $yaw$ ), gearbox ( $gearbox$ ), base of tower ( $tbase$ ) or tower top ( $top$ ).
4. Label4. Type of post-processing. Maximum ( $max$ ), minimum ( $min$ ), mean ( $mean$ ), standard deviation ( $std$ ) or damage equivalent load ( $del$ ).
5. Label5. In the outputs that result from dynamic simulations, this label indicates the mean wind speed of the simulation.

For example, the post-processed result labeled as  $fxd\_yaw\_del\_14$  means the damage equivalent load of force  $Fx$  obtained in yaw center that results from dynamic simulation with a wind field of mean wind speed 14 m/s. The list of wind turbine outputs generated from aeroelastic simulations are listed in appendix C.

### 3.5.9 Aero-acoustic calculation

Optionally, if requested by the user, AGORA launches an aeroacoustic code (*Silant*) in order to calculate the total acoustic emission. In advance, AGORA should modify the (*Silant*) input file with the appropriate geometrical and aerodynamic data obtained from previous stages.

### 3.5.10 Spar cap longitudinal strain estimation

In the structural verification phase (subsection 3.6.3), which is performed to a potential solution after the optimization phase, the blade and the wind turbine components are subjected to structural calculations to verify the integrity under the loads obtained in the loads calculation (subsection 3.6.2). These structural calculations get out of the scope of the code *AGORA*. However, in *AGORA*, a simplified estimation of the longitudinal strains in the spar cap is calculated. This estimation can be incorporated as constraint or objective function in the optimization statement. The estimation is based on the simplified assumption that the spar cap is a straight beam of rectangular cross-section under a flapwise bending moment. This moment is obtained from steady aeroelastic simulations. Thus, the longitudinal strains  $\epsilon_{cap}$  are calculated according to equation 3.4 (Case and Chilver, 1971).

$$\epsilon_{cap} = \frac{M_{flap} X_{na}}{EI_{flap}} \quad (3.4)$$

Where  $M_{flap}$  is the flapwise bending moment,  $X_{na}$  is the distance of the spar cap middle line to the neutral axis and  $EI_{flap}$  is the flapwise bending stiffness.

## 3.6 Verifications post-optimization

The potential solution provided by the optimization should satisfy several verifications before being admitted as the definitive solution. These verifications involve different technical tasks performed by different specialized engineers with the aid of specific computational tools.

### 3.6.1 Control setting adjustment

Based on the control features defined in section 3.3, a professional detailed control should be adjusted by a control engineer (Bossanyi, 2003). The control engineer assesses that the design is suitable and provides a control setting that protects the wind turbine under the events contemplated in the specification (IEC61400-1, 2005).

### 3.6.2 Complete aeroelastic calculation set

As requested by the design specification (IEC61400-1, 2005) a complete set of aeroelastic calculations should be performed taking into consideration the design situations and the associated types of load cases.

### 3.6.3 Structural verification of components

The previous aeroelastic calculations provide a set of ultimate and fatigue loads in different appropriate formats that are employed by expert structural engineers to evaluate the integrity of the different wind turbine components, blade included.

### 3.6.4 Surface interrogation

The fairness of the blade surface is assessed with interrogation methods. In the stage described in section 3.5.1, surface interrogation properties are automatically generated by *AGORA*. Paraview (Ahrens, 2005) is an appropriate tool for the visualization of the blade surface interrogation properties. *AGORA* generates an input file for

(Ahrens, 2005) with the suitable format. In addition, CAD tools provide the functions to carry out a complete fairness evaluation of the surface.

### 3.6.5 Aerodynamic assessment

Subsequently to the complete aeroelastic loads calculation, the aerodynamic information from simulations is inspected to assess the aerodynamic behavior of the blade. It is recommendable that angles of attack of airfoils are not operating in stall regime. Besides, the performance under non standard aerodynamic situation, e.g. iced or rough condition of airfoils (Ehrmann, 2014) is assessed. The aeroelastic stability (Holierhoek, 2008) is evaluated with specific aeroelastic simulations. The occurrence of resonances or aeroelastic instabilities should be discarded.

### 3.6.6 Manufacturing and logistic viability

The details of the geometry and structural layout are provided to blade process engineers that evaluate the viability of the design. Distances calculated in subsection 3.5.5 are relevant to determine the accessibility in the manufacturing process. In addition, logistic technicians assess that the blade can be transported and handled.

## Chapter 4

# Representation of airfoils with B-splines

### 4.1 Introduction of chapter

B-splines are able to generate airfoil geometries by defining coordinates of the control points as design variables. (Sartori, 2013) and (Fuglsang and Dahl, 1999) presented airfoil design studies where geometry is represented by thirteen control points and (Ribeiro, Awruch, and Gomes, 2012) used twelve control points to generate the candidate geometries. However, the justification of these elections has not been deeply presented in the papers. A priori, the B-spline configurations with higher number of control points imply more flexibility to achieve different geometries and thus they are the preferred ones. However, the B-spline configuration that results of this analysis will be employed to design new geometries in the optimization problem and due to the curse of dimensionality phenomenon, it is recommendable to have a low number of design variables to avoid an excessive computational cost.

This chapter presents a justification of the necessary number of airfoil design variables and the suitable type of independent parametrization to design airfoils. In order to justify the selection, several candidate configurations of B-splines are employed to approximate different existing test airfoils represented as sets of points. It is assumed that the configurations that approximate better the existing assorted geometries are the most suitable to design new geometries. Each approximation is stated as an optimization problem that minimizes geometrical, aerodynamic or performance errors which are previously defined. The computation of the approximation errors involves several practical detailed aspects that are dealt. Furthermore, a method based on statistical hypothesis testing applied to the approximation errors is presented to assess the accuracy of types of B-splines approximating airfoil geometries.

The chapter is organized as follows: section 4.2 presents the types of approximating errors, section 4.3 describes the method to perform the optimizations and section 4.4 presents the statistical analysis.

### 4.2 Type of approximating error

This section describes the different types of errors to assess the accuracy of the approximation of airfoils with B-splines. The baseline airfoil is represented as a set of points  $D$  and the approximation is performed with a B-spline curve  $C(t)$ .

### 4.2.1 Geometrical error

The geometrical error measurement is the sum of squared distances between each baseline point  $D_i$  and the approximating B-spline curve evaluated in the corresponding independent parameter  $C(t_i)$ . Figure 4.1 shows the distances between baseline points to be approximated and the B-spline curve evaluated in the corresponding values of the independent parameter.

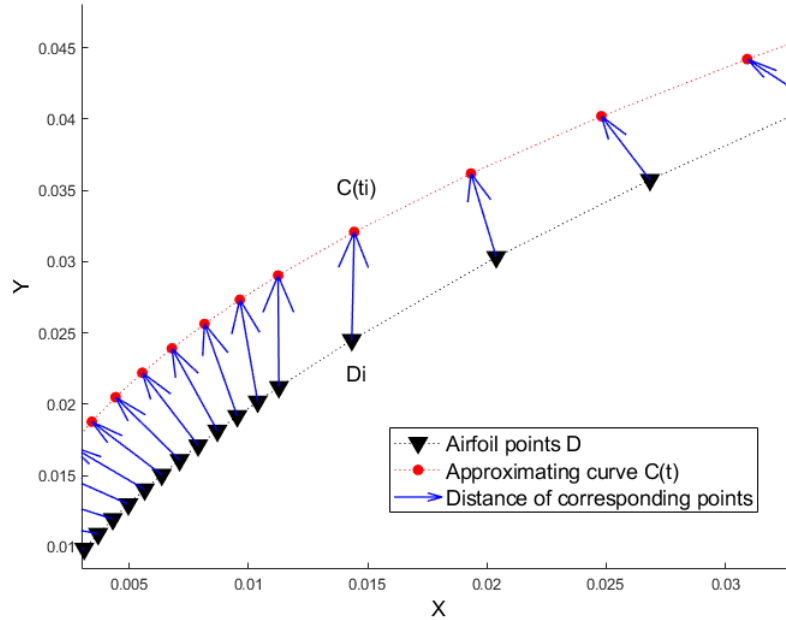


FIGURE 4.1: Geometrical error of an approximating curve  $C(t)$

An alternative method consists in calculating distances between each baseline point  $D_i$  and a band of ten points around the corresponding approximating point:  $\{C(t_i - 5) \dots C(t_i) \dots C(t_i + 5)\}$ . The minimum of these distances is used to compute the error as the sum of squared distances of all points. This method requires an increment in the computational cost but improves significantly the approximations.

Furthermore, an improved approach to measure geometrical error lies in calculating the minimum distance between each point  $D_i$  and the approximate B-spline  $C(t)$ . To calculate this distance, it is necessary to find the point in the B-spline  $C(t_m)$  curve that fulfills equation 4.1.

$$\frac{dC(t_m)}{dt} \cdot (D_i - C(t_m)) = 0 \quad (4.1)$$

This equation is solved numerically obtaining the set of points in the approximating B-spline that have the minimum distance to the baseline points. Geometrical error is the sum of the calculated squared distances. The computational cost is increased but the resulting approximations are more accurate than previous alternatives.

### 4.2.2 Aerodynamic error

Instead of inspecting the differences regarding geometry, the aerodynamic error compares the aerodynamic performance. The aerodynamic error is calculated by measuring the distances between the aerodynamic curves of the baseline airfoil and

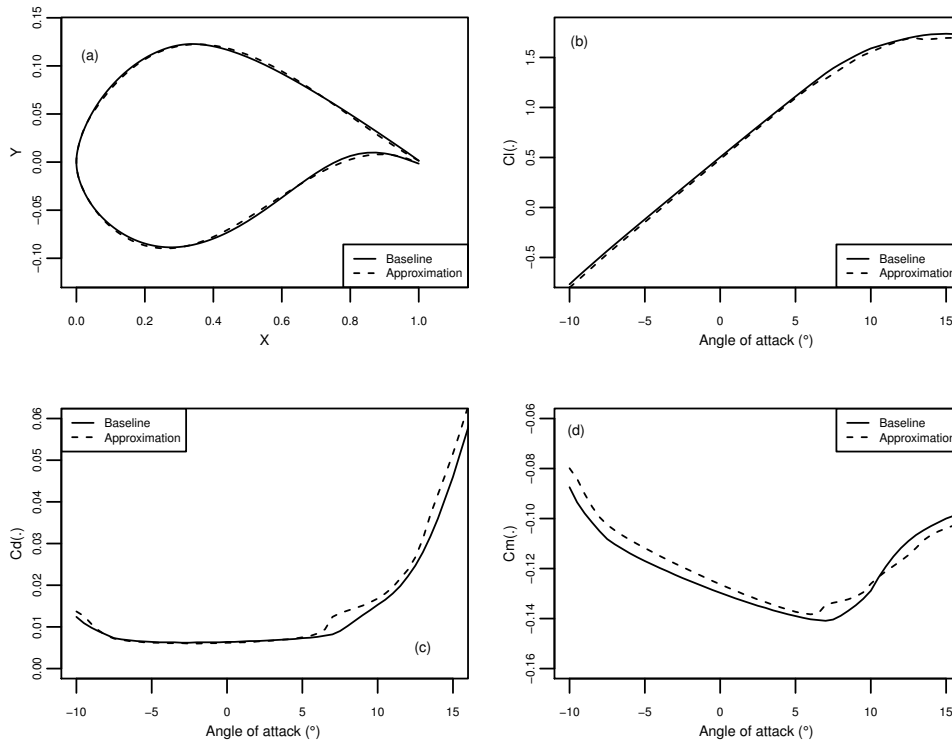


FIGURE 4.2: (a) Baseline airfoil and approximating B-spline. (b) Comparison of lift coefficient in function of angle of attack. (c) Comparison of drag coefficient in function of angle of attack (d) Comparison of moment coefficient in function of angle of attack.

the approximation. The  $C_l$  (lift coefficient),  $C_d$  (drag coefficient) and  $C_m$  (moment coefficient) curves are calculated with a panel method code. The sum of squared distances between aerodynamic curves results the aerodynamic error. Figure 4.2 shows the baseline airfoil, the approximating B-spline and comparative plots of the aerodynamic coefficients.

### 4.2.3 Wind turbine performance error

On step further, the wind turbine performance error evaluates the difference in performance of the wind turbine between using the baseline airfoil and the approximation. The blade selected for the analysis presents the baseline airfoil which is subjected to approximation in a significant portion of the blade span (40%) and thus it is very relevant. For the approximating B-spline, the aerodynamic coefficients are calculated in a panel method code and the wind turbine aeroelastic model is updated with the new aerodynamics. The aerodynamic curves of the approximating airfoil are included in the aeroelastic wind turbine model instead of the baseline aerodynamic curves. Subsequently, steady simulations are performed, the power curve is obtained and the AEP is calculated for specific environmental conditions. The difference of AEP with respect to the original AEP calculated with the baseline aerodynamic curves is called performance error.

### 4.3 Methodology of approximation

The method consists on evaluating the goodness of the approximation performed with each configuration of B-spline to several airfoil geometries represented as set of points. The approximation is formulated as an optimization problem with the following premises:

- A fixed maximum number of iterations is set in all the optimizations.
- The design variables are the airfoil control point ordinates.
- The objective function is the minimization of the approximation error.

The results are collected and treated statistically according to next section.

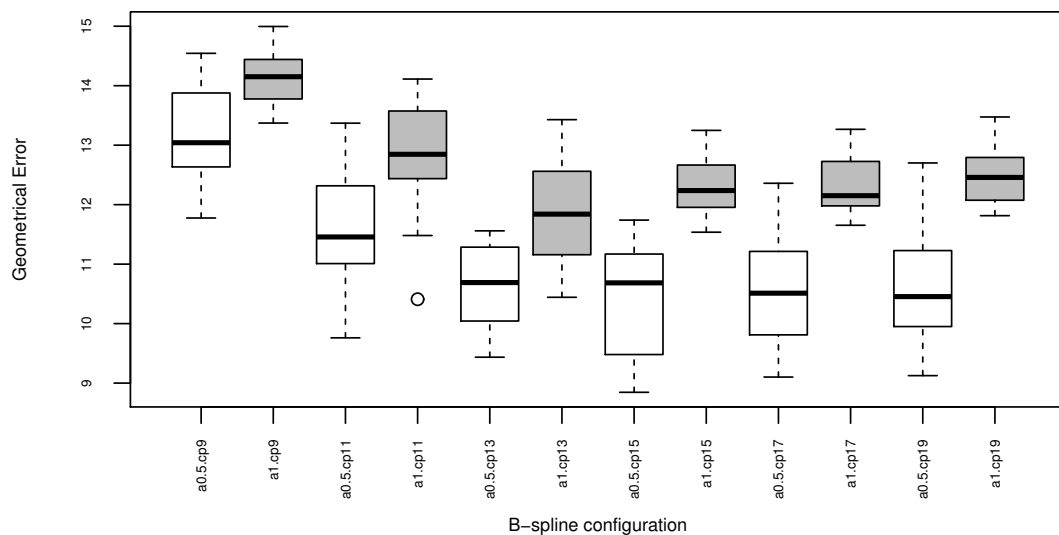


FIGURE 4.3: Box-and-whisker diagram for the geometrical errors of the approximating B-spline configurations. White boxes correspond to errors for approximations with centripetal parametrization ( $a = 0.5$ ). Grey boxes correspond to errors for approximations with chordal parametrization ( $a = 1$ ).

### 4.4 Statistical treatment

The approximation errors are treated to infer if there is significant difference between the B-spline configurations and conclude which one is most appropriate. The statistical hypothesis testing serves to decide about a null hypothesis  $H_0$  which is considered as true a priori and an alternative hypothesis  $H_1$ . The analysis is divided in three stages where the number of samples is increased as far as the configurations are discarded and consequently the computational cost is reduced.



#### 4.4.1 B-splines candidate configurations

Different number of control points and types of parametrization methods are considered:

- Number of control points. As it is usual practice to employ around thirteen control points (Fuglsang and Dahl, 1999), the considered candidates are nine (*cp9*), eleven (*cp11*), thirteen (*cp13*), fifteen (*cp15*), seventeen (*cp17*) and nineteen (*cp19*).
- Independent parametrization. The considered options are centripetal (blending parameter  $a = \frac{1}{2}$ ) and chord length parametrization ( $a = 1$ ). These two options are named  $a_{0.5}$  and  $a_1$  respectively.

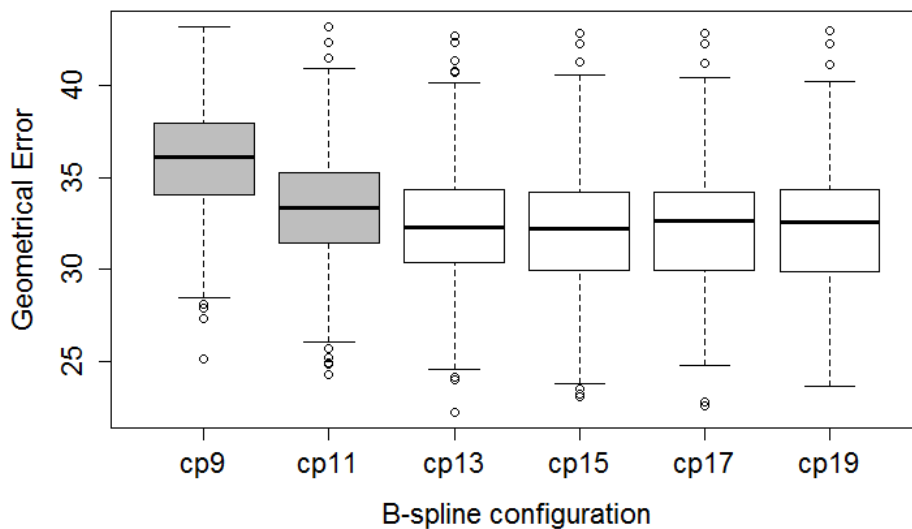


FIGURE 4.4: Box-and-whisker diagram for the geometrical error of the approximating B-spline configurations with centripetal parametrization. Grey boxes (configurations *cp9* and *cp11*) show differences with respect other groups (white boxes).

#### 4.4.2 First analysis. Independent parametrization

The analysis is performed with the following characteristics:

- The test airfoils to be approximated are twenty common airfoils from wind energy industry with assorted geometry. Due to confidentiality concerns, the names of the airfoils are not revealed.
- The type of approximation error to be analysed is the geometrical error.
- All the candidate configurations are taken into consideration. The box and whisker in figure 4.3 shows differences between groups with centripetal parametrization ( $a_{0.5}$ ) and chord length parametrization ( $a_1$ ).

- Statistical analysis. According to the difference observed in figure 4.3, statistical hypothesis tests are performed comparing groups with same number of control points but different parametrization. The null hypothesis states that  $\mu_{a_{0,5}} = \mu_{a_1}$  meaning that there is not significant difference between means of groups with different methods of parametrization if there is an equal number of control points. The alternative hypothesis rejects the null hypothesis. The paired t-tests result  $\rho$ -values lower than the significance level in all cases. Moreover, Wilcoxon non-parametric tests are performed and paired  $\rho$ -values are much lower than the significance level.
- Thus, it is concluded that the null hypothesis  $\mu_{a_{0,5}} = \mu_{a_1}$  is discarded. Consequently  $a_1$  parametrization is rejected because it is statistically different and besides provides higher approximation errors.

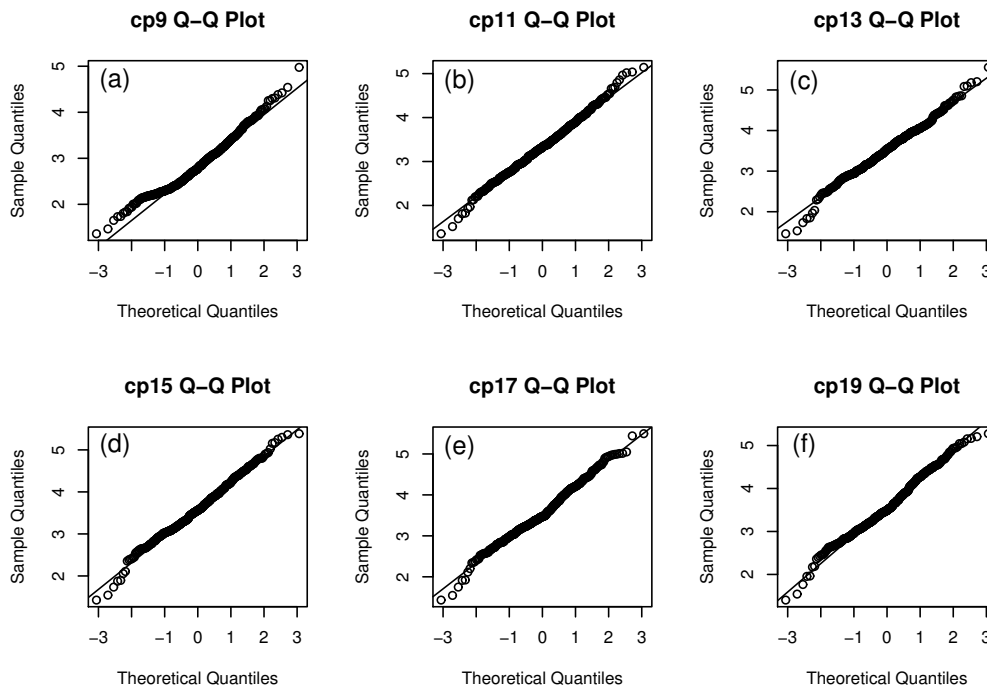


FIGURE 4.5: QQ plots of the errors associated to the approximating B-spline configurations with centripetal parametrization: (a)  $cp_9$ , (b)  $cp_{11}$ , (c)  $cp_{13}$ , (d)  $cp_{15}$ , (e)  $cp_{17}$  and (f)  $cp_{19}$ .

#### 4.4.3 Second analysis. Control point selection.

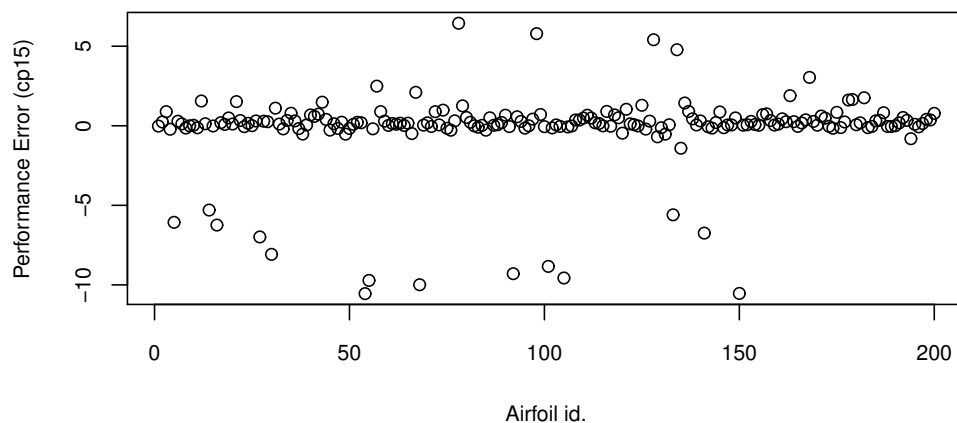
Once  $a_1$  parametrization has been discarded, this subsection assesses the size of the control polygon.

- The test airfoils to be approximated are five-hundred airfoils from University of Illinois Urbana-Champaign (UIUC) airfoil database ([UIUC Airfoil Data Site](#)). The UIUC airfoil coordinates database covers a wide range of applications from low Reynolds number airfoils for unmanned aerial vehicle and model aircraft to jet transports and wind turbines.

- The type of approximation error to be analysed is the geometrical error.
- The candidate configurations are the sizes of the control polygon ( $cp9$ ,  $cp11$ ,  $cp13$ ,  $cp15$ ,  $cp17$  and  $cp19$ ). All B-spline curves are built with centripetal method. The box-and-whisker diagram in figure 4.4 shows differences of  $cp9$  and  $cp11$  groups with respect to other groups. The errors of these groups are significantly higher.
- Statistical analysis. The purpose consists on confirming that  $cp9$  and  $cp11$  are significantly different than the rest of groups. QQ plots presented in figure 4.5 show a behavior not far from normal in the distributions of the errors in each group. However, the normality tests reject the hypothesis of normality and thus the non-parametric Wilcoxon paired test is applied. The  $p$ -values are presented in table 4.1. The values are lower than the significance level in all tests where  $cp9$  and  $cp11$  are involved and consequently null hypothesis is rejected and it is stated that there are significant differences between these groups and the others. The paired Friedman test (non-parametric randomized block analysis of variance) also confirms the rejection of null hypothesis and therefore the differences of  $cp9$  and  $cp11$  with respect to others are proved. Nevertheless, no significant difference between other groups is found. To confirm the last aspect, a test based on performance approximation error is performed in the third statistical analysis.

TABLE 4.1:  $p$ -values of Wilcoxon paired hypothesis test

	cp9	cp11	cp13	cp15	cp17
cp11	<2.2e-16	*	*	*	*
cp13	<2.2e-16	5.72E-07	*	*	*
cp15	<2.2e-16	3.61E-10	0.126	*	*
cp17	<2.2e-16	1.36E-07	0.585	0.324	*
cp19	<2.2e-16	5.27E-08	0.485	0.437	0.813

FIGURE 4.6: Wind turbine performance errors of airfoil approximations performed with B-splines of 15 control points ( $cp15$ ).

#### 4.4.4 Third analysis. Control point selection based on performance error

- The test airfoils to be approximated are two-hundred airfoils from different engineering applications from Illinois university airfoil database ([UIUC Airfoil Data Site](#)).
- The type of approximation error to be analysed is the performance error.
- The candidate configurations are three possible sizes of control polygon: *cp13*, *cp15* and *cp17*. *cp19* is discarded in advance due to convergence problems in panel method calculations.
- Statistical analysis. Figure 4.6 shows the wind turbine performance error for *cp15* configuration. Most of performance errors are close to zero, but the number of outliers presenting a very high error is significant. According to the type of distribution, a permutation test is employed. This test is a randomization method that does not require the assumption of normality. The null hypothesis  $H_0$  states that difference of means of errors between groups is zero. Two permutation tests are performed to compare *cp13* against *cp15* and *cp13* against *cp17*. The error values of *cp13* and *cp15* groups are randomly rearranged  $10^4$  times. For each permutation, differences of means between groups are computed. Same process is followed with *cp13* and *cp17*. Figure 4.7 shows histograms for the permutations. The vertical lines point out the observed differences of means. In both cases, the proportion of random absolute differences higher than the observed one is much higher than the significance level. It is concluded that the null hypothesis can not be rejected. Therefore, no relevant improvement has been found in using more control points, and thirteen control points (*cp13*) is fixed as a sufficient number of design variables to approximate airfoils.

## 4.5 Conclusions of the chapter

The suitability of types of airfoils is investigated. It is assumed that the configurations that approximate better the existing airfoils are more suitable to explore the design space in the optimization. The approximation errors in different forms have been collected and treated statistically. Statistical hypothesis tests are used to conclude that centripetal parametrization and thirteen control points is the most appropriate configuration to design airfoils. Figure 4.8 shows the approximations performed to several airfoils ([UIUC Airfoil Data Site](#)) with the selected B-spline configuration.

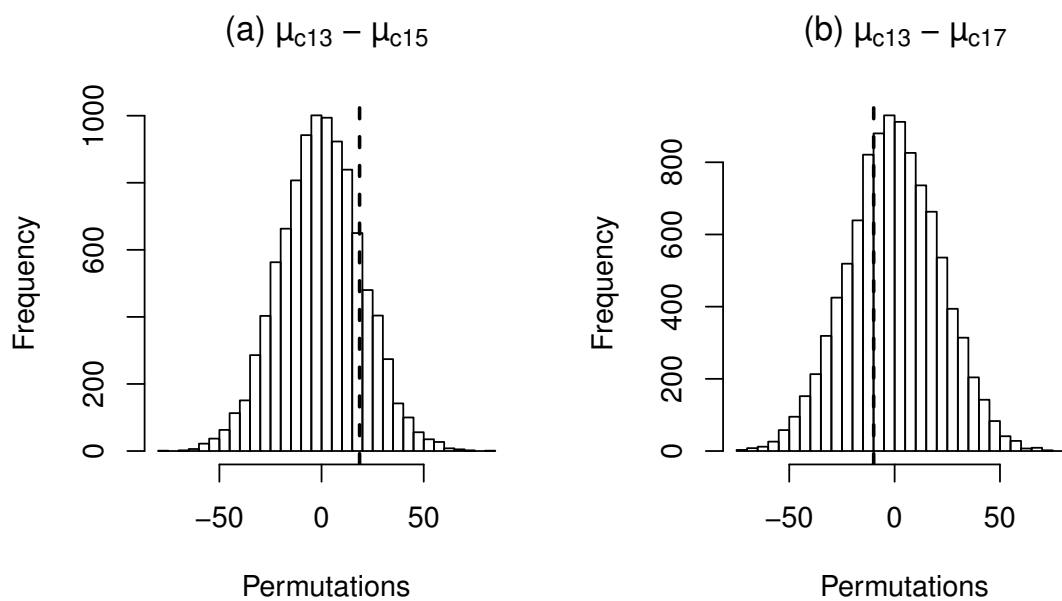


FIGURE 4.7: Histogram of (a)  $\mu_{cp13} - \mu_{cp15}$ . Differences of means of groups  $cp13$  and  $cp15$  from all permutations. (b)  $\mu_{cp13} - \mu_{cp17}$ . Differences of means of groups  $cp13$  and  $cp17$  from all permutations. The vertical dashed lines indicate the observed values.

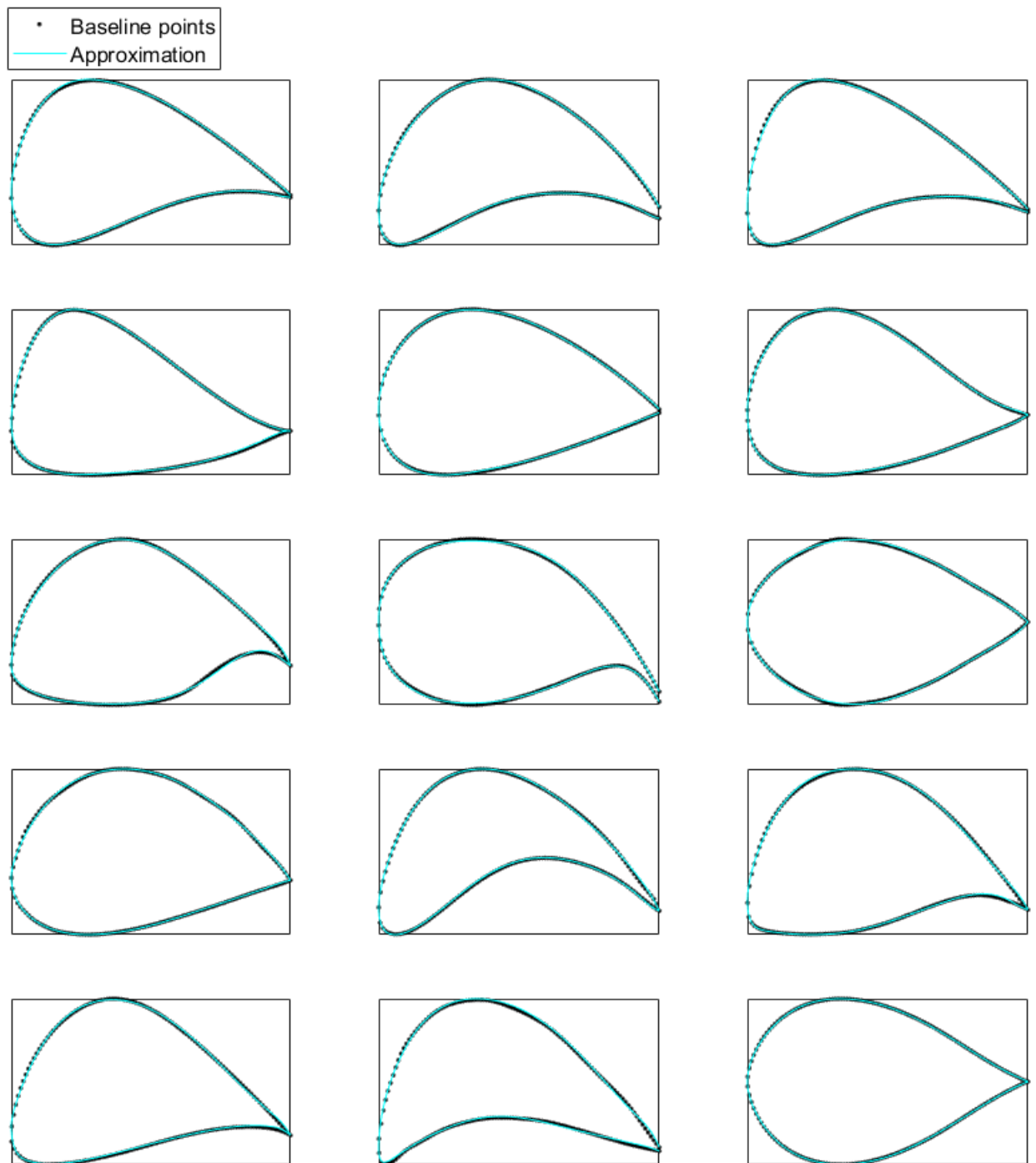


FIGURE 4.8: Approximations with thirteen control points and centripetal parametrization to fifteen airfoils of UIIC database.

## Chapter 5

# Fatigue estimation in the frequency domain

The blade design has important influence in the fatigue loads that the different wind turbine components receive, thus, it is recommendable to include the fatigue loads in the blade optimization. Nevertheless, the calculation of the fatigue loads in the multidisciplinary optimization presents a large challenge due to its huge computational cost that makes the optimization iterations be too long.

To address this issue, this chapter proposes a method to estimate the fatigue loads by means of a frequency domain calculation. The frequency domain methods for the calculation of the damage equivalent loads (DEL) have been widely applied for wind turbine support structures (Sorensen, Larsen, and Christensen, 1995). In the design of off-shore support structures these methods are valid alternatives to the large computational cost involved in the analysis of the wind and wave casuistry in the time domain (Halfpenny, 1998), (Ziegler et al., 2015), (Tempel, 2010).

In this chapter, a frequency domain fatigue calculation method is proposed to be incorporated in the blade optimization.

The proposed method estimates the signal of one specific load by calculating the linearized model of the wind turbine with an aeroelastic code and generating the frequency response function (FRF) that relates the inputs (wind speed, pitch and torque) with the load signal. Then, the fatigue damage of this estimated signal is calculated. The calculation of the linearized models involves a much lower computational cost than the time domain simulations required to calculate the fatigue in the time domain.

Section 5.1 introduces the fundamentals of the method. In section 5.2, the method is validated by comparing calculations of the fatigue damage in the time and in the frequency domain. Finally, in section 5.3 an optimization problem that calculates the fatigue damage in the frequency domain is performed.

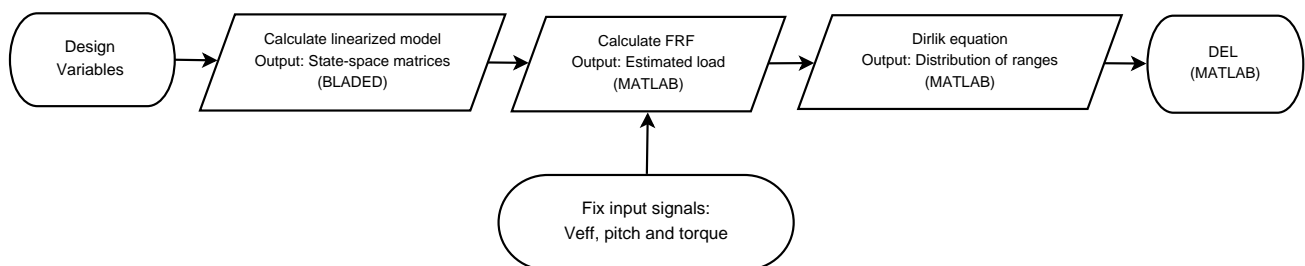


FIGURE 5.1: Flow chart describing the DEL calculation in the frequency domain

## 5.1 Fatigue estimation in the frequency domain

The proposed frequency domain method is divided in the stages described in flowchart of figure 5.1. The inputs of the process are the wind speed and the control signals: pitch and torque.

1. A wind turbine load signal in the frequency domain is calculated by scaling the wind turbine input signals by the FRF of the wind turbine. This FRF is calculated from a simplified linearized model of the wind turbine calculated with an aeroelastic code.
2. The Dirlik equations (Dirlik, 1985) are applied to the power spectral density (PSD) of the estimated load signal. The DEL is obtained applying the Miner rule (Passipoularidis and Brøndsted, 2010).

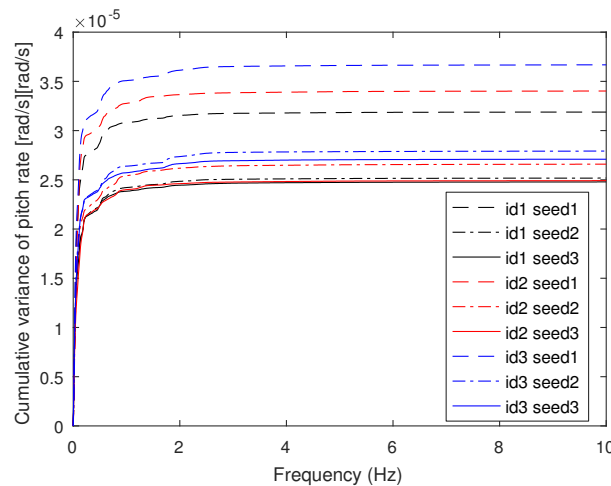


FIGURE 5.2: Cumulative variance of the PSD of the pitch rate signals under three blades id1, id2 and id3 and three wind fields seed1, seed2 and seed3.

The pitch angle and torque input signals are assumed to be invariant in spite of changes in the blade geometry or wind field. Figure 5.2 shows the cumulative variance of the PSD of pitch rate under different blade geometries (id1, id2 and id3) and wind seeds (seed1, seed2 and seed3). The wind seeds are different wind fields calculated by the aeroelastic code that share the same mean wind speed and turbulence intensity. Figure 5.3 presents same cumulative variance of PSD for generator torque signal. The figures reveal differences in the frequency content of the signals between blades and wind seeds that conflict with the assumption that pitch and torque are invariant signals. The validity of the method with this assumption is assessed in section 5.2.

### 5.1.1 Wind turbine linearized model

The aeroelastic codes provide the capability of extracting linearized representations of the complete nonlinear wind turbine equations for developing state-space matrices. The complete nonlinear aeroelastic equations of a wind turbine are (manual [FAST](#)):



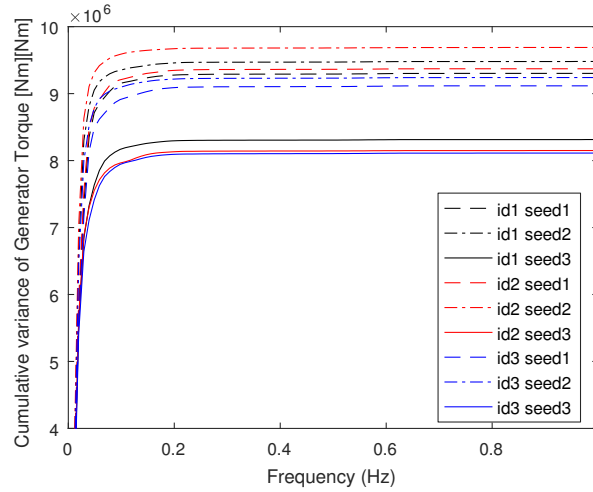


FIGURE 5.3: Cumulative variance of the PSD of the generator torque signals under three blades id1, id2 and id3 and three wind fields seed1, seed2 and seed3.

$$M(q, u, t)\ddot{q} + f(q, \dot{q}, u, t) = 0 \quad (5.1)$$

Where  $M$  is the mass matrix,  $f$  is the nonlinear forcing function vector,  $q$  is the vector of displacements, (and  $\dot{q}$  and  $\ddot{q}$  are the vectors of velocities and accelerations),  $u$  is the vector of inputs, and  $t$  is time. After linearization, the state-spaces equations can be stated as follows:

$$\dot{x} = Ax + Bu \quad (5.2)$$

$$y = Cx + Du \quad (5.3)$$

Where  $A$  is the state-space matrix,  $B$  is the input matrix,  $C$  is the output state-space matrix and  $D$  is the feed-through matrix.

The transfer function is a representation of the relation between the input and output of a linear time-invariant system. In the Laplace domain the transfer function  $G(s)$ , is stated as:

$$G(s) = \frac{y(s)}{u(s)} = C(sI - A)^{-1}B + D \quad (5.4)$$

The aeroelastic codes such as (*BLADED*) provide the state-space matrices  $A$ ,  $B$ ,  $C$ ,  $D$  that are necessary to calculate the transfer function in the Laplace domain which is converted into FRF. The FRF relates in the frequency domain these inputs with any force or moment resultant on the components of the wind turbine (blade, hub, nacelle, tower ...). Therefore a wind turbine load can be estimated by multiplying the wind turbine inputs by the corresponding FRF.

### 5.1.2 Effective wind speed

In the case of the wind signal employed as input, further considerations should be taken into account. The wind field that effectively affects the linearized model is the rotor effective wind speed  $V_{eff}$ , which can be regarded as the scalar wind field that

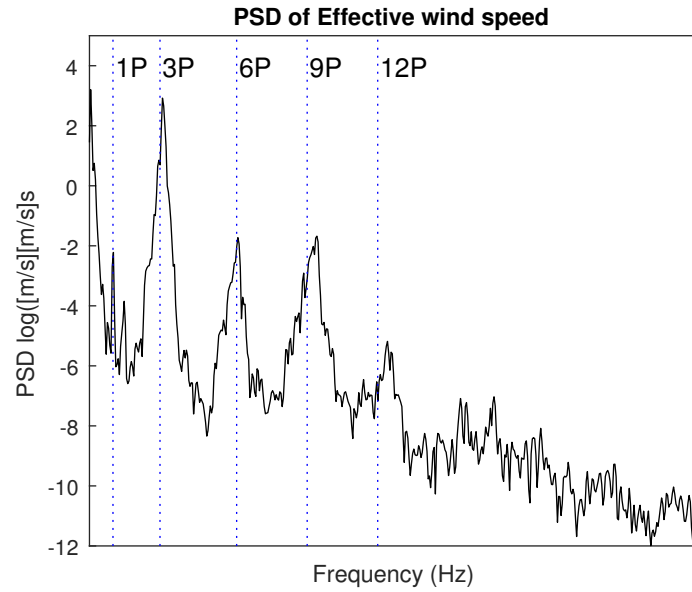


FIGURE 5.4: Power spectral density (PSD) of effective wind speed ( $V_{eff}$ ). Excitation frequencies 1P, 3P, 6P, 9P and 12P are presented as vertical lines.

yields the same aerodynamic torque as the one achieved with the three-dimensional wind speed field (Bianchi, Battista, and Mantz, 2007). The calculation of the frequency spectrum of  $V_{eff}$  has been investigated due to its usefulness in the control field (Burlibasa and Ceanga, 2013), (Ostergaard, Brath, and Stoustrup, 2007). It is estimated by weighting wind speeds at all points on the rotor disk according to their contribution to total aerodynamic power (Simley and Pao, 2013). In this paper, a simplified alternative of the  $V_{eff}$  based on the low-speed shaft torque time series of ten-minute turbulent simulations is applied:

$$V_{eff} = \left( \frac{2Q\omega}{C_p\rho A} \right)^{\frac{1}{3}} \quad (5.5)$$

Where  $C_p$  is the power coefficient,  $\rho$  is the air density,  $A$  is the rotor area,  $\omega$  is rotational speed and  $Q$  is the low-speed shaft torque.

Figure 5.4 shows the PSD of the  $V_{eff}$  for a ten-minute simulation of 10 m/s mean turbulent wind speed. The integer multiples of the rotational frequency are distinguished.

### 5.1.3 Calculation of the DEL of the signal PSD

There is a large bibliography on the development of methods for calculating the DEL from the PSD of a signal. (Passipoularidis and Brøndsted, 2010) and (Sorensen, Larsen, and Christensen, 1995) published a review of fatigue frequency domain techniques. (Ragan and Manuel, 2007) compared estimations of wind turbine fatigue loads using time-domain and spectral methods. These methods correlate the histogram of cycle ranges with the  $n$  moment  $m_n$  of the PSD of the signal:

$$m_n = \int f^n G(f) df \quad (5.6)$$

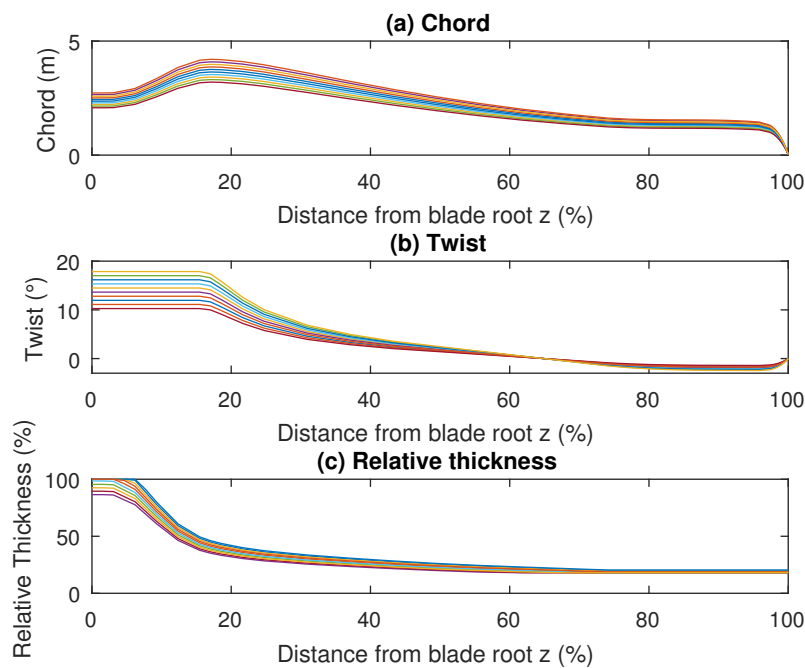


FIGURE 5.5: Spanwise distributions: (a) chord, (b) twist and (c) relative thickness of the ten test blades.

Where  $f$  is the frequency and  $G(f)$  is power spectral density function.

Depending on the nature of the signal, the frequency domain methods are classified on narrow band methods when there is a dominant frequency in the spectra and broad-band methods when the signal presents a wide distribution among a range of frequencies. The present research adopts the Dirlik method (Dirlik, 1985) for the assessment, which is a well-known method generally applied for dynamic structures subjected to loads that are caused by the environment and therefore present a random behavior (Halfpenny, 1998), (Ziegler et al., 2015), (Tempel, 2010). The Dirlik method applies for intermediate type of signals between narrow and wide band by combining empirically one exponential and two Rayleigh distributions. These equations have validity if the signals are closed to random and ergodic. The Dirlik equations can be found in a large amount of publications (Halfpenny, 1998), (Ragan and Manuel, 2007), (Matjaz Mrsnik, 2013). The output of the Dirlik equations is a probability distribution function of ranges. The DEL is obtained following same methodology as the time domain process.

## 5.2 Validation of the frequency domain method

In this section, a practical exercise is described to validate the methodology explained in section 5.1. The objective is to assess the correlation between the DEL of the time domain method, based on ten-minute simulations, and the proposed frequency domain method.

A baseline wind turbine model created in the aeroelastic code (*BLADED*) is selected for the exercise. Ten test blades are created by modifying the geometry of the baseline blade. These test blades differ in their spanwise distributions, i.e the chord,

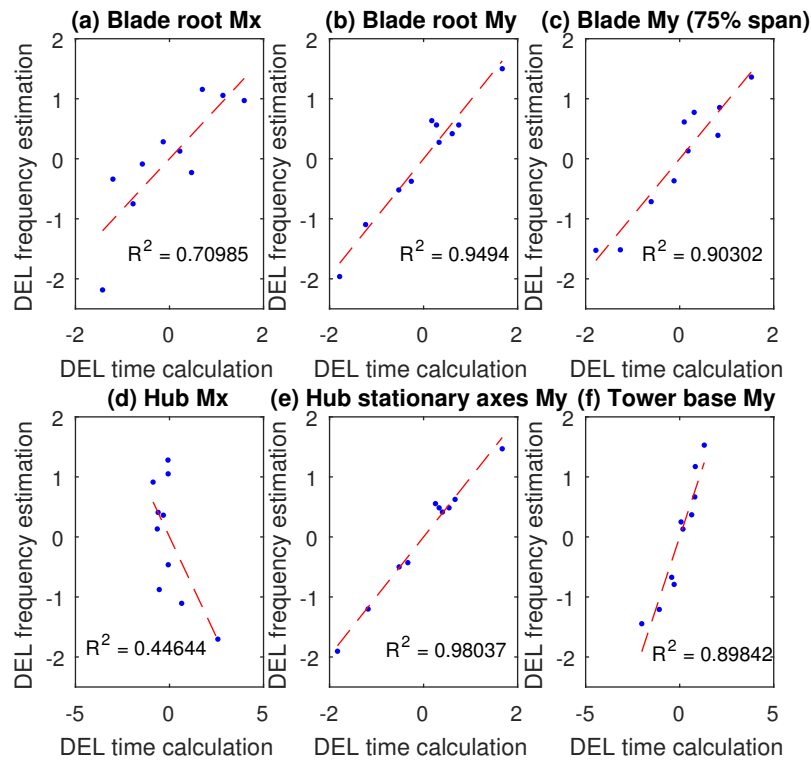


FIGURE 5.6: DEL calculated in the frequency domain versus calculated in the time domain. Each point represents the result for one blade (mean wind speed of 14 m/s). (a) Blade root Mx, (b) Blade root My, (c) Blade 75% span My, (d) Hub Mx, (e) Hub My in stationary axes and (f) Tower base My.

twist and relative thickness are different. The distributions are scaled with respect to the baseline blade according to three factors. The internal structure of the blade is a cross section beam with two spar caps and one shear web. A change in the blade thickness produces a modification of the distance from the spar caps to the neutral axis and therefore a modification of the bending stiffness and the dynamics of the blade. Figure 5.5 shows the test spanwise distributions.

The internal structural layout is scaled and rotated accordingly with the change of the external geometry. The cross sectional structural properties (stiffness, mass and relevant structural points) are calculated. In addition, the blade natural frequencies and mode shapes are updated. In contrast, the control parameters, the blade length and the rest of wind turbine components are maintained invariant for all the test blades. Significant differences in terms of fatigue loads and energy generation are expected between test blade due to the considerable changes of geometry.

### 5.2.1 DEL calculation in the time domain.

The test aeroelastic models are subjected to ten-minute simulations for a wide range of wind speeds that cover the operation of the wind turbine. The wind synthetic files (one seed per wind speed) follow a normal turbulence model (NTM). The resultant outputs are post-processed to obtain a DEL by applying a rainflow cycle counting algorithm. The selected loads for the assessment are the moments Mx and My in

different wind turbine locations: the blade root, blade in 75% of the span, hub center and tower base.

### 5.2.2 DEL calculation in the frequency domain.

A calculation of DEL is also implemented in the frequency domain as follows. A linearized model in (*BLADED*) is calculated for each wind turbine model that contains a specific test blade. The FRFs that relate the three inputs ( $V_{eff}$ , pitch and generator torque) with the different outputs (moments in blade, hub center and tower base) are derived. The input signals are collected in advance from baseline ten-minute wind turbulent simulations and are considered the same for all the linear models of the different test blades. The output moments are calculated by multiplying the input signals and the FRFs. Afterward, the PSD of the moments are calculated. The Dirlik equations are applied to obtain the probability distributions and the DEL of each moment.

### 5.2.3 Results

First of all, it is remarkable that the response of the wind turbine, in terms of DEL, is sensitive to the considered sampling variation of the blade geometry parameters. Furthermore, it is worth noting that the difference in time invested in obtaining the results from time and frequency methods. The frequency domain presents a ratio of duration of 1/35 with respect to the time domain calculations.

The results of DEL are compared graphically for both methods. The results for the same wind speeds are collected in groups and plotted together after prior normalization. Linear regressions are fitted to minimize the least square error. Figure 5.6 shows the results for several variables. Besides, tables 5.2, 5.3, 5.4, 5.5 and 5.6 present the linear regressions coefficients (RC) and the goodness of fit  $R^2$ . Each table presents the data for the linear regression of one wind speed. The maximum and minimum expected regression coefficients are calculated by applying the bootstrapping method (Efron, 1982) with a confidence level of 98%.

In spite of simplifications of the method, e.g. the consideration of invariant input signals for all the calculations, reasonable accurate linear fitting ( $R^2 > 0.85$ ) is found for the moments  $M_y$  in hub, tower and blade. However, the moments  $M_x$  present poor linear correlation. An inverse proportionality is found in hub  $M_x$  moment as figure 5.6(d) shows. This incorrect estimation is caused by different factors due to the simplifications of the frequency domain method, mainly for its time invariant nature. The signals of the  $M_x$  moment in the blade present a form essentially driven by the periodic gravity loading on the blade, resulting in a sinusoidally varying moment that reaches a maximum when the blade is horizontal and changes sign from one horizontal position to the other. Figure 5.7 shows in the (a) time domain and (b) frequency domain the periodicity of the blade root  $M_x$  signal at the rotation frequency. Two blade test models that experiment significant differences in terms of  $M_x$  damage equivalent load are chosen.

In the frequency domain method, the time invariant linearized model does not reflect the change of amplitude of this type of periodic loading. In contrast, a different approach is proposed: the first-order mass moment of the blade is proportional to the amplitude of the load cycle at the rotation frequency and therefore gives an estimation of the DEL. Figure 5.8 depicts the first-order mass moments in function of the DEL. The DEL of moments  $M_x$  in the blade root, 75% blade span and tower base have been satisfactorily estimated ( $R^2 > 0.85$ ) by the first-order mass moment.

However, the DEL of  $M_x$  in the hub and the first-order mass moment are inversely proportional, and consequently the estimation is not satisfactory.

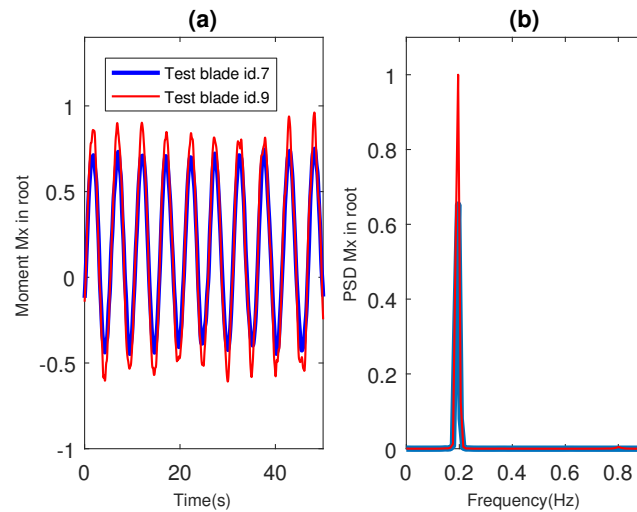


FIGURE 5.7: Time series (a) and PSD (b) of moment  $M_x$  in root for two test blade models (id7 and id9).

The time domain fatigue calculations are obtained from one single simulation per wind speed. This introduces uncertainty about the robustness of the frequency domain method when compared to the mean DEL calculated from several seeds, all sharing the same turbulence intensity. To assess this uncertainty, thirty different wind seeds with same mean wind speed of 10 m/s and same turbulence intensity are calculated. Each test blade is subjected to thirty simulations including thirty different wind seeds. The DELs of  $M_y$  moment in hub calculated from these time domain simulations are shown in figure 5.9.

The variation of DEL within wind seeds is high (about 15%). However, the relative differences between blades remain when the seeds change, as figure 5.9 shows. As performed to previous linear regressions, the DEL obtained in the frequency domain is compared to the mean DEL within thirty seeds. The regression coefficients in table 5.7 show consistency with respect to the one seed linear regression shown in table 5.3.  $M_y$  moments present accurate linear relationship.

### 5.3 The frequency domain fatigue calculation in a blade design optimization

In this section, an optimization case is performed. The fatigue damage calculation in the frequency domain is introduced in the code *AGORA*. The aim of this practical case is to demonstrate that the frequency domain fatigue calculation can be used to design a blade with a determinate target of damage equivalent load in one of specific load. A baseline existing blade is identified as starting point of the optimization.

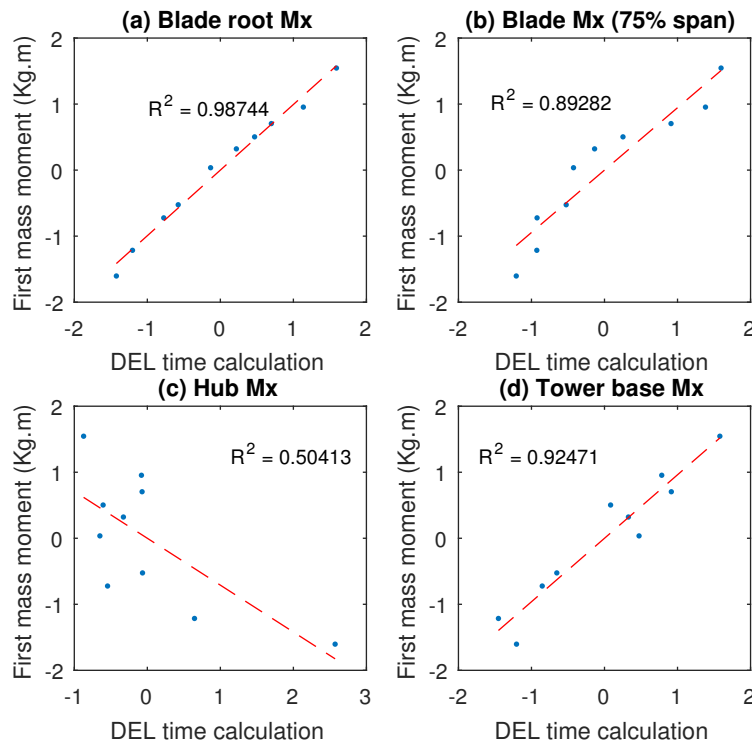


FIGURE 5.8: First-order mass function versus DEL in the time domain. Each point represents the results for one blade. (a) Blade root Mx, (b) Blade root My, (c) Blade Mx (75% span) and (d) Tower base Mx.

$$\text{Find } X = \left\{ \begin{array}{l} X_{Chord} \\ X_{Twist} \\ X_{R.thickness} \end{array} \right\} \text{ which minimizes } DEL_{My,14 \text{ m/s}} \quad (5.7)$$

s.t.

$$AEP \geq 0.992 * AEP_{baseline}$$

As stated in equation 5.7, the objective function is to minimize the DEL of My moment in hub center at 14 m/s of mean wind speed. One constraint is defined: a maximum loss of 0.8% of AEP is permitted with respect to the baseline blade. The design variables are control points of the B-spline functions that define the chord, twist and relative thickness distributions.

The resulting geometry of the optimization is shown in figure 5.10 in comparison with the baseline blade. The differences in the chord and twist are very relevant. However, the relative thickness distributions are identical. The solution provides an expected DEL reduction of 11.3% and a AEP loss of 0.8% with respect to the baseline design. Therefore, the constraint of AEP is fulfilled.

After the completion of the optimization, the solution is subjected to fatigue equivalent load calculation in the time domain in order to assess the precision of the estimation performed in the optimization. Figure 5.11 shows time history of the hub My moment of both blades for a 14 m/s mean wind speed dynamic simulation.



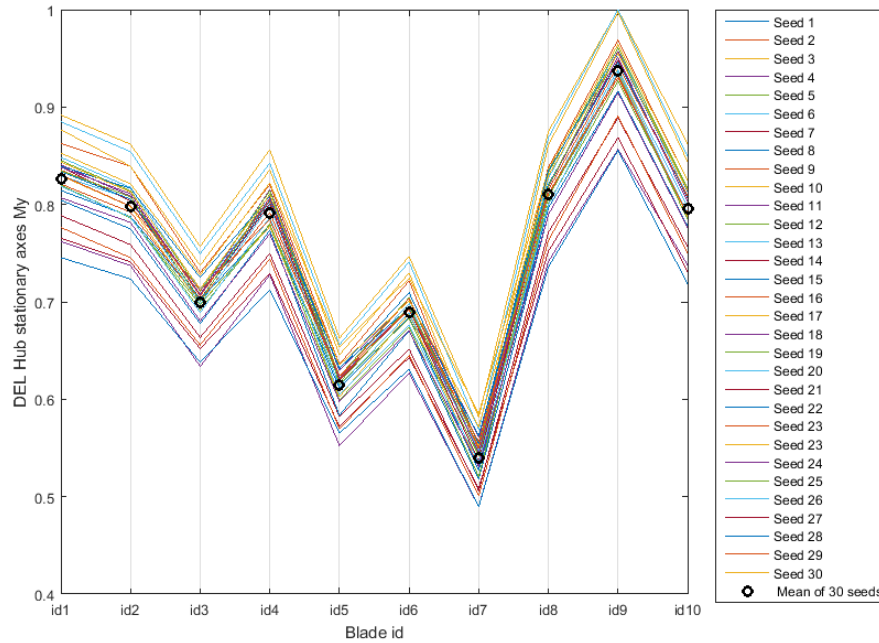


FIGURE 5.9: DEL of stationary hub  $M_y$  with respect to blade. Values for the thirty wind seeds and the mean are presented.

The reduction of the variance of  $M_y$  moment in the solution is very significant.

TABLE 5.1: Ratio between DEL of solution with respect to baseline: (a) Nominal expected, (b) Maximum expected, (c) Minimum expected and (d) Real.

Case	Ratio of reduction of DEL (%)
(a) Nominal expected	11.30%
(b) Maximum expected	14.05%
(c) Minimum expected	8.91%
(d) Real	13.31%

The DEL calculated in the time domain shows a reduction of 13.3 % with respect to the baseline. In contrast, the expected reduction was 11.3 % in the frequency domain. Table 5.1 shows the expected band of DEL reduction according to the linear regression of table 5.4 and the real reduction found in the time domain calculation. The result in the time domain lays inside the bootstrapping confidence band.

Therefore, the introduction of the frequency domain DEL calculation in the optimization provides a useful direction of design to reduce the fatigue equivalent loads of moment  $M_y$  in hub.

## 5.4 Conclusions of the chapter

The proposed frequency domain fatigue method addresses the expensive computational cost of fatigue calculation in the multidisciplinary blade optimization. The frequency domain method is compared to the time domain DEL calculation, showing that the out of plane variables ( $M_y$ ), mainly driven by short-term wind variation, are suitable for the method. Nevertheless, other loads determined by large periodic components are not properly estimated. The frequency domain method is



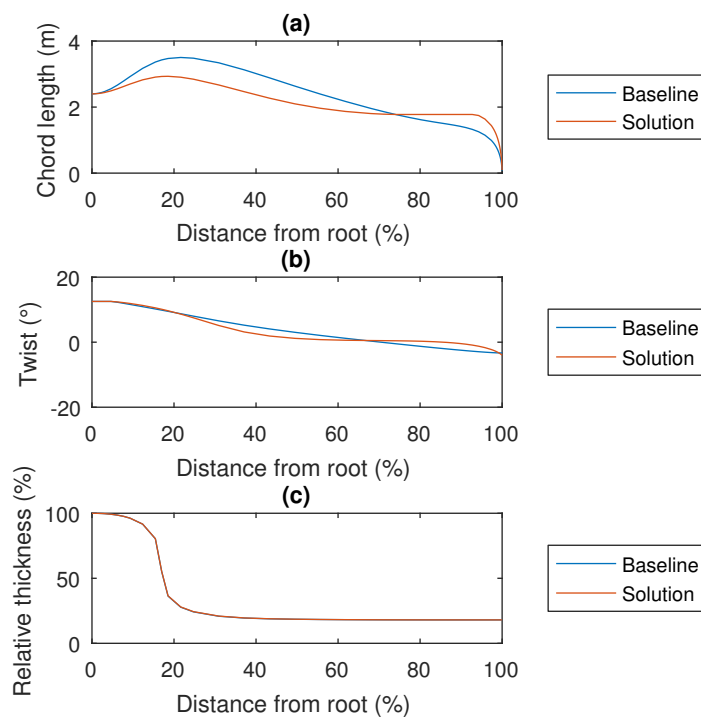


FIGURE 5.10: Spanwise distributions: (a) Chord (b) Twist and (c) Relative thickness of solution and baseline.

introduced in a practical blade optimization. The DEL calculation in the frequency domain provides the direction of design to minimize the fatigue damage. The solution is validated under time domain calculations. Nevertheless, the DEL estimation in the frequency domain is not totally precise and differences are found between the time and frequency domain calculations. The method is sufficient in the preliminary stages of the blade design but does not avoid the time domain calculations needed to determine the fatigue response of the wind turbine. The reduction of the simulation time is very important. The ratio of the computational time is 1/35 between the frequency and time domain calculations.

TABLE 5.2: Linear regression fitness for 6 m/s: Goodness of fit  $R^2$  and regression coefficients.

Variable	$R^2$	Regression coefficient (RC)	Minimum RC	Maximum RC
Blade root Mx	0.46	0.68	0.05	1.33
Blade root My	0.87	0.93	0.64	1.24
Blade z48 m principal axes Mx	0.75	0.87	0.55	1.33
Blade z48 m principal axes My	0.89	0.95	0.60	1.39
Hub Mx	0.01	-0.12	-2.06	0.93
Hub stationary axes My	0.95	0.97	0.70	1.21
Tower base Mx	0.01	-0.08	-0.88	0.48
Tower base My	0.87	0.93	0.54	1.24

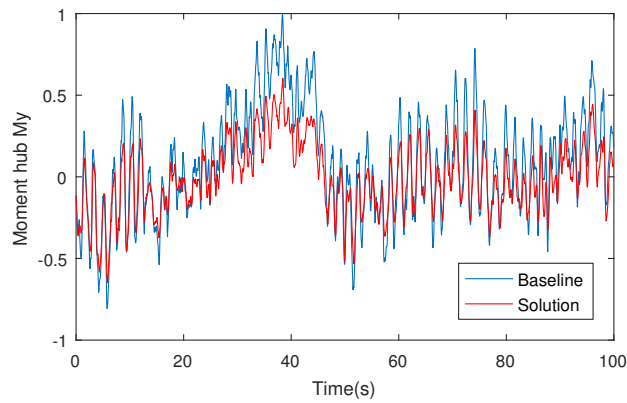


FIGURE 5.11: Time history of the moment  $M_y$  in hub for baseline and solution (simulation with 14  $m/s$  mean wind speed).

TABLE 5.3: Linear regression fitness for 10  $m/s$ : Goodness of fit  $R^2$  and regression coefficients.

Variable	$R^2$	Regression coefficient (RC)	Minimum RC	Maximum RC
Blade root Mx	0.17	0.41	-1.15	0.58
Blade root My	0.95	0.98	0.78	1.29
Blade z48m principal axes Mx	0.56	-0.75	-1.28	0.57
Blade z48m principal axes My	0.98	0.99	0.79	1.10
Hub Mx	0.51	-0.72	-1.03	1.28
Hub stationary axes My	0.96	0.98	0.78	1.25
Tower base Mx	0.15	0.39	-0.81	1.37
Tower base My	0.97	0.93	0.52	1.38

TABLE 5.4: Linear regression fitness for 14  $m/s$ : Goodness of fit  $R^2$  and regression coefficients.

Variable	$R^2$	Regression coefficient (RC)	Minimum RC	Maximum RC
Blade root Mx	0.71	0.84	0.31	1.27
Blade root My	0.95	0.97	0.77	1.23
Blade z48m principal axes Mx	0.36	0.60	-0.14	1.34
Blade z48m principal axes My	0.90	0.95	0.64	1.21
Hub Mx	0.45	-0.67	-3.06	-0.03
Hub stationary axes My	0.98	0.99	0.85	1.15
Tower base Mx	0.59	0.77	0.11	1.52
Tower base My	0.90	0.95	0.47	1.18

TABLE 5.5: Linear regression fitness for 18  $m/s$ : Goodness of fit  $R^2$  and regression coefficients.

Variable	$R^2$	Regression coefficient (RC)	Minimum RC	Maximum RC
Blade root Mx	0.50	0.71	-0.07	1.26
Blade root My	0.94	0.97	0.78	1.21
Blade z48m principal axes Mx	0.81	0.90	0.34	1.21
Blade z48m principal axes My	0.92	0.96	0.64	1.18
Hub Mx	0.30	-0.55	-2.63	0.10
Hub stationary axes My	0.97	0.99	0.79	1.19
Tower base Mx	0.57	0.75	-0.15	1.90
Tower base My	0.86	0.93	0.36	1.14

TABLE 5.6: Linear regression fitness for 22 m/s: Goodness of fit  $R^2$  and regression coefficients.

Variable	$R^2$	Regression coefficient (RC)	Minimum RC	Maximum RC
Blade root Mx	0.25	0.50	-0.41	1.29
Blade root My	0.92	0.96	0.73	1.24
Blade z48m principal axes Mx	0.97	0.98	0.84	1.17
Blade z48m principal axes My	0.88	0.94	0.64	1.16
Hub Mx	0.64	0.80	0.29	1.44
Hub stationary axes My	0.97	0.98	0.83	1.16
Tower base Mx	0.34	0.58	-0.02	1.47
Tower base My	0.90	0.95	0.76	1.39

TABLE 5.7: Linear regression fitness for 10 m/s: Goodness of fit  $R^2$  and regression coefficients. The time domain DLE values are the mean values of the simulations with thirty wind seeds.

Variable	$R^2$	Regression coefficient (RC)	Minimum RC	Maximum RC
Blade root Mx	0.156	-0.394	-1.118	0.569
Blade root My	0.935	0.967	0.700	1.310
Blade z = 48 m Mx	0.416	-0.645	-1.097	0.709
Blade z = 48 m My	0.974	0.987	0.865	1.155
Hub Mx	-0.328	-0.573	-0.792	11.701
Stationary hub My	0.953	0.976	0.769	1.252
Tower base Mx	0.496	0.704	-0.327	1.160
Tower base My	0.747	0.864	0.306	1.353



## Chapter 6

# Analysis prior to the optimization

Prior to perform the optimization, design exploration comprises several statistical techniques to investigate the design space with the intent of obtaining knowledge to understand the relationships between design variables and outputs. In the chapter two practical exercises are performed with similar approach but with different design variables and objectives.

Section 6.1 describes a global sensitivity analysis that provides information about the relevant geometrical design variables in different important wind turbine outputs. The analysis is based on steady aeroelastic simulations.

In section 6.2 an analysis based on combined dynamic and steady aeroelastic simulations is presented. As result of a preliminary inspection, an undesired load amplification phenomenon is detected in unknown combinations of design variables. With the aid of data analysis techniques, the amplified response is predicted and important knowledge about the involved design variables is obtained.

### 6.1 Global sensitivity analysis

The purpose of this section consists on assessing the influence of several geometrical design variables (coordinates of airfoil, chord and twist control points) in the wind turbine regarding AEP, maximum blade tip deflection ( $dxs\_tip\_max$ ), overall sound power level (OAPWL) and blade total mass (BTM) by means of global sensitivity analysis. The conclusions provide useful information to rank the variables in terms of impact in the wind turbine performance and consequently remove the non-significant design variables from the optimization. Other sensitivity analysis are found in the literature but do not provide the knowledge that is investigated here. (Bak et al., 2014) published a paper where relationship between aerodynamics (lift-drag ratio) and blade stiffness are inspected for airfoil families and different structural layouts. (Nilsson et al., 2014) carried out a sensitivity analysis to determine how the performance characteristics of wind farms (wake flow, power production and thrust) depend on the choice of airfoil data and blade geometry. These analyses do not evaluate sensitivity of the blade geometry in the wind turbine outputs. (Bak et al., 2014) does not provide insight into wind turbine outputs and is focused on specific airfoil families. (Nilsson et al., 2014) determines the influence in a wind farm level. Furthermore, these research papers do not employ global sensitivity techniques for the analysis.

#### 6.1.1 Input variables

Twenty-one design variables are considered in the analysis. Airfoil design variables are presented in figure 6.1. The last two airfoil control points that govern the TE are fixed. The effect of opening the TE segment is out of the scope of this analysis. Chord

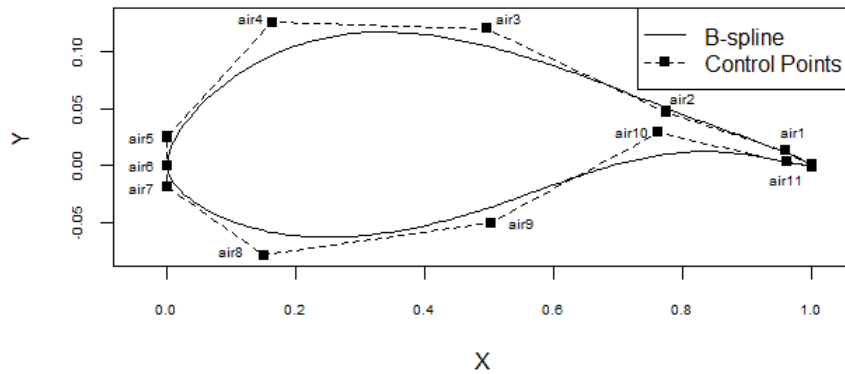


FIGURE 6.1: Airfoil design variables in the sensitivity analysis.

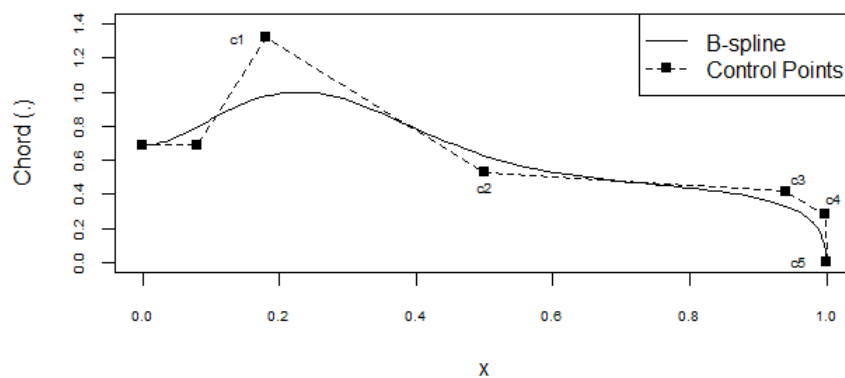


FIGURE 6.2: Chord design variables in the sensitivity analysis.

design variables are shown in figure 6.2 and twist design variables are presented in figure 6.3. The relative thickness law is maintained unaltered in the sampling. Consequently, the chord distribution determines the blade total thickness. The variables are sampled around the baseline values which correspond to an existing serial production blade. One airfoil is selected for the analysis which is known in the wind energy industry. This master airfoil is selected due to its importance in the baseline serial production blade as it is located in the 40% outer span part of the blade. The variation of the sampling is intended to modify the geometry without altering significantly the total thickness of the airfoil with respect to the baseline master airfoil.

LHS method generates seven hundred combinations of input variables with the computational tool (R, 2017). AGORA performs the steady calculations to obtain AEP,  $dxs_{tip\_max}$ , BTM and OAPWL for the corresponding set of design variables. They involve automatic sub-calculations with the subordinate tools (aerodynamic, structural, aeroelastic and noise codes).

### 6.1.2 Sensitivity analysis based on regression techniques

Once the sampling is generated and the aeroelastic simulations are completed, the sensitivity analysis is performed by calculating multi-variable linear regression in a statistical package (R, 2017). The outputs of the simulations (AEP,  $dxs_{tip\_max}$ , BTM and OAPWL) are described as a linear combination of the input factors. In figure 6.4, the linear regressions for *air6*, *c3* and *tw4* input variables in the output AEP are shown. Dashed lines represent the projection of the multi-variable regression in

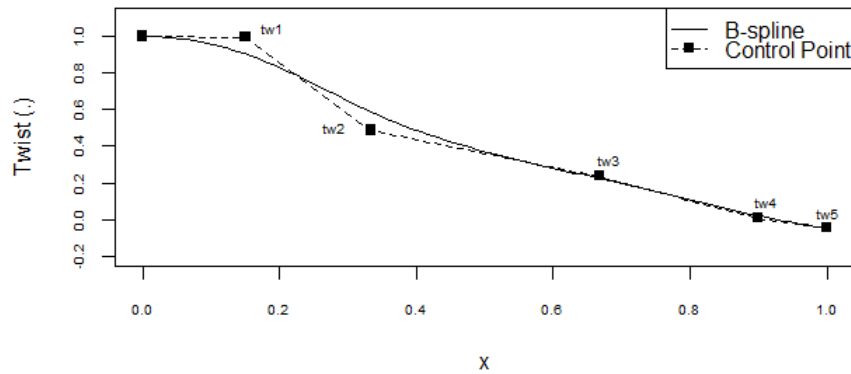
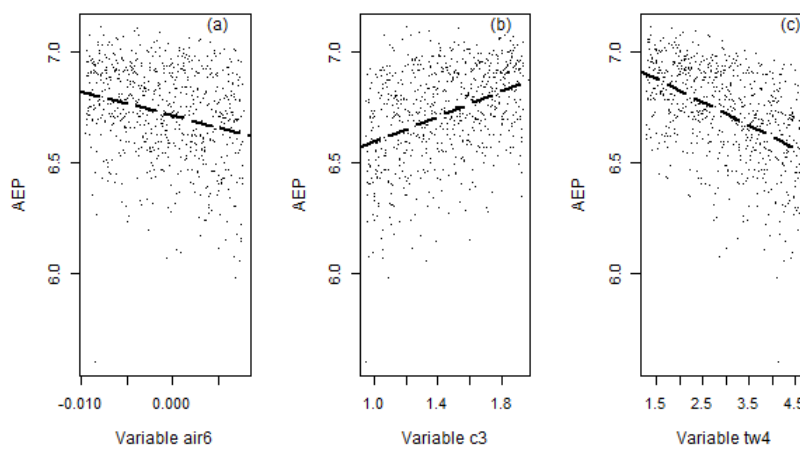


FIGURE 6.3: Twist design variables in the sensitivity analysis.

FIGURE 6.4: AEP as function of the input variables: (a) *air6*, (b) *c3* and (c) *tw4*.

the corresponding input variable. The data present a very high dispersion but linear correlation is found in some cases. The standardized regression coefficients are inspected to evaluate the sensitivity of input factors in the outputs. The purpose of regressions does not consist in obtaining an accurate model of the inputs and output relations. The objective is deducing if the relations between inputs and outputs exist.

The standardized regression coefficients for AEP, *dvs\_tip\_max*, BTM and OAPWL are respectively presented in figures 6.5, 6.6, 6.7 and 6.8. The confidence intervals at the 95% level of the standardized regression coefficients are calculated by bootstrapping sampling (Efron, 1982). The coefficients with confidence interval containing zero are considered not significant. For instance, variable *air10* presents a slight positive standardized regression coefficient (see figure 6.5) that suggests a positive proportionality between the input variable *air10* and AEP. However, the confidence intervals contain zero; therefore the coefficient is considered not significant. The variables with the highest absolute value of the associated regression coefficients are identified as the most influencing variables in the model output.

The results show that the variables *c5*, *air2*, *air4*, *air5*, *air7*, *air9* and *air10* present a small or null effect in any of the considered outputs. In contrast *c2* and *c3* are the most influencing variables, as present a high impact in all outputs.

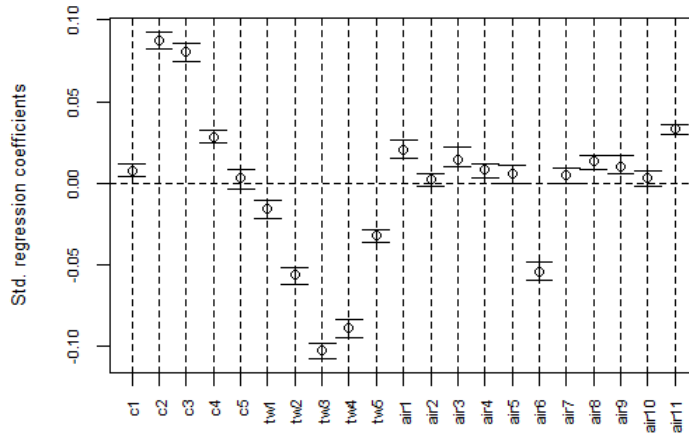


FIGURE 6.5: Standardized regression coefficients of multi-variable linear regression of **AEP**. Vertical lines represent the 95% confidence intervals.

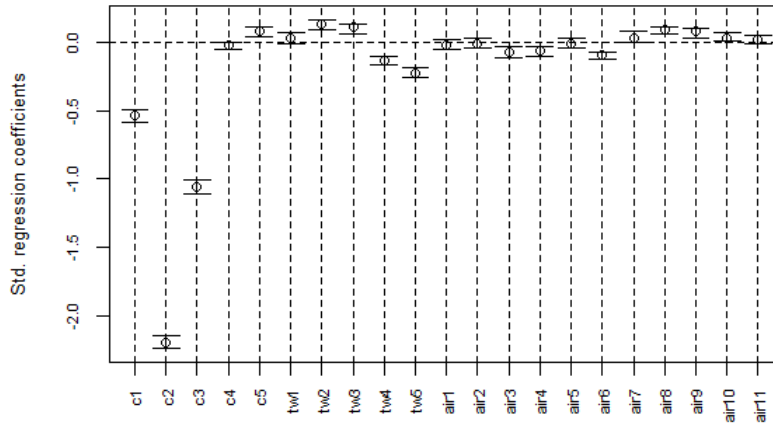


FIGURE 6.6: Standardized regression coefficients of linear regression of  $dxs\_tip\_max$ . 95% confidence intervals are included.

Focusing on AEP,  $tw3$  presents the highest impact in AEP although chord variables are very important with the exception of chord tip ( $c5$ ). Variables  $air1$ ,  $air6$  and  $air11$  within airfoil group are the most important for AEP. This result was expected as these design variables govern the leading edge and near trailing edge geometry.

The  $dxs\_tip\_max$  and blade mass are driven by the chord variables. This result is expected as the increment of chord length implies an associated increase of blade total thickness. Within the twist variables,  $tw5$  presents the highest impact in  $dxs\_tip\_max$ . The airfoil variables have very limited influence, only the leading edge has some importance ( $air6$ ).

The OAPWL is affected mainly by the chord variables. The airfoil variables  $a6$  and  $a11$  present short influence.

Generally, wind turbine outputs are much more sensitive to chord and twist variables than to airfoil variables.



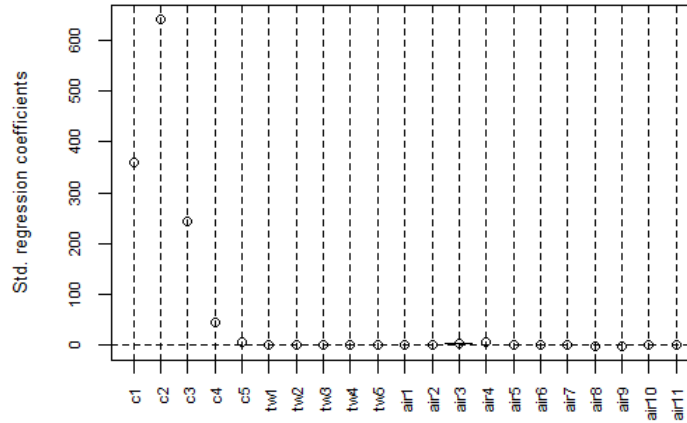


FIGURE 6.7: Standardized regression coefficients of linear of blade mass. 95% confidence intervals are included.

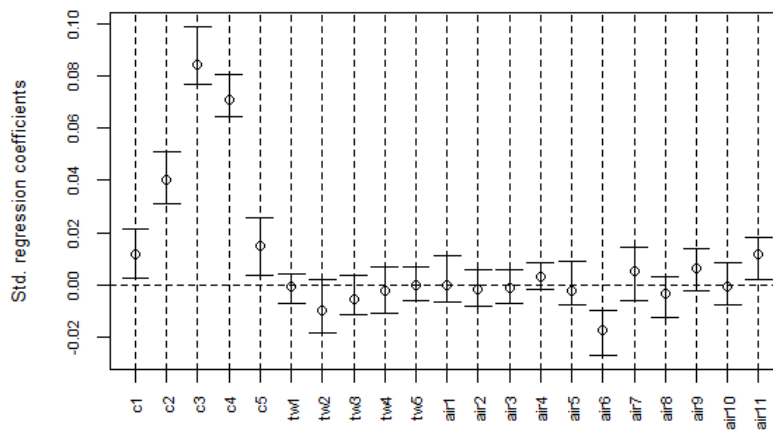


FIGURE 6.8: Standardized regression coefficients of linear regression of OAPWL. 95% confidence intervals are included.

### 6.1.3 Sensitivity Analysis based on Sobol-Saltelli indexes

The multi-variable linear regressions can provide invalid conclusions if significant non-linear relationships between inputs and outputs are taking place. To overcome this aspect and in order to confirm the results obtained with linear regressions, variance based sensitivity analysis is carried out.

Figure 6.9 shows the total Sobol indexes which measure the impact of each input variance in the output variance taking into account the interactions between inputs.

Most influencing variables coincide with regression's results. Twist variables *tw3* and *tw4* and chord variables *c2* and *c3* present the highest impact in AEP. For *dxs\_tip\_max* and BTM, only *c1*, *c2* and *c3* are significant. The chord variables *c2*, *c3* and *c4*, and of minor importance, airfoil variables *air6* and *air11* have the highest impact in OAPWL. The results endorse the previous conclusions from regression techniques. The wind turbine outputs are not sensitive to variables *c5*, *air2*, *air4*, *air5*, *air7*, *air9* and *air10*.

### 6.1.4 Conclusions of the sensitivity analysis

The AEP is affected by chord and twist variables. Within the airfoil design variables, only the ones governing LE and near TE area have moderate impact. The noise emission is mainly affected by the chord variables. The blade mass and  $dxs\_tip\_max$  depend highly on the chord variables as determine the total blade thickness. The sensitivity analyses have shown much lower influence of the airfoil variables in comparison to chord and twist distributions.

The decision to include the airfoil geometry in the blade design optimization should take into account important considerations. The aerodynamic performance of the available master airfoils is validated with expensive wind tunnel tests. The re-design of the airfoil master geometry implies to perform new wind tunnel tests or to assume the uncertainty of the computational calculations. Based on these considerations and the results from the sensitivity analyses that reveal less influence of the airfoil geometry than the spanwise laws, the design variables of airfoils are considered fixed parameters in the following analyses so existing master airfoils will be employed for the blade designs.

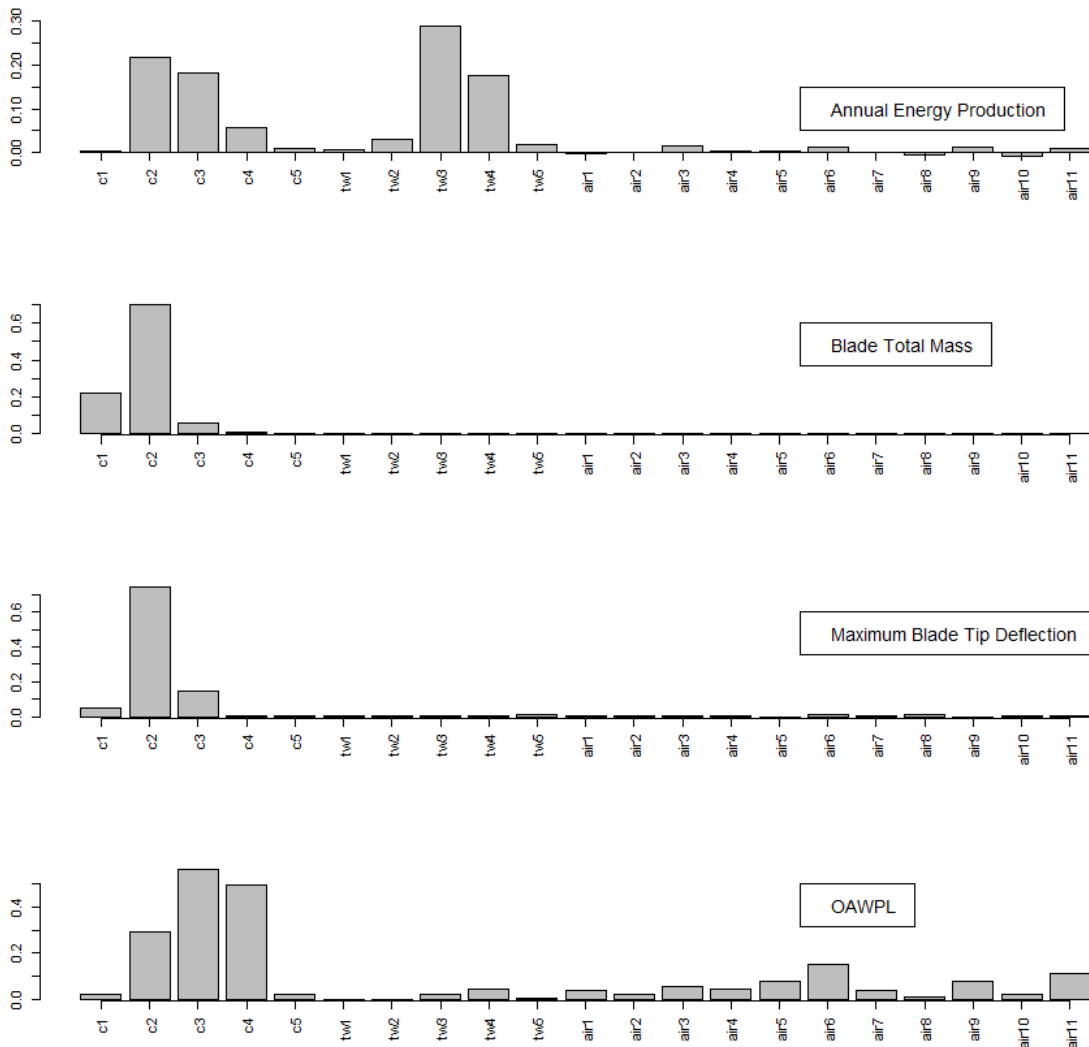


FIGURE 6.9: Sobol-Saltelli sensitivity indexes.

## 6.2 Prediction of dynamic amplification of loads

In this section, the procedure based on varying the design variables following LHS method, performing aeroelastic simulations and assessing the relationships between inputs and outputs is repeated as in previous section. Besides, the set of design variables is extended to other geometrical distributions (prebending, stacking, thickness), structural layout and controls. In contrast, airfoil design variables are removed from the analysis. Accordingly, the list of design variables is the following:

$$\text{Design Variables} = \left\{ \begin{array}{l} X_1 = cknots(9) : \text{Inboard chord knot} \\ X_2 = cknots(10) : \text{Outboard chord knot} \\ X_3 = ccoefs(6) : \text{Inboard chord coeff.} \\ X_4 = ccoefs(7) : \text{Inner-intermediate chord coeff.} \\ X_5 = ccoefs(8) : \text{Intermediate chord coeff.} \\ X_6 = ccoefs(9) : \text{Outer-intermediate chord coeff.} \\ X_7 = ccoefs(10) : \text{Outer chord coeff.} \\ X_8 = tknots(9) : \text{Twist knot} \\ X_9 = tcoefs(8) : \text{Inner twist coeff.} \\ X_{10} = tcoefs(9) : \text{Intermediate twist coeff.} \\ X_{11} = tcoefs(10) : \text{Outer twist coeff.} \\ X_{12} = eknots(8) : \text{Inboard thickness knot} \\ X_{13} = eknots(9) : \text{Outboard thickness knot} \\ X_{14} = ecoefs(6) : \text{Inboard thickness coeff.} \\ X_{15} = ecoefs(7) : \text{Intermediate thickness coeff.} \\ X_{16} = ecoefs(8) : \text{Outboard thickness coeff.} \\ X_{17} = pknots(1, 8) : \text{Prebending knot} \\ X_{18} = pcoefs(1, 7) : \text{Prebending coeff.} \\ X_{19} = sry_coeefs(6) : \text{Inboard stacking coeff.} \\ X_{20} = sry_coeefs(7) : \text{Intermediate stacking coeff.} \\ X_{21} = sry_coeefs(8) : \text{Outboard stacking coeff.} \\ X_{22} = cap1_e1 : \text{Outboard CAP1 thickness} \\ X_{23} = cap1_e2 : \text{Intermediate CAP1 thickness} \\ X_{24} = cap1_e3 : \text{Inboard CAP1 thickness} \\ X_{25} = gain_tsr : \text{Optimal gain} \\ X_{26} = gbx : \text{Gearbox ratio} \end{array} \right. \quad (6.1)$$

The responses to be analysed are the forces and moments in the main wind turbine locations (blade root, hub center, tower base,...). The blade deflections and the electrical power are also inspected.

The design variables are sampled using LHS method. The sampling data follow a uniform distribution. In figure 6.10, histogram of design variable  $X_1 = cknots(9)$  and  $X_{26} = gbx$  are shown. The allowable variation of each variable is selected to cover the reasonable design space as shown in figures of appendix B.

For each observation provided by LHS, B-spline baseline longitudinal laws are re-constructed introducing new values of design variables  $X_1, \dots, X_{21}$ . New spar cap thickness distribution is created according to design variables  $X_{22}, X_{23}$  and  $X_{24}$ . Besides, torque-speed gain ( $X_{25}$ ) and gearbox ratio ( $X_{26}$ ) are also modified.

AGORA is the computational tool employed to run the aeroelastic simulations and obtain loads and deflections. One task is completed when AGORA performs the internal operations to generate the blade geometry and structural layout, calculate the cross sectional structural properties, run the aeroelastic simulations and post-process the outputs. One task is performed per observation and implies twenty-six aeroelastic simulations. The time that each simulation requires is presented in table 6.1. The completion of the simulations calculated sequentially would require more

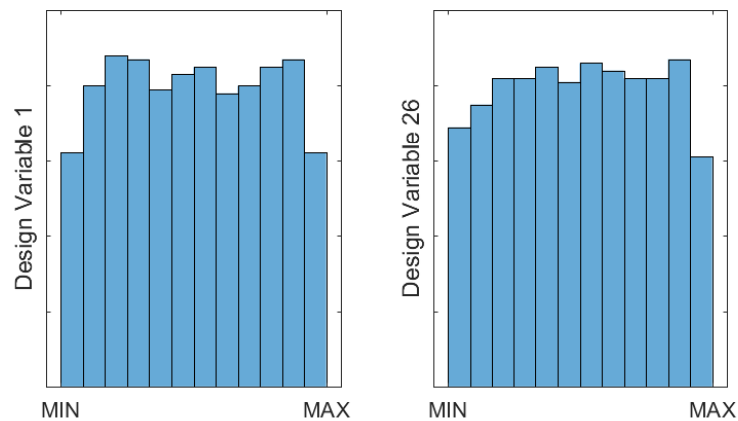


FIGURE 6.10: Histogram of design Variable  $X_1$  (Chord inboard knot) and  $X_{26}$  (Gearbox ratio).

than eight-hundred days. To reduce the computational time, the simulations are run in parallel with (*MATLAB Parallel Computing Toolbox 2019*). The completion of all simulations with a thirty cores computer is performed in one month.

TABLE 6.1: Description of aeroelastic simulations of one task.

Type	No. of simulations	Wind speed (m/s)	TI	Simulation time (min)	Completion time (min)
Eigen frequencies	1	NA	NA	NA	0.5
Steady	1	{3 3.1 ... 13.9 14}	NA	NA	1
Dynamic1	5	{8 10 12 14 18}	Specific	10	50
Dynamic2	19	{3 3.5 ... 11.5 12}	10%	10	50

TABLE 6.2: Wind turbulence intensities (%) of *DYNAMIC 1* group of simulations

label	Time (s)	Mean wind speed (m/s)	Longitudinal TI (%)	Lateral TI (%)	Vertical TI (%)
id1	600	8	19.5	15.6	11.6
id2	600	10	18.0	14.3	10.5
id3	600	12	17.0	13.5	9.8
id4	600	14	16.3	12.9	9.3
id5	600	18	15.3	12.1	8.6

Three types of simulations are performed for each task: eigen-frequencies calculations, steady simulations and dynamic simulations. Table 6.1 shows a summary of characteristics of the calculations.

The dynamic simulations are divided in two groups with different types of turbulence and for different purposes:

- *Dynamic1*. In this group of dynamic simulations specific TI values according to table 6.2 are employed. These simulations are used to obtain fatigue loads, ultimate loads and maximum blade deflections.
- *Dynamic2*. These simulations are performed with wind fields of turbulence TI= 10%. The power curve and subsequent AEP are calculated from this group of simulations.

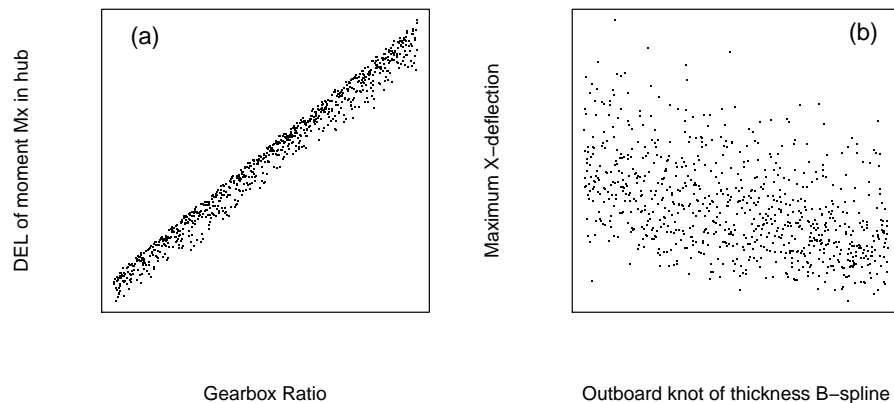


FIGURE 6.11: (a) DEL of moment  $M_x$  in drive train in function of Gearbox Ratio.(b) Maximum tip deflection along X-axis in function of outboard thickness knot.

### 6.2.1 Graphical inspection

The results obtained in the aeroelastic simulations are inspected with different graphical methods.

The correlations between pairs of design variable-response are investigated with scatter plots. In the scatter plots, the linear correlation between one design variable and one output is significant in some cases. Figure 6.11 (a) shows an example of high linear correlation between gearbox ratio and fatigue damage of  $M_x$  moment in drive train. The higher gearbox ratio the lower rotor speed (for the same generator speed) and thus higher generator torque to develop same rated power which involves more fatigue loads in the gearbox. In contrast, the correlation is not so significant or non-existent in other pairs. Figure 6.11 (b) shows one case with moderate correlation. The outboard thickness knot and maximum deflection along X-axis present an inverse linear correlation. Higher knot values implies higher thickness distribution and hence lower deflection along X-axis.

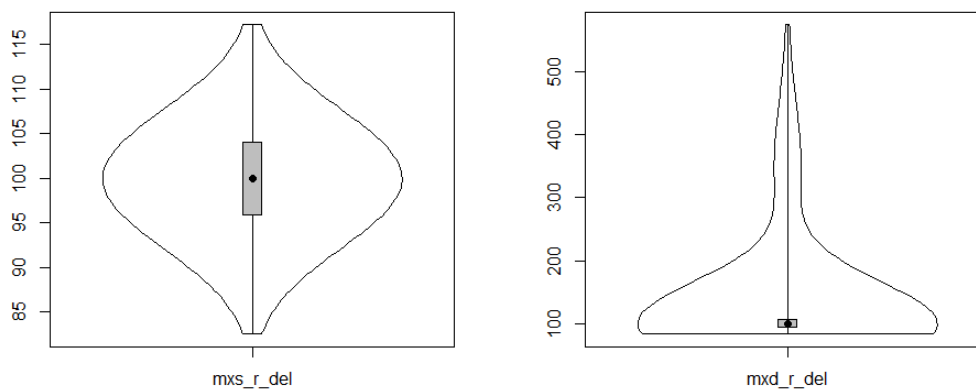


FIGURE 6.12: Left: violin plot of DEL of  $M_x$  moment in blade root based on gravitational cyclical loads. Right: violin plot of DEL calculated from dynamic aeroelastic calculations

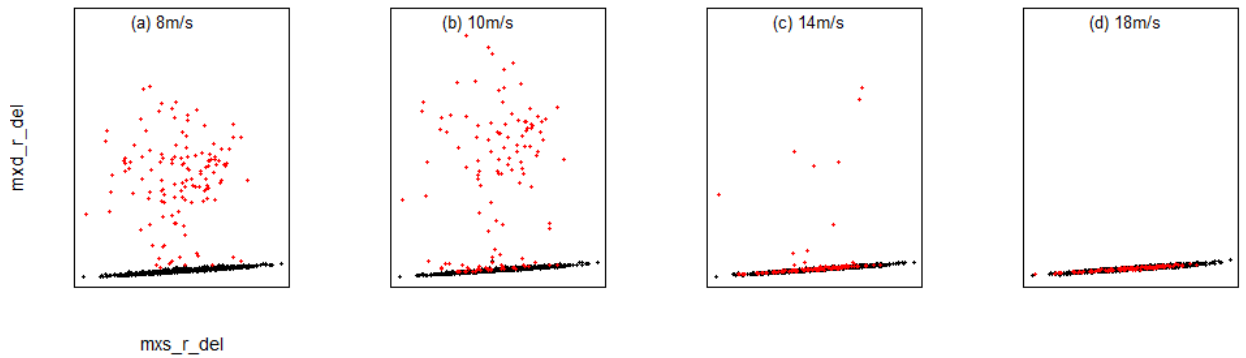


FIGURE 6.13: DEL of  $M_x$  moment in blade root based on gravitational cyclical loads with respect to DEL calculated from dynamic aeroelastic calculations: (a) 8 m/s, (b) 10 m/s, (c) 14 m/s and (d) 18 m/s

Violin plots are graphical methods that show the distribution of the responses and serve to identify outliers. In this thesis violin plot of the different responses are created with the package (Adler, 2005) of (R, 2017). Figure 6.12 shows violin plots of two post-processed DEL of  $M_x$  moment in blade root. On the left part it is shown the violin plot of DEL calculated according to equation 3.3 that provides the fatigue damage due to gravitational source ( $mxs\_r\_del$ ). On the right part, it is presented the violin plot of the DEL calculated from dynamic aeroelastic simulations and that takes into account dynamic effects ( $mxd\_r\_del$ ). The violin plots reveal significant differences. The left part violin plot shows a symmetric distribution with respect to median value. In contrast, the right part violin plot shows an asymmetric distribution with a significant number of outliers. These outliers suggest some type of dynamic load amplification.

## 6.2.2 Analysis of outliers

The presence of dynamic load amplification loading in some observations is confirmed and investigated in this subsection. In figure 6.13, the fatigue damage based on equation 3.3 is presented with respect to fatigue damage calculated from dynamic calculation. Results of simulations with different wind speeds are presented: 8, 10, 14 and 18 m/s. The linear relationship of most of observations is strong. However, some observations show a very significant deviation from linear relationship: the number of these observations is high at 8 m/s and 10 m/s, but at 14 m/s there are less and at 18 m/s none. The observations that present a significant deviation from linearity in any of the simulations is represented in figure 6.13 as red dots.

On figure 6.14 AEP calculated from dynamic simulations are presented in function of AEP calculated from steady simulations. Although most of observations present a significant linear relationship, others which are represented as red dots show a strong departure from it involving a high loss of AEP with respect to steady state calculation.

One observation that presents this dynamic amplification is identified. For this observation, the time history of the dynamic simulation at 8 m/s is analysed. Figure 6.15 shows signal of blade root  $M_x$  moment in time (a) and frequency domain (b). The time history reveals amplification of the signal in the last part of the simulation. The frequency domain signal shows significant peaks along the spectrum.

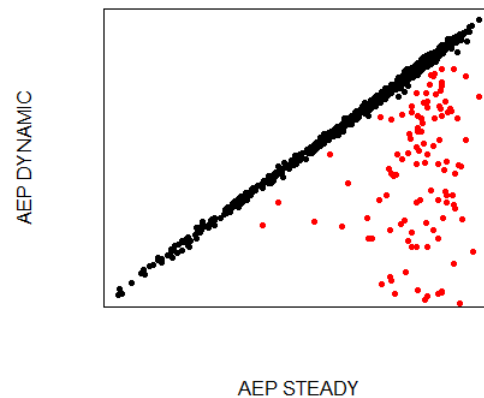


FIGURE 6.14: AEP from dynamic simulation. with respect to AEP from steady simulations.

The analysis has revealed a dynamic load amplification in some observations that corresponds to specific combinations of design variables. The amplification produces elevated loads and an important reduction of energy. This phenomenon should be avoided in the blade design.

The load amplification could be caused by different effects. On the one hand, a resonance is produced by the proximity of the excitations (1P, 2P, 3P...) and wind turbine coupled eigen-frequencies. If the aeroelastic damping values of a mode is low, the associated resonance involves important load amplifications. In this case, the Campbell diagram (Burton, 2001), performed in the frequency domain, is inspected without evidence of this aspect. On the other hand, the aeroelastic instabilities are caused by the existence of modes with reduced or even negative aeroelastic damping. Several types of instabilities are relevant in wind turbines such as classical flutter, stall flutter, or torsion-edgewise vibrations (Holierhoek, 2008). These phenomena can provoke the sudden collapse of a structure (*NASA video flutter*) and are subject of research due to their importance to ensure the integrity of the wind turbines.

The following investigates the combinations of design variables that produce the instability. The underlying physical reasons that produce the phenomenon and the identification of the type of instability involved are investigated as a separate research out of the scope of this thesis.

In order to assess the phenomenon, a qualitative response named *UNSTABLE* is artificially created and assigned to the observations according to their departure from linear relationship with steady response. This response is set as 0 in observations with no load amplification and 1 in samples that present the undesirable behavior.

Two statistical techniques are employed to predict the binary response: logistic regression (James and Witten, 2013) and fast and frugal trees (FFtrees) (Phillips et al., 2017).

To avoid over-fitting, the observations are randomly divided into two groups. The first larger group (80%) serves to train the prediction model and the second group (20%) is used for accuracy validation and assessment under unknown data.

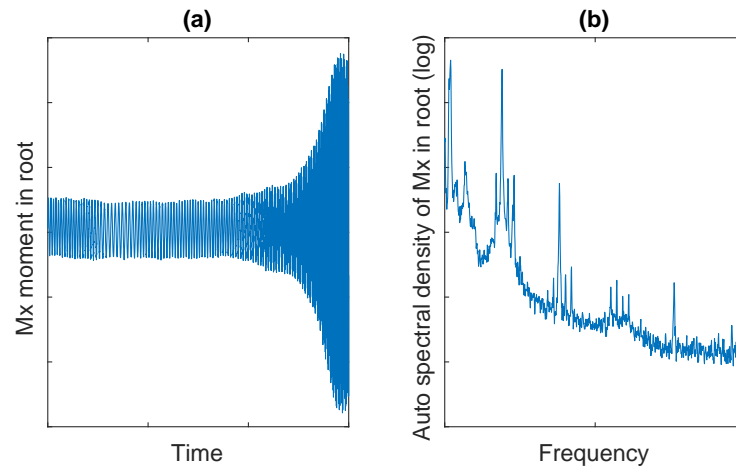


FIGURE 6.15: Mx moment in root at 8 m/s mean wind speed in (a) Time domain and (b) Frequency domain.

### 6.2.3 Multiple logistic regression

Logistic regression is an appropriate tool for the assessment of the relationship between the design variables and a binary response (James and Witten, 2013). The multiple logistic regression models are fitted with the statistical code (R, 2017). The table 6.3 shows the calculated logistic regression coefficients, the associated  $\varphi$  - values and a code that informs about the significance of each design variable:

- \*\*\* high significance ( $\varphi$  - value  $\leq 0.001$ ).
- \*\* medium significance ( $0.001 \leq \varphi$  - value  $\leq 0.01$ ).
- \* low significance ( $0.01 \leq \varphi$  - value  $\leq 0.05$ ).
- Very low significance ( $0.05 \leq \varphi$  - value  $\leq 0.1$ ).
- No significance ( $\varphi$  - value  $\geq 0.1$ ).

The confusion matrix describes the accuracy of the model. Table 6.4 shows the results for the 80% of observation that are employed to fit the model. Table 6.5 presents the table for the validation observations (20%).

The performance parameters: sensitivity, specificity and accuracy are presented for the prediction models in table 6.10. The logistic regression model predicts with an accuracy of 98% the response when the model is tested with the same observations employed for fitting. However, the accuracy of the model is reduced to 92% for the 20% of unknown observation.

The threshold probability  $P_{th}$  that determines if the response *UNSTABLE* is predicted as a 0 or 1 is defined normally as  $P_{th} = 0.5$  meaning that probabilities higher than 0.5 are assigned with a value of 1 and probabilities lower than 0.5 with 0. However, this threshold can be changed to modify sensitivity and specificity. The appropriate balance between sensitivity and specificity is a solution of compromise and depends on the prediction model purpose. If the model is used to specify a constraint in an optimization problem, it is preferable to have a low number of false alarms (high specificity) and high number of misses (low sensitivity) than vice versa.



TABLE 6.3: Coefficients and p-values of logistic regression performed to the binary response *UNSTABLE*

Design variable	Coefficient	p-value	Significance code
Intercept	-13.11047	6.74E-11	***
cknots9	0.84081	0.017164	*
cknots10	-0.06642	0.831261	
ccoefs6	-0.14651	0.588551	
ccoefs7	-0.04	0.897739	
ccoefs8	0.1679	0.571639	
ccoefs9	-0.54125	0.096745	.
ccoefs10	2.16091	8.92E-06	***
tknots9	-1.09584	0.000764	***
tcoefs8	-0.46139	0.094309	.
tcoefs9	-0.69767	0.012121	*
tcoefs10	-0.58443	0.046484	*
eknots8	-2.23679	5.62E-07	***
eknots9	-3.689	2.46E-09	***
ecoefs6	-1.85332	3.03E-06	***
ecoefs7	-3.69268	2.18E-09	***
ecoefs8	-4.09223	1.44E-09	***
pknots8	4.70583	2.59E-09	***
pcoefs7	5.05378	1.27E-09	***
sry_coefs6	-0.19783	0.557785	
sry_coefs7	-0.27095	0.342562	
sry_coefs8	0.33989	0.283738	
cap1_e1	-0.15048	0.615736	
cap1_e2	1.23911	0.00055	***
cap1_e3	-0.94374	0.004705	**
gain_tsr	-0.73746	0.013818	*
gbx	-1.40391	8.63E-05	***

TABLE 6.4: Confusion table of multiple logistic regression (fitting observations).  $P_{th} = 0.5$ 

		Truth	
		1	0
Prediction	1	95	7
	0	11	627

One missed prediction provided incorrectly by the optimization as a feasible solution can be identified afterward by performing aeroelastic simulation to verify the prediction goodness. Nevertheless, a false alarm means a possible feasible solution that the optimization has incorrectly rejected without being known. To increase specificity in this model the threshold probability is increased to  $P_{th} = 0.85$ . In tables 6.6 and 6.7 results for  $P_{th} = 0.85$  reveal that as expected false alarms have decreased but number of misses have increased.

#### 6.2.4 Analysis with fast and frugal trees

As proceeded with logistic regression, FFTree is fitted with the most of observations (80%) and validated with a reduced subgroup of 20% of observations. Figure 6.16 shows the proposed decision tree. Confusion tables 6.8 and 6.9 show the results for both group of observations and the summary of performance parameters are presented in table 6.10.

TABLE 6.5: Confusion table of multiple logistic regression (validation observations).  $P_{th} = 0.5$ 

		Truth	
		1	0
Prediction	1	22	10
	0	6	162

TABLE 6.6: Confusion table of multiple logistic regression (fitting observations).  $P_{th} = 0.85$ 

		Truth	
		1	0
Prediction	1	78	1
	0	28	633

The FFTree provides a less accurate set of predictions (83% for unknown observations) than multiple logistic regression (92%). However, the visual tree scheme offers an advantage for implementation in an optimization problem constraint and for understanding the phenomenon. According to significance codes of multiple logistic regression in table 6.3 eleven design variables involving chord, twist, thickness, prebending, spar-cap thickness and gearbox ratio exhibit high significance. Nevertheless, only three design variables involving prebending and blade thickness have relevance according to FFTree.

TABLE 6.7: Confusion table of multiple logistic regression (validation observations).  $P_{th} = 0.85$ 

		Truth	
		1	0
Prediction	1	18	5
	0	10	167

TABLE 6.8: Confusion table of FFTree (fitting observations)

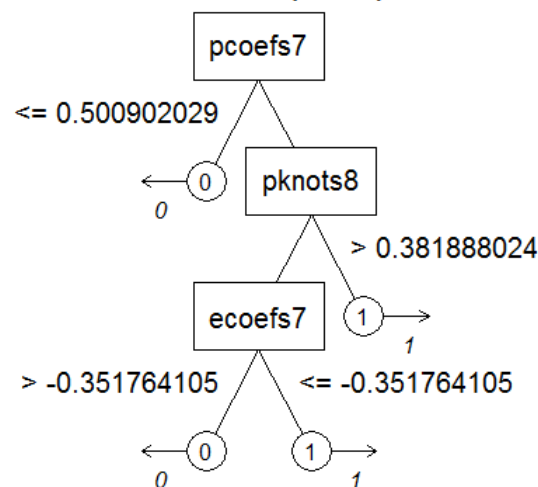
		Truth	
		1	0
Prediction	1	69	105
	0	34	532

TABLE 6.9: Confusion table of FFTree (validation observations)

		Truth	
		1	0
Prediction	1	25	29
	0	6	140

TABLE 6.10: Summary of prediction performance of logistic regression and FFTrees

Model	Observations	Sensitivity	Specificity	Accuracy
Logistic (p=0.5)	Fitting (80%)	90	99	98
Logistic (p=0.5)	Validation (20%)	79	94	92
Logistic (p=0.85)	Fitting (80%)	74	99	96
Logistic (p=0.85)	Validation (20%)	64	97	93
FFTree	Fitting (80%)	67	84	81
FFTree	Validation (20%)	81	83	83

FIGURE 6.16: Decision tree calculated with FFTree technique to predict binary response *UNSTABLE*



## Chapter 7

# Application of the blade optimization methodology

The purpose of the chapter is to illustrate the methodology and techniques proposed in this thesis with a real case and to determine the influence of the optimization techniques and the optimization statement in the final blade design.

The optimization algorithms proposed in this chapter are governed by several parameters that affect the efficiency of the optimizations. In order to determine the most suitable values, a surrogate model created in a design space exploration phase, is evaluated in hundreds of optimizations with different sets of parameters. The results are compared to infer the most appropriate setting parameters to be employed in the real optimizations.

Once the algorithm parameters are determined, different optimizations in different scenarios are performed. The scenarios evolve from a non realistic case where the energy production is the objective function with no other constraints to more complicated design scenarios where other practical considerations are taken into account such as blade mass, blade deflections and loads. The final scenario solves a constrained problem where a specific surface fairness parameter should be minimized and other blade features should be respected. In each scenario, the performance of the different optimization algorithms is compared.

The baseline wind turbine of the optimization scenarios is a public available model created with the aim of comparing research studies.

The chapter is divided in the following sections:

- Section 7.1 introduces the main features of the reference model and describes the methods to reproduce it with *AGORA*.
- Section 7.2 introduces the studies performed prior to the optimizations such as the definition of design variables and a design space exploration. Furthermore, the most appropriate setting parameters of the optimization algorithms are calculated with the aid of the surrogate model adjusted in the design space exploration.
- Section 7.3 presents the optimizations grouped according to four optimization statements called scenarios A, B, C and D.

### 7.1 DTU reference model

The *Light Rotor project* between Technical University of Denmark (DTU) and Vestas company was conceived with the main objective of optimizing the design of

TABLE 7.1: Main features of the DTU 10MW reference wind turbine

Wind regime	.	IEC Class 1A
Control concept	.	Variable speed pitch regulated
Rated power	[MW]	10
Rotor diameter	[m]	178.3
Blade length	[m]	86.4
Minimum rotor speed	[rpm]	6
Maximum rotor speed	[rpm]	9.6
Gearbox ratio	[.]	50
Hub height	[m]	119

the blades to increase the stiffness and overall performance of the rotor taking into account both aerodynamic, aero-servo-elastic and structural considerations. In the project, a 10-MW reference rotor is designed, so that future designs can be compared to the rotor, also called the DTU 10-MW Reference Rotor (DTU 10MW RWT). Besides, a full wind turbine model is established. Detailed information of the whole wind turbine can be found in report I-0092 (Bak, 2013). The information is free to use for investigations of new blade designs. Main features of the wind turbine are shown in table 7.1.

Basis for the wind turbine was an upscale of NREL 5MW RWT (Jonkman et al., 2009). The family of airfoils is the public available FFA-W3 airfoil series. The airfoils have 24.1, 30.1 and 36% relative thickness. In addition, a 48% airfoil is created by multiplication of 36% coordinates and a 60% airfoil by interpolation between 48% airfoil and circle. The 2D aerodynamic coefficients are obtained from CFD calculations. The spanwise laws chord, twist and relative thickness were designed to maximize the power coefficient  $C_p$  at a tip speed ratio of 7.5. A maximum thrust force of 1500 kN at operation conditions is established as constraint. Regarding blade deflection, tower clearance is ensured with a safety margin of 32%. The spanwise laws are available in form of cubic piecewise polynomial splines (pp form). The blade presents a sheared blade shape with a prebending of 3.332 m in tip.

The reference structural layout is made from glass fiber reinforced composites and balsa wood used as a sandwich core material. The multi-directional plies are made of three types: uniax (fibers at 0 and 90°), biax (fibers at +45 and -45°) and triax (fibers at 0, +45 and -45°).

The structural layout incorporates a box girder with two shear webs. The caps were placed at the maximum thickness in order to obtain maximum flapwise bending stiffness. The spar caps are formed mainly by stacking of uniax material. A third shear web is close to the trailing edge. Width of the cap is variable along span which is not beneficial from the manufacturing perspective.

### 7.1.1 Validation of DTU 10MW RWT model in AGORA

Based on the information of (Bak, 2013), AGORA code is used to calculate the performance of the DTU 10MW RWT.

To reproduce the DTU 10MW RWT, the preliminary stage consists on approximating baseline pp-form splines by cubic B-splines that will be modified in the optimizations by changing their control points. Besides spanwise laws, FFA-W3 airfoils available in form of points are approximated by B-splines. With all the geometrical information expressed as B-splines the blade surface is replicated as a B-spline lofted surface.

TABLE 7.2: Comparison of main parameters of DTU 10MW RWT

Feature	Units	AGORA	Report I-0092	Ratio
Blade mass	(Tn)	42.1	41.7	101%
Fm	(Tnm)	1096.6	1092.1	100%
Thrust Max	(kNm)	1466.0	1507.4	97%
Blade eigen frequency (flap)	(Hz)	0.610	0.610	100%
Blade eigen frequency (edge)	(Hz)	0.961	0.930	103%
Blade eigen frequency (flap)	(Hz)	1.756	1.740	101%
Blade eigen frequency (edge)	(Hz)	2.960	2.760	107%
Blade eigen frequency (flap)	(Hz)	3.657	3.570	102%
Blade eigen frequency (torsion)	(Hz)	5.508	5.690	97%
Blade eigen frequency (flap)	(Hz)	6.163	6.110	101%
Blade eigen frequency (edge)	(Hz)	6.527	6.660	98%
Tower eigen frequency (side-side)	(Hz)	0.254	0.250	102%
Tower eigen frequency (fore-side)	(Hz)	0.255	0.250	102%
Drive train eigen frequency (torsion)	(Hz)	1.759	1.803	98%

Furthermore, the structural layout of DTU 10MW RWT is reproduced and cross sectional properties are calculated. Blade geometry and structural properties, in conjunction with wind turbine parameters of DTU 10MW RWT that define nacelle, rotor, tower, drive train and control, are introduced in an aeroelastic wind turbine model of (*BLADED*). Finally, polar curves of master airfoils are also included in the model. The eigen frequencies of the flexible bodies are calculated and steady state calculations are performed. Table 7.2 compares main results of the baseline wind turbine model according to the public available documentation of DTU 10MW RWT in report I-0092 (Bak, 2013) with respect to approximation model performed in *AGORA*. Figure 7.1 shows the curves of mechanical power, thrust force, rotor speed and pitch angle.

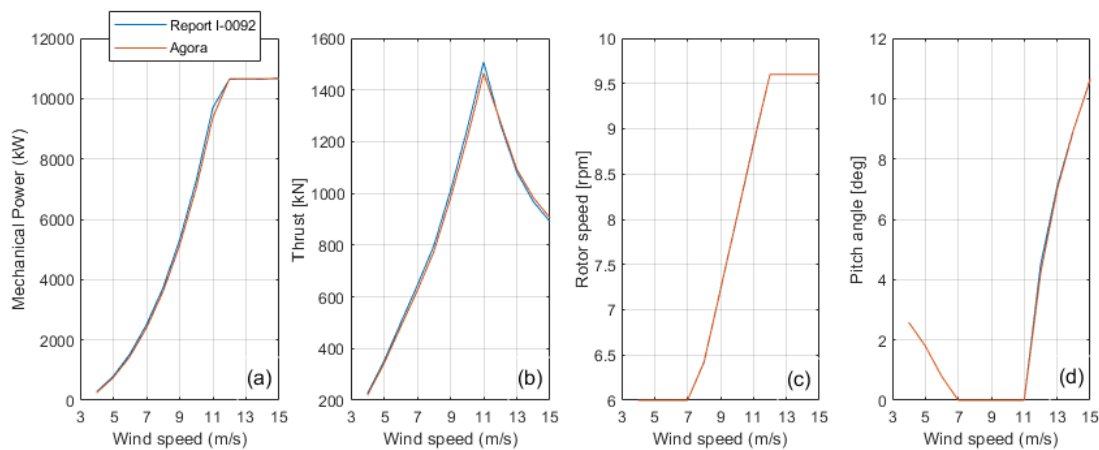


FIGURE 7.1: Comparison of performance of DTU 10MW RWT: report I-0092 (table 3.5) versus model created in *AGORA*: (a) Mechanical power, (b) Thrust Force, (c) Rotor speed and (d) Pitch angle.

The usage of different aeroelastic and structural codes imply deviations in the results. Several benchmark projects between aeroelastic codes reveal that differences in the results of the aeroelastic simulations under same conditions are usually found (Jonkman and Musial, 2010). In this case, minor deviations in the eigen-frequencies and main features of the aeroelastic performance are shown with respect to report I-0092 (Bak, 2013). Thus, the *AGORA* model is considered representative of the

DTU 10MW RWT. In order to avoid distortion due to the differences found between AGORA and report I-0092 (Bak, 2013), the reference values of DTU 10MW RWT are the ones calculated in AGORA. The outcomes of the following optimizations of the chapter are presented as a relative ratio or difference with respect to DTU 10MW RWT. As example, a solution that presents 101% of AEP and +1 Tn of blade mass mean a ratio increase of 1% of AEP and 1 Tn more of blade mass than DTU 10MW RWT.

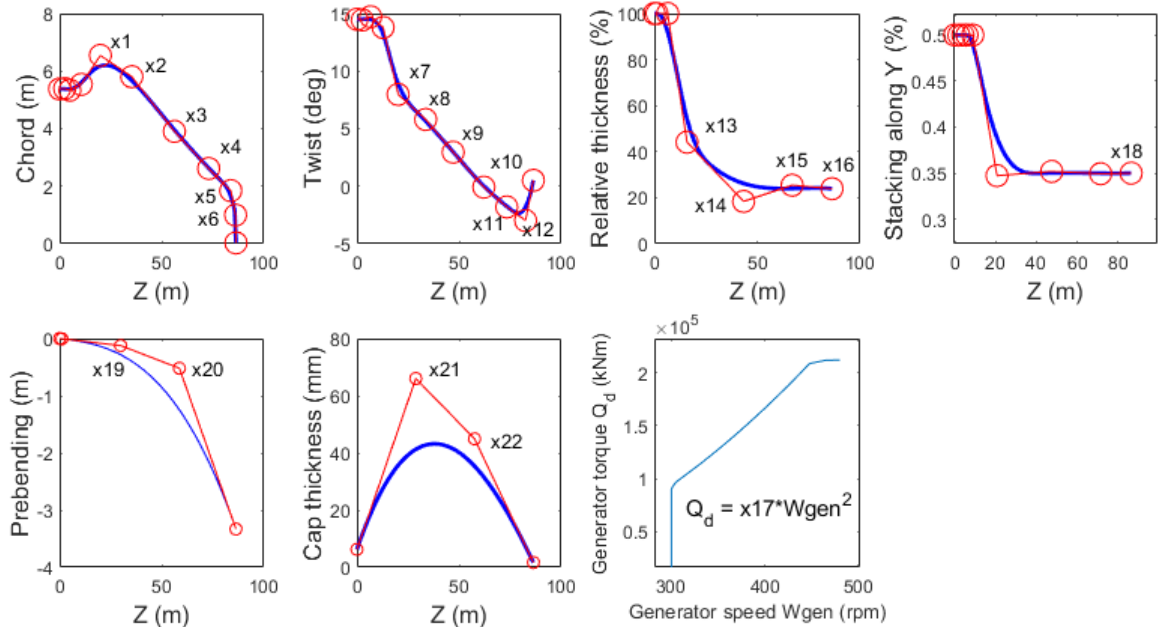


FIGURE 7.2: Design variables  $x_1$  to  $x_{22}$

## 7.2 Introduction to optimizations

The objective function and constraints change between the optimization scenarios. The number of constraints is increased in each consecutive scenario. This aspect affects the performance of the algorithms and the results.

With respect to DTU 10MW RWT, some of the features of the wind turbine are optimized. The blade geometry is changed by modifying the control points of spanwise B-spline laws: chord, twist, relative thickness, stacking law and prebending curve. The spar cap thickness distribution is also modified. The baseline spar cap thickness distribution is approximated with a cubic B-spline and two intermediate control points are identified as design variables for the optimization. Finally, gain between demanded torque and rotor speed in the variable speed area  $gain_{tsr}$  is also set as design variable. Figure 7.2 shows the twenty-two design variables. The rest of features of DTU 10MW RWT are maintained unchanged in the optimizations. Due to the lack of a professional control setting which is necessary to perform dynamic simulations, the optimizations are based on steady state calculations.

### 7.2.1 Design space exploration

Prior to start with the optimizations and following methodology introduced in chapter 6 a design space exploration is performed by varying the design variables and



TABLE 7.3: Goodness of fit ( $R^2$ ) of surrogate models.

Response	Linear	Quadratic
AEP	0.62	0.95
Mass	0.98	0.99
Maximum deflection	0.67	0.80
Thrust maximum	0.92	0.97

assessing their relationships with wind turbine outputs resulting from steady aeroelastic simulations: AEP, maximum thrust ( $fxs\_yaw\_max$ ), maximum blade tip deflection ( $dxs\_tip\_max$ ) and blade mass. LHS method is again employed to construct the sampling data. One steady simulation is performed per observation. Each simulation incorporates calculations for several wind speeds from cut-in to cut-out. Linear and quadratic surrogate models are fit. The goodness of fit in form of  $R^2$  statistic is presented in table 7.3. For adjustment of mass and maximum thrust, linear models present sufficient accuracy. However, for AEP and maximum blade deflection at least a quadratic model is necessary as linear models have low accuracy.

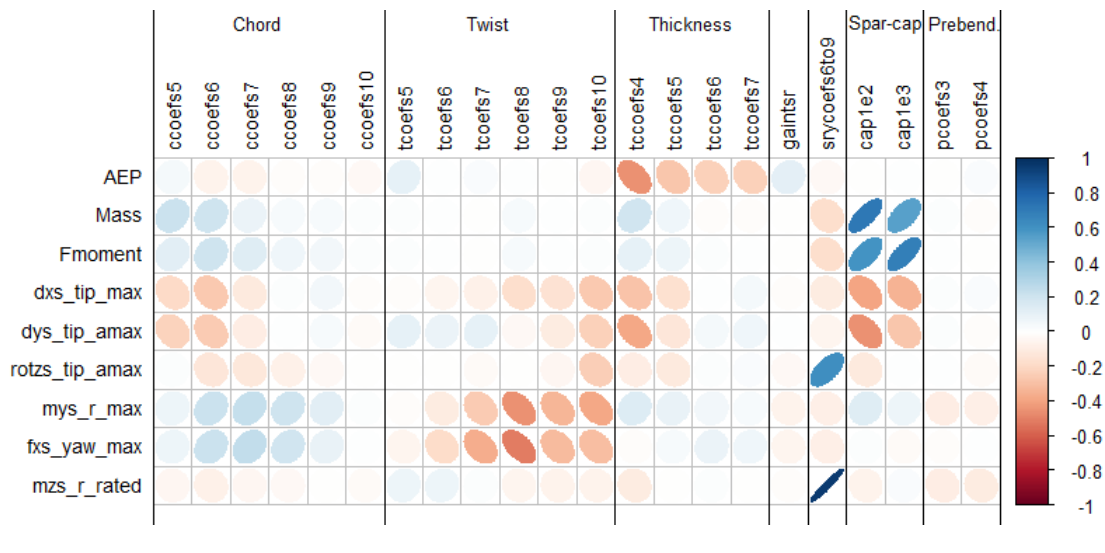


FIGURE 7.3: Matrix of Pearson's coefficients between responses (rows) and design variables (columns).

The correlation matrix in figure 7.3 shows the strength of association between design variables and responses. The matrix has been created with a package of (R, 2017)(Wei and Simko, 2016). The more representative responses are considered in the correlation matrix: AEP, mass, first static mass moment ( $Fm$ ), maximum blade deflections ( $dxs\_tip\_max$ ,  $dys\_tip\_max$  and  $rotzs\_tip\_amax$ ), maximum out of plane bending moment in root ( $mys\_r\_max$ ), maximum thrust force in yaw bearing ( $fxs\_yaw\_max$ ) and torsional moment in root at rated wind speed ( $mzs\_r\_rated$ ).

## 7.2.2 Optimization techniques

Different optimization techniques are employed in this chapter with assorted methodology: NM, GB, PS, GA, PSO and SA. These algorithms incorporate specific optional parameters that are defined by the user. Try and error optimizations with same conditions but containing different algorithm parameters provide information about the

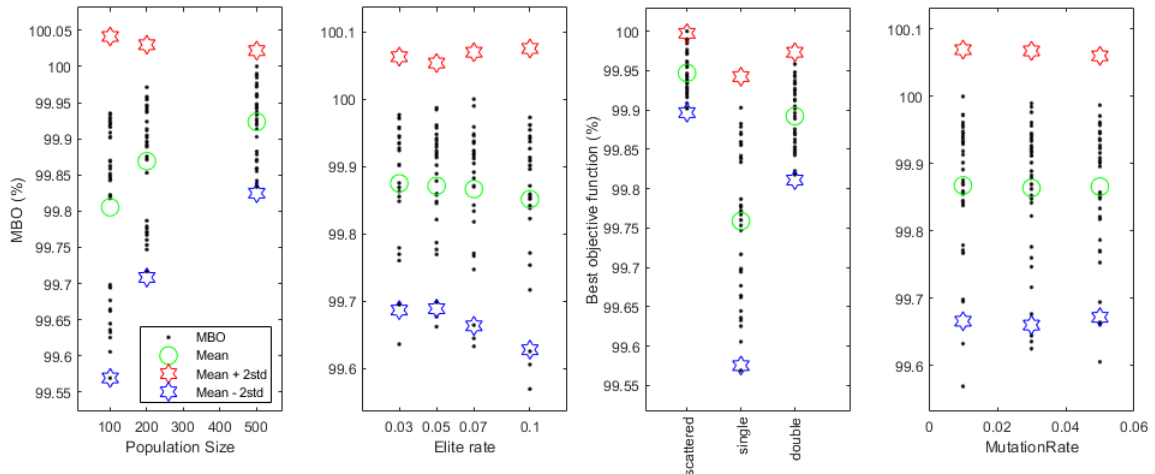


FIGURE 7.4: MBO versus population size, number of elite individuals, crossover function and mutation rate.

most suitable values to be employed. The number of evaluations required to achieve convergence and the value of the best objective function are compared to conclude the most appropriate values for the algorithm parameters. However, the multidisciplinary optimizations in the blade design involve a computationally expensive evaluation of the objective functions and constraints which impedes to perform the large number of optimizations that requires this assessment. Alternatively, the use of a surrogate model makes possible to perform the assessment as the evaluation of the objective function is very fast. The following process is implemented for each algorithm:

- Identify the significant setting parameters that govern the algorithm.
- Assign potential values for these parameters and build the list of combinations of parameters.
- Perform optimizations for each combination of parameters. For this analysis a maximization of the AEP with no constraint is stated. The stochastic nature of some algorithms makes necessary to repeat the optimization several times for the same combination of parameters as the results are variable although the problem statement is the same. Twenty-five realizations are performed for the same set of parameters.
- For each combination of algorithm parameters, two aspects are evaluated regarding the efficiency of the algorithm. The number of evaluations that are necessary to achieve convergence is denominated evaluations to convergence (ETC). The mean value of ETC for the twenty-five realizations under same combination of setting parameters is denominated mean of evaluations to convergence (METC). On the other hand, the best value of the objective function as a ratio with respect to DTU 10MW RWT is denominated best objective (BO) and the mean value of BO for the twenty-five realizations under the same setting parameters is denominated mean best objective (MBO). These two metrics are incorporated in the assessment figures to identify the optimum configurations. The mean and the mean  $\pm 2\sigma$  of METC and MBO are also included to evaluate the scattering of the metrics.

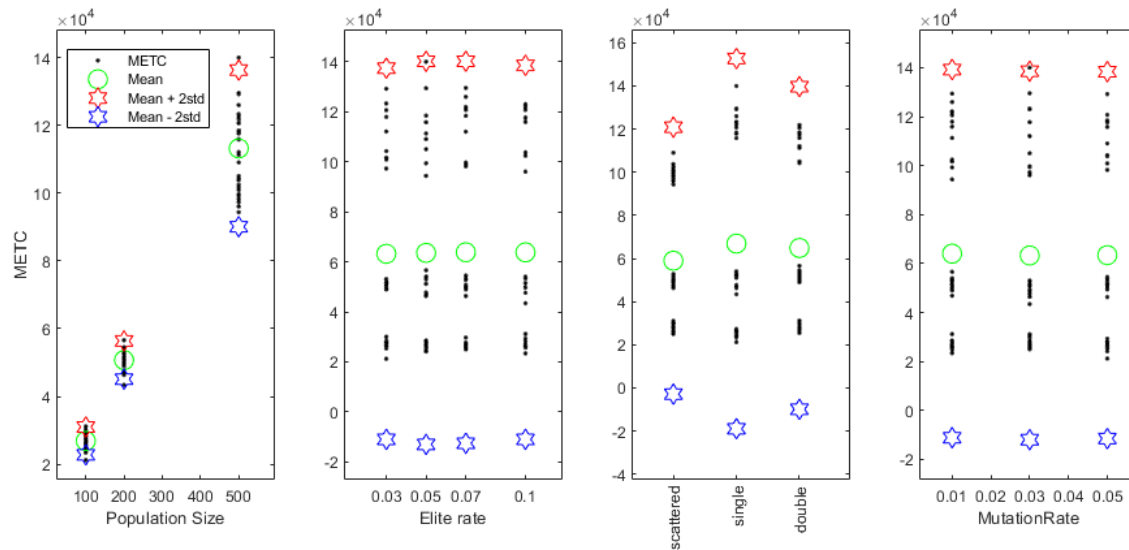


FIGURE 7.5: METC versus population size, number of elite individuals, crossover function and mutation rate.

### 7.2.3 Setting parameters of genetic algorithm (GA)

The operations that GA performs during the optimization are governed by the following options (manual [MATLAB Global Optimization Toolbox 2019](#)). In addition, some potential values for the parameters are selected for the analysis.

- Size of the generations: one hundred, two hundred or five hundred.
- Rate of individuals that are guaranteed to survive to the next generation (elite rate): 0.01, 0.02 or 0.03.
- Method to interchange information between individuals in the crossover operation (*CrossoverFunc*): *scattered*, *single-point* or *two-points*. Information about the fundamentals of the crossover methods is found in (manual [MATLAB Global Optimization Toolbox 2019](#)).
- Rate of individuals that are mutated (*MutationRate*): 0.01, 0.02 or 0.03.

All in, twenty-seven combinations are tested. Each one is repeated twenty-five times.

Figure 7.4 shows the MBO in function of the GA setting parameters and figure 7.5 presents the METC in function of the GA setting parameters.

The increase of population size causes an increment of the mean and scattering of the METC. Besides, it increases the mean and decreases the scattering of the MBO. A size of two hundred individuals is a suitable compromise between both. No significant impact on the METC is found when modifying the elite rate, method of crossover or rate of mutation. The *scattered* method is the preferred option to obtain a high MBO with low scattering. No significant impact of the mutation nor elite rate in the MBO is observed.

### 7.2.4 Setting parameters of particle swarm optimization (PSO)

The size of the swarm and the weights  $c_1$  and  $c_2$  of the individual and global terms of the particle velocity equation are inspected. The following values of the swarm

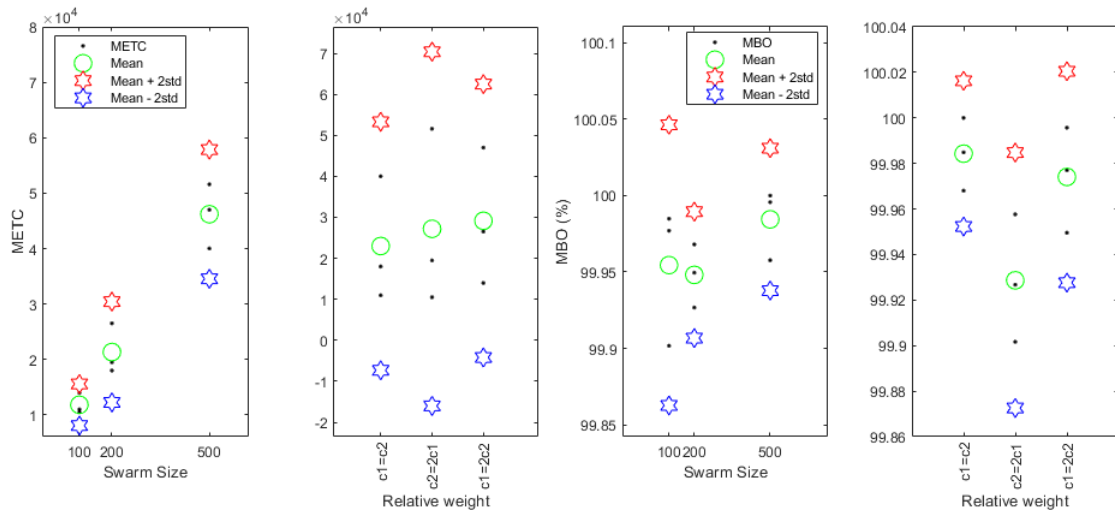


FIGURE 7.6: METC versus swarm size and relative weight. MBO versus swarm size and relative weight

size are taken into consideration: one hundred, two hundred and five hundred. Regarding the relative weights, three options are inspected:  $c1 = c2$ ,  $c2 = 2c1$  and  $c1 = 2c2$ . In total, nine combinations of parameters. Each one is repeated in twenty-five optimizations.

Figure 7.6 shows the influence of the swarm size and relative weight in the METC and MBO. The increase of swarm size causes a significant increment of the mean and scattering of the METC. The option of specifying an equal individual and global relative weights ( $c1 = c2$ ) provides slightly lower mean and scattering of the METC.

The highest swarm size (five hundred) provides the highest mean of MBO but with low difference with respect to smaller sizes. Equal individual and global relative weights ( $c1 = c2$ ) provide the highest mean of MBO and the minimum scattering.

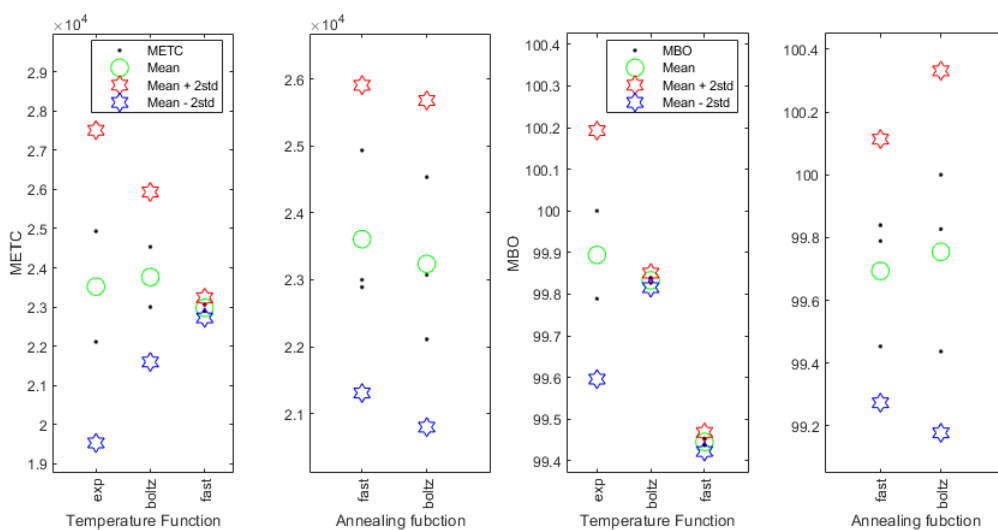


FIGURE 7.7: METC versus temperature function and annealing function. MBO versus temperature function and annealing function

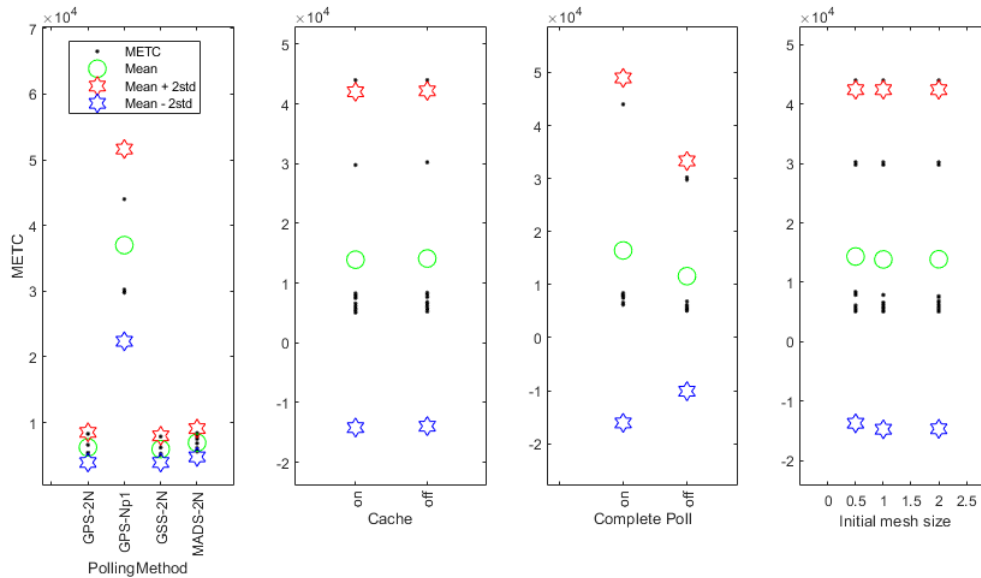


FIGURE 7.8: METC versus polling method, cache option, complete poll option and initial mesh

All in, an appropriate compromise between speed of convergence and performance is achieved with a swarm size of two hundred and the equal relative weight ( $c1 = c2$ ) is the most convenient option.

### 7.2.5 Setting parameters of simulated annealing (SA)

The temperature and annealing functions determine the performance of SA (manual [MATLAB Global Optimization Toolbox 2019](#)). The temperature function defines the reduction of the temperature along optimization and thus the decreasing probability of accepting worse candidates. The following temperature functions are investigated:

- Exponential:  $T = T_0 0.95^{K_t}$
- Boltzmann:  $T = T_0 / \ln(K_t)$
- Fast:  $T = T_0 / K_t$

Where  $T_0$  is the initial temperature and  $K_t$  is the annealing parameter.

The annealing function generates new points for next iterations in function of the step length and search direction. Two options are taken into consideration: fast function where the step length is proportional to the temperature and Boltzmann where the step length is proportional to the square of the temperature.

Thus, there are six combinations of parameters which are repeated in twenty-five optimizations.

In figure 7.7, it is observed that the fast temperature function provides the lowest mean and scattering of METC. The Boltzmann annealing function results the lowest mean of METC while the scattering is similar. The exponential temperature function provides the highest mean of MBO although the scattering is high. The Boltzmann annealing function presents higher mean and scattering of the MBO than the fast annealing function.

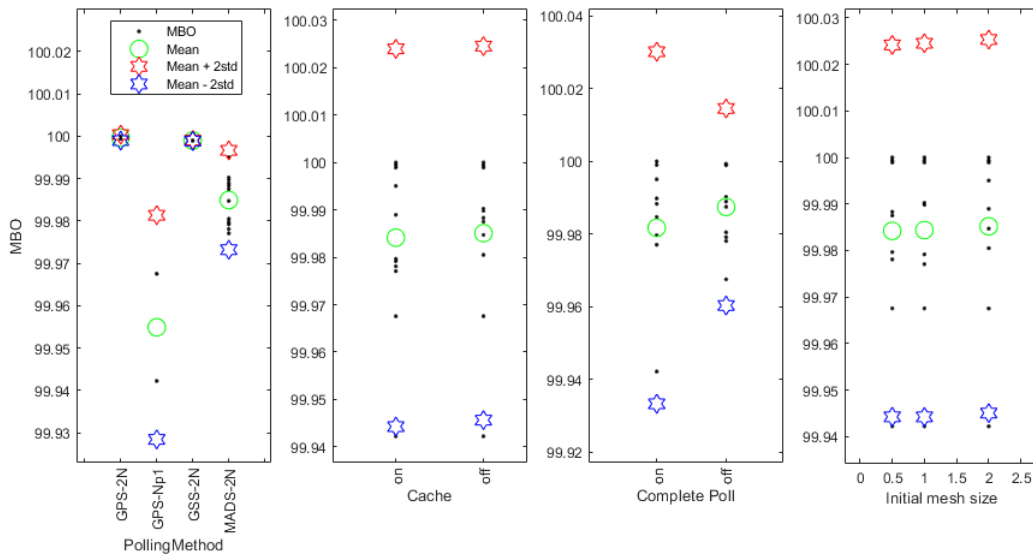


FIGURE 7.9: MBO versus polling method, cache option, complete poll option and initial mesh

### 7.2.6 Setting parameters of pattern search (PS)

The performance of PS depends on several optional parameters. The polling method determines the pattern to be added to the current point to generate new candidates. The methods denominated *GPS-2N*, *GPS-Np1*, *GSS-2N* and *MADS-2N* are investigated (manual [MATLAB Global Optimization Toolbox 2019](#)). By enabling option *cache* the algorithm keeps information of past polls and avoids searching near points already polled. Besides, with the *CompletePoll* option the algorithm completes the poll around the current point with the given pattern although a better point is found. Finally, the initial mesh sizes of 0.5, 1 and 2 are taken into consideration. Therefore, there are forty-eight combinations which are repeated in twenty-five optimizations each.

Regarding METC presented in figure 7.8, no significant impact is found when changing the initial mesh or the option *Cache*. Polling method *GPS-Np1* provides the higher METC while other polling methods show similar performance. The option of not completing the poll is beneficial to reduce the mean and scattering of METC.

Regarding MBO shown in figure 7.9, only the polling method shows importance. Methods *GPS-2N* and *GSS-2N* provide the highest mean of MBO with very low scattering.

### 7.2.7 Setting parameters of gradient based algorithm (GB)

Three gradient based algorithms are included under the function *fmincon* of (manual [MATLAB Optimization Toolbox 2019](#)): *interior-point*, *sqp* and *active-set*. Detailed information of the fundamentals is available in (manual [MATLAB Optimization Toolbox 2019](#)). The type of algorithm is contemplated in this analysis. Moreover, six step sizes are inspected. Therefore, eighteen combinations are tested, each one is repeated in twenty-five optimizations.

Figure 7.10 shows that *sqp* provides the lowest mean and scattering of METC. A step size equal or lower than  $1e-2$  is recommendable to avoid a high mean and scattering of the METC. With respect to MBO, a lower value than  $1e-2$  is suitable to

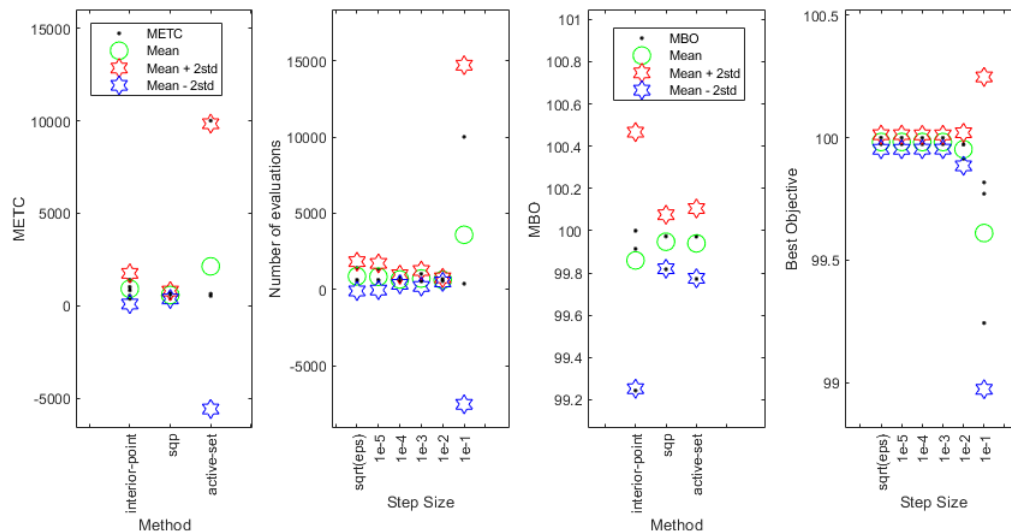


FIGURE 7.10: METC versus method (a) and step size (b). MBO versus method (c) and step size (d)

achieve a high MBO. sqp and active-set algorithms provide higher mean and lower scattering than interior-point.

In table 7.4, the recommended options that are obtained from the previous analyses are summarized.

TABLE 7.4: Summary of recommended algorithm options

Algorithm	Options
GA	Population size: 200. Cross-over function: scattered
PSO	Swarm size: 200. Relative weight: equal
SA	T <sup>n</sup> function: Boltzmann, Annealing function: Boltzmann
PS	Polling method: GPS-2N, Complete Poll: off
GB	Algorithm: sqp, step size: <1e-2

TABLE 7.5: Summary of optimizations of scenario A

id	Algorithm	Code	Initial point	AEP initial (%)	Evaluations	Time (h)	Parallel pools	AEP (%)
A1	GA	AGORA	None	*	60800	45	24	101.7
A2	NM	AGORA	DTU 10MW RWT	100.0	1017	11.5	0	101.6
A3	NM	AGORA	Poor	96.5	2495	24.5	0	99.7
A4	PS	AGORA	Poor	96.5	11122	12.5	24	101.7
A5	GB	AGORA	Poor	96.5	858	3.3	38	101.3
A6	GA	Surrogate	Poor	96.5	55000	«0.1	38	100.6
A7	PSO	AGORA	None	*	18205	14	38	101.8
A8	NM	AGORA	A7 solution	101.8	641	6	0	101.8
A9	SA	AGORA	Poor	96.5	11980	114	0	100.7

### 7.3 Optimization scenarios

In this section, several optimization scenarios are contemplated. Each scenario consists of several optimizations denominated cases that share the same statement but which are performed with different algorithms or initial points.



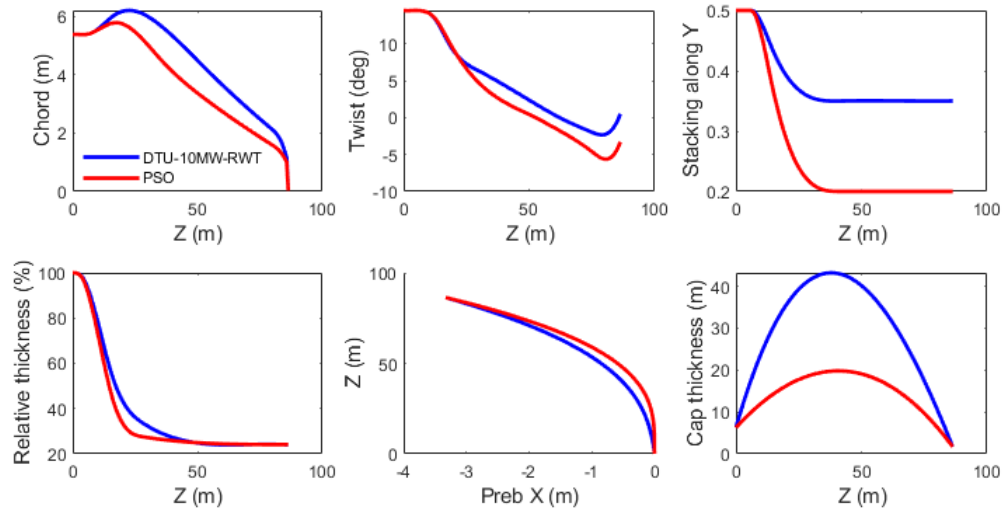


FIGURE 7.11: Spanwise distributions of A7 optimization (PSO) and DTU 10MW RWT

### 7.3.1 Scenario A

In this scenario a mono-objective unconstrained optimization problem is contemplated. The objective function is the maximization of the AEP as equation 7.1 states. This scenario represents the statement of the traditional design process described in section 1.4 for determining the geometry of the blade. Considerations regarding loads, structural integrity or others are not taken into account.

$$\text{Find } X = \left\{ \begin{array}{c} x_1 \\ x_2 \\ x_3 \\ \vdots \\ x_{22} \end{array} \right\} \text{ which maximizes AEP} \quad (7.1)$$

Table 7.5 shows a description of the optimization cases and results. The initial points of the optimizations are presented. The optimization cases A1 and A7, performed with GA and PSO respectively, do not require a starting point specified by the user. The starting point denominated as *Poor* in table 7.5 corresponds to a low AEP design with -3.5% with respect to DTU 10MW RWT. The number of evaluations, total time and number of parallel polls (calculations in parallel with different computer cores) are included in the table. NM and SA algorithms do not permit the calculation in parallel.

The best solution is provided by PSO optimization (case A7) with 101.8% of AEP more than DTU 10MW RWT. Figure 7.12 shows the ratio of AEP for different mean annual wind speeds. GA (case A1) and PS (case A4) provide similar AEP (101.7%). NM achieves only 99.7% when starting from *poor* initial point (case A3). Nevertheless, the resultant AEP is 101.6% when the initial point is DTU 10MW RWT (case A2) thus the sensitivity to the initial point is high in NM algorithm. GB achieves a 101.3% when starting from the *poor* initial point (case A5). SA provides a 100.7% starting from *poor* start (case A9). NM is also run in case A8 from the solution of



PSO (case A7) with the aim of improving the best solution found but no improvement is achieved in the solution with respect to the initial point. In case A6, instead of *AGORA*, a surrogate quadratic model is employed to evaluate the objective function and with GA as algorithm. The AEP of the solution in case A6 is calculated with *AGORA* resulting a 100.6%. The differences of this case with respect to case A1 performed also with GA are due to the inaccuracies of the surrogate quadratic model.

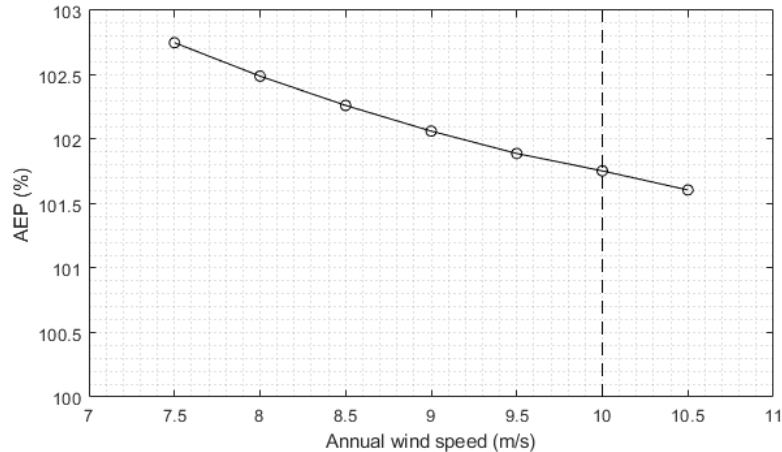


FIGURE 7.12: Ratio of AEP in function of the mean annual wind speed of case A7 solution.

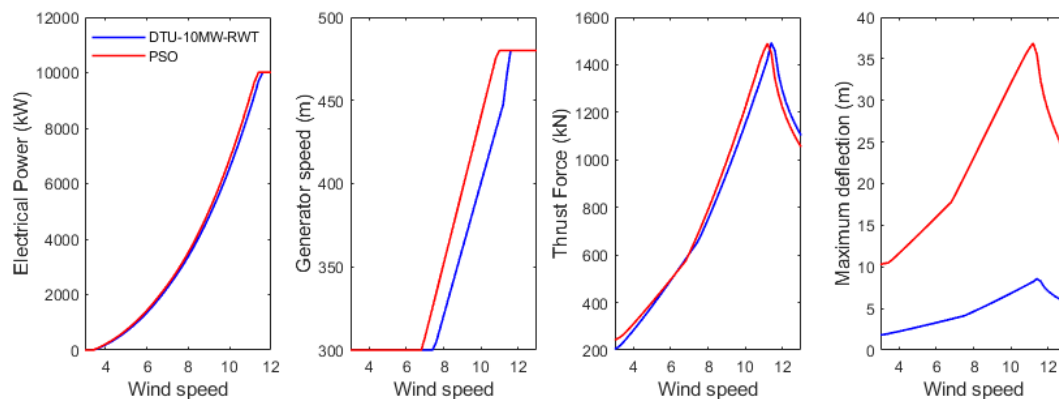


FIGURE 7.13: Electrical power, generator speed, maximum thrust force and maximum tip deflection of A7 optimization and DTU 10MW RWT

Figure 7.11 presents spanwise laws and spar cap thickness of case A7 solution in conjunction with those of DTU 10MW RWT and figure 7.13 compares the basic performance of both. The algorithm has found a solution with a very low chord and lower twist angles which correspond to high operating angles of attack in the blade. The resulting relative thickness is as low as possible taking into account the design variables boundaries. The 24.1% master airfoil is the prevailing one along span. The rotational speed as result of the *gain\_tsr* obtained is higher than DTU 10MW RWT.

The maximum thrust is similar as DTU 10MW RWT, however the maximum deflection is extremely high (37 m) and not acceptable in a real design case as would

cause a catastrophic collision with the tower. This result reveals that more features should be taken into account in the problem. At least, it is necessary to contemplate a constraint about the maximum deflection. The flexibility of the blade can be reduced by modifying the geometry or by increasing the thickness of the spar cap which implies an increase of the mass (and cost) of the blade. In the scenario B, the trade-off between blade mass and AEP is assessed under a constraint of maximum deflection that should be respected.

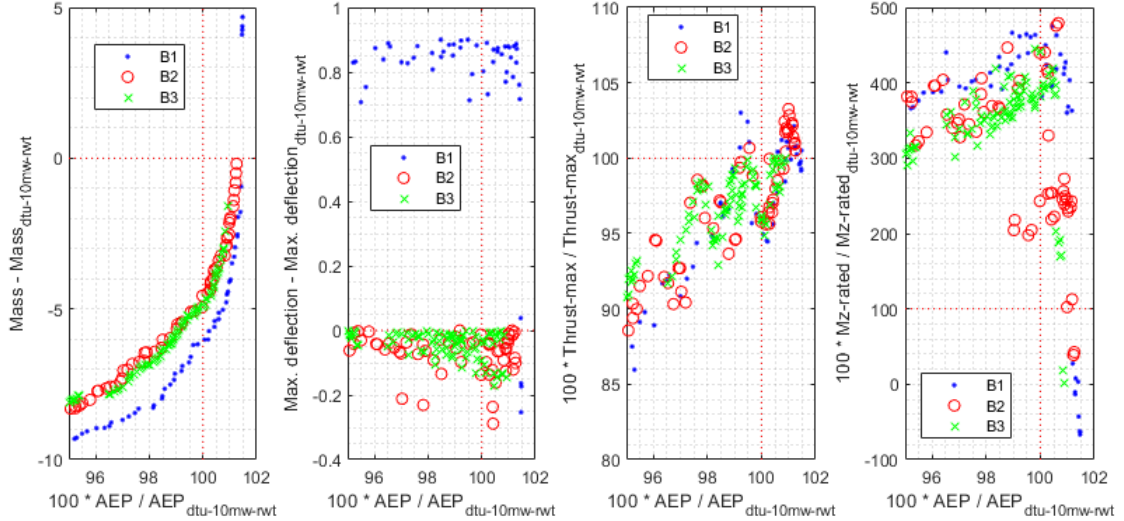


FIGURE 7.14: Pareto points: Blade mass versus AEP, maximum blade tip deflection versus AEP, maximum thrust versus AEP and Mz at rated wind speed versus AEP

### 7.3.2 Scenario B

In this scenario a bi-objective constrained optimization problem is contemplated. The objective function is stated in equation 7.2.

$$\text{Find } X = \left\{ \begin{array}{l} x_1 \\ x_2 \\ x_3 \\ \vdots \\ \vdots \\ x_{22} \end{array} \right\} \text{ which minimizes blade mass \& maximizes AEP} \quad (7.2)$$

Regarding the constraints, three options are taken into consideration. Optimization case B1 presents one constraint that restricts maximum deflection  $dxs_{tip\_max}$  according to equation 7.3 with an allowable margin of 1 m with respect to the maximum deflection of DTU 10MW RWT. Optimization B2 tightens the constraint according to equation 7.4. Optimization B3 includes an additional constraint of maximum thrust  $fxs_{yaw\_max}$  according to equation 7.5.

$$dxs_{tip\_max} \leq dxs_{tip\_max_{rwt}} + 1 \quad (7.3)$$

$$dxs_{tip\_max} \leq dxs_{tip\_max_{rwt}} \quad (7.4)$$

$$\begin{aligned} dxs\_tip\_max &\leq dxs\_tip\_max_{rwt} \\ fxs\_yaw\_max &\leq fxs\_yaw\_max_{rwt} \end{aligned} \quad (7.5)$$

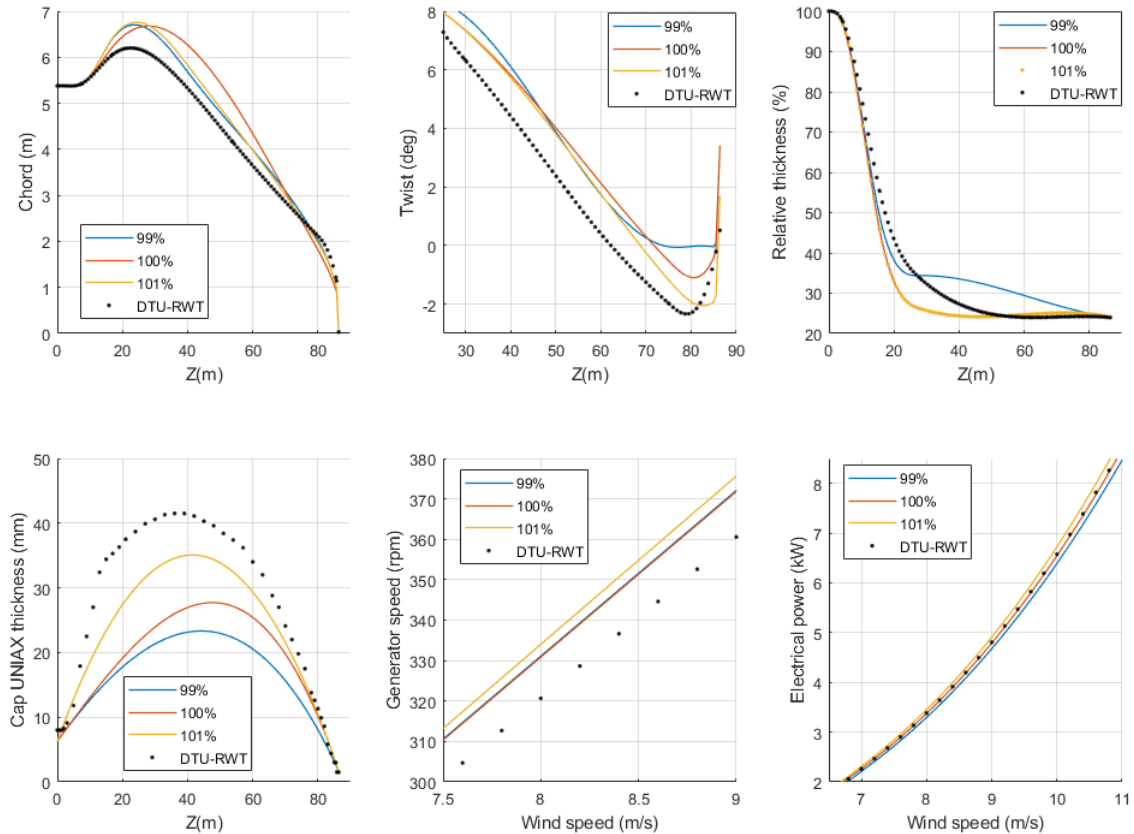


FIGURE 7.15: Spanwise laws and main performance of B3 pareto points with AEP 99%, 100% and 101%.

GA is employed for the optimizations of the scenario B. Figure 7.14 presents several plots for the pareto designs of cases B1, B2 and B3 optimizations. The values of the pareto are included as increments of mass and ratio of AEP with respect to DTU 10W RWT. Accordingly, the features of DTU 10W RWT correspond to increment of mass = 0 and AEP = 100. The AEP versus mass plot shows that it is possible to achieve less mass with the same AEP as DTU 10W RWT or more AEP with the same mass in the pareto solutions of cases B1, B2 and B3. The plots also show that constraints of maximum blade tip deflection and maximum thrust are respected in the three optimizations. The non-constrained torsional moment  $M_z$  exceeds significantly the value of DTU 10W RWT in most of pareto points of the three cases.

In figure 7.15 the spanwise distributions and main performance of three B3 pareto designs with 99%, 100% and 101% of AEP are compared with DTU 10MW RWT. Chord and twist distributions of these solutions are higher. In 100% and 101% AEP points, the prevailing airfoil is the 24.1% relative thickness airfoil. Nevertheless, the 99% solution presents thicker airfoils. The algorithm proposes lower spar cap thickness distributions than DTU 10MW RWT to minimize blade mass. The rotational speed is higher in all cases.

At this point, by inspecting the pareto front it is revealed that DTU 10MW RWT design is not in the pareto front. Besides, if an additional constraint that estimates

the general loading level such as the maximum thrust is incorporated, the pareto front is not significantly affected as the comparison of pareto fronts of B2 and B3 reveals. However, figure 7.14 presents the maximum  $Mz$  moment (torsional) in blade root which determines the necessary pitch actuation moment at rated power. The figure reveals the high increment with respect to DTU 10MW RWT of the most of pareto front solutions that in fact would lead to a not acceptable solution. Furthermore, several solutions of the pareto front present a high maximum chord ( $>6.5$  m) which in reality is not acceptable due to transportation considerations. These results indicate that the statement of scenario B is not covering sufficiently all the design requirements and more elements should be added in the statement.

### 7.3.3 Scenario C

The scenario C is a mono-objective and high constrained optimization problem with the statement presented in equation 7.6. This scenario represents a realistic optimization case where the objective function is the blade mass. Six constraints are incorporated in the problem. The AEP is considered as a constraint that should be at least equalized. The AEP of DTU 10MW RWT is set as the minimum permissible limit. The blade stiffness should be sufficient to avoid an excessive maximum blade tip deflection ( $dxs\_tip\_max$ ) that would cause the collision with tower. The  $dxs\_tip\_max$  of DTU 10MW RWT is defined as limit. Besides, excessive longitudinal strains in the spar cap should be avoided thus a maximum value is defined as allowable limit. Regarding maximum thrust force constraint, same threshold value as used in the design of DTU 10MW RWT is employed as restriction (1500 kN). The maximum chord is usually restricted due to transportation issues. In this scenario chord lengths higher than 6.2 m (maximum chord in DTU 10MW RWT) are not allowed. Finally, the torsional moment  $Mz$  in root ( $mzs\_rated$ ) in rated wind speed is restricted to 127.5 kN in order to avoid excessive pitch actuation force. As proceeded in previous scenarios, the objective function (blade mass) is provided as a relative incremental value with respect to DTU 10MW RWT.

$$\text{Find } X = \left\{ \begin{array}{c} x_1 \\ x_2 \\ x_3 \\ \cdot \\ \cdot \\ x_{22} \end{array} \right\} \text{ which minimizes blade mass}$$

s.t. (7.6)

$$\left\{ \begin{array}{l} (1) AEP \geq AEP_{rwt} \\ (2) dxs\_tip\_max \leq dxs\_tip\_max_{rwt} \\ (3) fxs\_yaw\_max \leq fxs\_yaw\_max_{rwt} \\ (4) maximumChord \leq MaximumChord_{rwt} \\ (5) mzs\_rated \leq 127.5kN \\ (6) \epsilon_{cap} \leq 3000 \end{array} \right\}$$

Table 7.6 summarizes the performed optimizations with the main characteristics and results. In this scenario, three initial points are set according to the following process:

A point is selected from B3 pareto front. The point does not respect constraints of maximum chord and maximum longitudinal strains. However, it is set as initial point in the optimizations C4 and C6.

Furthermore, this non-feasible point is modified to reach the feasible design space with no care in the result of the objective function. Accordingly, the initial point employed in C3, C5, C7, C8 and C11 is a feasible design with a poor value of the objective function (+11.2 Tn).

For the C9 optimization, a different feasible starting point is chosen with an improved value of the objective function (+6 Tn).

Finally C1 and C10 optimizations do not require an initial point due to the nature of the algorithms.

Case C2 is set as a two step optimization. At first, a search of a feasible initial population with GB algorithm is performed and later GA is launched. However, GB algorithm does not achieve to create a feasible initial population and the optimization is stopped with no successful solution.

TABLE 7.6: Summary of optimizations of scenario C

id	Algorithm	Initial point	Mass initial (Tn)	Evaluations	Time (h)	Parallel pools	Feasibility	Mass (Tn)
C1	GA	None	*	29387	44	15	No	-8.2
C2	GB +GA	None	*	21686	18	24	No	-10.4
C3	PS	Feasible	11.2	13238	24	36	Yes	-1.5
C4	PS	Non-feasible	-1.2	2157	11	32	No	-1.2
C5	GB	Feasible	11.2	1175	4	15	No	-3.4
C6	GB	Non-feasible	-1.2	158	0.4	32	No	-5.1
C7	GB	Feasible	11.2	273	1.5	32	Yes	-1.6
C8	NM	Feasible	11.2	1230	10	1	Yes	8.9
C9	NM	Feasible	6.0	1170	9	1	Yes	-1.4
C10	PSO	None	*	11330	17	32	No	-12
C11	SA	Feasible	11.2	2660	24	1	Yes	-2.2

The results summarized on table 7.6 reveal the following conclusions:

- Global algorithms GA and PSO are not able to find any feasible solution (cases C1 and C10).
- The feasibility of the starting point is very relevant. PS and GB do not find a feasible solution if the starting point is non-feasible (cases C4 and C6). Other algorithms such as NM and SA can not even be employed without providing a feasible starting point.
- PS, NM and SA provide a feasible solution if the supplied initial point is feasible (cases C3, C8 and C11 respectively). PS and SA find a solution with less mass than DTU 10MW RWT (-1.5 Tn and -2.2 Tn respectively). With the same starting point as C3 and C8, NM provides a poor feasible solution of +8.9 Tn (case C8). Nevertheless, when starting from a feasible point with an improved objective function (case C9), the solution found by NM improves significantly (-1.4 Tn).
- GB provides a non-feasible solution even when supplied with a feasible starting point (case C5). To overcome this issue, in case C7, the magnitudes of the constraints are scaled to increase significance of constraints with respect to objective function. With this modification, the algorithm finds a feasible solution resulting a bladed mass of -1.6 Tn.

All in, the search of feasible points to initiate the optimization is fundamental to obtain a feasible solution. PS and SA achieve a significant improvement even when

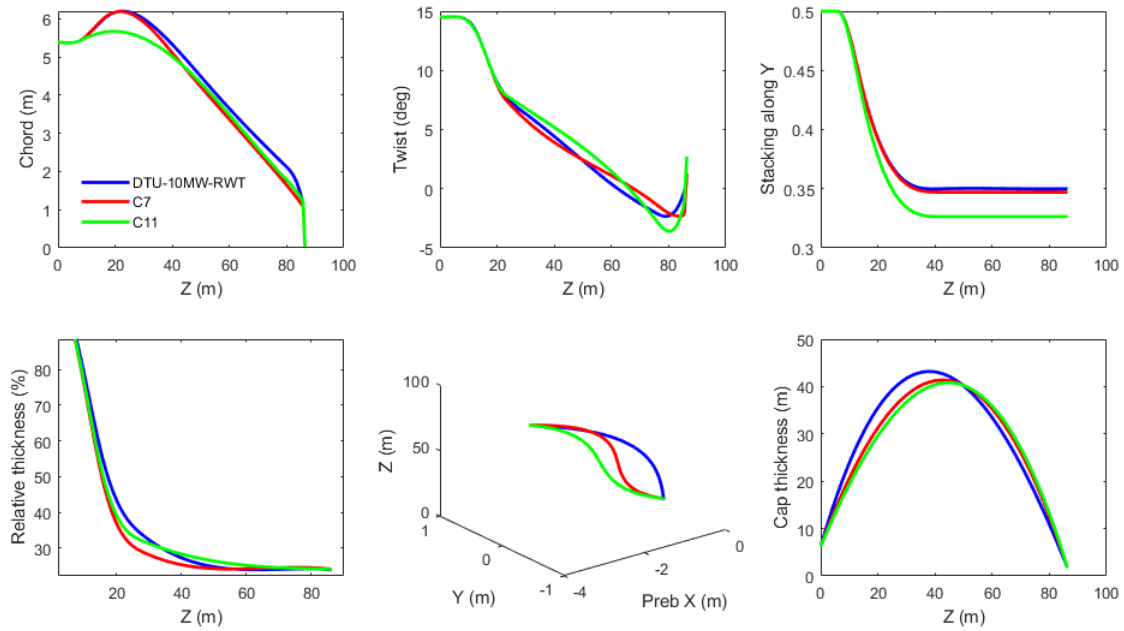


FIGURE 7.16: Spanwise distributions of DTU 10MW RWT, solution of C7 and solution of C11

initiating the optimization from a feasible point far from the optimum. The solution of NM is highly sensitive to the objective value of the initial feasible point. Finally, GB do not ensure feasibility of the solution, the suitable scaling of the constraints with respect to the objective function helps to find a feasible solution.

Figure 7.16 compares spanwise distributions of successful optimizations C7 and C11 with respect to DTU 10MW RWT. Both optimizations provide distributions with significant differences between them and with respect to DTU 10MW RWT. The resulting chord distributions of C7 and C11 are lower than DTU 10MW RWT. Twist angles are generally higher meaning lower operating angles of attack. The spar cap thickness distributions are lower in C7 and C11. The maximum spar cap thickness is displaced towards tip.

In spite of the differences found between solutions of cases C7 and C11, the performance in terms of AEP, maximum tip deflection and maximum thrust is similar between them as figure 7.17 shows. However, the solutions from C7 and C11 operate at higher rotor speeds in the variable speed area.

This scenario has demonstrated that a solution with less mass and same AEP than DTU 10MW RWT while respecting the important constraints is obtained. Nevertheless, the surface fairness of the solution is not assessed and this aspect can invalidate an a priori successful solution. Figure 7.18 shows the blade surface of DTU 10MW RWT and solution of case C11 which resulted the best objective function in all scenario C. The color map represents the isoparametric longitudinal curvature  $k_v$ .

### 7.3.4 Scenario D

The solution of case C11 that provided the lowest blade mass in previous scenario is inspected in terms of surface fairness. The color map of spanwise isoparametric curvature  $k_v$  in figure 7.18 reveals a zone between  $z = 15$  m and  $z = 20$  m with high absolute values that invalidates the suitability of the solution provided. The high



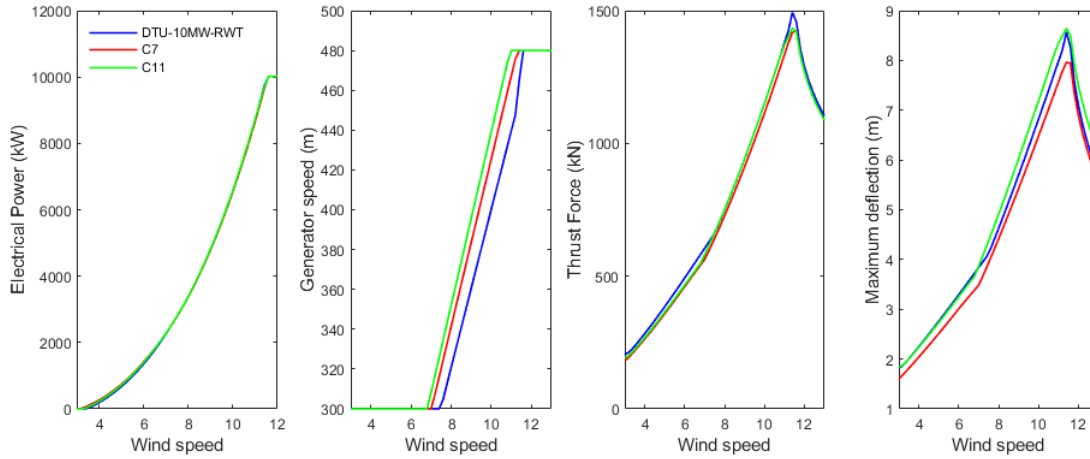


FIGURE 7.17: Performance of DTU 10MW RWT, solution of C7 and solution of C11: electrical power, generator speed, thrust force and maximum blade tip deflection.

curvatures in this span zone are also visible in the DTU 10MW RWT but with lower magnitude. As these high curvature values should be reduced, the maximum of them is set as objective function to be minimized in this scenario. This is a highly realistic case where the detailed inspection of the solution shows that a potential successful solution requires to be modified. In the optimization statement, the blade mass is incorporated to the list of constraints. The constraint values are relaxed with respect to scenario C as the statement in equation 7.7 shows. PS is the selected algorithm for the optimization.

$$\text{Find } X = \begin{pmatrix} x_1 \\ x_2 \\ x_3 \\ \cdot \\ \cdot \\ x_{22} \end{pmatrix} \text{ which minimizes } \max(k_v)$$

s.t.

(7.7)

$$\left\{ \begin{array}{l} (1) AEP \geq AEP_{rwt} * 0.99 \\ (2) dxs_{tip\_max} \leq dxs_{tip\_max_{rwt}} * 1.1 \\ (3) fxs_{yaw\_max} \leq fxs_{yaw\_max_{rwt}} * 1.05 \\ (4) MaximumChord \leq MaximumChord_{rwt} \\ (5) mzs_{rated} \leq 134 \text{ kN} \\ (6) \epsilon_{cap} \leq 3150 \\ (7) Mass \leq Mass_{rwt} - 0.5 Tn \end{array} \right\}$$

The algorithm found a feasible solution after 10120 evaluations and nine hours of computation. The maximum absolute value of  $k_v$  is decreased a 41% with respect to solution of scenario C. The solution fulfills all the constraints of the problem. Figure 7.19 shows the initial  $k_v$  surface and the resulting surface of scenario D where the reduction of curvature  $k_v$  is evident according to the color map. Only span length between  $z = 10 \text{ m}$  and  $z = 25 \text{ m}$  is included in the figure.

This scenario has described a typical issue that appears in the last stages of the

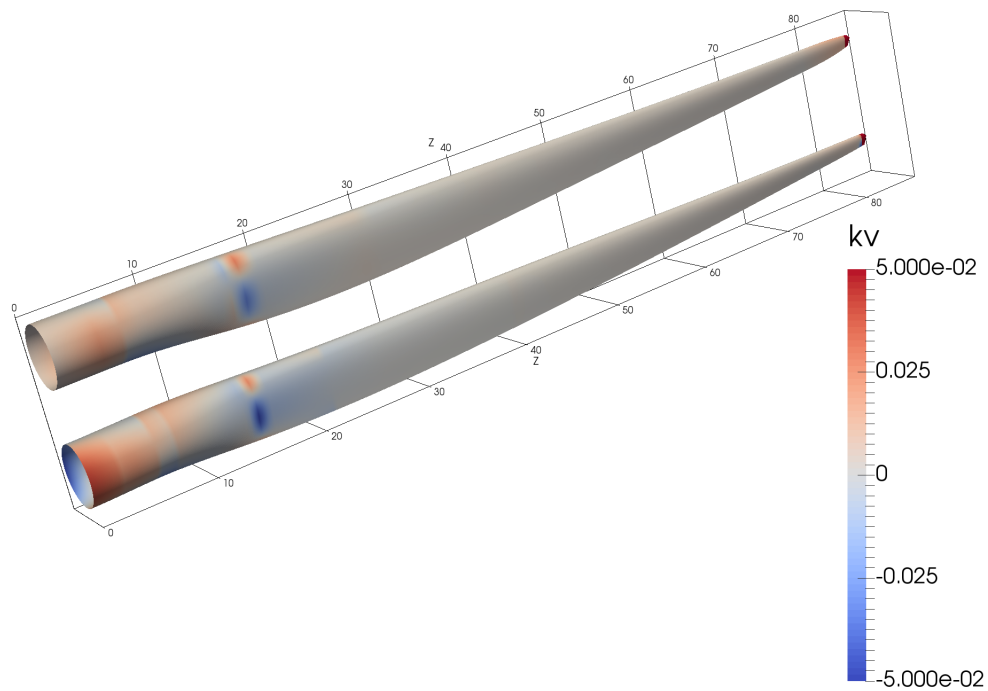


FIGURE 7.18: Surface of DTU 10MW RWT (upper surface) and C11 solution (lower surface). Color map represent longitudinal curvatures  $k_v$

traditional design process. The design process proposed in this thesis, that incorporates the surface interrogation in conjunction with other multidisciplinary features, permits to address the problem of lack of surface fairness efficiently avoiding time consuming trial and test loops based on the experience and intuition of the designers.



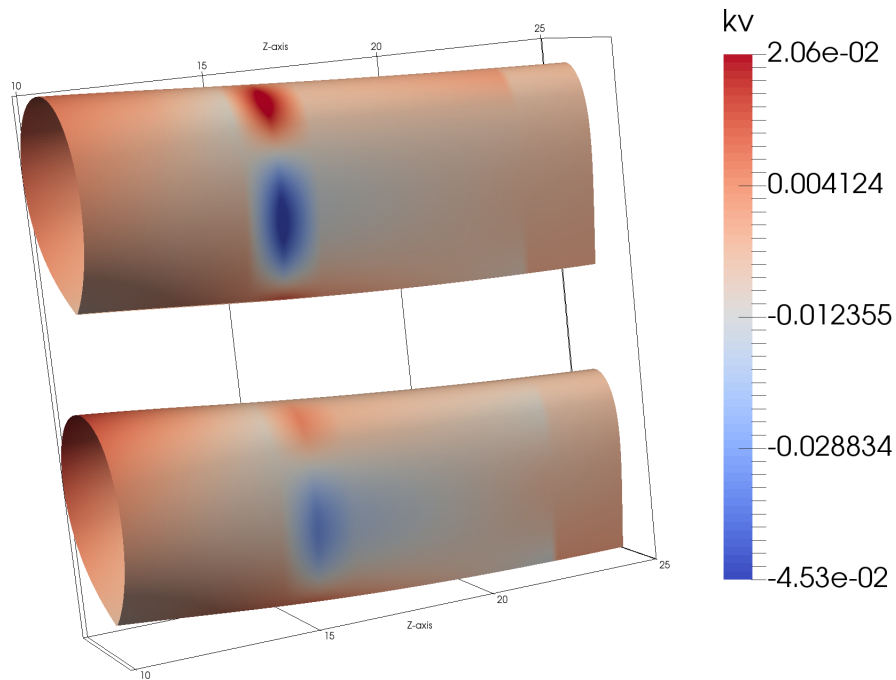


FIGURE 7.19: Surface between  $z= 10\text{m}$  and  $z= 25\text{m}$  of C11 solution (upper surface) and solution of scenario D (lower surface). Color map represent longitudinal curvatures  $k_v$



## Chapter 8

# Conclusions

This section assesses the compliance of the thesis objectives stated in section 1.6, summarizes the main conclusions and indicates future research.

Regarding the first thesis objective, the author has developed successfully a blade design process described in chapter 3 with an important core stage of optimization. The optimization is able to contemplate the interactions between different technical fields involved in the design (blade geometry design, main structural layout design, control, loads and acoustic emission).

The second thesis objective is fulfilled with the development of *AGORA*. The code couples aerodynamic, structural, aeroelastic, and aeroacoustic subordinate codes in order to calculate the potential objective functions and constraints that may be set in the blade design phase. The code is run with a reasonable computational cost and thus is able to be included as calculation engine in the optimizations. The evaluation of the objective function and constraints with the basis of steady aeroelastic simulations is performed in less than one minute. The optimization frame is flexible enough to respond under different optimization statements as result of non compliance points detected in the verification phase (excessive loads and/or deflections, low energy yield, transportation constraints, low surface fairness,...).

Moreover, the optimization is conceived as a global unique problem where all the design variables that belong to different technical fields are designed together at the same level without prior assumptions. Consequently, for example, the blade does not have to provide a maximum power coefficient  $C_p$ . The design variables are calculated with the aim of optimizing the objective function and fulfill the constraints.

With respect to the third thesis objective, the geometry source distributions (airfoils and spanwise laws) and the blade surface are successfully represented as B-splines. This approach provides an important advantage as avoids the representation of the blade geometry as a hull of points. The complex work in CAD to approximate points by a surface is not anymore needed. The uncertainties of the results due to the difference between the points and the approximating surface are therefore removed.

The fourth thesis objective is accomplished by performing several investigations that reveal the important design variables in the blade design. The curse of dimensionality phenomenon states that the increase of number of design variables involves a dramatic increment of the number of evaluations of the objective function to get the convergence and a decrease of the probabilities of achieving the optimum. To deal with this aspect in chapter 4 the most suitable configuration of B-splines to design airfoils in terms of number of control points and type of parametrization is evaluated by statistical techniques concluding that thirteen control points and the

centripetal parametrization is a suitable choice. More complex configurations of B-splines would not explore more extensive design space but in contrast would extend significantly the time of the optimizations.

Furthermore, the master airfoils and spanwise laws are inspected in chapter 6 to evaluate the impact of the associated design variables in the wind turbine outputs by means of global sensitivity analyses. This type of assessment is novel in the wind energy. The results of multi-variable linear regressions are validated with variance based methods. The main conclusion is that airfoil geometry is relatively much less important than chord and twist distributions. Based on these results, the author decides to fix the geometry of airfoils for next chapters, in spite of the great effort invested in analysis of chapter 4.

In addition, another research is carried out in chapter 6 with steady and dynamic aeroelastic simulations. The visual inspection of the results reveals abnormal dynamic amplifications of loads that should be avoided. Instead of focusing in identifying the type of aeroelastic instability, the objective consists of the avoidance of the phenomenon by identifying the combinations of design variables that are involved. Data analysis techniques such as logistic regression or fast and frugal trees are employed to predict the abnormal phenomenon with a high success rate.

Regarding the fifth thesis objective, chapter 5 deals with the computation of fatigue loads which are in essence computationally expensive in the time domain as requires performing many ten-minute aeroelastic simulations. The use of frequency domain methods is common in the design of other support structures but had not been incorporated in the blade optimization. The conclusion of the chapter states that the frequency domain method is useful in the blade design for some types of loads, the ones with important stochastic nature as the out of plane moments that are mainly influenced by the wind turbulence. The frequency domain method provides an useful direction of design.

In order to accomplish the sixth thesis objective, chapter 7 presents several optimization cases that are representative of real blade designs. A public available wind turbine model is selected to perform the research. Prior to the optimizations, surrogate models are adjusted to predict the outputs under different design variables. Optimizations are run with these surrogate models to infer the most recommendable options of the optimization algorithms. This study would not be affordable with the real optimizations due to the huge amount of necessary time. Subsequently, four optimization scenarios are carried out with *AGORA*. Different types of algorithms are tested. The efficiency of the algorithms changes with the type of scenario and depends highly on the existence of constraints. The last two scenarios present high constrained realistic statements which are not suitable for global algorithms due to their inability to find feasible solutions. Regarding local search, the initial point is strongly recommended to be feasible to achieve a feasible solution. The last scenario shows a blade surface fairness optimization that has to be solved in conjunction with other types of constraints. In the traditional design process this high constrained problem would be solved by many try and test design loops involving a huge time in CAD and in other technical tasks. In addition, the probabilities of finding a feasible solution would be low.

All in, the thesis objectives are achieved. Nevertheless, several aspects of this thesis require of further research. The mass is an important feature that indicates the blade cost. However, a detailed cost model that incorporates the cost of the materials, the manufacturing process, considerations regarding logistics and other detailed aspects would be beneficial in order to design blades that minimize the cost of energy. Besides, the coupling of more sophisticated codes such as CFD for calculating

the aerodynamics could increment the precision of the results but requires of important research effort due to the huge computational cost. Similar issue happens with the cross sectional structural properties calculation. More sophisticated and precise tools require high computational cost and thus important research work is needed in order to accomplish a reasonable optimization time.



## Appendix A

# Open inputs of AGORA

## A.1 Geometrical inputs

### A.1.1 Spanwise laws

- Blade length [ $m$ ]  $L$
- Chord knots [ $adim$ ]  $cknots$
- Chord coefficients [ $m$ ]  $ccoefs$
- Twist knots [ $adim$ ]  $tknots$
- Twist coefficients [ $rad$ ]  $tcoefs$
- Relative thickness knots [ $adim$ ]  $tcknots$
- Relative thickness coefficients [%]  $tccoefs$
- Thickness knots [ $adim$ ]  $eknots$
- Thickness coefficients [ $m$ ]  $ecoefs$
- Prebending knots [ $adim$ ]  $pknots$
- Prebending coefficients along X [ $m$ ]  $pcoefs_1$
- Prebending coefficients along [ $m$ ]  $pcoefs_2$
- Stacking law along Y axis knots [ $adim$ ]  $sry_knots$
- Stacking law along Y axis coefficients [ $.$ ]  $sry_coefs$
- Stacking law along X axis knots [ $adim$ ]  $srx_knots$
- Stacking law along X axis coefficients [ $.$ ]  $srx_coefs$
- Master airfoil knots [ $adim$ ]  $air_knots$
- Master airfoil coefficients along X [ $adim$ ]  $air_coefs1$
- Master airfoil coefficients along Y [ $adim$ ]  $air_coefs2$
- Span length of root cylinder [ $adim$ ]  $cyl_zd$

### A.1.2 Master airfoils

- Array of mixing law [%]  $master\_mix$
- MATLAB structure containing B-splines of master airfoils  $master\_S$
- Airfoil labeling for polar curve assignment in BLADED [%]  $assign\_label$
- Foil number for polar curve assignment in BLADED  $assign\_foil$

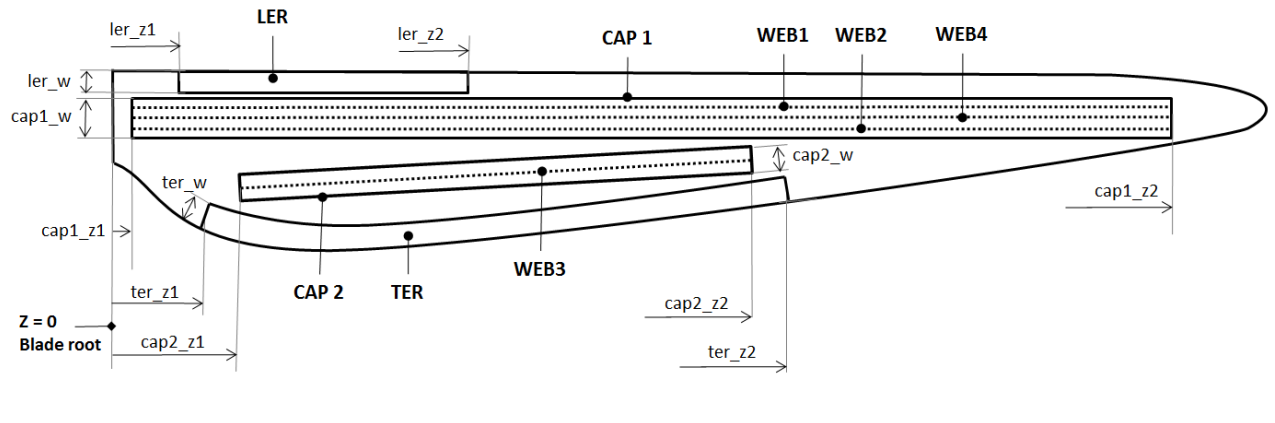


FIGURE A.1: Main structural components.

## A.2 Structural inputs

### A.2.1 Skin 1

- Skin 1 starting span [adim]  $skin\_z1$
- Skin 1 end span [adim]  $skin\_z2$
- Skin 1 number of laminae in suction side (1/2) [num]  $skins\_e$
- Skin 1 number of laminae in pressure side (1/2) [num]  $skinp\_e$
- Material of skin 1  $skin\_mat$
- Skin 1 lamina thickness [m]  $skin\_th$

### A.2.2 Skin2

- Skin 2 starting span [adim]  $skin2\_z1$
- Skin 2 end span [adim]  $skin2\_z2$
- Skin 2 number of laminae in suction side (1/2)  $skin2s\_e$
- Skin 2 number of laminae in pressure side (1/2)  $skin2p\_e$
- Material of skin 2  $skin2\_mat$
- Skin 2 lamina thickness [m]  $skin2\_th$



### A.2.3 Skin3

- Skin 3 starting span [*adim*] *skin3\_z1*
- Skin 3 end span [*adim*] *skin3\_z2*
- Skin 3 number of laminae in suction side (1/2) *skin3s\_e*
- Skin 3 number of laminae in pressure side (1/2) *skin3p\_e*
- Material of skin 3 *skin3\_mat*
- Skin 3 lamina thickness [*m*] *skin3\_th*

### A.2.4 Skin4

- Skin 4 starting span [*adim*] *skin4\_z1*
- Skin 4 end span [*adim*] *skin4\_z2*
- Skin 4 number of laminae in suction side (1/2) *skin4s\_e*
- Skin 4 number of laminae in pressure side (1/2) *skin4p\_e*
- Material of skin 4 *skin4\_mat*
- Skin 4 lamina thickness [*m*] *skin4\_th*

### A.2.5 Root 1

- Root 1 end span [*adim*] *root1\_z1*
- Root 1 number of laminae *root1\_e1*
- Root 1 number of laminae *root1\_e2*
- Root 1 offset beginning of span [*m/layers*] *root1\_of f1*
- Root 1 offset end of span [*m/layers*] *root1\_of f2*
- Material of root 1 *root1\_mat*
- Root 1 lamina thickness [*m*] *root1\_th*

### A.2.6 Root 2

- Root 2 end span [*adim*] *root2\_z2*
- Root 2 intermediate span [*adim*] *root2\_z3*
- Root 2 number of laminae *root2\_e1*
- Root 2 number of laminae *root2\_e2*
- Material of root 2 *root2\_mat*
- Root 2 lamina thickness [*m*] *root2\_th*
- Root 2 offset [*layers/m*] *root2\_of f*

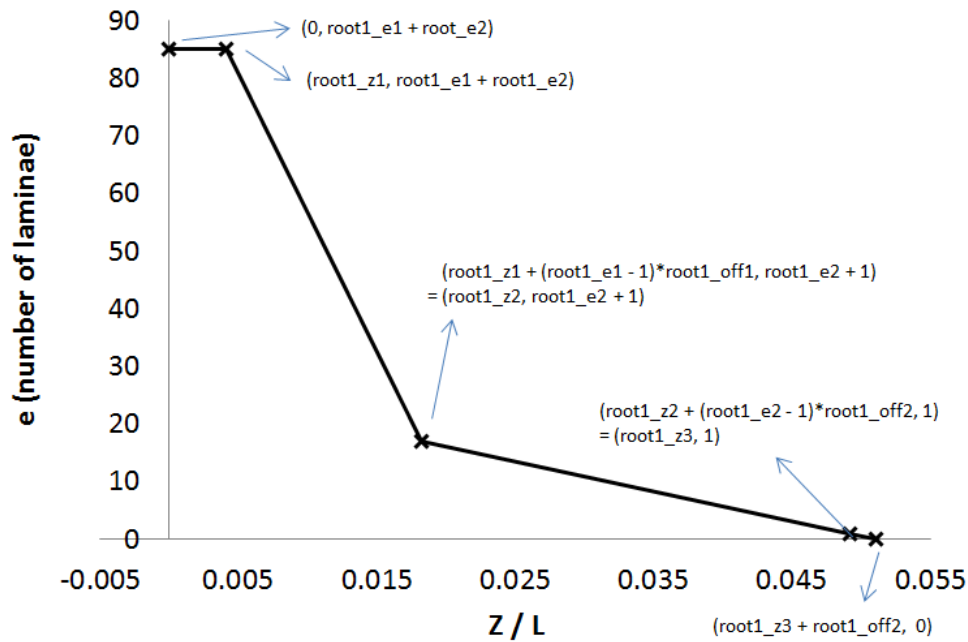


FIGURE A.2: Laminae along span in Root1

### A.2.7 Cap 1

- Cap 1 starting span [dim]  $\text{cap1\_z1}$
- Cap 1 intermediate span in suction side [dim]  $\text{cap1s\_z3}$
- Cap 1 intermediate span in pressure side [dim]  $\text{cap1p\_z3}$
- Cap 1 intermediate span in suction side [dim]  $\text{cap1s\_z4}$
- Cap 1 intermediate span in pressure side [dim]  $\text{cap1p\_z4}$
- Cap 1 maximum allowable ending span [dim]  $\text{cap1\_z2\_max}$
- Cap 1 number of laminae 1 in suction side  $\text{cap1s\_e1}$
- Cap 1 number of laminae 1 in pressure side  $\text{cap1p\_e1}$
- Cap 1 number of laminae 2 in suction side  $\text{cap1s\_e2}$
- Cap 1 number of laminae 2 in pressure side  $\text{cap1p\_e2}$
- Cap 1 number of laminae 3 in suction side  $\text{cap1s\_e3}$
- Cap 1 number of laminae 3 in pressure side  $\text{cap1p\_e3}$
- Material of cap 1  $\text{cap1\_mat}$
- Cap 1 lamina thickness [m]  $\text{cap1\_th}$
- Cap 1 width [m]  $\text{cap1\_w}$
- Cap 1 offset in suction side in beginning span [layers/m]  $\text{cap1s\_of1}$
- Cap 1 offset in suction side in end of span [layers/m]  $\text{cap1s\_of2}$

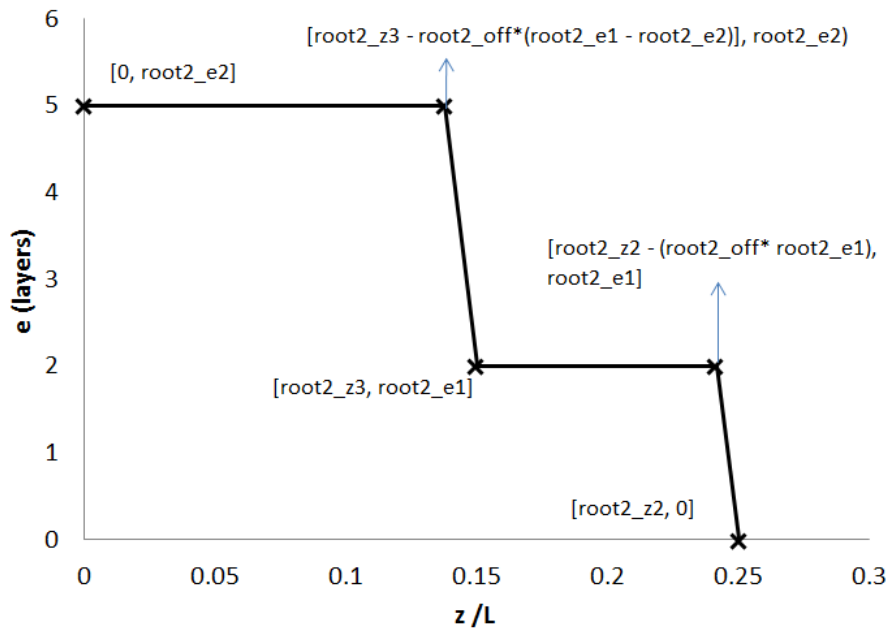


FIGURE A.3: Laminae along span in Root2

- Cap 1 offset in pressure side in beginning span  $[layers/m]$   $cap1p\_off1$
- Cap 1 offset in pressure side in end of span  $[layers/m]$   $cap1p\_off2$

### A.2.8 Cap 2

- Cap 2 starting span  $[adim]$   $cap2\_z1$
- Cap 2 intermediate span in suction side  $[adim]$   $cap2s\_z3$
- Cap 2 intermediate span in pressure side  $[adim]$   $cap2p\_z3$
- Cap 2 intermediate span in suction side  $[adim]$   $cap2s\_z4$
- Cap 2 intermediate span in pressure side  $[adim]$   $cap2p\_z4$
- Cap 2 maximum ending span  $[adim]$   $cap2\_z2\_max$
- Cap 2 number of laminae 1 in suction side  $cap2s\_e1$
- Cap 2 number of laminae 1 in pressure side  $cap2p\_e1$
- Cap 2 number of laminae 2 in suction side  $cap2s\_e2$
- Cap 2 number of laminae 2 in pressure side  $cap2p\_e2$
- Cap 2 number of laminae 3 in suction side  $cap2s\_e3$
- Cap 2 number of laminae 3 in pressure side  $cap2p\_e3$
- Material of cap 2  $cap2\_mat$
- Cap 2 lamina thickness  $[m]$   $cap2\_th$

- Cap 2 width  $[m]$   $cap2_w$
- Cap 2 offset in suction side in beginning span  $[layers/m]$   $cap2s_of f1$
- Cap 2 offset in suction side in end of span  $[layers/m]$   $cap2s_of f2$
- Cap 2 offset in pressure side in beginning span  $[layers/m]$   $cap2p_of f1$
- Cap 2 offset in pressure side in end of span  $[layers/m]$   $cap2p_of f2$

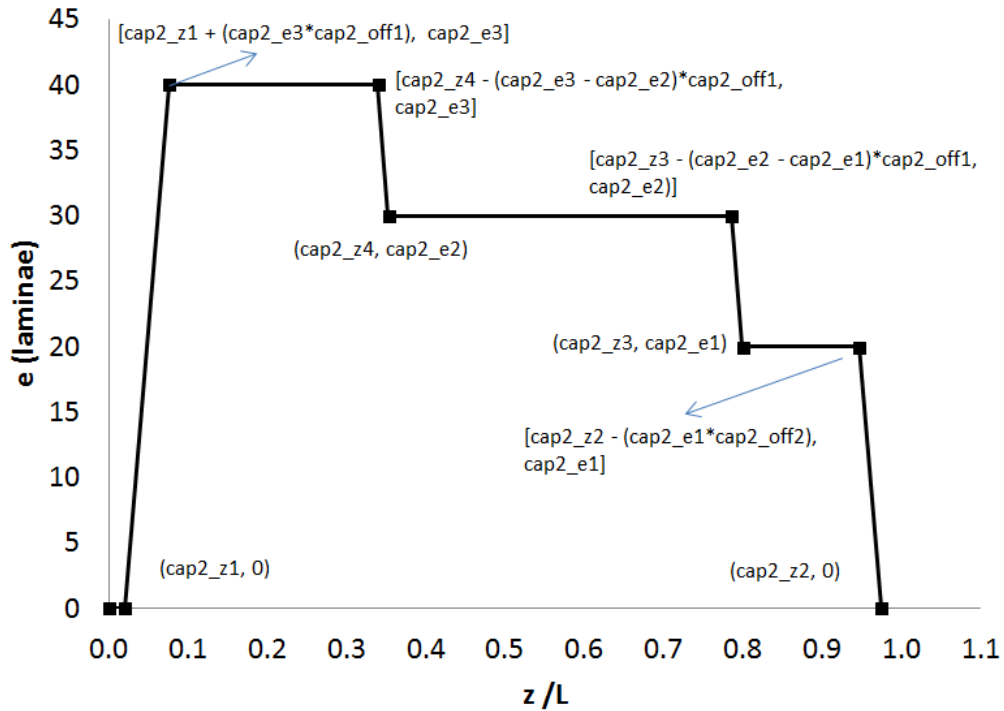


FIGURE A.4: Laminae along span in cap2

### A.2.9 Shear webs

- Web 1 beginning span  $[adim]$   $web1_z1$
- Web 1 end span  $[adim]$   $web1_z2$
- Web 1 number of laminae (1/2)  $web1_e$
- Material of web 1  $web1_mat$
- Distance from cap1 middle line to web1  $[m]$   $web1_d$
- Web 1 lamina thickness  $[m]$   $web1_th$
- Web 2 beginning span  $[adim]$   $web2_z1$
- Web 2 end span  $[adim]$   $web2_z2$
- Web 2 number of laminae (1/2)  $web2_e$

- Material of web 2  $web2\_mat$
- Distance from cap1 middle line to web2 [m]  $web2\_d$
- Web 2 lamina thickness [m]  $web2\_th$
- Web 3 beginning span [adim]  $web3\_z1$
- Web 3 end span [adim]  $web3\_z2$
- Web 3 number of laminae (1/2)  $web3\_e$
- Material of web 3  $web3\_mat$
- Web 3 lamina thickness [m]  $web3\_th$
- Web 4 beginning span [adim]  $web4\_z1$
- Web 4 end span [adim]  $web4\_z2$
- Web 4 number of laminae (1/2)  $web4\_e$
- Material of web 4  $web4\_mat$
- Web 4 lamina thickness [m]  $web4\_th$

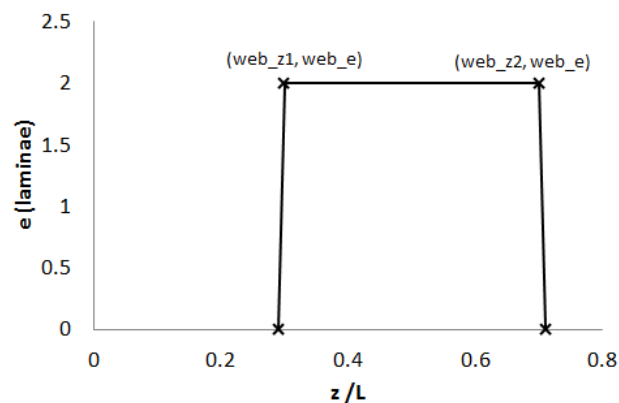


FIGURE A.5: Laminae along span in web

#### A.2.10 Trailing edge reinforcement (TER)

- Trailing edge starting span [adim]  $ter\_z1$
- Trailing edge end span [adim]  $ter\_z2$
- Trailing edge intermediate span in suction side [adim]  $ters\_z3$
- Trailing edge intermediate span in pressure side [adim]  $terp\_z3$
- Trailing edge number of laminae 1 in suction side  $ters\_e1$
- Trailing edge number of laminae 2 in suction side  $ters\_e2$
- Trailing edge number of laminae 1 in pressure side  $terp\_e1$

- Trailing edge number of laminae 2 in pressure side  $terp\_e2$
- Trailing edge offset in suction side  $[num/m] ters\_off$
- Trailing edge offset in pressure side  $[num/m] terp\_off$
- Trailing edge material  $ter\_mat$
- Trailing edge width  $[m] ter\_w$
- Trailing edge lamina thickness  $[m] ter\_th$

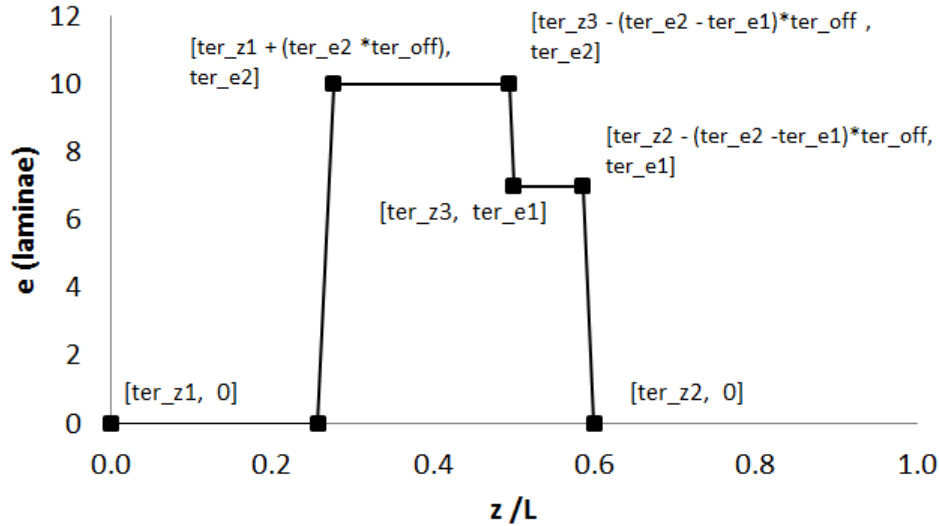


FIGURE A.6: Laminae along span in TER

### A.2.11 Leading edge reinforcement (LER)

- Leading edge starting span  $[adim] ler\_z1$
- Leading edge end span  $[adim] ler\_z2$
- Leading edge intermediate span in suction side  $[adim] lers\_z3$
- Leading edge intermediate span in pressure side  $[adim] lerp\_z3$
- Leading edge number of laminae 1 in suction side  $lers\_e1$
- Leading edge number of laminae 2 in suction side  $lers\_e2$
- Leading edge number of laminae 1 in pressure side  $lerp\_e1$
- Leading edge number of laminae 2 in pressure side  $lerp\_e2$
- Leading edge offset in suction side  $[num/m] lers\_off$
- Leading edge offset in pressure side  $[num/m] lerp\_off$
- Leading edge material  $ler\_mat$
- Leading edge width  $[m] ler\_w$
- Leading edge lamina thickness  $[m] ler\_th$

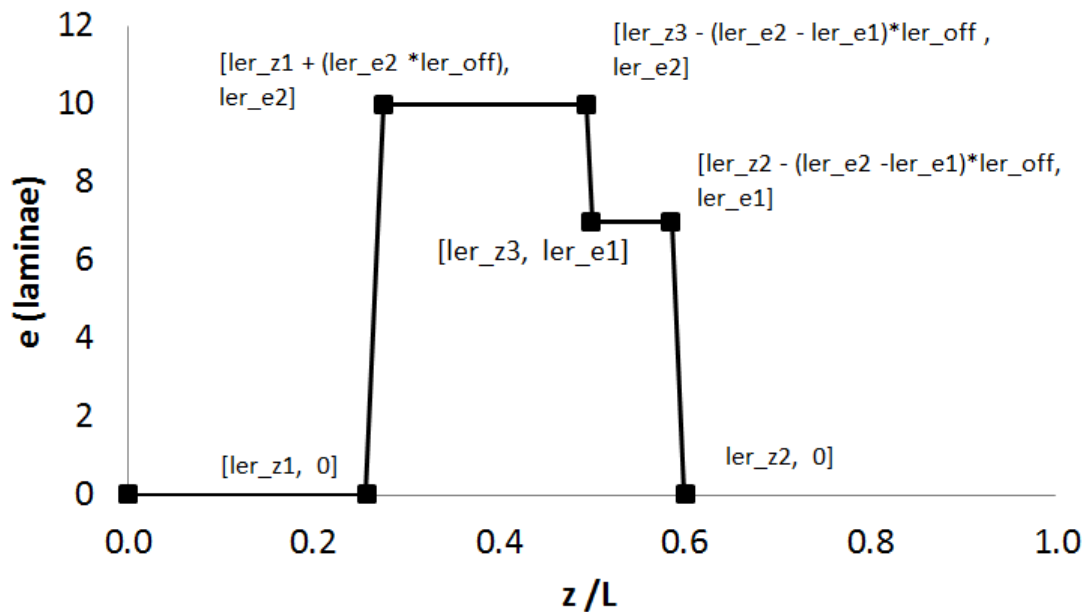


FIGURE A.7: Laminae along span in LER

#### A.2.12 Core near LE

- Core starting span in suction side  $[adim]$   $coreles\_z$
- Core thickness in suction side  $[m]$   $coreles\_th$
- Core material in suction side  $coreles\_mat$
- Core end span in pressure side  $[adim]$   $corelep\_z$
- Core thickness in pressure side  $[m]$   $corelep\_th$
- Core end span in pressure side  $corelep\_mat$

#### A.2.13 Core near TE

- Core starting span in suction side  $[adim]$   $coretes\_z$
- Core thickness in suction side  $[m]$   $coretes\_th$
- Core material in suction side  $coretes\_mat$
- Core end span in pressure side  $[adim]$   $coretep\_z$
- Core thickness in pressure side  $[m]$   $coretep\_th$
- Core end span in pressure side  $coretep\_mat$

#### A.2.14 Core between caps

- Core starting span in suction side  $[adim]$   $corebets\_z$
- Core thickness in suction side  $[m]$   $corebets\_th$
- Core material in suction side  $corebets\_mat$

- Core end span in pressure side [*adim*] *corebetp\_z*
- Core thickness in pressure side [*m*] *corebetp\_th*
- Core end span in pressure side *corebetp\_mat*

#### A.2.15 Core of shear webs

- Core span in web1 *adim corew1\_z*
- Core thickness in web1 *m corew1\_th*
- Core material in web1 *corew1\_mat*
- Core span in web2 *adim corew2\_z*
- Core thickness in web2 *m corew2\_th*
- Core material in web2 *corew2\_mat*
- Core span in web3 *adim corew3\_z*
- Core thickness in web3 *m corew3\_th*
- Core material in web3 *corew3\_mat*
- Core span in web4 *adim corew4\_z*
- Core thickness in web4 *m corew4\_th*
- Core material in web4 *corew4\_mat*

#### A.2.16 Extra mass

- Painting material *paint\_mat*
- Painting thickness [*m*] *paint\_th*
- Adhesive mass along LE [*kg/m*] *adhle\_massl*
- Adhesive mass along TE [*kg/m*] *adhle\_massl*
- Adhesive mass along shear web [*kg/m*] *adhweb\_massl*
- Adhesive mass along shear web [*kg/m*] *adhweb3\_massl*
- Extra mass along LE (over-laminated) [*kg/m*] *adhle\_massl*
- Extra mass along TE (over-laminated) [*kg/m*] *adhle\_massl*
- Extra mass along LE (tab) [*kg/m*] *pestle\_massl*
- Extra mass along TE (tab) [*kg/m*] *pestle\_massl*
- Extra mass CSM CAP1 [*kg/m*] *csmmain\_massl*
- Extra mass CSM CAP2 [*kg/m*] *csmsec\_massl*



### A.2.17 Positioning of structural layout

- Angle of rotation performed to prebending curve about Z-axis [*deg*] *p\_rotationd*
- Rotation angle about Z-axis to define CAP1 and CAP2 reference planes. [*deg*] *alpha1d*
- Rotation angle about X-axis to define CAP2 reference plane [*deg*] *alpha2d*
- Rotation angle about X-axis to define CAP1 reference plane [*deg*] *alpha3d*
- Reference point of CAP1 reference plane [*adim; adim; m*] *cap1\_ptsref*
- Reference point of CAP2 reference plane [*adim; adim; m*] *cap2\_ptsref*

## A.3 Environmental inputs

- Annual wind speed for AEP calculation [*m/s*] *um1*
- Annual wind speed for loads calculation [*m/s*] *um2*
- Shape of Weibull for AEP calculation [*adim*] *kshape1*
- Shape of Weibull for loads calculation [*adim*] *kshape2*
- Air density *kg/m<sup>3</sup>* *rho*

## A.4 Control inputs

- Rated power [*kW*] *potr*
- Optimal gain [*Nm/(rad/s)<sup>2</sup>*] *gain\_tsr*
- Gearbox ratio [*adim*] *gbx*
- Minimum generator speed [*rpm*] *ommin*
- Nominal generator speed [*rpm*] *ommax*
- Demanded generator torque [*Nm*] *gtorref*
- Pitch angle in torque regulation area [*deg*] *pitmin*

## A.5 Other inputs

- Cone angle [*deg*] *cone*
- Tilt angle [*deg*] *tilt*
- Overhang distance [*m*] *ovrhng*
- Root length [*m*] *rootl*



## Appendix B

# Sampling variation in Design Exploration

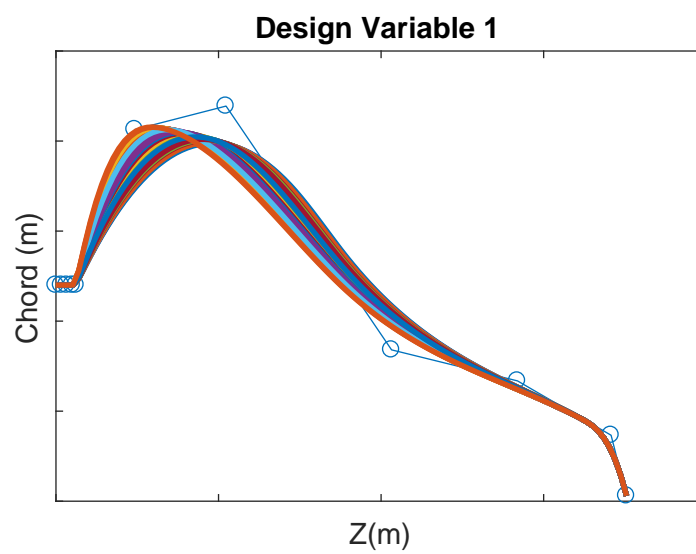


FIGURE B.1: Design variable 1. Chord knot inner (scknots9)

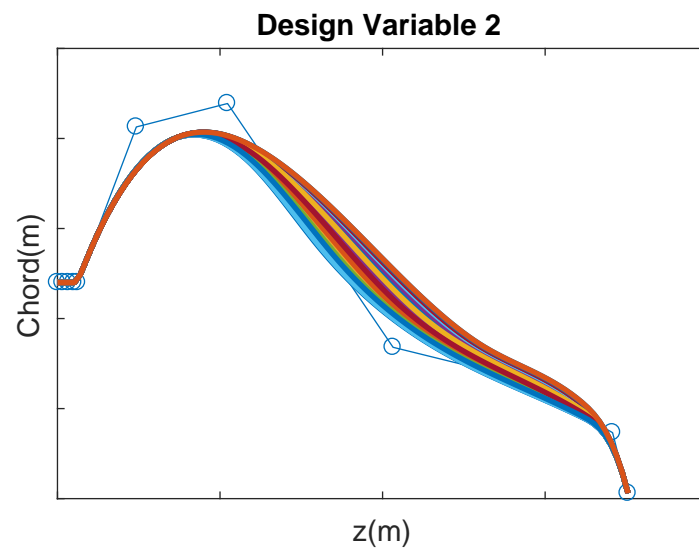


FIGURE B.2: Design variable 2. Chord knot outer (scknots10)

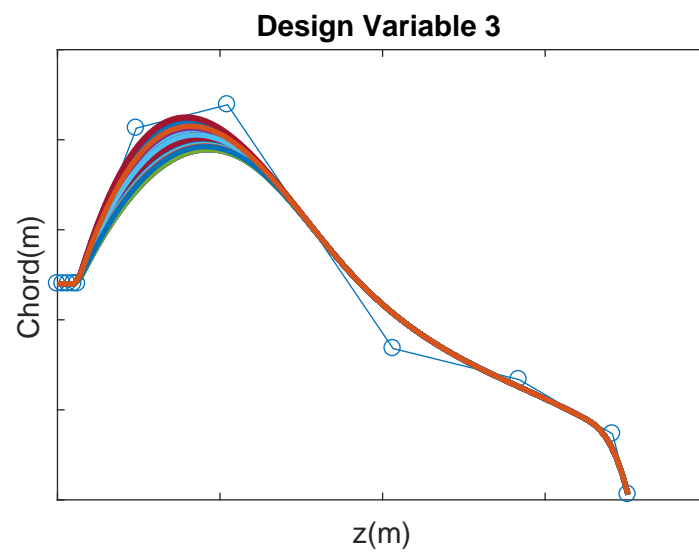


FIGURE B.3: Design variable 3. Chord coefficient inner (sccoefs6)

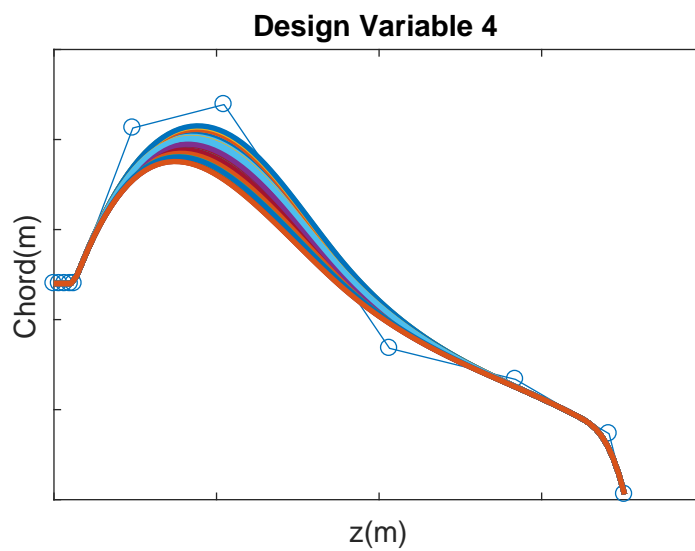


FIGURE B.4: Design variable 4. Chord coefficient inner-intermediate (sccoefs7)

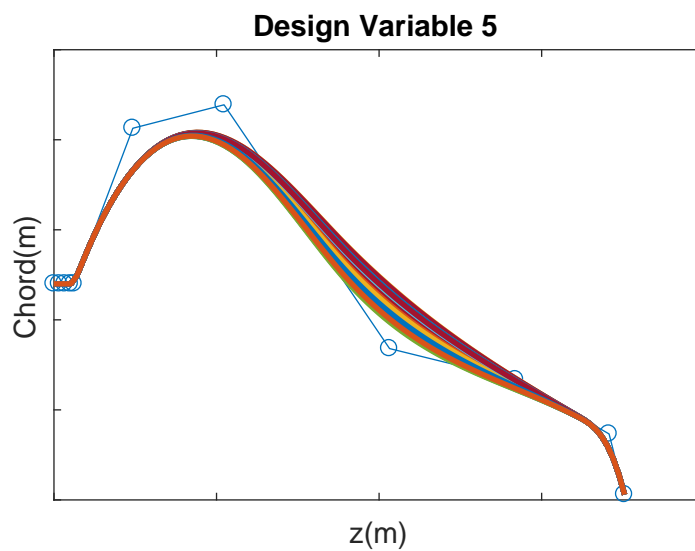


FIGURE B.5: Design variable 5. Chord coefficient intermediate (sc-coefs8)

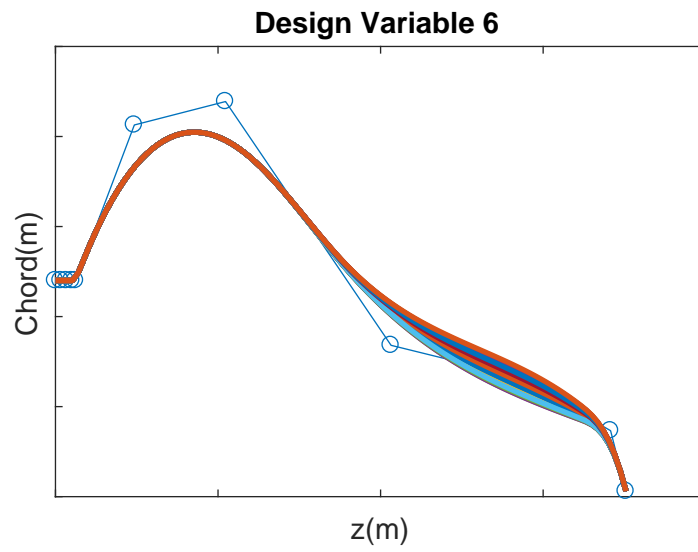


FIGURE B.6: Design variable 6. Chord coefficient outer intermediate (sccoefs9)

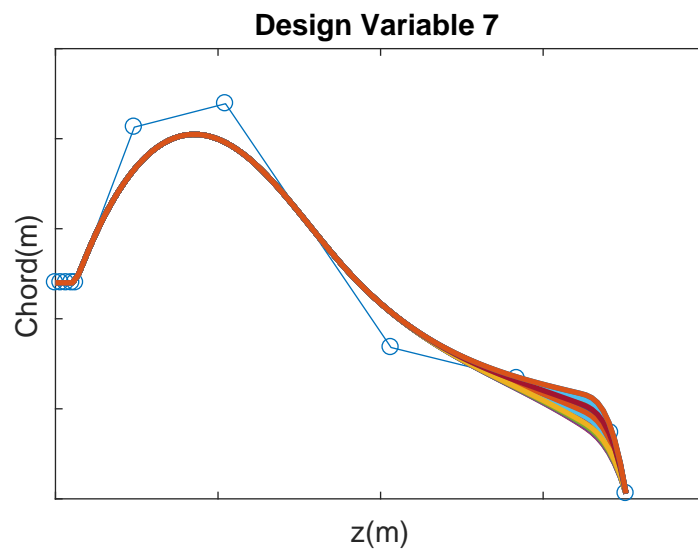


FIGURE B.7: Design variable 7. Chord coefficient outer (sccoefs10)

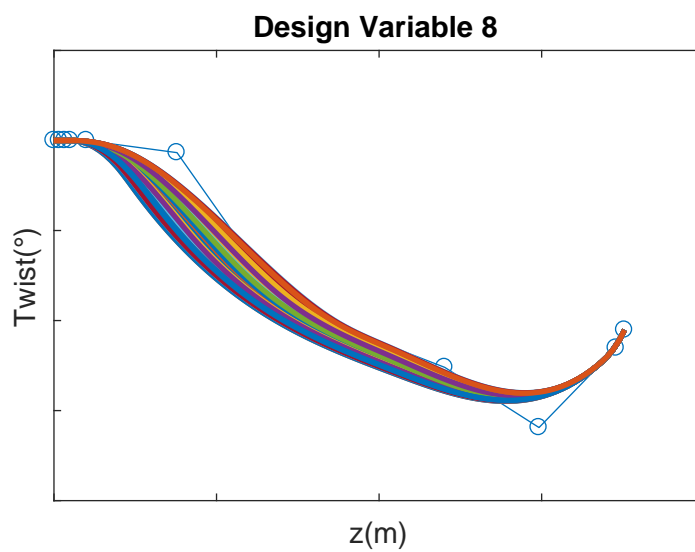


FIGURE B.8: Design variable 8. Twist knot (stknots9)

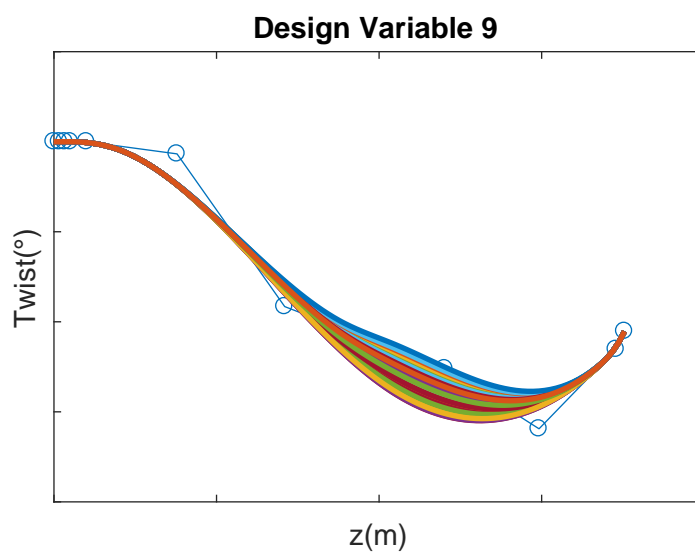


FIGURE B.9: Design variable 9. Twist coefficient inner (stcoefs8)

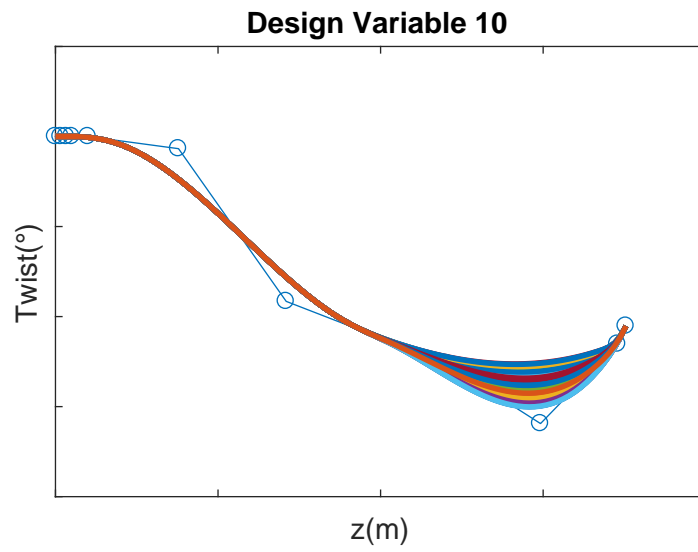


FIGURE B.10: Design variable 10. Twist coefficient intermediate (stcoefs9)

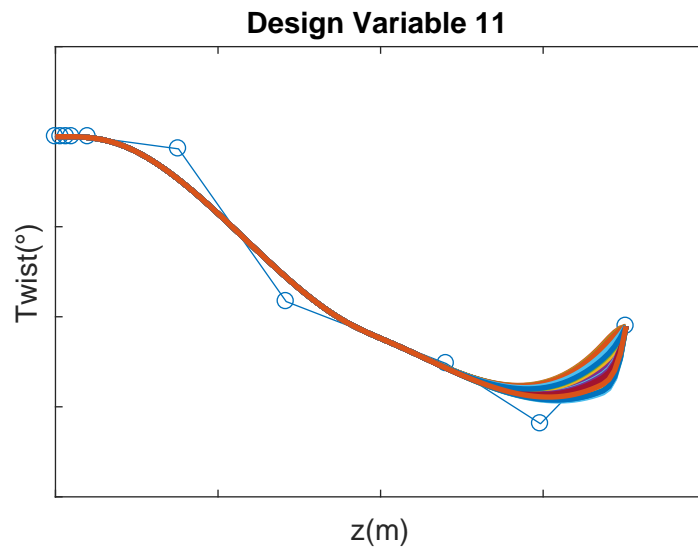


FIGURE B.11: Design variable 11. Twist coefficient outer (stcoefs10)



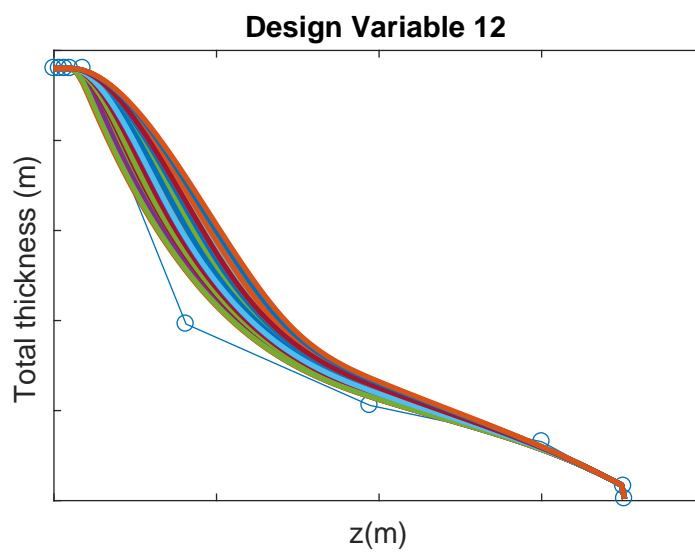


FIGURE B.12: Design variable 12. Thickness knot inner (seknots8)

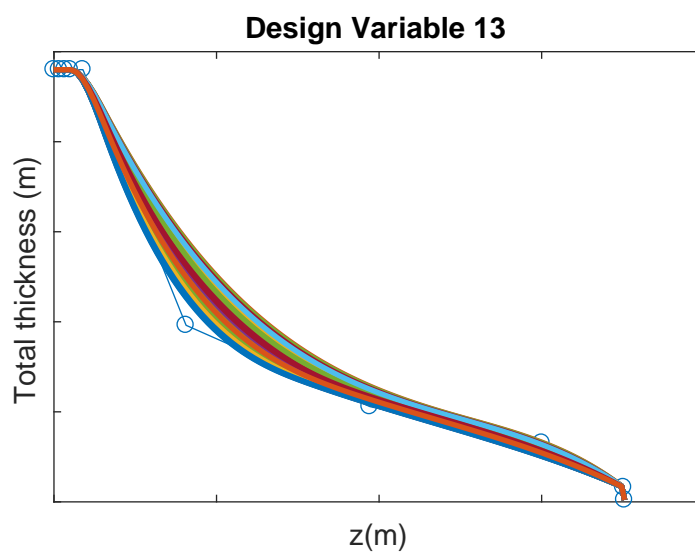


FIGURE B.13: Design variable 13. Thickness knot outer (seknots9)

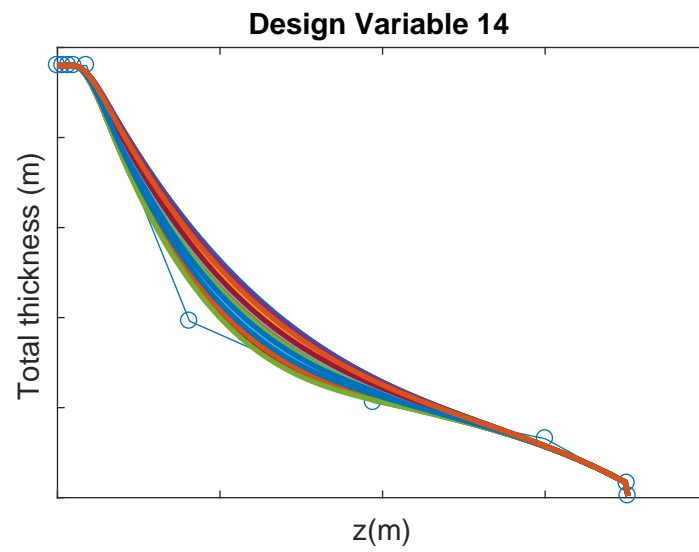


FIGURE B.14: Design variable 14. Thickness coefficient inner (secoefs6)

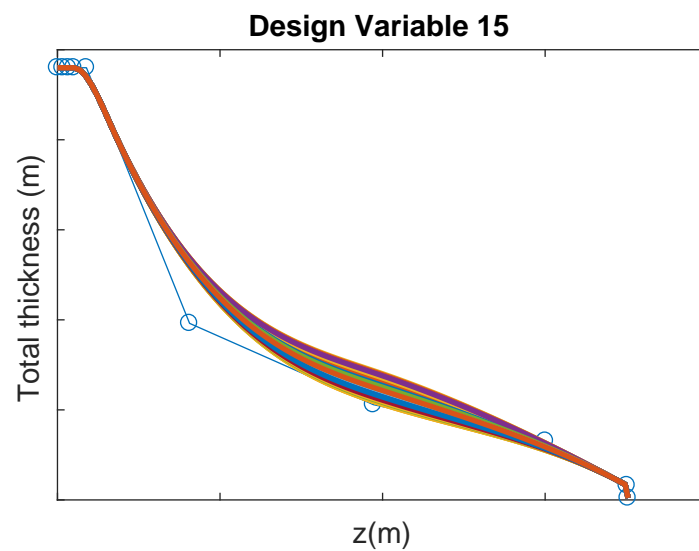


FIGURE B.15: Design variable 15. Thickness coefficient intermediate (secoefs7)

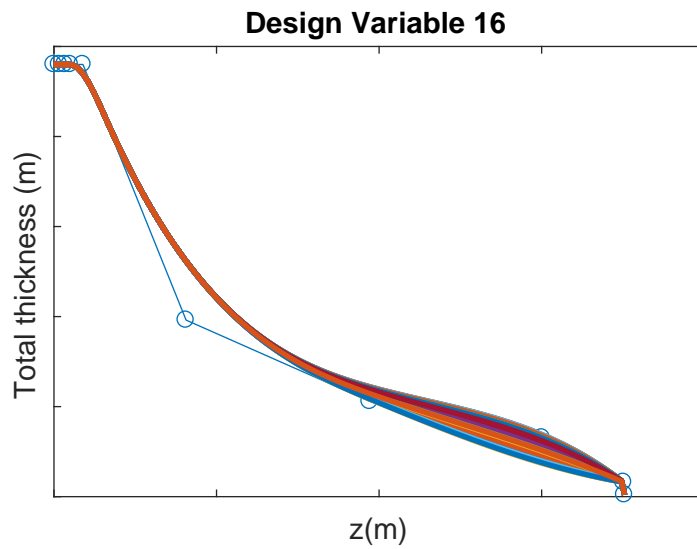


FIGURE B.16: Design variable 16. Thickness coefficient outter (sec-  
oefs8)

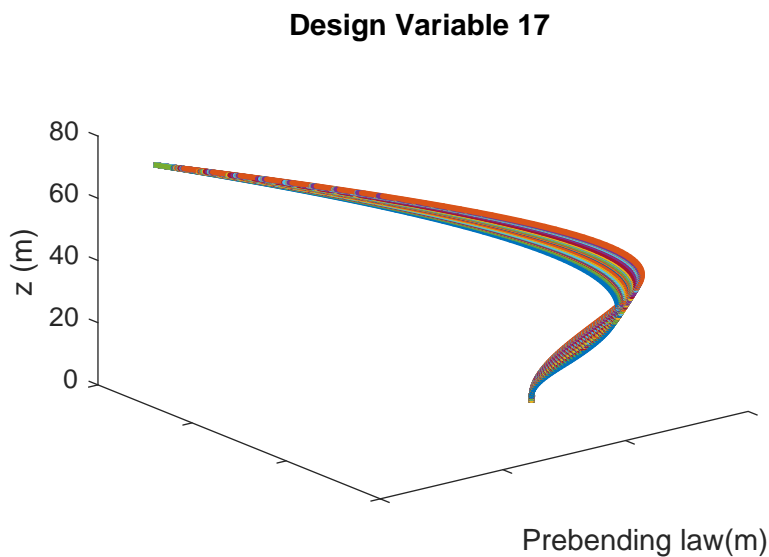


FIGURE B.17: Design variable 17. Prebending knot (pknots8)

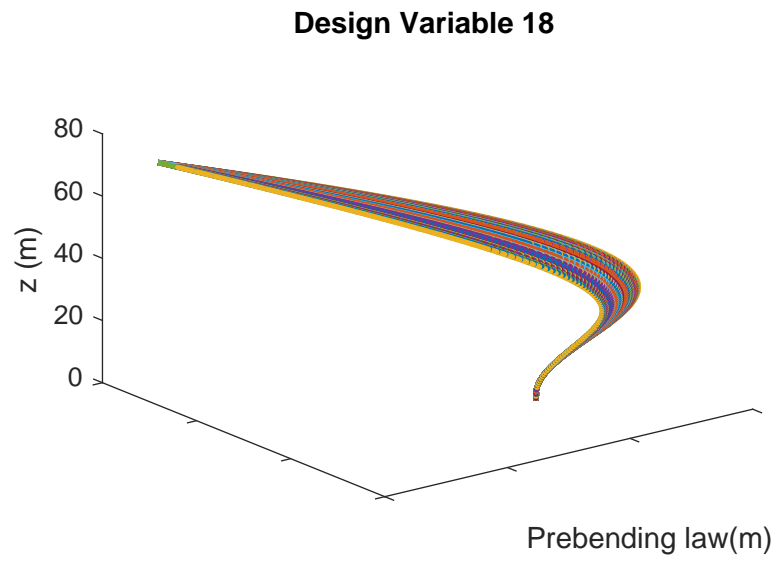


FIGURE B.18: Design variable 18. Prebending coefficient (pcoefs7)

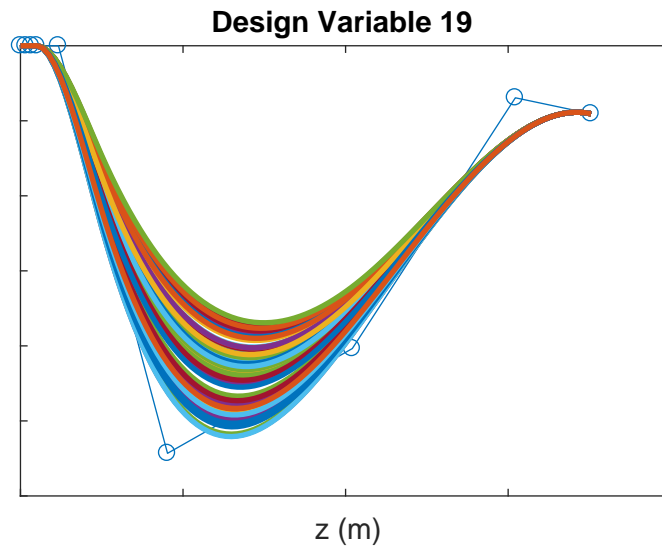


FIGURE B.19: Design variable 19. Stacking law along y inner coefficient (srycoefs6)

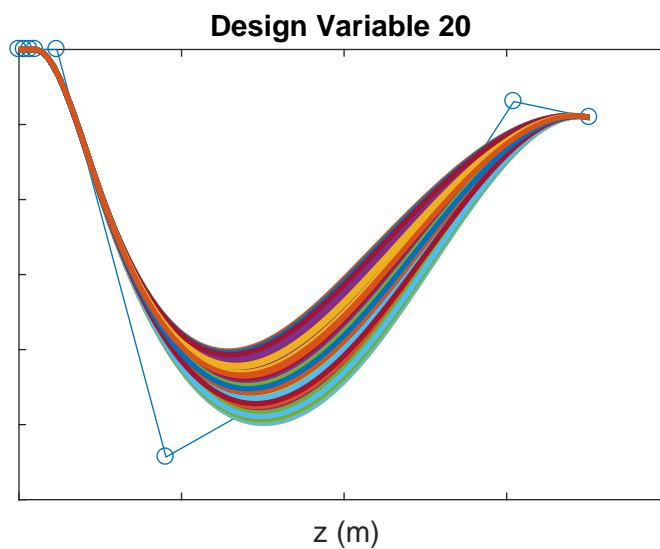


FIGURE B.20: Design variable 20. Stacking law along y intermediate coefficient (srycoefs7)

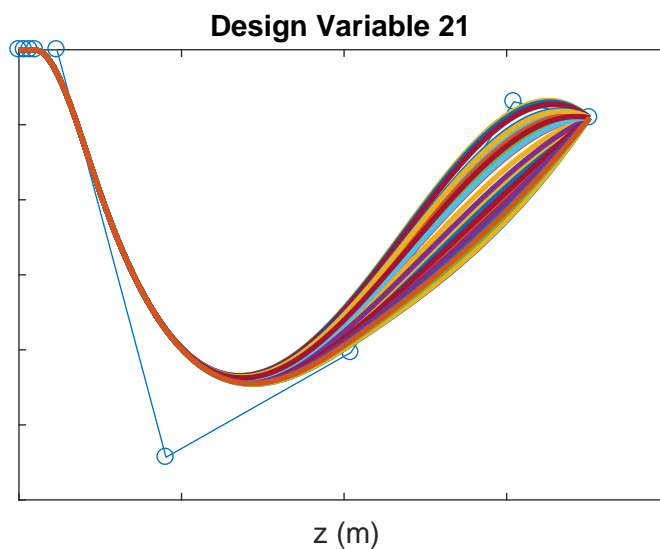


FIGURE B.21: Design variable 21. Stacking law along y outer coefficient (srycoefs8)

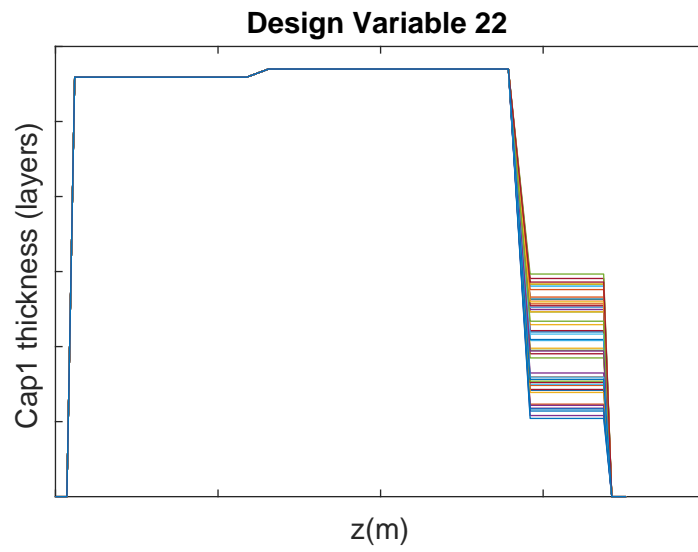


FIGURE B.22: Design variable 22. Main cap outer Thickness (cap1e1)

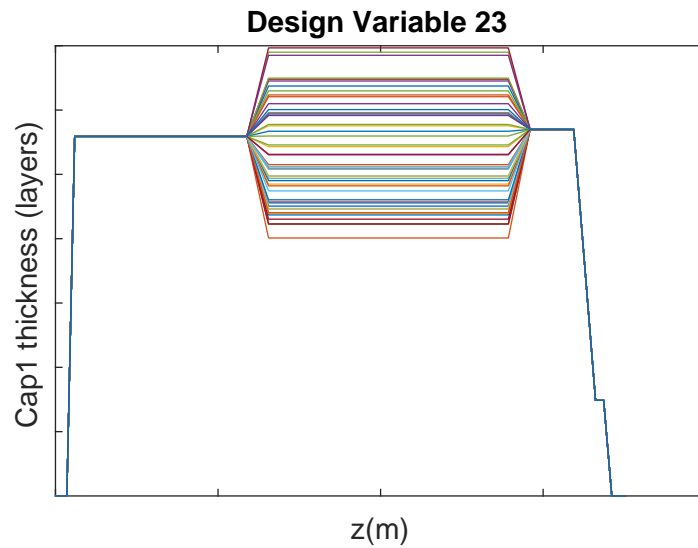


FIGURE B.23: Design variable 23. Main cap intermediate Thickness (cap1e2)

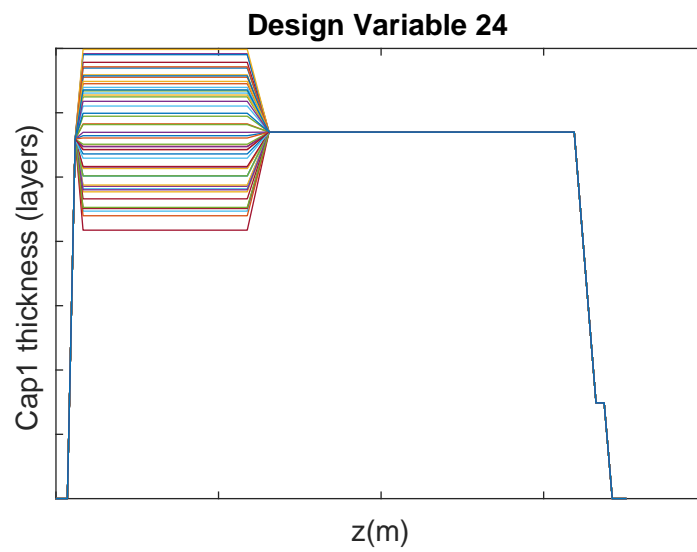


FIGURE B.24: Design variable 24. Main cap outer Thickness (cap1e3)

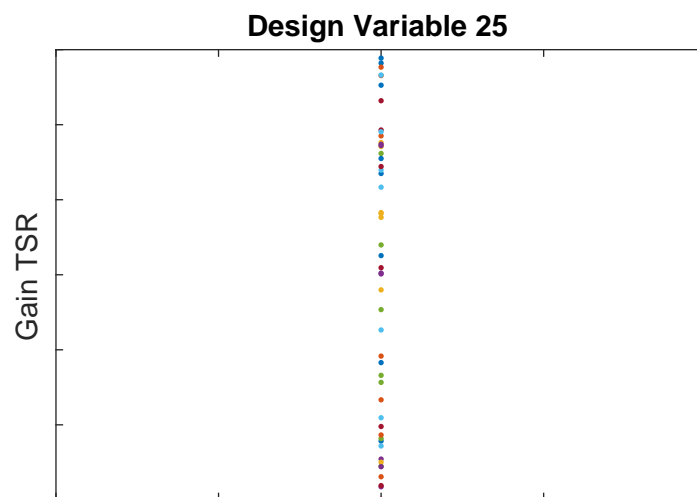


FIGURE B.25: Design variable 25. Optimal gain

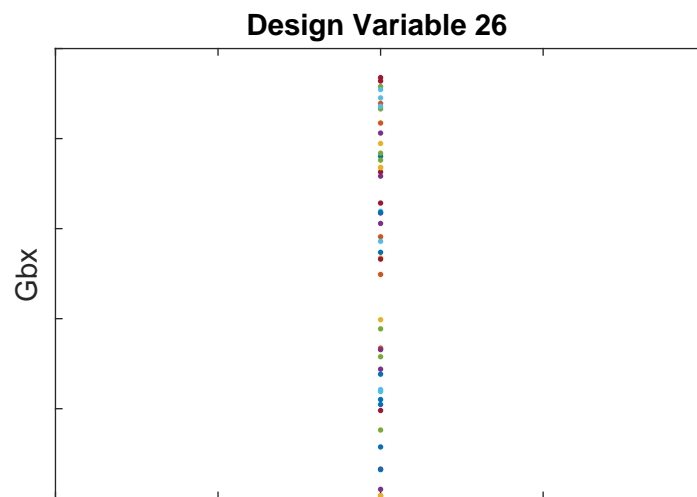


FIGURE B.26: Design variable 26. Gearbox Ratio



## Appendix C

# List of outputs from aeroelastic simulation

TABLE C.1

id	Name	Simulation source	Variable	Statistic
1	AEPs	STEADY	Annual Energy Production (AEP)	According to equation 2.11
2	AEPd	DYNAMIC 2	Annual Energy Production (AEP)	According to equation 2.11
3	dxs-tip-max	STEADY	Deflection along X - axis in tip (direction of tower)	Maximum
4	dys-tip-amax	STEADY	Deflection along Y - axis in tip	Maximum of absolute value
5	rotzs-tip-amax	STEADY	Rotation about Z -axis in tip	Maximum of absolute value
6	rotzs-tip-mean	STEADY	Rotation about Z -axis in tip	Mean
7	mys-r-max	STEADY	Bending moment My in root (flap)	Maximum
8	fxs-yaw-max	STEADY	Thrust force Fx in yaw bearing	Maximum
9	mzs-r-rated	STEADY	Torsional moment Mz in root	Value at rated wind speed
10	mxs-r-del	STEADY	Bending moment Mx in root (edge)	Damage equivalent load
11	mxs-hub-ddd1	STEADY	Torsional moment Mx in drive train	Damage equivalent load
12	mass	AGORA	Blade total mass	Value
13	Fm	AGORA	Blade first moment of mass	Value
14	costT	AGORA	Blade total cost	Value
15	freq1	EIGENFREQUENCIES	First frequency (flap)	Value
16	freq2	EIGENFREQUENCIES	Second frequency (edge)	Value
17	dxd-tip-max-10ms	DYNAMIC 1	Deflection along X - axis in tip (direction of tower)	Maximum
18	dxd-tip-max-12ms	DYNAMIC 1	Deflection along X - axis in tip (direction of tower)	Maximum
19	dxd-tip-max-14ms	DYNAMIC 1	Deflection along X - axis in tip (direction of tower)	Maximum
20	dxd-tip-max-18ms	DYNAMIC 1	Deflection along X - axis in tip (direction of tower)	Maximum
21	dxd-tip-max-8ms	DYNAMIC 1	Deflection along X - axis in tip (direction of tower)	Maximum
22	dyd-tip-amax-10ms	DYNAMIC 1	Deflection along Y - axis in tip	Maximum of absolute value
23	dyd-tip-amax-12ms	DYNAMIC 1	Deflection along Y - axis in tip	Maximum of absolute value
24	dyd-tip-amax-14ms	DYNAMIC 1	Deflection along Y - axis in tip	Maximum of absolute value
25	dyd-tip-amax-18ms	DYNAMIC 1	Deflection along Y - axis in tip	Maximum of absolute value
26	dyd-tip-amax-8ms	DYNAMIC 1	Deflection along Y - axis in tip	Maximum of absolute value
27	fxd-yaw-amax-10ms	DYNAMIC 1	Thrust force Fx in yaw bearing	Maximum of absolute value
28	fxd-yaw-amax-12ms	DYNAMIC 1	Thrust force Fx in yaw bearing	Maximum of absolute value
29	fxd-yaw-amax-14ms	DYNAMIC 1	Thrust force Fx in yaw bearing	Maximum of absolute value
30	fxd-yaw-amax-18ms	DYNAMIC 1	Thrust force Fx in yaw bearing	Maximum of absolute value
31	fxd-yaw-amax-8ms	DYNAMIC 1	Thrust force Fx in yaw bearing	Maximum of absolute value
32	fxd-yaw-del-10ms	DYNAMIC 1	Thrust force Fx in yaw bearing	Damage equivalent load
33	fxd-yaw-del-12ms	DYNAMIC 1	Thrust force Fx in yaw bearing	Damage equivalent load
34	fxd-yaw-del-14ms	DYNAMIC 1	Thrust force Fx in yaw bearing	Damage equivalent load
35	fxd-yaw-del-18ms	DYNAMIC 1	Thrust force Fx in yaw bearing	Damage equivalent load
36	fxd-yaw-del-8ms	DYNAMIC 1	Thrust force Fx in yaw bearing	Damage equivalent load
37	mxd-r-amax-10ms	DYNAMIC 1	Bending moment Mx in root (edge)	Maximum of absolute value
38	mxd-r-amax-12ms	DYNAMIC 1	Bending moment Mx in root (edge)	Maximum of absolute value
39	mxd-r-amax-14ms	DYNAMIC 1	Bending moment Mx in root (edge)	Maximum of absolute value
40	mxd-r-amax-18ms	DYNAMIC 1	Bending moment Mx in root (edge)	Maximum of absolute value
41	mxd-r-amax-8ms	DYNAMIC 1	Bending moment Mx in root (edge)	Maximum of absolute value
42	mxd-r-del-10ms	DYNAMIC 1	Bending moment Mx in root (edge)	Damage equivalent load
43	mxd-r-del-12ms	DYNAMIC 1	Bending moment Mx in root (edge)	Damage equivalent load
44	mxd-r-del-14ms	DYNAMIC 1	Bending moment Mx in root (edge)	Damage equivalent load
45	mxd-r-del-18ms	DYNAMIC 1	Bending moment Mx in root (edge)	Damage equivalent load
46	mxd-r-del-8ms	DYNAMIC 1	Bending moment Mx in root (edge)	Damage equivalent load
47	myd-r-amax-10ms	DYNAMIC 1	Bending moment My in root (flap)	Maximum of absolute value
48	myd-r-amax-12ms	DYNAMIC 1	Bending moment My in root (flap)	Maximum of absolute value
49	myd-r-amax-14ms	DYNAMIC 1	Bending moment My in root (flap)	Maximum of absolute value
50	myd-r-amax-18ms	DYNAMIC 1	Bending moment My in root (flap)	Maximum of absolute value
51	myd-r-amax-8ms	DYNAMIC 1	Bending moment My in root (flap)	Maximum of absolute value
52	myd-r-del-10ms	DYNAMIC 1	Bending moment My in root (flap)	Damage equivalent load
53	myd-r-del-12ms	DYNAMIC 1	Bending moment My in root (flap)	Damage equivalent load
54	myd-r-del-14ms	DYNAMIC 1	Bending moment My in root (flap)	Damage equivalent load
55	myd-r-del-18ms	DYNAMIC 1	Bending moment My in root (flap)	Damage equivalent load
56	myd-r-del-8ms	DYNAMIC 1	Bending moment My in root (flap)	Damage equivalent load
57	mzd-r-amax-10ms	DYNAMIC 1	Torsional moment Mz in root	Maximum of absolute value
58	mzd-r-amax-12ms	DYNAMIC 1	Torsional moment Mz in root	Maximum of absolute value
59	mzd-r-amax-14ms	DYNAMIC 1	Torsional moment Mz in root	Maximum of absolute value
60	mzd-r-amax-18ms	DYNAMIC 1	Torsional moment Mz in root	Maximum of absolute value
61	mzd-r-amax-8ms	DYNAMIC 1	Torsional moment Mz in root	Maximum of absolute value
62	mzd-r-del-10ms	DYNAMIC 1	Torsional moment Mz in root	Damage equivalent load
63	mzd-r-del-12ms	DYNAMIC 1	Torsional moment Mz in root	Damage equivalent load
64	mzd-r-del-14ms	DYNAMIC 1	Torsional moment Mz in root	Damage equivalent load
65	mzd-r-del-18ms	DYNAMIC 1	Torsional moment Mz in root	Damage equivalent load
66	mzd-r-del-8ms	DYNAMIC 1	Torsional moment Mz in root	Damage equivalent load
67	mzd-r-mean-10ms	DYNAMIC 1	Torsional moment Mz in root	Mean
68	mzd-r-mean-12ms	DYNAMIC 1	Torsional moment Mz in root	Mean
69	mzd-r-mean-14ms	DYNAMIC 1	Torsional moment Mz in root	Mean
70	mzd-r-mean-18ms	DYNAMIC 1	Torsional moment Mz in root	Mean
71	mzd-r-mean-8ms	DYNAMIC 1	Torsional moment Mz in root	Mean
72	pd-mean-10ms	DYNAMIC 1	Electrical power	Mean
73	pd-mean-12ms	DYNAMIC 1	Electrical power	Mean
74	pd-mean-14ms	DYNAMIC 1	Electrical power	Mean
75	pd-mean-18ms	DYNAMIC 1	Electrical power	Mean
76	pd-mean-8ms	DYNAMIC 1	Electrical power	Mean
77	rotzd-tip-amax-10ms	DYNAMIC 1	Rotation about Z -axis in tip	Maximum of absolute value
78	rotzd-tip-amax-12ms	DYNAMIC 1	Rotation about Z -axis in tip	Maximum of absolute value
79	rotzd-tip-amax-14ms	DYNAMIC 1	Rotation about Z -axis in tip	Maximum of absolute value
80	rotzd-tip-amax-18ms	DYNAMIC 1	Rotation about Z -axis in tip	Maximum of absolute value
81	rotzd-tip-amax-8ms	DYNAMIC 1	Rotation about Z -axis in tip	Maximum of absolute value
82	rotzd-tip-mean-10ms	DYNAMIC 1	Rotation about Z -axis in tip	Mean
83	rotzd-tip-mean-12ms	DYNAMIC 1	Rotation about Z -axis in tip	Mean
84	rotzd-tip-mean-14ms	DYNAMIC 1	Rotation about Z -axis in tip	Mean
85	rotzd-tip-mean-18ms	DYNAMIC 1	Rotation about Z -axis in tip	Mean
86	rotzd-tip-mean-8ms	DYNAMIC 1	Rotation about Z -axis in tip	Mean

# Bibliography

- ACCIONA Windpower products. URL: <http://www.acciona-windpower.com/products-and-services/>.
- Adler, Daniel (2005). *vioplot: Violin plot*. R package version 0.2. URL: <http://wsopuppenkiste.wiso.uni-goettingen.de/~dadler>.
- Ageze, Mesfin Belayneh, Yefa Hu, and Huachun Wu (2017). *Wind Turbine Aeroelastic Modeling: Basics and Cutting Edge Trends*. DOI: 10.1155/2017/5263897. URL: <https://doi.org/10.1155/2017/5263897>.
- Ahrens, James (2005). *ParaView: An End-User Tool for Large Data Visualization, Visualization Handbook*. Ed. by Charles D. Hansen and Chris R. Johnson. Elsevier.
- AIRBOYD. NASA video flutter. URL: <https://www.youtube.com/watch?v=qpJBvQXQC2M>.
- Alba, Enrique et al. (2009). *Optimization Techniques for Solving Complex Problems*. Ed. by Wiley. Wiley Publishing. ISBN: 0470293322, 9780470293324.
- Amiet (1975). "Acoustic radiation from an airfoil in a turbulent stream". In: *Journal of Sound and Vibration* 41.4, pp. 407–420. ISSN: 0022-460X. DOI: [https://doi.org/10.1016/S0022-460X\(75\)80105-2](https://doi.org/10.1016/S0022-460X(75)80105-2).
- Antoniou, Andreas and Wu-Sheng Lu (2007). *Practical Optimization. Algorithms and Engineering Applications*. Ed. by Springer. Springer US. DOI: 10.1007/978-0-387-71107-2.
- Ashuri, T. et al. (2014). "Multidisciplinary design optimization of offshore wind turbines for minimum levelized cost of energy". In: *Renewable Energy* 68.C, pp. 893–905.
- Audet, Charles and Jr. Dennis (Aug. 2002). "Analysis of Generalized Pattern Searches". In: *SIAM J. on Optimization* 13.3, pp. 889–903. ISSN: 1052-6234. DOI: 10.1137/S1052623400378742. URL: <http://dx.doi.org/10.1137/S1052623400378742>.
- Bak, Chistian (2013). *Design and performance of a 10 MW wind turbine*. Tech. rep. Wind energy.
- Bak, Christian and Peter Fuglsang (Nov. 2002). "Modification of the NACA 632-415 Leading Edge for Better Aerodynamic Performance". In: *Journal of Solar Energy Engineering* 124.4. Airfoil design., pp. 327–334. ISSN: 0199-6231. DOI: 10.1115/1.1506324. URL: <http://dx.doi.org/10.1115/1.1506324>.
- Bak, Christian et al. (2014). "Airfoil design: Finding the balance between design lift and structural stiffness". In: *Journal of Physics* 524. ISSN: 1742-6596. DOI: 10.1088/1742-6596/524/1/012017.
- Bampton and Craig (July 1968). "Coupling of substructures for dynamic analyses". In: *AIAA Journal* 6.7, pp. 1313–1319. ISSN: 0001-1452. DOI: 10.2514/3.4741. URL: <https://doi.org/10.2514/3.4741>.
- Bazilevs, Y. et al. (2012). "A computational procedure for prebending of wind turbine blades". In: *International Journal for Numerical Methods in Engineering* 89.3, pp. 323–336. ISSN: 1097-0207. DOI: 10.1002/nme.3244. URL: <http://dx.doi.org/10.1002/nme.3244>.
- Bellman, R. and Rand Corporation (1957). *Dynamic Programming*. Rand Corporation research study. Princeton University Press. ISBN: 9780691079516.

- Benini, Ernesto and Andrea Toffolo (Nov. 2002). "Optimal Design of Horizontal-Axis Wind Turbines Using Blade-Element Theory and Evolutionary Computation". In: *Journal of Solar Energy Engineering* 124.4, pp. 357–363. ISSN: 0199-6231. DOI: [10.1115/1.1510868](https://doi.org/10.1115/1.1510868). URL: <http://dx.doi.org/10.1115/1.1510868>.
- Bianchi, Fernando D., Hernán de Battista, and Ricardo J. Mantz (2007). *Wind Turbine Control Systems. Principles, Modelling and Gain Scheduling Design*. Springer-Verlag London. ISBN: 978-1-84628-493-9. DOI: [10.1007/1-84628-493-7](https://doi.org/10.1007/1-84628-493-7).
- Bir, Gunjit and Rick Damiani. *PreComp*. NREL National Renewable Energy Laboratory. 15013 Denver West Parkway Golden, CO 80401 303-275-3000. URL: <https://nwtc.nrel.gov/PreComp>.
- Bir, Gunjit S. (2001). "Computerized Method for Preliminary Structural Design of Composite Wind Turbine Blades". In: *Journal of Solar Energy Engineering* 123 (4). DOI: [10.1115/1.1413217](https://doi.org/10.1115/1.1413217).
- Bishop, R. E. D. (1987). "Arthur Roderick Collar. 22 February 1908-12 February 1986". In: *Biographical Memoirs of Fellows of the Royal Society*. DOI: [10.2307/769949](https://doi.org/10.2307/769949).
- Bizzarrini, N., F. Grasso, and D.P. Coiro (2011). *Genetic Algorithms in Wind Turbine Airfoil Design*. Technical report ECN-M-11-035. Westerduinweg 3 1755 LE Petten The Netherlands: Energy research Center of Netherlands.
- BLADED. Garrad Hassan & Partners Ltd. St Vincent's Works, Silverthorne Lane, Bristol BS2 0QD England. URL: <https://www.dnvg1.com/services/bladed-3775>.
- Blair, Wenbin Yu; Maxwell (2012). "GEBT: A general-purpose nonlinear analysis tool for composite beams". In: *Composite Structures* 94 (9). DOI: [10.1016/j.compstruct.2012.04.007](https://doi.org/10.1016/j.compstruct.2012.04.007).
- Boor, C. de (2001). *A Practical Guide to Splines*. Applied Mathematical Sciences. Springer New York. ISBN: 9780387953663.
- Boor, Carl de (2002). "Chapter 6 - Spline Basics". In: *Handbook of Computer Aided Geometric Design*. Ed. by Gerald Farin, Josef Hoschek, and Myung-Soo Kim. Amsterdam: North-Holland, pp. 141–163. ISBN: 978-0-444-51104-1. DOI: <https://doi.org/10.1016/B978-044451104-1/50007-1>. URL: <http://www.sciencedirect.com/science/article/pii/B9780444511041500071>.
- Boorsma, K. and B. H. Bulder. *Silant*. ECN Energy Research Centre of the Netherlands. P.O. Box 1, 1755 ZG Petten, the Netherlands. URL: <https://www.ecn.nl>.
- Bortolotti, P., C. L. Bottasso, and A. Croce (2016). "Combined preliminary detailed design of wind turbines". In: *Wind Energy Science* 1.1, pp. 71–88. DOI: [10.5194/wes-1-71-2016](https://doi.org/10.5194/wes-1-71-2016). URL: <https://www.wind-energ-sci.net/1/71/2016/>.
- Bortolotti, P et al. (2018). "Integrated design optimization of wind turbines with noise emission constraints". In: *Journal of Physics: Conference Series* 1037.4, p. 042005.
- Bossanyi, E. A. (2003). "Wind Turbine Control for Load Reduction". In: *Wind Energy* 6.3, pp. 229–244. ISSN: 1099-1824. DOI: [10.1002/we.95](https://doi.org/10.1002/we.95). URL: <http://dx.doi.org/10.1002/we.95>.
- Bottasso, C.L., F. Campagnolo, and A. Croce (2012). "Multi-disciplinary constrained optimization of wind turbines". English. In: *Multibody System Dynamics* 27.1, pp. 21–53. ISSN: 1384-5640. DOI: [10.1007/s11044-011-9271-x](https://doi.org/10.1007/s11044-011-9271-x). URL: <http://dx.doi.org/10.1007/s11044-011-9271-x>.
- Brooks, Pope and Marcolini (1989). *Airfoil self-noise and prediction*. Tech. rep. NASA.
- Buckley, Howard P., Beckett Y. Zhou, and David W. Zingg (Sept. 2010). "Airfoil Optimization Using Practical Aerodynamic Design Requirements". In: *Journal of Aircraft* 47.5. Zingg, pp. 1707–1719. ISSN: 0021-8669. DOI: [10.2514/1.C000256](https://doi.org/10.2514/1.C000256).

- Buckney, Neil et al. (2012). "On the structural topology of wind turbine blades". In: *Wind Energy* 16.4, pp. 545–560. DOI: [10.1002/we.1504](https://doi.org/10.1002/we.1504).
- Burlibasa, A. and E. Ceanga (2013). "Rotationally sampled spectrum approach for simulation of wind speed turbulence in large wind turbines". In: *Applied Energy* 111, pp. 624–635. ISSN: 0306-2619. DOI: <http://dx.doi.org/10.1016/j.apenergy.2013.05.002>.
- Burton, Tony (2001). *Wind energy: handbook*. Ed. by Wiley. J. Wiley. ISBN: 9780471489979.
- Byrd, Richard H., Mary E. Hribar, and Jorge Nocedal (Apr. 1999). "An Interior Point Algorithm for Large-Scale Nonlinear Programming". In: *SIAM J. on Optimization* 9.4, pp. 877–900. ISSN: 1052-6234. DOI: [10.1137/S1052623497325107](https://doi.org/10.1137/S1052623497325107). URL: <http://dx.doi.org/10.1137/S1052623497325107>.
- Caboni, M., E. Minisci, and A. Riccardi (2018). "Aerodynamic Design Optimization of Wind Turbine Airfoils under Aleatory and Epistemic Uncertainty". In: *Journal of Physics: Conference Series* 1037.4, p. 042011.
- Case, John and A.H. Chilver (1971). "9 - Longitudinal stresses in beams". In: *Strength of Materials and Structures (Second Edition)*. Ed. by John Case and A.H. Chilver. Second Edition. Academic Press, pp. 149–172. ISBN: 978-0-7131-3244-1. DOI: <https://doi.org/10.1016/B978-0-7131-3244-1.50014-4>.
- Chase, Hunter S. (2012). "Fundamental forms of surfaces and the Gauss-Bonnet theorem". In: *Mathematics University of Chicago*.
- Chen, Jin et al. (Apr. 2013). "Structural optimization study of composite wind turbine blade". In: *Materials and Design. Elsevier* 46, pp. 247–255.
- Chung, Deborah D. L. (2010). *Composite Materials*. Ed. by 2. Springer-Verlag London. DOI: [10.1007/978-1-84882-831-5](https://doi.org/10.1007/978-1-84882-831-5).
- Conn, Andrew R., Nicholas I. M. Gould, and Philippe Toint (1991). "A Globally Convergent Augmented Lagrangian Algorithm for Optimization with General Constraints and Simple Bounds". In: *SIAM Journal on Numerical Analysis* 28.2, pp. 545–572. DOI: [10.1137/0728030](https://doi.org/10.1137/0728030). eprint: <https://doi.org/10.1137/0728030>. URL: <https://doi.org/10.1137/0728030>.
- Crawley, M.J. (2011). *Statistics: An Introduction using R*. Ed. by Imperial College London. Wiley. ISBN: 9780470022993.
- Croce, A et al. (2016). "Lightweight rotor design by optimal spar cap offset". In: *Journal of Physics: Conference Series* 753.6, p. 062003.
- Dahl, Kristian S. and Peter Fuglsang (1998). "Design of the Wind Turbine Airfoil Family RISØ-A-XX". In: *Riso -R RISØ-R-1024*. Airfoil design. Danish wind industry association website. URL: [http://www.windpower.org/en/knowledge/windpower\\_wiki.html](http://www.windpower.org/en/knowledge/windpower_wiki.html).
- Deb, Kalyanmoy (1998). "An Efficient Constraint Handling Method for Genetic Algorithms". In: *Computer Methods in Applied Mechanics and Engineering*, pp. 311–338.
- Derakhshan, Shahram, Ali Tavaziani, and Nemat Kasaeian (July 2015). "Numerical Shape Optimization of a Wind Turbine Blades Using Artificial Bee Colony Algorithm". In: *Journal of Energy Resources Technology* 137.5, pp. 051210–051210–12. ISSN: 0195-0738. DOI: [10.1115/1.4031043](https://doi.org/10.1115/1.4031043). URL: <http://dx.doi.org/10.1115/1.4031043>.
- Dirlik, Turan (1985). "Application of computers in fatigue analysis." PHD. University of Warwick.
- Dreo, Johann et al. (2006). *Metaheuristics for hard optimization : methods and case studies*. Springer-Verlag, p. 372.



- Døssing, Mads et al. (2012). "Aerodynamic optimization of wind turbine rotors using a blade element momentum method with corrections for wake rotation and expansion". In: *Wind Energy* 15.4. Risoe optimizer., pp. 563–574. ISSN: 1095-4244.
- Dykes, K., R. Damiani, and A Ning (2017). *Wind Turbine Optimization with WISDEM*. Tech. rep. NREL.
- Ebrahimi, M. and A. Jahangirian (2014). "Aerodynamic Optimization of Airfoils Using Adaptive Parameterization and Genetic Algorithm". English. In: *Journal of Optimization Theory and Applications* 162.1, pp. 257–271. ISSN: 0022-3239. DOI: [10.1007/s10957-013-0442-1](https://doi.org/10.1007/s10957-013-0442-1). URL: <http://dx.doi.org/10.1007/s10957-013-0442-1>.
- Echeverria, Fernando, Fermin Mallor, and Unai San Miguel (2017). "Global sensitivity analysis of the blade geometry variables on the wind turbine performance". In: *Wind Energy*. WE-15-0066.R2. ISSN: 1099-1824. DOI: [10.1002/we.2111](https://doi.org/10.1002/we.2111). URL: <http://dx.doi.org/10.1002/we.2111>.
- (2018). "Design exploration prior to blade multi-disciplinary optimisation". In: *Journal of Physics: Conference Series*.
- Echeverria, Fernando, Fermín Mallor, and Javier Sanz (May 2017). "Fast Estimation of the Damage Equivalent Load in Blade Geometry Multidisciplinary Optimization". In: *Journal of Solar Energy Engineering* 139.4, pp. 041008–041008–10. ISSN: 0199-6231. DOI: [10.1115/1.4036636](https://doi.org/10.1115/1.4036636). URL: <http://dx.doi.org/10.1115/1.4036636>.
- Edgington, Eugene S (1986). *Randomization Tests*. New York, NY, USA: Marcel Dekker, Inc. ISBN: 0-824-77656-9.
- Efron, B. (1982). *The Jackknife, the Bootstrap and Other Resampling Plans*. Ed. by SIAM. Society for Industrial and Applied Mathematics. DOI: [10.1137/1.9781611970319](https://doi.org/10.1137/1.9781611970319).
- Ehrmann, Robert Schaefer (2014). "Effect of Surface Roughness on Wind Turbine Performance". PhD thesis. Texas University.
- Erickson, Larry (1990). *Panel methods: An introduction*. Technical Report NASA-TP-2995. NASA Ames Research Center; Moffett Field, CA, United States: NASA. *European Commission website*. URL: <https://ec.europa.eu/energy/en/topics/renewable-energy>.
- FAST. NREL. NREL National Renewable Energy Laboratory. 1617 Cole Boulevard, Golden, Colorado 80401-3393.
- Fischer, Gunter, Timoleon Kipouros, and A Mark Savill (Apr. 2012). "Multi-objective Shape Optimisation for Horizontal-Axis Wind Turbine Blades". In: *Structures, Structural Dynamics, and Materials and Co-located Conferences*. American Institute of Aeronautics and Astronautics, pp. –. DOI: [10.2514/6.2012-1353](https://doi.org/10.2514/6.2012-1353). URL: <http://dx.doi.org/10.2514/6.2012-1353>.
- Fischer, Gunter Reinald, Timoleon Kipouros, and Anthony Mark Savill (2014). "Multi-objective optimisation of horizontal axis wind turbine structure and energy production using aerofoil and blade properties as design variables". In: *Renewable Energy* 62, pp. 506 –515. ISSN: 0960-1481. DOI: [http://dx.doi.org/10.1016/j.renene.2013.08.009](https://doi.org/10.1016/j.renene.2013.08.009).
- Floater, Michael S. and Tatiana Surazhsky (2006). "Parameterization for Curve Interpolation". In: *Topics in Multivariate Approximation and Interpolation*. Ed. by Kurt Jetter et al. Vol. 12. Studies in Computational Mathematics. Elsevier, pp. 39 –54. DOI: [http://doi.org/10.1016/S1570-579X\(06\)80004-2](https://doi.org/10.1016/S1570-579X(06)80004-2).
- Fuglsang, P. and K.S. Dahl (1999). "Design of the new Risø-A1 airfoil family for wind turbines". In: *Wind energy for the next millennium. Proceedings*. Ed. by E.L. Petersen et al. James and James Science Publishers, pp. 134–137. ISBN: 1-902916-00-X.

- Fuglsang, P. and H.A. Madsen (Mar. 1999). "Optimization method for wind turbine rotors". In: *Journal of Wind Engineering and Industrial Aerodynamics* 80, pp. 191–206. ISSN: 0167-6105.
- Gagnon, Hugo and David Zingg (Sept. 2012). "Two-Level Free-Form Deformation for High-Fidelity Aerodynamic Shape Optimization". In: *Aviation Technology, Integration, and Operations (ATIO) Conferences*. American Institute of Aeronautics and Astronautics, pp. -. DOI: [10.2514/6.2012-5447](https://doi.org/10.2514/6.2012-5447). URL: <http://dx.doi.org/10.2514/6.2012-5447>.
- Garrel, A. van (2001). *Requirements for a Wind Turbine Aerodynamics Simulation Module*. Tech. rep. Netherlands Energy Research Foundation ECN.
- Garrick (1963). "A survey of aerothermoelasticity". In: *Nasa Center*.
- Gaudern, Nicholas and Dr. Digby Symons (2010). "Comparison of Theoretical and Numerical Buckling Loads for Wind Turbine Blade Panels". In: *Wind engineering*.
- Gigerenzer, G. and L. Czerlinski J. and Martignon (1999). "How good are fast and frugal heuristics? In Decision science and technology". In: *Springer*, pp. 81–103.
- Gigerenzer, G. and P Todd (1999). "Fast and frugal heuristics: The adaptive toolbox. In Simple heuristics that make us smart." In: *Oxford University Press*, 3–34.
- Giguere, Philippe and Michael Selig (2000). "Blade geometry optimization for the design of wind turbine rotors". In: *Aerospace Sciences Meetings*. American Institute of Aeronautics and Astronautics. DOI: [10.2514/6.2000-45](https://doi.org/10.2514/6.2000-45). URL: <http://dx.doi.org/10.2514/6.2000-45>.
- Glauert, H. (1935). "Airplane Propellers". In: *Aerodynamic Theory: A General Review of Progress Under a Grant of the Guggenheim Fund for the Promotion of Aeronautics*. Ed. by Springer. Berlin, Heidelberg: Springer Berlin Heidelberg. Chap. 1, pp. 169–360. ISBN: 978-3-642-91487-4. DOI: [10.1007/978-3-642-91487-4\\_3](https://doi.org/10.1007/978-3-642-91487-4_3). URL: [https://doi.org/10.1007/978-3-642-91487-4\\_3](https://doi.org/10.1007/978-3-642-91487-4_3).
- Grasso, Francesco (2008). "Multi-Objective Numerical Optimization Applied to Aircraft Design". PhD thesis. Facoltà Ingegneria Dipartimento Ingegneria Aerospaziale.
- Guid, Nikola, Crtomir Oblonsek, and Borut Zalik (1995). "Surface interrogation methods". In: *Computers & Graphics* 19.4. Computer Graphics Art, pp. 557–574. ISSN: 0097-8493. DOI: [http://dx.doi.org/10.1016/0097-8493\(95\)00034-A](http://dx.doi.org/10.1016/0097-8493(95)00034-A).
- Hagen, H., Th. Schreiber, and E. Gschwind (1990). "Methods for Surface Interrogation". In: *Proceedings of the 1st Conference on Visualization '90*. VIS '90. San Francisco, California: IEEE Computer Society Press, pp. 187–193. ISBN: 0-8186-2083-8.
- Halfpenny, Andrew (1998). "Dynamics of both on and offshore wind turbines in the frequency domain". PhD thesis. University college London.
- Hamby, D.M. (1994). "A review of techniques for parameter sensitivity analysis of environmental models". English. In: *Environmental Monitoring and Assessment* 32.2, pp. 135–154. ISSN: 0167-6369. DOI: [10.1007/BF00547132](https://doi.org/10.1007/BF00547132). URL: <http://dx.doi.org/10.1007/BF00547132>.
- Han, X. (2011). *An Evolutionary Geometry Parametrization for Aerodynamic Shape Optimization*. Parameterization. Han and Zingg. Ver OutBox page for David W. Zingg.url. University of Toronto. ISBN: 9780494767337.
- Hansen, Anca et al. (2004). "Review of Contemporary Wind Turbine Concepts and their Market Penetration". In: *Wind Engineering* (3). DOI: [10.1260/0309524041590099](https://doi.org/10.1260/0309524041590099).
- Hansen, Flemming Rasmussen; Morten Hartvig Hansen; Kenneth Thomsen; Torben Juul Larsen; Franck Bertagnolio; Jeppe Johansen; Helge Aagaard Madsen; Christian Bak; Anders Melchior (2003). "Present Status of Aeroelasticity of Wind Turbines". In: *Wind Energy* 6 (3). DOI: [10.1002/we.98](https://doi.org/10.1002/we.98).
- Hansen, M et al. (June 2006). "State of the art in wind turbine aerodynamics and aeroelasticity". In: 42, pp. 285–330.

- Hansen, Martin Otto Laver (2008). *Aerodynamics of Wind Turbines: second edition*. 2nd ed. Earthscan Publications Ltd. ISBN: 978-1-84407-438-9.
- Hartmann, Erich (2003). *Geometry and algorithms for computer aided design*. Ed. by Darmstadt University of Technology. Department of Mathematics.
- Hau, Erich (2006). *Wind Turbines. Fundamentals, Technologies, Application, Economics*. Ed. by Springer. 2nd ed. Springer Verlag Berlin Heidelberg. DOI: [10.1007/3-540-29284-5](https://doi.org/10.1007/3-540-29284-5).
- HAWC2. DTU Denmark technical university. DTU Wind Energy Risø Campus Frederiksborgvej 399 Building 118 4000 Roskilde Denmark CVR: DK30060946. URL: <http://www.hawc2.dk/>.
- Hicks, Raymond M. and Preston A. Henne (July 1978). "Wing Design by Numerical Optimization". In: *Journal of Aircraft* 15.7, pp. 407–412. ISSN: 0021-8669. DOI: [10.2514/3.58379](https://doi.org/10.2514/3.58379). URL: <http://dx.doi.org/10.2514/3.58379>.
- Hodges, Dewey H. (2006). "Nonlinear Composite Beam Theory Introduction". In: vol. 10.2514/4.866821. ISBN: 978-1-56347-697-6, 978-1-60086-682-1. DOI: [10.2514/5.9781600866821.0001.0022](https://doi.org/10.2514/5.9781600866821.0001.0022).
- Hoffmann, Rolf (2002). "A comparison of control concepts for wind turbines in terms of energy capture". PhD thesis. Technischen Universität Darmstadt.
- Holierhoek, Jessica G. (2008). "Aeroelasticity of Large Wind Turbines". PhD thesis. Technische Universiteit Delft.
- Holland, John H. (1992). *Adaptation in Natural and Artificial Systems: An Introductory Analysis with Applications to Biology, Control and Artificial Intelligence*. Ed. by MIT. Cambridge, MA, USA: MIT Press. ISBN: 0262082136.
- Hosseini Seyed Farhad; Moetakef-Imani, Behnam (Apr. 2017). "Innovative approach to computer-aided design of horizontal axis wind turbine blades". In: *Journal of Computational Design and Engineering* 4 (2). DOI: [10.1016/j.jcde.2016.11.001](https://doi.org/10.1016/j.jcde.2016.11.001).
- Hui, Chen, Yu Wenbin, and Capellaro Mark (2010). "A critical assessment of computer tools for calculating composite wind turbine blade properties". In: *Wind Energy* 13.6, pp. 497–516. DOI: [10.1002/we.372](https://doi.org/10.1002/we.372).
- IEC61400-1 (2005). *IEC 61400-1 Wind Turbines - Part 1: Design Requirements*. IEC International Standards. Edition 3. International Electrotechnical Commission.
- IEC61400-12-2 (2013). *IEC 61400 Wind Turbines- part 12-2: Performance of electricity-producing wind turbines based on nacelle anemometry*. International standard.
- Illinois, University of, ed. *UIUC Airfoil Data Site*. URL: <https://m-selig.ae.illinois.edu/ads.html>.
- J. Méndez, D. Greiner (2006). "Wind Blade Chord and Twist Angle Optimization Using Genetic Algorithms". In: *Proceedings of the Fifth International Conference on Engineering Computational Technology*. Twist and chord optimization. Reference not completed.
- James, Gareth and Daniela Witten (2013). *An Introduction to Statistical Learning*. Ed. by I. Olkin G. Casella S. Fienberg. Vol. 103. Springer New York. DOI: [10.1007/978-1-4614-7138-7](https://doi.org/10.1007/978-1-4614-7138-7).
- Jelena, S. et al. (2016). "Rapid multidisciplinary, multi-objective optimization of composite horizontal-axis wind turbine blade". In: *2016 International Conference Multidisciplinary Engineering Design Optimization (MEDO)*. DOI: [10.1109/MEDO.2016.7746538](https://doi.org/10.1109/MEDO.2016.7746538).
- Jones, R.M. (1998). *Mechanics Of Composite Materials*. Ed. by CRC Press. Materials Science and Engineering Series. Taylor and Francis. ISBN: 9781560327127.



- Jonkman, J. and W. Musial (2010). *Offshore Code Comparison Collaboration (OC3) for IEA Task 23 Offshore Wind Technology and Deployment*. Tech. rep. NREL/TP-5000-48191. NREL.
- Jonkman, J. et al. (2009). *Definition of a 5-MW reference wind turbine for offshore system development*. Tech. rep. TP-500-38060. NREL.
- Jorge Nocedal, Stephen J. Wright (1999). *Numerical Optimization*. Ed. by Springer. Springer series in operations research and financial engineering. Springer. ISBN: 9780387987934. DOI: [10.1007/978-0-387-40065-5](https://doi.org/10.1007/978-0-387-40065-5).
- Kleinmichel, H. (1970). "The Theory of Splines and Their Applications." In: *ZAMM - Journal of Applied Mathematics and Mechanics / Zeitschrift Angewandte Mathematik und Mechanik* 50.6, pp. 441–442. ISSN: 1521-4001. DOI: [10.1002/zamm.19700500646](https://doi.org/10.1002/zamm.19700500646). URL: <http://dx.doi.org/10.1002/zamm.19700500646>.
- Koziel, Slawomir and Leifur Leifsson (2011). "Airfoil Shape Optimization Using Variable-Fidelity Modeling and Shape-Preserving Response Prediction". English. In: *Computational Optimization and Applications in Engineering and Industry*. Ed. by Xin-She Yang and Slawomir Koziel. Vol. 359. Studies in Computational Intelligence. Springer Berlin Heidelberg, pp. 99–124. ISBN: 978-3-642-20985-7. DOI: [10.1007/978-3-642-20986-4\\_4](https://doi.org/10.1007/978-3-642-20986-4_4). URL: [http://dx.doi.org/10.1007/978-3-642-20986-4\\_4](http://dx.doi.org/10.1007/978-3-642-20986-4_4).
- Kwon, HyungIl, JuYeol You, and OhJoon Kwon (2012). "Enhancement of wind turbine aerodynamic performance by a numerical optimization technique". English. In: *Journal of Mechanical Science and Technology* 26.2, pp. 455–462. ISSN: 1738-494X. DOI: [10.1007/s12206-011-1035-2](https://doi.org/10.1007/s12206-011-1035-2). URL: <http://dx.doi.org/10.1007/s12206-011-1035-2>.
- Lagaros, Nikos D. and Manolis Papadrakakis (2016). *Engineering and Applied Sciences Optimization: Dedicated to the Memory of Professor M.G. Karlaftis*. Ed. by Manolis Papadrakakis. Springer Publishing Company, Incorporated. ISBN: 3319364650, 9783319364650.
- Lee, E. T. Y. (July 1989). "Choosing Nodes in Parametric Curve Interpolation". In: *Comput. Aided Des.* 21.6, pp. 363–370. ISSN: 0010-4485. DOI: [10.1016/0010-4485\(89\)90003-1](https://doi.org/10.1016/0010-4485(89)90003-1). URL: [http://dx.doi.org/10.1016/0010-4485\(89\)90003-1](http://dx.doi.org/10.1016/0010-4485(89)90003-1).
- Lee, Seunghoon et al. (2013). "Design optimization of wind turbine blades for reduction of airfoil self-noise". In: *Journal of Mechanical Science and Technology* 27.2, pp. 413–420. ISSN: 1976-3824. DOI: [10.1007/s12206-012-1254-1](https://doi.org/10.1007/s12206-012-1254-1). URL: <http://dx.doi.org/10.1007/s12206-012-1254-1>.
- Llorente, E et al. (2014). "Wind Tunnel Tests of Wind Turbine Airfoils at High Reynolds Numbers". In: *Journal of Physics: Conference Series* 524.1, p. 012012.
- Love, Augustus (1888). "The small free vibrations and deformation of a thin elastic shell". In: *Philosophical Transactions of the Royal Society of London A: Mathematical, Physical and Engineering Sciences* 179, pp. 491–546. ISSN: 0264-3820. DOI: [10.1098/rsta.1888.0016](https://doi.org/10.1098/rsta.1888.0016).
- Lowson (1993). "Assessment and Prediction of Wind Turbine Noise". In: *Department of Trade and Industry*.
- Macquart, T. et al. (2017). "A New Optimisation Framework for Investigating Wind Turbine Blade Designs". In: *Advances in Structural and Multidisciplinary Optimization*. Springer International Publishing, pp. 2044–2060.
- Matjaz Msrnik Janko Slavic, Miha Boltezar (2013). "Frequency-domain methods for a vibration-fatigue-life estimation—Application to real data". In: *International journal of fatigue* 47, pp. 8–17.

- MATLAB (2019). Version 9.1. The MathWorks. 1 Apple Hill Drive Natick, MA 01760-2098 USA.
- MATLAB *curve fitting toolbox* (2019). Version 3.5.8. 1 Apple Hill Drive Natick, MA 01760-2098 USA.
- MATLAB *Global Optimization Toolbox* (2019). Version 3.4.1. The MathWorks. 1 Apple Hill Drive Natick, MA 01760-2098 USA.
- MATLAB *Optimization Toolbox* (2019). Version 7.5. The MathWorks. 1 Apple Hill Drive Natick, MA 01760-2098 UNITED STATES.
- MATLAB *Parallel Computing Toolbox* (2019). Version 6.9. The MathWorks. 1 Apple Hill Drive Natick, MA 01760-2098 USA.
- McKay, Michael D. (1992). "Latin Hypercube Sampling As a Tool in Uncertainty Analysis of Computer Models". In: *Proceedings of the 24th Conference on Winter Simulation*. WSC '92. Arlington, Virginia, USA: ACM, pp. 557–564. ISBN: 0-7803-0798-4. DOI: [10.1145/167293.167637](https://doi.org/10.1145/167293.167637). URL: <http://doi.acm.org/10.1145/167293.167637>.
- McWilliam, Michael K. et al. (2018). "Optimal Aero-Elastic Design of a Rotor with Bend-Twist Coupling". In: *Journal of Physics: Conference Series* 1037.4, p. 042009.
- Méndez, Munduate, and SanMiguel (2014). "Airfoil family design for large offshore wind turbine blades". In: *Journal of Physics: Conference Series* 524.1, p. 012022.
- Molga, Marcin and Czeslaw Smutnicki (2005). "Test functions for optimization needs". In:
- Mukesh, R., K. Lingadurai, and S. Karthick (2012). "Aerodynamic optimization using proficient optimization algorithms". In: *Computing, Communication and Applications (ICCCA), 2012 International Conference on*. PARSEC, pp. 1–5. DOI: [10.1109/ICCCA.2012.6179183](https://doi.org/10.1109/ICCCA.2012.6179183).
- NASA *guide to Aeronautics* (2019). URL: <https://www.grc.nasa.gov/www/k-12/airplane/>.
- Nelder, J. A. and R. Mead (1965). "A Simplex Method for Function Minimization". In: *The Computer Journal*. DOI: [10.1093/comjnl/7.4.308](https://doi.org/10.1093/comjnl/7.4.308).
- Nilsson, Karl et al. (2014). "Airfoil data sensitivity analysis for actuator disc simulations used in wind turbine applications". In: *Journal of Physics: Conference Series (Online)* 524.1. ISSN: 1742-6596. DOI: [10.1088/1742-6596/524/1/012135](https://doi.org/10.1088/1742-6596/524/1/012135).
- Ning, S. Andrew, Rick Damiani, and Patrick J. Moriarty (2014). "Objectives and Constraints for Wind Turbine Optimization". In: *Journal of Solar Energy Engineering* 136.4.
- Obayashi, S., T. Tsukahara, and T. Nakamura (2000). "Multiobjective genetic algorithm applied to aerodynamic design of cascade airfoils". In: *Industrial Electronics, IEEE Transactions on* 47.1, pp. 211–216. ISSN: 0278-0046. DOI: [10.1109/41.824144](https://doi.org/10.1109/41.824144).
- Ostergaard, P Brath, and J Stoustrup (2007). "Estimation of effective wind speed". In: *Journal of Physics: Conference Series* 75.1, p. 012082.
- Overgaard, Lars Chr. T. and Erik Lund (2005). "Structural Design Sensitivity Analysis and Optimization of Vestas V52 Wind Turbine Blade". In: *World Congress on Structural and Multidisciplinary Optimization*.
- Passipoularidis, Vaggelis and Povl Brøndsted (2010). *Fatigue Evaluation Algorithms: Review*. Denmark. Forskningscenter Risoe. Risoe-R. Danmarks Tekniske Universitet, Risø Nationallaboratoriet for Bæredygtig Energi. ISBN: 978-87-550-3835-6.
- Paterson and Amiet (July 1976). "Acoustic radiation and surface pressure characteristics of an airfoil due to incident turbulence". In: *Aeroacoustics Conferences*. American Institute of Aeronautics and Astronautics, pp. -. DOI: [10.2514/6.1976-571](https://doi.org/10.2514/6.1976-571). URL: <https://doi.org/10.2514/6.1976-571>.

- Patrikalakis M. Maekawa T., Cho W. (2009). *Shape interrogation for computer aided design and manufacturing*. Ed. by Massachusetts Institute of Technology. Massachusetts Institute of Technology. URL: <http://web.mit.edu/hyperbook/Patrikalakis-Maekawa-Cho/>.
- Pavese, Christian et al. (2017). "Aeroelastic multidisciplinary design optimization of a swept wind turbine blade". In: *Wind Energy* 20.12. we.2131, pp. 1941–1953. ISSN: 1099-1824. DOI: [10.1002/we.2131](https://doi.org/10.1002/we.2131). URL: <http://dx.doi.org/10.1002/we.2131>.
- Petrone, Giovanni et al. (June 2011). "Wind Turbine Optimization Under Uncertainty with High Performance Computing". In: *AIAA Journal*.
- Phillips, Nathaniel D et al. (2017). "FFTrees: A toolbox to create, visualize, and evaluate fast-and-frugal decision trees". In: *Judgment and Decision Making* 12.4, pp. 344–368.
- Piegl, L. and W. Tiller (1997). *The NURBS Book*. Ed. by 1995 Springer. 2nd ed. Berlin, Heidelberg.
- Pourrajabian, Abolfazl et al. (Sept. 2016). "Hollow Blades for Small Wind Turbines Operating at High Altitudes". In: *Journal of Solar Energy Engineering* 138.6, pp. 061001–061001–8. ISSN: 0199-6231. DOI: [10.1115/1.4034333](https://doi.org/10.1115/1.4034333). URL: <http://dx.doi.org/10.1115/1.4034333>.
- Przemieniecki, Janusz S. (1968). *Theory of matrix structural analysis*. Ed. by McGraw-Hill. New York; London: McGraw-Hill, pp. –.
- R (2017). *R: A Language and Environment for Statistical Computing*. R Foundation for Statistical Computing. Vienna, Austria. URL: <https://www.R-project.org/>.
- Ragan, Patrick and Lance Manuel (2007). "Comparing Estimates of Wind Turbine Fatigue Loads using Time-Domain and Spectral Methods". In: *Wind Engineering* 31.2, pp. 83–99. DOI: [10.1260/030952407781494494](https://doi.org/10.1260/030952407781494494). URL: <http://dx.doi.org/10.1260/030952407781494494>.
- Rao, Singiresu S. (2009). "Introduction to Optimization". In: *Engineering Optimization*. John Wiley & Sons, Inc., pp. 1–62. ISBN: 9780470549124. DOI: [10.1002/9780470549124.ch1](https://doi.org/10.1002/9780470549124.ch1). URL: <http://dx.doi.org/10.1002/9780470549124.ch1>.
- Rechenberg, I. (Aug. 1965). "Cybernetic solution path of an experimental problem". In: *Royal Aircraft Establishment Translation No. 1122, B. F. Toms, Trans.* Farnborough Hants: Ministry of Aviation, Royal Aircraft Establishment.
- Ribeiro, A.F.P., A.M. Awruch, and H.M. Gomes (Oct. 2012). "An airfoil optimization technique for wind turbines". In: *Applied Mathematical Modelling* 36.10, pp. 4898–4907. ISSN: 0307-904X.
- Richard W. Vesel, Jr. (2009). "Optimization of a wind turbine rotor with variable airfoil shape via a genetic algorithm". PhD thesis. Aeronautical and Astronautical Engineering The Ohio State University.
- Saltelli, Andrea (2004). *Sensitivity Analysis in Practice: A Guide to Assessing Scientific Models*. Ed. by John Wiley and 2004 Sons. John Wiley and Sons, 2004. ISBN: 9780470870945. DOI: [10.1002/0470870958](https://doi.org/10.1002/0470870958).
- Samareh, Jamshid A. (May 2001). "Survey of Shape Parameterization Techniques for High-Fidelity Multidisciplinary Shape Optimization". In: *AIAA Journal* 39.5. Summary of individual parameterization techniques., pp. 877–884. ISSN: 0001-1452. DOI: [10.2514/2.1391](https://doi.org/10.2514/2.1391). URL: <http://dx.doi.org/10.2514/2.1391>.
- Sapidis, Nickolas S. (1994). *Designing fair curves and surfaces: shape quality in geometric modeling and computer-aided design*. Ed. by Cambridge. SIAM.

- Sartori, L et al. (2016). "Integration of prebend optimization in a holistic wind turbine design tool". In: *Journal of Physics: Conference Series* 753.6, p. 062006.
- Sartori, L et al. (2018). "Preliminary design and optimization of a 20MW reference wind turbine". In: *Journal of Physics: Conference Series* 1037.4, p. 042003.
- Sartori, Luca (2013). "Free-form methodology for aero-structural optimization of wind turbine blades." De Bottasso. PhD thesis. Facoltà di Ingegneria Industriale Politecnico de Milano.
- Schepers, J. P. (2007). "SIROCCO: Silent Rotors by Acoustic Optimization." In: *Second International Meeting on Wind Turbine Noise*.
- Shapiro, S. S. and M. B. Wilk (1965). "An Analysis of Variance Test for Normality (Complete Samples)". In: *Biometrika* 52.3/4, pp. 591–611. ISSN: 00063444.
- Shene, C.-K. (2011). *CS3621 Introduction to Computing with Geometry Notes*. Department of Computer Science Michigan Technological University. URL: <http://www.cs.mtu.edu/~shene/COURSES/cs3621/NOTES/notes.html>.
- Simley, Eric and Lucy Pao (2013). "Correlation between Rotating LIDAR Measurements and Blade Effective Wind Speed". In: *Aerospace Sciences Meetings*. American Institute of Aeronautics and Astronautics. DOI: 10.2514/6.2013-749. URL: <http://dx.doi.org/10.2514/6.2013-749>.
- Snel, H, J G Schepers, and B Montgomerie (2007). "The MEXICO project (Model Experiments in Controlled Conditions): The database and first results of data processing and interpretation". In: *Journal of Physics: Conference Series* 75.1, p. 012014.
- Sorensen, P., G. C. Larsen, and C. J. Christensen (Nov. 1995). "A Complex Frequency Domain Model of Wind Turbine Structures". In: *Journal of Solar Energy Engineering* 117.4, pp. 311–317. ISSN: 0199-6231. DOI: 10.1115/1.2847866. URL: <http://dx.doi.org/10.1115/1.2847866>.
- Stablein, Alexander R. and Morten H. Hansen (2016). "Effect of Turbulence on Power for Bend-Twist Coupled Blades". In: *Journal of Physics: Conference Series* 753.4, p. 042018.
- Struik, D.J. (1961). *Lectures on Classical Differential Geometry*. Addison-Wesley series in mathematics. Addison-Wesley Publishing Company. ISBN: 9780486656090.
- Sucameli, CR et al. (2018). "Comparison of some wind turbine noise emission models coupled to BEM aerodynamics". In: *Journal of Physics: Conference Series* 1037.2, p. 022038.
- Tegen, S. (2011). *2011 Cost of wind energy review*. Tech. rep. NREL (National Renewable Energy Laboratory).
- Tempel, J. van der (2010). "Design Of Support Structures For Offshore Wind Turbines". PhD thesis. Technische Universiteit Delft. DOI: 10.2495/978-1-84564-205-1/17.
- Thomsen, Ole Thybo (2009). "Sandwich Materials for Wind Turbine Blades. Present and Future". In: *Journal of Sandwich Structures & Materials* 11.1, pp. 7–26. DOI: 10.1177/1099636208099710. URL: <https://doi.org/10.1177/1099636208099710>.
- Tibaldi, C. et al. (July 2016). "Wind turbine fatigue damage evaluation based on a linear model and a spectral method". In: *Wind Energy* 19 (7). DOI: 10.1002/we.1898.
- Vecchia, Pierluigi Della, Elia Daniele, and Egidio DAMato (2014). "An airfoil shape optimization technique coupling {PARSEC} parameterization and evolutionary algorithm". In: *Aerospace Science and Technology* 32.1. PARSEC method. Optimization with GA., pp. 103–110. ISSN: 1270-9638. DOI: <http://dx.doi.org/10.1016/j.ast.2013.11.006>.



- Verelst, David Robert and Torben J. Larsen (2010). *Load Consequences when Sweeping Blades - A Case Study of a 5 MW Pitch Controlled Wind Turbine*. Ed. by DTU. Danmarks Tekniske Universitet, Risø Nationallaboratoriet for Bæredygtig Energi.
- Viterna, L A and D C Janetzke (1982). *Theoretical and experimental power from large horizontal-axis wind turbines*. DOI: [10.2172/6763041](https://doi.org/10.2172/6763041).
- Wagner, S., R. Bareiss, and G. Guidati (1996). *Wind turbine noise*. Environmental engineering. Springer. ISBN: 9783540605928.
- Wainwright, Haruko M. et al. (2014). "Making sense of global sensitivity analyses". In: *Computers & Geosciences* 65.0, pp. 84–94. ISSN: 0098-3004.
- Wang, Lin, Xiongwei Liu, and Athanasios Kolios (Oct. 2016). "State of the art in the aeroelasticity of wind turbine blades: Aeroelastic modelling". In: *Renewable and Sustainable Energy Reviews* 64. DOI: [10.1016/j.rser.2016.06.007](https://doi.org/10.1016/j.rser.2016.06.007).
- Wei, Taiyun and Viliam Simko (2016). *corrplot: Visualization of a Correlation Matrix*. R package version 0.77. URL: <https://CRAN.R-project.org/package=corrplot>.
- Wilcoxon, Frank (1945). "Individual Comparisons by Ranking Methods". In: *Biometrics Bulletin* 1.6, pp. 80–83. ISSN: 00994987.
- Williams, Ffowcs and Hawkins (1969). "Sound generation by turbulence and surfaces in arbitrary motion". In: *Philosophical Transactions of the Royal Society of London A: Mathematical, Physical and Engineering Sciences* 264.1151, pp. 321–342. ISSN: 0080-4614. DOI: [10.1098/rsta.1969.0031](https://doi.org/10.1098/rsta.1969.0031).
- Woodward, F. A. (Nov. 1968). "Analysis and design of wing-body combinations at subsonic and supersonic speeds." In: *Journal of Aircraft* 5 (6). DOI: [10.2514/3.43979](https://doi.org/10.2514/3.43979).
- XFOIL (2013). 6.99. Massachusetts Institute of Technology (MIT). Cambridge, Massachusetts, United States.
- Xudong, Wang et al. (2009). "Shape optimization of wind turbine blades". In: *Wind Energ.* 12.8, pp. 781–803. ISSN: 1099-1824. URL: <http://dx.doi.org/10.1002/we.335>.
- Zahle, Frederik et al. (2015). "Aero-Elastic Optimization of a 10 MW Wind Turbine". In: *AIAA SciTech Forum*. American Institute of Aeronautics and Astronautics. DOI: [10.2514/6.2015-0491](https://doi.org/10.2514/6.2015-0491). URL: <http://dx.doi.org/10.2514/6.2015-0491>.
- Zahle, Frederik et al. (2018). "Computational fluid dynamics-based surrogate optimization of a wind turbine blade tip extension for maximising energy production". In: *Journal of Physics: Conference Series* 1037.4, p. 042013.
- Ziegler, Lisa et al. (2015). "Sensitivity of Wave Fatigue Loads on Offshore Wind Turbines under Varying Site Conditions". In: *Energy Procedia* 80. 12th Deep Sea Offshore Wind R&D Conference, {EERA} DeepWind'2015, pp. 193–200. ISSN: 1876-6102. DOI: <http://dx.doi.org/10.1016/j.egypro.2015.11.422>.